POLITECNICO DI TORINO

Master's Degree in Computer Engineering

Master's Degree Thesis

Assessing microstructural brain differences in epileptic patients with vagus nerve stimulation via diffusion MRI, tractography and machine learning

Supervisors

Prof. Santa DI CATALDO

Ph.D Francesco PONZIO

Prof. Benoît MACQ

Ph.D Alexandre BERGER

Ph.D Nicolas DELINTE

Candidate

Michele CERRA

10 2023

Abstract

Objective: Vagus Nerve Stimulation (VNS) offers treatment for drug-resistant epilepsy, but the mechanism underlying its efficacy remains unclear. This study aimed to uncover microstructural features in VNS responders and non-responders using diffusion magnetic resonance imaging (dMRI), diffusion models and machine learning techniques.

Methods: Data were collected from 19 patients with drug-resistant epilepsy. Diffusion tensor imaging and other multi-compartment models (NODDI, DIAMOND and Microstructure Fingerprinting) were used to compute microstructural metrics within distinct regions of interest (ROIs) outlined on tractography pathways estimated using FreeSurfer and MRtrix3. We calculated the weighted mean, standard deviation, skewness, and kurtosis of the metrics along the tracts for summarising their distribution. Univariate analysis has been performed through non-parametric statistical tests: Mann-Whitney U rank, Kruskal-Wallis and Barnard exact tests. Multivariate analysis has been performed by a sequential feature selector to select the best classifying set of microstructural metrics. The extraction of Radiomics features has been conducted to get more informative characteristics about the shape and voxel intensities of the selected regions, feature selection algorithms together with classification algorithms have allowed us to classify non-responder patients. Deep Learning methodologies have been applied to classify patients without the use of precomputed ROIs. A pre-trained 3D encoder was used to reduce the size of the volumes and classify the responsiveness.

Results: Treatment in non-responders demonstrated a greater mean diffusivity (MD) in the thalamocortical connections, the fornix, and the anterior commissure ($p < 0.01$), as well as the feature selector, selected the fornix as best classifying features. Wavelet and local binary pattern features have been the most frequently selected by the Radiomics pipeline, reaching an accuracy above 0.9. Expected results have been found with deep learning approaches, overfitting has been observed due to the lack of a large dataset.

Interpretation: Further studies are needed to fully understand the roles of the corpus callosum, anterior commissure and longitudinal fasciculus in mediating the effect of VNS. Our results emphasize the potential of microstructural connections, machine learning and deep learning to guide personalized VNS treatment adjustments and prediction of non-responders patients to VNS.

Acknowledgements

I would like to thank my supervisor, Pr. Benoît Macq for giving me the opportunity to discover an interesting topic.

I am also grateful to Ph.D. Alexandre Berger and PhD. Nicolas Delinte. Their expertise, patience, and dedication guided me through the realization of this Master's thesis.

Finally, I am fortunate to have had the support of my family and friends throughout my studies.

Table of Contents

List of Tables

List of Figures

Acronyms

ACT Anatomically-constrained tractography
AD Axial Diffusivity
AED Anti-epileptic drug
AUC Area under the ROC Curve

CSD Constrained Spherical Deconvolution
CSF Cerebro Spinal Fluid
CV Cross Validation

DIAMOND DIstribution of 3D Anisotropic MicrOstructural eNvironments in Diffusion-compartment imaging
dMRI diffusion MRI
DRE Drug-Resistant Epilepsy
DRN Dorsal Raphe Nucleus
DTI Diffusion Tensor Imaging
DWI Diffusion Weighted Imaging
DW-MRI Diffusion-Weighted MRI

FA Fractional Anisotropy
FDA Food and Drug Administration
fMRI Functional Magnetic Resonance Imaging
FOD fiber Orientation Density Function

GLCM Gray Level Co-occurrence Matrix
GLDM Gray Level Dependence Matrix
GLRLM Gray Level Run Length Matrix
GLSZM Gray Level Size Zone Matrix
GM Grey Matter

HC Healthy Control

ICA Indipendent Component Analysis
ILF Inferior longitudinal fasciculus

IQR Interquartile Range

LC Locus Coeruleus
LOO Leave One Out

MAD Median Absolute Deviation
MD Mean Diffusivity
MF Microstructure fingerprinting
ML Machine Learning
MNI Montreal Neurological Institute
MRI Magnetic Resonance Imaging
MSMT-CSD Multi-shell Multi-tissue CSD

NE Norepinephrine
NGTDM Neighbouring Gray Tone Difference Matrix
NODDI Neurite Orientation Dispersion and Density Imaging
NR Non-responders to VNS
NTS Nucleus Tractus Solitarius

ODI Orientation Dispersion Index

PBN Parabrachial Nucleus
PCA Principal Component Analysis
PGSE Pulse Gradient Spin Echo
PR Partial responders to VNS

R Responders to VNS
RD Radial Diffusivity
RF Radio Frequency
ROI Region Of Interest

SD Standard Deviation
SFS Sequential Feature Selection
SLF Superior longitudinal fasciculus
ST Stria Terminalis
SUDEP Sudden Unexpected Death in Epilepsy
SVM Support Vector Machine

TE Echo time
TR Repetition time

VNS Vagus Nerve Stimulation

WM White Matter

Introduction

Epilepsy is a significant neurological disorder that affects millions of people worldwide [1]. Up to a third of epileptic patients have drug-resistant epilepsy [2]. In recent years, Vagus Nerve Stimulation (VNS) has emerged as a promising therapeutic intervention for drug-resistant epilepsy. Despite its clinical effectiveness, the underlying mechanisms of VNS are poorly understood, particularly concerning variability in treatment response [3].

Several studies have been conducted to predict the response to VNS. Mithani et al. [4] employed connectome profiling to identify responders to VNS, using machine learning algorithms to analyse diffusion data. This approach allowed them to find more connectivity and robust microstructures in the left-lateralized limbic system, thalamocortical connections and association fibres. Ibrahim et al. [5] highlighted the importance of presurgical thalamocortical connectivity in predicting response to VNS. They used machine learning algorithms to classify responders and non-responders based on functional MRI data (fMRI). Enhanced connectivity in thalamocortical connections, anterior cingulate cortex and insular cortex were found.

Leveraging advanced diffusion magnetic resonance imaging (dMRI) techniques, including DTI, NODDI [6], DIAMOND [7] and Microstructure Fingerprinting [8], we quantitatively assess various microstructural metrics within specific regions of interest (ROI). These advanced models enable the computation of various metrics representing distinct biological aspects of microstructure.

By employing these techniques, we aim to identify specific biomarkers associated with responders and non-responders. We extend the method by incorporating machine learning algorithms to predict responders to VNS based on the relations of microstructural metrics.

In the following chapters, we will discuss the method used in data collection, the computation of microstructural metrics using advanced dMRI techniques, the selection of specific ROIs and the statistical analyses performed. Our goal is to contribute to a deeper understanding of the neurobiological mechanisms of VNS response by examining the microstructural alterations induced, thus advancing personalised treatment approaches for drug-resistant epilepsy.

Chapter 1

Theoretical background

1.1 Magnetic Resonance Imaging

1.1.1 Magnetic properties of nuclei

Biological organisms and tissues are naturally rich in hydrogen atoms, mostly in water and fats. Magnetic Resonance Imaging (MRI) principles are based on the physical properties of hydrogen atoms of the body, allowing the reconstruction of anatomical, structural, and functional images.

From a classical point of view, an atomic nucleus can be assumed as a sphere rotating around its axis, as shown in Figure 1.1a. This rotation is called *spin* and it is the intrinsic angular momentum of the nucleus, and it can be an integer or a half-integer depending on the mass number[1] and the atomic number[2]. Spin can be observed in nuclei belonging to elements with odd atomic numbers or odd mass numbers. Hydrogen is composed of one proton. Therefore, the spin can take only the values $1/2$ and $-1/2$ [9].
Since the nucleus is a charged particle, a rotation of it creates a magnetic field. From this point of view, the particle behaves like a small magnetic dipole, as shown in Figure 1.1a: $\vec{\mu} = i\mathbf{S}$ where $\vec{\mu}$ is the intrinsic magnetic momentum that is aligned on its spin $\mathbf{S}$.
Normally the orientation of $\vec{\mu}$ is completely random due to thermal random motion, therefore, the sum of the magnetic momentum is null ($\sum_i \mu_i = 0$).
In an external magnetic field $\mathbf{B_0}$, a magnetic dipole can take two orientations: *parallel* or *anti-parallel*. The rotation of the particle and the external magnetic field create a *precession* around $\mathbf{B_0}$ like a spinning top, as shown in Figure 1.1b:

[1]Mass number: number of protons and neutrons

[2]Atomic number: number of protons

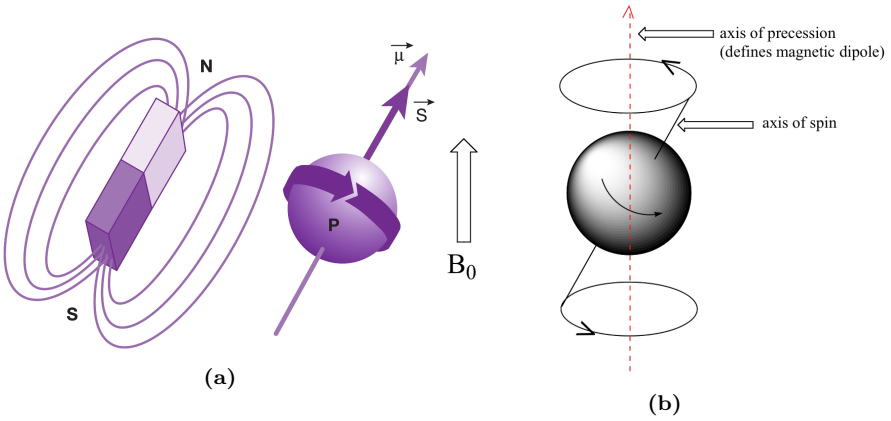

Figure 1.1: (a) Representation of the spin and the magnetic moment [10]; (b) Precessional motion of a proton spin in an applied magnetic field. [11]

$\mathbf{\Gamma} = \vec{\mu} \times \mathbf{B_0}$ where $\mathbf{\Gamma}$ is the *torque*. The axis rotates around the area of a "cone", with an angular speed proportional to the applied field following *Larmor's Law*:

$$f_0 = \frac{\gamma}{2\pi} B_0, \tag{1.1}$$

γ is the gyromagnetic ratio and it is a characteristic of the nucleus (for the atoms of hydrogen $\gamma = 42.58\,\mathrm{MHz\,T^{-1}}$). The frequency of precession is called *Larmor frequency*.
From a global point of view, the populations of protons moments create a macroscope magnetisation when an external magnetic field is applied, with the direction equal to the external field, as shown in Figure 1.2 on the right, defined by [9]:

$$\mathbf{M} = \frac{1}{V} \sum_i \vec{\mu_i}. \tag{1.2}$$

The transversal magnetization in xy plane is null since the components μ_{xy} rotates with distinct phases and overall, they nullify themselves, as shown on the left of Figure 1.2.
Without the magnetic field, it does not exist any difference between the two orientations (parallel and anti-parallel), because they are equiprobable, as shown in Figure 1.2 on the left. With the application of the static magnetic field, the antiparallel orientation will have higher energy ($N\downarrow$) than the parallel orientation with lower energy ($N\uparrow$) since it must be the opposite of the external field. The *occupation ratio* of the two energy levels is described by the *Boltzmann distribution*:

$$\frac{N_\uparrow}{N_\downarrow} = e^{-\frac{\Delta E}{kT}}, \tag{1.3}$$

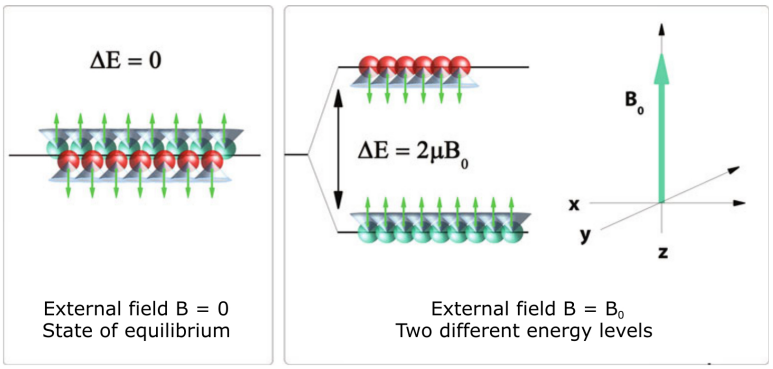

Figure 1.2: Separation of different energy levels after the application of the external field B_0. The proportion of low-level spins (i.e., parallel to the direction of the external magnetic field) is greater than the proportion of spins of higher energy (i.e., antiparallel to the direction of the external magnetic field). [12] Translated.

where k is the Boltzmann's constant, and T is the absolute temperature in [K]. The energy of a magnetic dipole in a magnetic field $\mathbf{B_0}$ can be defined by:

$$E = -\vec{\mu} \cdot \mathbf{B_0} = -\mu_z B_0 \Rightarrow,$$

where $\mu_z = \gamma \frac{h}{2\pi} I$, and continuing it:

$$\Rightarrow E_I = -\gamma \frac{h}{2\pi} I B_0,$$

where h is Planck's constant, and I is the spin orientation for the Hydrogen. Knowing that:

$$\Delta E = E_{-\frac{1}{2}} - E_{\frac{1}{2}} = h\frac{\gamma}{2\pi} B_0 = h f_0,$$

we find that there are more spins in $E_\uparrow$ (lower energy) state than in $E_\downarrow$ (higher energy) state, as shown in Figure 1.2.
The equilibrium macroscopic magnetization is non-zero and is defined by [9]:

$$M_0 = \frac{(\frac{\gamma}{2\pi})^2 h^2 \rho B_0 I(I+1)}{3kT}, \tag{1.4}$$

where ρ is the spin density[3]. $I = 1/2$ for Hydrogen.

1.1.2 Radiofrequency pulse

Measuring the M0 is easier with a variation of itself than a static magnetic field. Therefore, a variable signal can be generated if controlled oscillations are inducted

[3]Spin density: number of spins per unit volume

in the spin system [9]. If a RF pulse is applied at the Larmor frequency ($f_{RF} = f_0$) we observe a *resonance condition* 1.3, and if the system resonates with the pulse it starts to absorb energy 1.4.

$$B_1(t) = 2B_1(t)\cos(2\pi f_{RF}t + \phi)\mathbf{1_{xy}}. \tag{1.5}$$

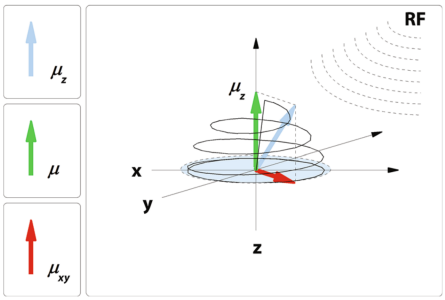

Figure 1.3: The trajectory of the magnetization vector. The vector describes a spiral trajectory by rotating at the Larmor frequency, tilting creates a transverse component of magnetisation, while the magnitude of the longitudinal component is reduced. [12]

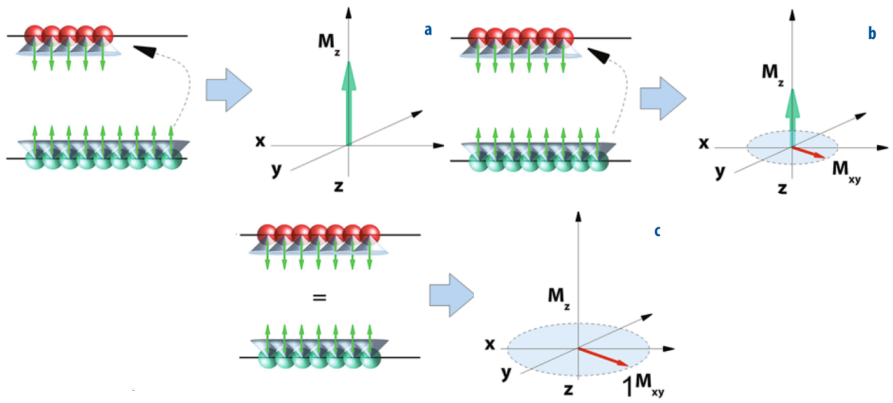

Figure 1.4: Effect of the RF impulse. (a) Initial situation; (b) Longitudinal and transverse components of the macroscopic magnetization; (c) State of the magnetization after applying a 90°-RF pulse. [12] Arranged.

The *flip angle* from the initial direction of the magnetization is defined by [9]:

$$\theta = \gamma B_1 T_{RF},$$

where T_{RF} is the duration of the RF pulse.
Now the magnetization vector can be represented with a longitudinal magnetization M_z and a transverse magnetization M_{xy} as in [9]:

$$\mathbf{M} = M_z\mathbf{1_z} + M_{xz}\mathbf{1_{xy}}. \tag{1.6}$$

1.1.3 Relaxation

After applying the RF pulse, it tends to return to the initial state, these phenomena are called *relaxation*.

$$\text{[Longitudinal magnetisation] } M_z \to M_0;$$

$$\text{[Transverse magnetisation] } M_{xy} \to 0.$$

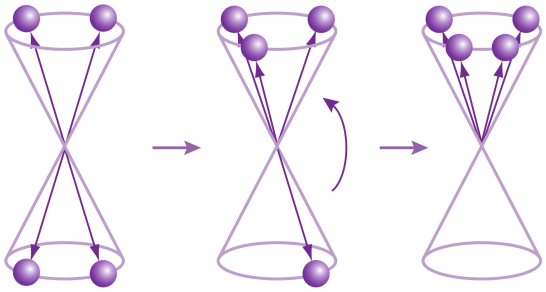

Figure 1.5: There is a progressive transition to the equilibrium from the high level to the lower level of energy. [10]

The first is the *longitudinal relaxation* (*spin-lattice relaxation* or *T1-relaxation*) in which the magnetisation recovers to its original M_0 because the energy state after the RF pulse is unstable, it will create a transition of spins from high energy to low energy, as shown in Figure 1.5. Can be mathematically described by [9]:

$$M_z(t) = M_0 + (M_z(0) - M_0)e^{-\frac{t}{T_1}}, \tag{1.7}$$

where T_1 is the time needed by M_z to reach 63% of the initial value M_0, as shown in Figure 1.6.
In the T_1-weighted image the signals must depend on the T_1 relaxation. Therefore, the time between the RF pulses must be brief, but sufficient to differentiate the different tissues, as shown in Figure 1.6. In these scans, the white matter (WM) is represented in light grey, the grey matter (GM) in a darker shade of grey, and the fluids in black.

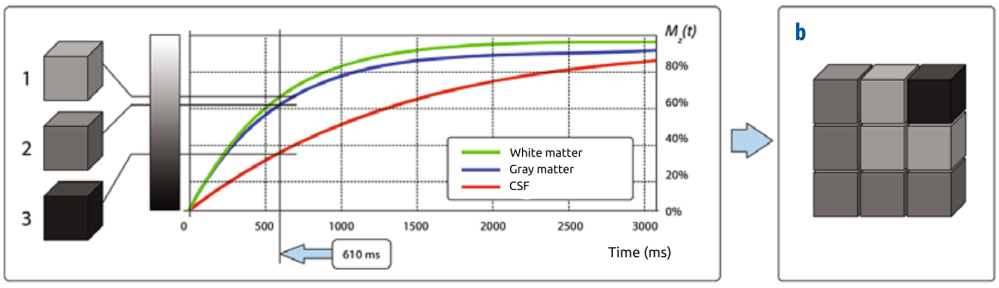

Figure 1.6: The T_1 relaxation time is different for types of tissue. [12] Translated.

The second phenomenon is the *transverse relaxation* (*spin-spin relaxation* or *T2-relaxation*) and it is characterized by a loss in the coherence of the spin phases, as shown in Figure 1.7. It can be written as [9]:

$$M_{xy}(t) = M_{xy}(0)e^{-\frac{t}{T_2}}, \tag{1.8}$$

where T_2 is the time needed to M_{xy} to reduce itself to 37% of the initial value 1.8.

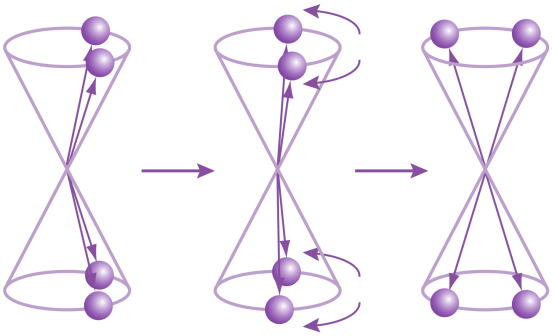

Figure 1.7: After the RF impulse there is a fast dephasing of the protons. The transversal magnetization M_{xy} decreases quickly. [10]

In the T_2-weighted image the signals must depend only on the T_2 relaxation. Therefore, we need to wait for the relaxation effects T_1 to be exhausted before reading the signal and sending a new one. In these scans, WM is dark grey, GM is light grey, and cerebral spinal fluid CSF is white, as shown in Figure 1.8.

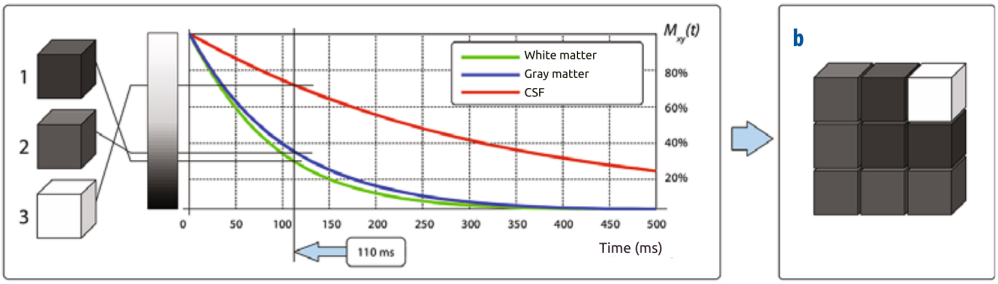

Figure 1.8: The T_2 relaxation time is different for types of tissue. [12] Translated.

In real conditions of an imperfect homogeneity of the field B_0 we see the *effective relaxation time*, defined by [9]:

$$\frac{1}{T_2*} = \frac{1}{T_2} + \gamma \Delta B_0, \tag{1.9}$$

where ΔB_0 are the inhomogeneities in the magnetic field.

1.1.4 Spin-echo sequence

To obtain images with different types of contrast is needed to control the time between RF pulses and the time between readings of the signal.

The first sequence used for clinical purposes is the *spin-echo*, which consists of a 90° RF pulse, a 180° RF pulse and an echo. It introduces two main parameters: the *Echo time* (TE) and the *Repetition time* (TR). The time between two 90° RF pulses is defined as TR, while the time between the RF pulse and the spin echo is defined as TE, as shown in Figure 1.9.

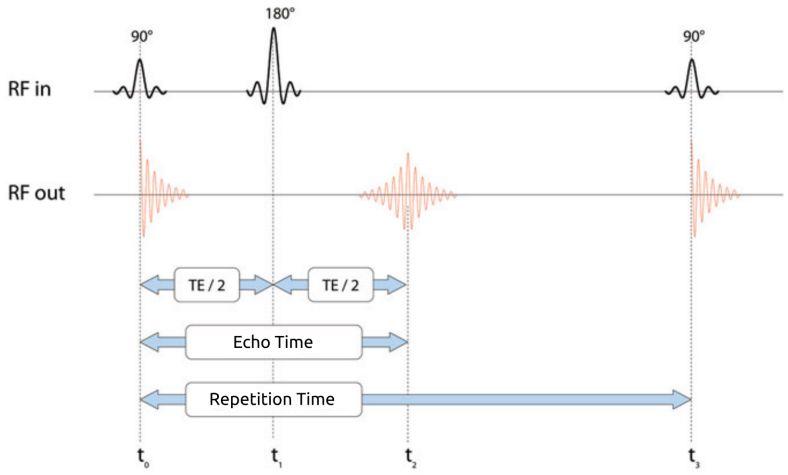

Figure 1.9: Diagram picturing the spin echo sequence. At the time t_0 is sent the first 90° pulse from which TE and TR start, all spins are tipped in the transverse plane. After $TE/2$ (t_1) the 180° pulse flips all the spins with respect to the transversal plane. At the time t_2 the spins are refocused, and they generate a spin echo, this is the Echo Time. After TR at t_3, a new spin echo sequence starts. Translated from [12].

The 180° RF pulse has a double intensity and is called *echo impulse*. An echo impulse mirrors all the spins of 180°, therefore, the faster spins and the slower ones are inverted in position, creating the possibility that all the spins are refocused at time TE. [9]

Contrast

By varying TE and TR, three types of contrast behaviour can be obtained, as shown in Figure 1.10:

- $TE << T_2$ and $TR = T_1$: T_1-contrast
- $TE = T_2$ and $TR >> T_1$: T_2-contrast
- $TE << T_2$ and $TR >> T_1$: ρ-contrast (proton density)

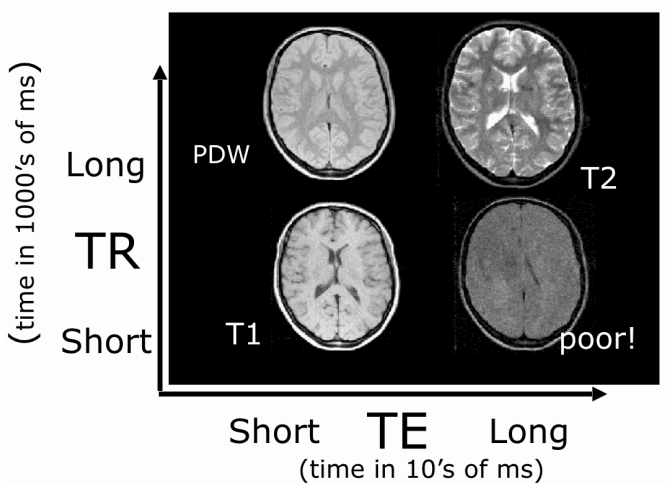

Figure 1.10: Matrix showing the different contrasts obtained with different TE and TR values. [13]

1.1.5 Spatial coding

To reconstruct the image, it is necessary to select a definite volume of tissue called *voxel*[4], three operations are needed to locate them in the tissue: selecting the layer (in the z-direction), selecting the column of the voxel (in the x-direction), and selecting the row (in the y-direction). These selections are done by linear variations of the magnetic field along a specific direction called *Gradient fields*.

To select a slice, a gradient is applied along the z direction, where the magnetic field changes from a minimum to a maximum, and at the point where the gradient is null the magnetic field is exactly B_0. Therefore, only the nuclei in the condition of resonance will generate a signal, see Figure 1.11.

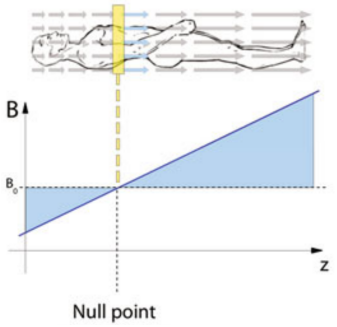

Figure 1.11: The effect of the gradient G_z is to resonate only the protons belonging to the slice in which the gradient is null (null point), only they have a field $B = B_0$ with a frequency equal to the Larmor frequency. [12]

[4]A voxel is the 3D expansion of a pixel

Using a gradient in the x-direction (G_x) creates a signal that is the *sum of the associated signals with different frequencies*. This gradient is called the *frequency encoding gradient* because the spins assume a precession frequency depending on the gradient. Successively, a gradient is applied along the y direction (G_y), called *Gradient of phase encoding*, it changes the spin phase depending on the gradient, as shown in Figure 1.12. In this way, each element of the section is different from the other by phase or frequency.

The raw data from these signals are collected in matrices that represent the *k-space* in the frequency domain, in which G_y selects the row and G_x scans it and saves it in the matrix. This sequence must be repeated n times for each line of the k-space to fill it, as shown in Figure 1.12. Then the *inverse Fourier transform* is applied to retrieve the image in the spatial domain.

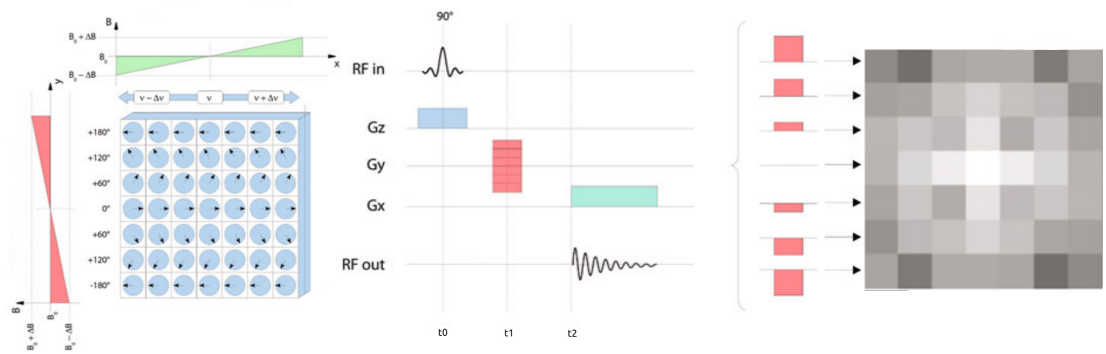

Figure 1.12: Gradients G_x and G_z, temporal diagram, and k-space. [12] Arranged.

1.2 Diffusion-Weighted MRI

Sequences of *Diffusion-Weighted MRI* (DW-MRI) can supply motion-dependent contrast of water molecules in tissues, which can significantly alter some brain diseases. These sequences are also known as *Diffusion Weighted Imaging* (DWI) or *diffusion MRI* (dMRI).

1.2.1 Pulse Gradient Spin Echo

The *Pulsed Gradient Spin Echo* (PGSE) sequence is the main diffusion-weighted sequence used, it is composed of two magnetic gradients, before and after the 180° RF pulse of the classic spin echo sequence. When the first diffusion gradient is applied, the water molecules are dephased and the second gradient, after the 180° RF pulse, will rephase the magnetisation, as shown in Figure 1.13. The difference in gradient intensity which is subject to the water molecule is proportional to the

distance travelled on the time between the two gradients and the gradient intensity. Therefore, the protons that move faster will have a greater dephase.[12]

The intensity of a voxel can be described by the Stejskal-Tanner equation as defined in [14], in which the signal will be equal to the intensity of a T_2-weighted image, reduced by a quantity that depends on the diffusion of the molecules.

$$I = I_0 \cdot e^{-b_{PGSE} \cdot D}, \tag{1.10}$$

where I is the intensity of the received signal, I_0 is the intensity of the base signal (T_2-weighted), b_{PGSE} is the factor of sensibility (parameters of PGSE sequence), and D is the coefficient of diffusivity (intrinsic characteristic of the tissue).

$$b_{PGSE} = (\gamma G \delta)^2 (\Delta - \frac{\delta}{3})[s/mm^2], \tag{1.11}$$

where G is the diffusion gradient intensity, δ is the duration of the diffusion gradient and Δ is the time between the first diffusion and the second.

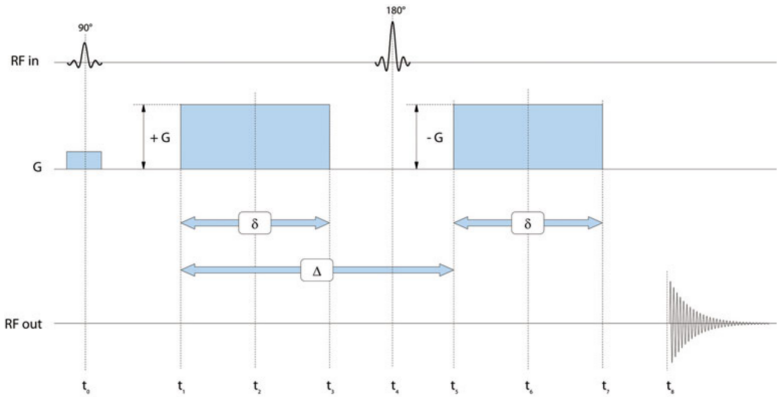

Figure 1.13: Between the two diffusion gradients is present the 180° RF pulse, therefore the second gradient is equal to the first one because the spin was already flipped by the 180° RF pulse. [12]

The diffusion can be affected even by pressure, temperature, and molecular interactions, and DW-MRI cannot distinguish between these different causes. Furthermore, if the path followed during diffusion is random rather than linear, the signal will be only a measure between the starting point and the endpoint. For these reasons, D is not correct and should be replaced by a coefficient called the *apparent diffusion coefficient* (ADC) [12].

$$I = I_0 \cdot e^{-b_{PGSE} \cdot ADC}. \tag{1.12}$$

Moreover, parts of the brain have free diffusion in all directions while in others the movement of water molecules is contained between tissues. For example, diffusion in WM will be higher along the direction of the axons rather than the perpendicular direction, the diffusion is called *anisotropic*. While, if the diffusion does not have any preferential direction, such as in the CSF, the diffusion is called *isotropic*, see Figure 1.14. In this case, the Stejskal-Tanner equation as defined in [14] becomes:

$$I = I_0 \cdot e^{-b_{PGSE} \cdot \hat{g}^T \mathbf{D} \hat{g}}, \tag{1.13}$$

where $\hat{g}$ is the gradient direction vector.

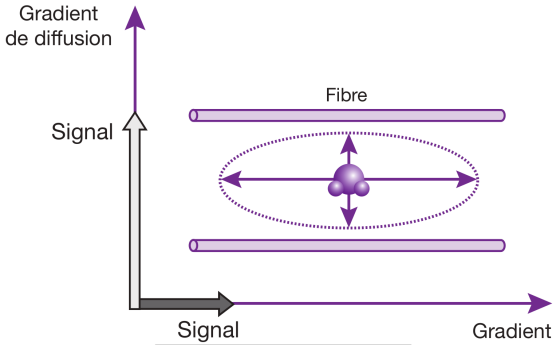

Figure 1.14: In the WM, the diffusion of the water molecules is free along the axon fibres, but it is reduced perpendicularly to the fibres. This is a case of Anisotropic diffusion. [10]

DWI collects data only from several gradient directions. The number of gradients depends on how many angles the 360-degree circle can be cut. For example, DWI with 12 gradient directions will take a scan every 30 degrees.[15]

1.2.2 Diffusion Tensor Imaging

One of the most popular and widely used mathematical models to describe the primary orientation of white matter axon path is called *diffusion tensor imaging* (DTI). This model was introduced in 1994 [16] and it consists of estimating an effective *diffusion tensor* ($\mathbf{D}$) within a voxel, which allows it to represent its properties with a 3D ellipse. The diffusion tensor is described by a 3x3 symmetric tensor that uses 6 PGSE sequences, one for each different orientation of the diffusion gradient, because $D_{yx} = D_{xy}$, $D_{zx} = D_{xz}$ and $D_{zy} = D_{yz}$.

$$\mathbf{D} = \begin{pmatrix} D_{xx} & D_{xy} & D_{xz} \\ D_{yx} & D_{yy} & D_{yz} \\ D_{zx} & D_{zy} & D_{zz} \end{pmatrix}. \tag{1.14}$$

Using the eigen decomposition of $\mathbf{D}$, eigenvectors and eigenvalues are computed and they are used to represent an ellipse in 3 orthogonal directions, as shown in Figure 1.15. The eigenvalues λ_i are the likelihoods of the diffusion direction of a voxel. The largest eigenvalue(λ_1) is the principal direction of axons in that voxel.

$$\mathbf{D} = \mathbf{Q}\mathbf{\Lambda}\mathbf{Q}^{-1},$$

$$\mathbf{\Lambda} = \begin{pmatrix} \lambda_1 & 0 & 0 \\ 0 & \lambda_2 & 0 \\ 0 & 0 & \lambda_3 \end{pmatrix}. \tag{1.15}$$

The result of DW-MRI is difficult to visualise in a single image. To summarise the information, the eigenvalues are used to compute some metrics that characterise

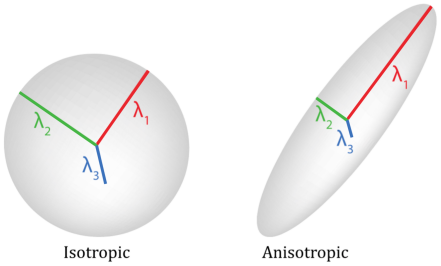

Figure 1.15: Isotropic and anisotropic tensor shapes that are characterized by the eigenvalues of **D** (λ_1, λ_2, λ_3). [17]

each voxel. The most used are the *Mean Diffusivity* (MD) and the *Fractional Anisotropy* (FA) and they are computed by the *Trace* of the diffusion matrix as defined in [14]:

$$MD = \frac{Tr(D)}{3} = \frac{\lambda_1 + \lambda_2 + \lambda_3}{3}, \tag{1.16}$$

$$FA = \sqrt{\frac{3}{2}} \frac{\sqrt{(\lambda_1 - MD)^2 + (\lambda_2 - MD)^2 + (\lambda_3 - MD)^2}}{\sqrt{\lambda_1^2 + \lambda_2^2 + \lambda_3^2}}. \tag{1.17}$$

The MD is proportional to the *Trace* and it quantifies the amplitude of the ellipse, or how much a particle is free to move, it is expressed in mm^2/s. Therefore, the MD does not give any information about the directions, but on how much free water is contained in a voxel. MD is considered to be an indicator of WM damage. The FA is a metric between 0 and 1 and it measures the degree of anisotropy in a voxel. The more the eigenvalues are similar, the more FA tends to 0. On the other hand, a fully anisotropic diffusion will have a value of 1.

Other metrics exist, such as the *Axial Diffusivity* (AD) and the *Radial Diffusivity* (AD), defined in [14]. AD is expressed in mm^2/s, and it is the diffusivity along the principal axis of the diffusion ellipsoid. While the RD is a measure used to express the diffusivity perpendicular to the principal direction of diffusion, expressed in mm^2/s.

$$AD = \lambda_1, \tag{1.18}$$

$$RD = \frac{\lambda_2 + \lambda_3}{2}. \tag{1.19}$$

Both FA and MD can be represented on the *diffusion direction maps*. The CSF will have a high MD since the water is free to move in all directions, while the WM will have a high FA because oriented in a single direction. The image obtained from FA is called *FA map* and it is often displayed as *RGB FA maps*, in which colours are used to stand for the principal direction of the diffusion (Red: left-right; Green: anterior-posterior; Blue: superior-inferior).

Metrics interpretation

The FA in WM measures the axonal integrity and organization in voxels with a single fibre population, it may be an indicator of packing of fibres, coherence in the main preferred diffusion direction [18] and myelination in a voxel [19]. The MD and the FA are often used as complementary measures [19].
The MD in WM is an indicator of fibre damage (cell membrane deterioration), it is similar for both GM and WM and higher for CSF [20].
AD tends to be variable in WM changes and it measures axonal damage and degeneration. The RD in WM measures the degree of myelination and changes in the axonal diameters or density may also influence RD. A higher RD indicates demyelination and a higher AD can mean "a reduction in crossing fibres that results in a higher principal axis of diffusion because fibres running in other directions are no longer present" [21].

Limitations of DTI

The main limitation of the DTI model is that water molecules follow a Gaussian distribution. Therefore, only a bundle of fibres can be modelled inside each voxel, but a complex organisation of fibres is present in every voxel. For example, a voxel having two crossing fibres is modelled by a large diffusion tensor rather than two narrow tensors, as shown in Figure 1.16. Therefore, in these voxels, the DTI model does not hold the assumption of a Gaussian distribution, and the resulting FA does not reflect the actual anatomical microstructure. [12]

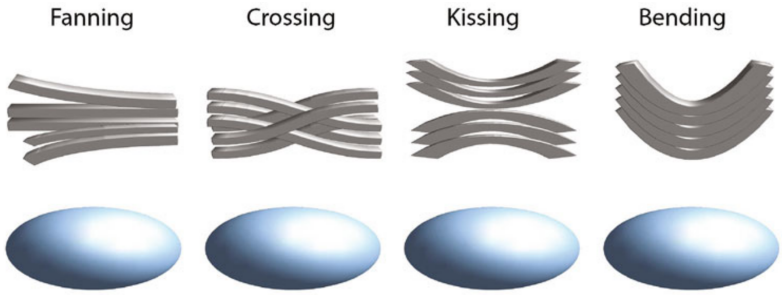

Figure 1.16: In the cases of *fanning*, *crossing*, *kissing*, and *bending* the DTI model is not capable to distinguish the differences. [12]

1.2.3 Tractography

Tractography is a technique to estimate the pathways of white matter fibres in the brain using data from DW-MRI. At first, tractography was introduced by [22] using his proposed DTI model [16] [23]. But DTI assumes that white matter

fibres have a single orientation (tensor) within each voxel, which can lead to false trajectory results in regions with crossing fibres, as explained in 1.2.2 and shown in Figure 1.16 [24]. To resolve these limitations more advanced algorithms such as Constrained Spherical Deconvolution (CSD) [25] are used.

CSD estimates the *fibre orientation distribution* (FOD) from diffusion data. This distribution value supplies information on other independent direction signals present within a voxel. In the CSD model, the signal $S(\theta, \phi)$ is assumed as convolution over the unit sphere between the FOD $F(\theta, \phi)$ and the response function $R(\theta)$, as defined in [26] and shown in Figure 1.17a:

$$S(\theta, \phi) = F(\theta, \phi) \circledast R(\theta). \tag{1.20}$$

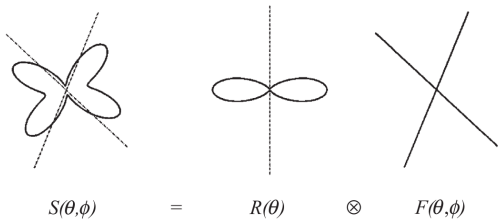

(a) 2D illustration of a voxel having two fibre populations. It can be expressed as a convolution over the unit sphere of an axially symmetric response function $R(\theta)$ with a fibre orientation density function $F(\theta, \phi)$. In this case $F(\theta, \phi) = \frac{1}{2}\delta(\theta_1, \phi_1) + \frac{1}{2}\delta(\theta_2, \phi_2)$. [26]

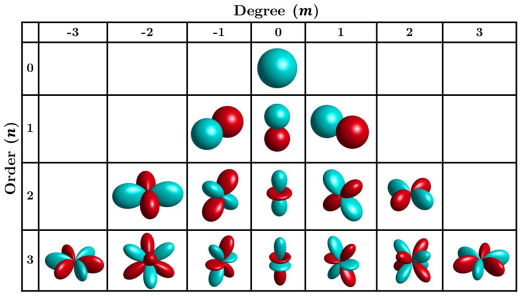

(b) Real parts of the spherical harmonics up to the third order (n = 0,1,2,3), for degree between $-3 \leq m \leq 3$, with lobes in cyan colour showing positive values and lobes in red colour showing negative values. [27]

To estimate the FOD using CSD, it is first necessary to write the FOD as a linear combination of *spherical harmonic basis functions* 1.17b. Then the FOD $F(\theta, \phi)$ can be obtained by performing the *spherical deconvolution* [28].
CSD supports only data acquired from a single shell[5] and can supply high-quality FOD estimates in voxel having WM only, in other cases the results may be unreliable and noisy. In [29] was developed a new model Multi-shell Multi-tissue CSD (MSMT-CSD), which considers also extra-cellular and other tissues for each voxel.

Deterministic and Probabilistic Tractography

There are two different strategies used in fibre tractography: deterministic and probabilistic algorithms, as shown in Figure 1.18. Both obtain as input diffusion

[5]In dMRI, a "shell" refers to a set of diffusion-weighted images acquired using the same b-value or a range of b-values. Multi-shell dMRI refers to the acquisition of diffusion-weighted images using multiple b-values (e.g., b=0, b=1000, b=2000, b=3000 $[s/mm^2]$)

data or a FOD, and starting from seed points they follow a preferred diffusion direction.

Deterministic tractography is a straightforward approach that involves tracking the dominant direction of diffusion in each voxel of the brain. Given a seed point exists a unique streamline. However, deterministic tractography is sensitive to noise and crossing fibres (e.g., the DTI model).

Probabilistic tractography models the distribution of pathways rather than a single deterministic solution, and the resulting tractography is based on a probability distribution of pathways. Due to the distribution, a seed point can generate different pathways to the target. Probabilistic tractography can supply a more robust estimate of the tracts in the brain (e.g., MSMT-CSD model). [30] For these reasons, we will use probabilistic algorithms in this study.

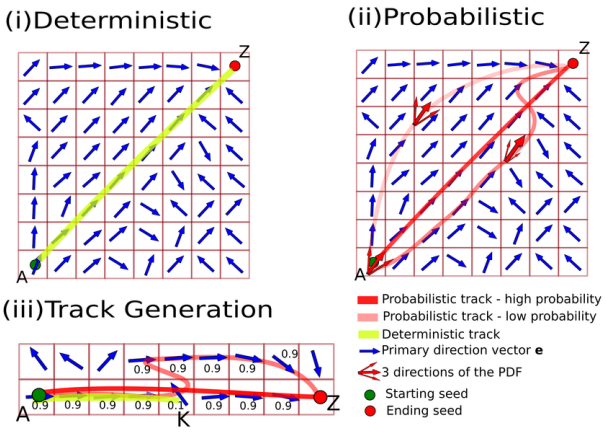

Figure 1.18: A Basic example shows the difference between deterministic and probabilistic tracking models. [31]

1.3 DW-MRI Microstructural models

1.3.1 NODDI (Neurite Orientation Dispersion and Density Imaging)

Dendrites and axons can be called neurites. Neurite Orientation Dispersion and Density Imaging (NODDI) is a three-compartment tissue model that models the microstructure complexity of neurites. Such indices of neurites supply more specific markers of brain tissue microstructure than DTI. [6]

NODDI distinguishes three types of microstructural environments: intra-cellular, extra-cellular and CSF compartments. Each compartment gives rise to a separate normalized MR signal A_i combined as:

$$A = (1 - \nu_{iso})(\nu_{ic}A_{ic} + (1 - \nu_{ic})A_{ec}) + \nu_{iso}A_{iso}, \tag{1.21}$$

where A_{ic}, A_{ec}, A_{iso}, and ν_{ic}, ν_{iso} are the normalized signals and volume fractions of intra-cellular, extra-cellular and CSF compartments, respectively.

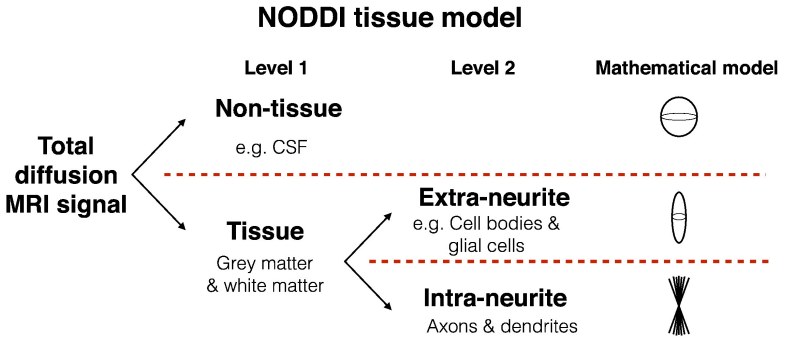

Figure 1.19: Different compartments modelled by NODDI. The non-tissue compartment is modelled by isotropic diffusion. The intra-neurite compartment models the fascicles as orientally dispersed sticks, while the space around the fascicles is modelled by an anisotropic diffusion model. [32]

The *intra-cellular* compartment models the space delimited by the membrane of neurons. This space is modelled by cylinders of zero radii (*sticks*), and their orientation distribution can range from highly parallel to highly dispersed. A *Watson distribution* models the orientation distribution function as:

$$f(\mathbf{n}) = M(\frac{1}{2}, \frac{3}{2}, \kappa)^{-1} e^{\kappa(\mu \mathbf{n})^2}, \tag{1.22}$$

where M is the hypergeometric function, μ is the mean orientation, and κ measures the orientation dispersion around μ. The normalized signal A_{ic} is expressed as follows:

$$A_{ic} = \int_{\mathbb{S}^2} f(\mathbf{n}) e^{-b d_{\parallel} (\mathbf{q}\cdot\mathbf{n})^2} \, d\mathbf{n}, \tag{1.23}$$

where $\mathbf{q}$ is the gradient direction and b is the b-value, $f(\mathbf{n})d\mathbf{n}$ gives the probability of finding sticks along orientation $\mathbf{n}$. The $e^{-b d_{\parallel} (\mathbf{q}\cdot\mathbf{n})^2}$ term gives the signal attenuation due to unhindered diffusion along a stick with intrinsic diffusivity $d_{\parallel}$ and orientation $\mathbf{n}$.

The *extra-cellular* compartment models the space around the neurons which is occupied by distinct types of glial cells and additionally, GM and cell bodies [6]. The diffusion motion is modelled by a Gaussian anisotropic distribution and the normalized signal is modelled with a tensor since the perpendicular diffusivity is considered:

$$\log A_{ec} = -b \mathbf{q}^T (\int_{\mathbb{S}^2} f(\mathbf{n}) D(\mathbf{n}) \, d\mathbf{n}) \mathbf{q}, \tag{1.24}$$

where $D(\mathbf{n})$ is the diffusion tensor with the principal diffusion direction $\mathbf{n}$, diffusion coefficients $d_{\parallel}$ and $d_{\perp}$ parallel and perpendicular to $\mathbf{n}$, respectively.

The CSF compartment models the space occupied by CSF and is modelled as isotropy Gaussian diffusion with diffusivity d_{iso}:

$$A_{ios} = e^{-bd_{iso}}. \tag{1.25}$$

Model parameters

The complete set of parameters for the NODDI model is composed of intra-cellular volume fraction (ν_{ic}) also called *Neurite Density Index* (NDI), parallel diffusion coefficient ($d_{\|}$), concentration parameter of Watson distribution (κ), mean orientation of Watson distribution (μ), isotropic volume fraction (ν_{iso}), isotropic diffusivity (d_{iso}) [6]. The diffusivities are fixed to typical values[6] and the remaining parameters are estimated. Furthermore, it is possible to compute the *Orientation Dispersion Index* (ODI) [6], which quantifies the angular variation of the orientation of the neurites, and that is defined as:

$$ODI = \frac{2}{\pi}\arctan(\frac{1}{\kappa}). \tag{1.26}$$

Model output

The outputs of the model are:

- icvf: Thresholded intra-cellular volume fraction
- ODI: Fibre orientation dispersion index
- f_{bundle}: Fibre bundles volume fraction
- f_{extra}: Extra-cellular volume fraction
- f_{intra}: Intra-cellular volume fraction
- f_{iso}: Free water volume fraction

where

$$(fextra + fintra) + fiso = fbundle + fiso = 1. \tag{1.27}$$

Metrics interpretation

f_{intra} stands for the intra-neurite compartment and can measure axonal regeneration. f_{extra} measures the variation of microglial cells which can be interpreted as an integrity measure of myelination. An increase in f_{iso} describes cell shrinkage and a decrease in tissue volume fraction. The ODI metric in WM may indicate loss of tissue structural integrity. While in the context of GM, it may reflect the degree of complexity of dendritic trees [33].

[6]The diffusivities are fixed to respective typical values: $d_{\|} = 1.7 \times 10^{-}3mm^2s^{-1}$ and $d_{iso} = 3 \times 10^{-3}mm^2s^{-1}$

Limitations

NODDI focuses on explicitly modelling the fascicle dispersion with a Watson distribution of sticks in each voxel, but this assumption is inconsistent with the know tissue microstructure: fascicles with various microstructures have been seen in the brain. Furthermore, it ignores intra-axonal radial diffusivity and considers only a single fascicle compartment per voxel, while fascicle crossing with an angle $> 40°$ occurs in $60 - 90\%$ of the voxels. Quoting what was written by Scherrer et al. [7], "NODDI can capture crossing fascicles as increased dispersion but cannot characterize each of them separately".

1.3.2 DIAMOND

The signal arising from a voxel is composed of signals arising from multiple compartments. The *DIstribution of 3D Anisotropic MicrOstructural eNvironments in Diffusion-compartment imaging* (DIAMOND) is a hybrid biophysical model of tissues that combines multicompartment and statistical modelling to supply insight into each compartment in each voxel [7].

It is inspired by the statistical framework of [34] which describes the diffusion of microstructural environments in a voxel with a 1D probability distribution, which explains the fraction of spin packets with a certain diffusion value in the voxel. From 'The basic of MRI' book [35] "a spin packet is a group of spins experiencing the same magnetic field strength".

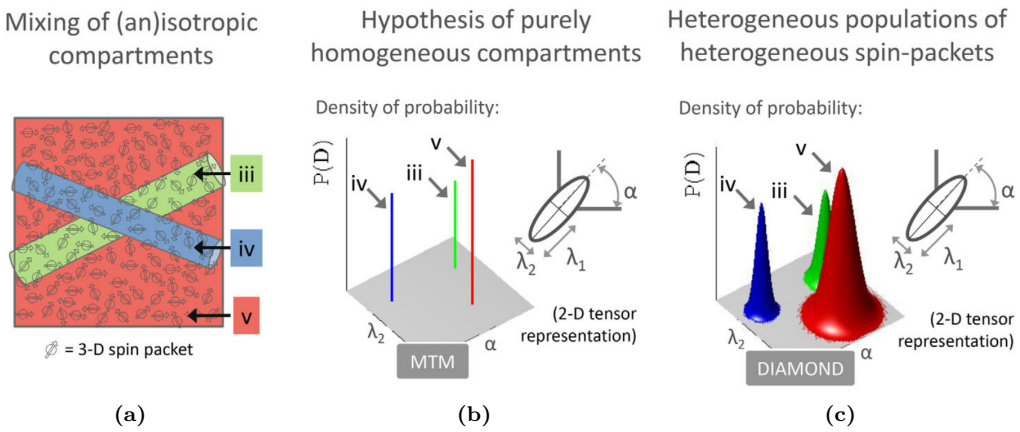

Figure 1.20: (a) Example of a voxel in which an isotropic (red) and two anisotropic (blue and green) compartments are mixed in DIAMOND; (b) The corresponding probability density function of diffusivities is composed of a mixture of delta functions; (c) Peak-shaped distributions of diffusivities. [7]

DIAMOND requires the estimation of the number of tissue compartments in each voxel, which enables direct assessment of compartment-specific diffusion characteristics such as the compartment to mean diffusivity (cMD), axial diffusivity (cAD), and radial diffusivity (cRD).

The *matrix-variate* distribution $P(\mathbf{D})$ gives the probability of the spin packet described by a 3D diffusivity $\mathbf{D}$ in the voxel [7]. Therefore, if a voxel consisted of exactly one *homogeneous* microstructural environment characterised by a tensor $\mathbf{D}^0$, then $P(\mathbf{D})$ would be a delta function $P(\mathbf{D}) = \delta(\mathbf{D} - \mathbf{D}^0)$ and the model would be equivalent to DTI. While, if it consisted of several identifiable homogeneous microstructural environments, a mixture of delta functions would be used [7], as shown in Figure 1.20b. Then the diffusion signal S_k is modelled by:

$$S_k = S_0 \int_{\mathbf{D}\in Sym^+(3)} P(\mathbf{D}) \exp(-b_k \mathbf{g}_k^T \mathbf{D} \mathbf{g}_k)\, d\mathbf{D}, \tag{1.28}$$

where $Sym^+(3)$ is the set of 3x3 SPD[7] matrices, $\mathbf{g}_k$ is the orientation of the diffusion gradient and b_k is the b-value of the sequence.

In reality, each microstructural environment is never *homogeneous*. DIAMOND uses a *matrix-variate Gamma* (mv-Γ) distribution centred in D^0 to model the population of spin packets, as shown in Figure 1.20c. The distribution shape can be modelled by the *shape* $\kappa > \frac{p-1}{2}$ and $\Sigma \in Sym^+(3)$ Sigma parameters [7].

$$P_{\kappa,\Gamma}(\mathbf{D}) = \frac{|\mathbf{D}|^{\kappa-(p+1)/2}}{|\Sigma|^{\kappa}\Gamma_p(\kappa)} \exp(-trace(\Sigma^{-1}\mathbf{D})), \tag{1.29}$$

where $|\cdot|$ is the matrix determinant and Γ_p is the multi-variate gamma function. Its expectation is $\mathbf{D}^0 = \kappa\Sigma$, and the shape parameter κ decides the concentration of the density around the mean value $\mathbf{D}^0$.
A heterogeneity index ($cHEI$) can be computed following the same transform as ODI in NODDI [6]: $cHEI(\kappa) = 2/\pi \arctan(1/\kappa)$.

Considering N_p populations each of them with a mv-Γ distribution $P_{\kappa_j,\Sigma_j}(\mathbf{D})$ with $j \in [1, ..., N_p]$ the matrix-variate distribution is defined as [7]:

$$P(\mathbf{D}) = \sum_{j=1}^{N_p} f_j P_{\kappa_j,\Sigma_j}(\mathbf{D}), \tag{1.30}$$

where f_j is the occupation fractions and $\sum_{j=1}^{N_p} f_j = 1$.

[7]SPD: symmetric positive-definite matrices 3x3

Combining 1.28 and 1.30 and using the Laplace transformation, the following model is found [7]:

$$S_k = S_0 \sum_{j=1}^{N_p} f_j \mathcal{D}(\mathbf{D}_j^0, \kappa_j), \tag{1.31}$$

where $\mathcal{D}(\mathbf{D}^0, \kappa) = S_0(1 + \frac{b_k \mathbf{g}_k^T \mathbf{D}^0 \mathbf{g}_k}{\kappa})^{-\kappa}$.

Model output

Considering only two compartments and the CSF, the resulting outputs of the model are:

- Fractions of all the population f_j and the CSF fraction;
- Fibre population tensor t_j for each compartment;
- Heterogeneity index $cHEI$ for each population and CSF.

From the tensor arrays, it is possible to compute the eigenvalues and DTI metrics for each voxel (see Section 1.2.2) for each compartment (cM_j). Therefore, we have DTI metrics for each compartment that can be merged with a weighted sum, as in the following formula:

$$wM = \frac{f_0 * cM_0 + f_1 * cM_1}{f_{tot}} = \frac{f_0 * cM_0 + f_1 * cM_1}{f_0 + f_1}. \tag{1.32}$$

Metric interpretation

Compartmentalized DTI metrics (wFA, wMD, wAD, wRD) can be extracted from t_0 and t_1 and they differ from the values obtained using DTI since more compartments are considered in a single voxel. They have the same interpretation of DTI metrics.

Limitations

To summarise, DIAMOND focuses on capturing the distribution of 3D diffusivity arising from each tissue compartment, and it requires the estimation of the number of tissue compartments (N_p) in each voxel, that is, the number of mv-Γ components. The estimation of N_p could be the only limitation of this model.

1.3.3 Microstructure fingerprinting

Microstructure fingerprinting (MF) is a model that uses Monte Carlo simulations to estimate physically interpretable microstructural parameters, both in single and in crossing fascicles of axons in each voxel [8]. It is a multi-compartment model,

each voxel is composed of different structures. The *fingerprints* are pre-computed DW-MRI signals that simulate a wide collection of a possible configurations of fibres in a voxel. At each voxel, the best sparse combination of fingerprints is found through an optimization solver, giving us microstructural parameters. [8]

MF is based on the *superposition principle* of crossing bundles, as shown in Figure 1.21. It assumes that the DW-MRI signal S of each voxel is composed of independent contributions of K bundles of axons with different orientations $\mathbf{u}_k$ occupying fractions ν_k of the physical volume and a partial volume ν_{CSF} of CSF [8]. S can be expressed as:

$$\begin{aligned} S &= M_0 \left[\sum_{k=1}^{K} \nu_k A_{fasc}(\, \mathbf{\Omega}_k, \mathbf{T}_k, \mathbf{u}_k; \mathbf{g}) \, + \nu_{csf} A_{csf}(\, D_{csf}, \mathbf{T}_{csf}; \mathbf{g}) \right], \\ &= \sum_{k=1}^{K} w_k A_k + w_{csf} A_{csf} \end{aligned} \tag{1.33}$$

where M_0 is the initial transverse magnetization of the voxel, $A_k := A_{fasc}(\, \mathbf{\Omega}_k, \mathbf{T}_k, \mathbf{u}_k; \mathbf{g})|$ is the normalized DW-MRI signal of the k-th fascicle, modelled by a Monte Carlo simulation, that would arise from an environment composed of fascicles with parameters $\mathbf{\Omega}_k$ and $\mathbf{T}_k$, and w_k is its weight defined as 1.34. Water is assumed to diffuse freely and isotropically with a scalar diffusivity D_{csf}.

$$w_k = M_0 \nu_k \iff \nu_k = \frac{w_k}{\sum_{k=1}^{K+1} w_k}. \tag{1.34}$$

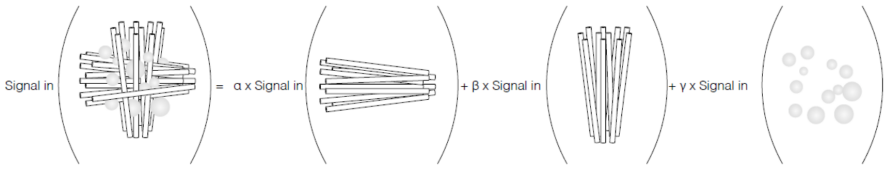

Figure 1.21: The total signal is the sum of the attenuation of each compartment weighted by the respective volume fractions. [36]

The dictionary is composed of DW-MRI signals (*fingerprints*) obtained by Monte Carlo simulations of the random walk of water molecules in environments defined by *hexagonal packing of impermeable cylinders* with different microstructural parameters Ω_k that represents axons [8]. The fascicles are modelled by an axonal radius (r) and separation between the cylinders (s), as shown in Figure 1.22.

Fascicle can be described by its intra-axonal volume fraction (or fibre volume fraction *fvf*), defined as the ratio between the area of axons within the hexagon and the area of the hexagon 1.35, and by extra-axonal diffusivity D_{ex}. The total

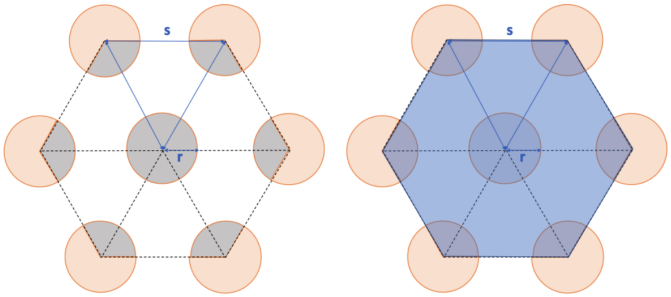

Figure 1.22: Representation of hexagonal packing of cylinders. At the left is a representation of the area of axons within the hexagon $A_{axons \subset hexagon}$, and at the right is the area of the hexagon $A_{hexagon}$. [37]

fibre volume fraction stands for the total fraction of water inside the axons in the voxel:

$$fvf_{fasc} = \frac{A_{axons \subset hexagon}}{A_{hexagon}} = \frac{2\pi}{\sqrt{3}} \left(\frac{r}{s}\right)^2. \tag{1.35}$$

A standard dictionary along the orientation $k = 0$, $C^0 = [A_1^0 \dots A_N^0] \in \mathbb{R}^{M \times N}$ is composed by concatenation of all the combinations of the possible fingerprints (*fvf* and D_{ex}). [38]

After pre-computing the standards dictionary, the optimal combination of configurations is found at run-time. The run-time method consists in concatenating all the rotations of C_0 along each population and then solving a *sparse optimisation problem* to find the best combination of fingerprints and orientations. The sparsity constraint ensures that only one fascicle is chosen out of all fascicles for a specific orientation [39]. The sparsity constraint problem can be defined as:

$$(\hat{j}_1, \dots, \hat{j}_K) = \underset{1 \le j_1, \dots, j_K \le N}{\operatorname{argmin}} \min_{\mathbf{w} \ge 0} \left\| \mathbf{y} - \left[\mathbf{A}_{j_1}^1 | \dots | \mathbf{A}_{j_K}^K | \mathbf{A}_{csf} \right] \cdot \begin{bmatrix} w_1 \\ \vdots \\ w_K \\ w_{csf} \end{bmatrix} \right\|, \tag{1.36}$$

where $\mathbf{y}$ is the measured signal, and $\mathbf{A}_{j_k}^k = \{A_{fasc}(\Omega_{j_k}, \mathbf{T}_k, \mathbf{u}_k; \mathbf{g}_i(t))\}_{i=1}^M, 1 \le j_k \le N$ is the signal from a fascicle with orientation u_k and microstructural parameters defined with index j. Finally, $\hat{j}_k$ is the index of the best fingerprint in the k-th direction.
From the optimal fingerprints and the weights, it is possible to extract the metrics by:

$$\nu_k = \frac{w_k}{(w_k + w_{k'})}; \; fvf_k = fvf_{\hat{j}_k}; \; D_{ex,k} = D_{ex,\hat{j}_k}.$$

Model output

Considering $K = 2$ the outputs of the model are:

- ν_0, ν_1: Volume fractions of fascicles 0 and 1
- ν_{tot}: Volume fractions of total fascicles
- ν_{csf}: Volume fraction of CSF
- fvf_0, fvf_1: Fiber volume fractions of the fascicles 0 and 1
- fvf_{tot}: Fiber volume fractions of all fascicles
- $D_{ex,0}$, $D_{ex,1}$: Extra-axonal diffusivity of fascicles 0 and 1
- $D_{ex,tot}$: Extra-axonal diffusivity of total fascicles

where

$$\nu_0 + \nu_1 + \nu_{csf} = \nu_{tot} + \nu_{csf} = 1. \tag{1.37}$$

Based on the estimated metrics, the weighted total fibre volume fraction within a voxel can be computed as:

$$wfvf = \frac{\nu_0 \cdot fvf_0 + \nu_1 \cdot fvf_1}{\nu_{tot}} = \frac{\nu_0 \cdot fvf_0 + \nu_1 \cdot fvf_1}{\nu_0 + \nu_1}. \tag{1.38}$$

Limitations

The use of single scalars r and s to characterise the intra-axonal signal and the assumption of its impermeability is an overestimation of the axons. Furthermore, the sparsity constraints do not allow mixtures of fingerprints to reconstruct the signal arising from a single fascicle of axons, this could be a limitation for fascicles with different microstructural properties in different subregions. [39]

1.4 Radiomics

We need to identify a reproducible technique capable of extracting quantitative features from the image volumes computed by the microstructural models. Radiomics is a practice where medical images are converted into mineable data, explaining different properties of the selected tissue, such as shape and heterogeneity, and used to predict outcomes [40] [41].

Hundreds of features are extracted from a single region by radiomics technique and can be subdivided into statistical-based, texture-based, and shape-based.
Statistical-based features express the distribution of the voxel intensities by ordinary metrics such as first-order statistics.
Texture-based features characterize different properties of matrices computed from voxel intensities. The matrices are Gray Level Co-occurrence Matrix (GLCM), Gray Level Size Zone Matrix (GLSZM), Gray Level Run Length Matrix (GLRLM),

Neighbouring Gray Tone Difference Matrix (NGTDM), and Gray Level Dependence Matrix (GLDM).
Shape-based features describe geometric properties of the 2D or 3D regions [40].

Before the feature extraction, several image transformations can be applied to the original volume to extract various properties of the tissues.
The high number of features creates data redundancy between them, requiring feature selection and dimensionality reduction [40]. The typical workflow followed in Radiomics is represented in Figure 1.23.

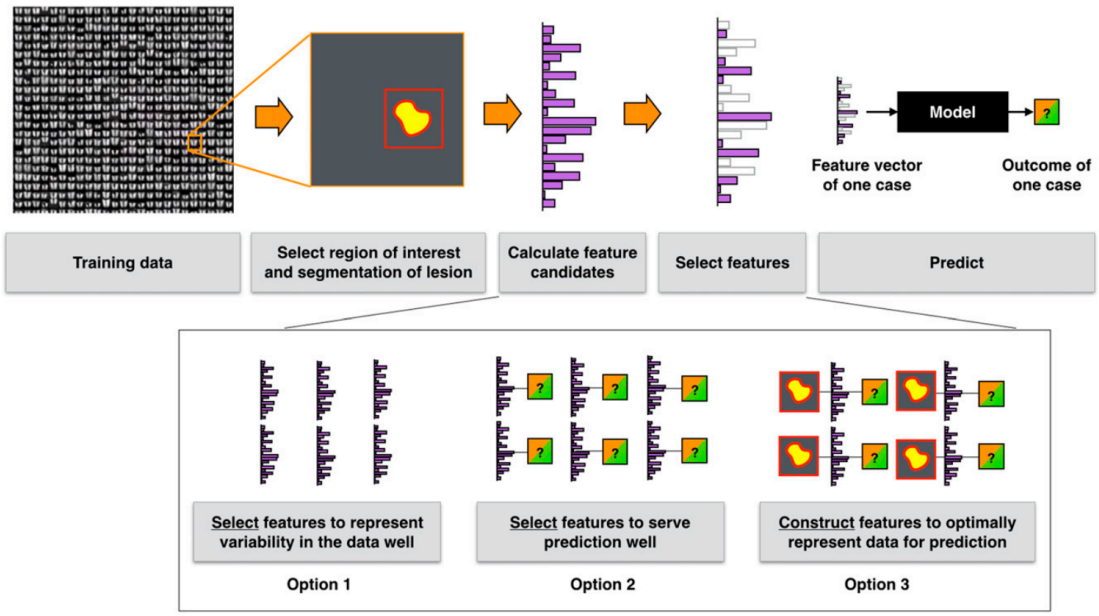

Figure 1.23: Radiomics workflow. First, ROI is defined, then for each ROI a large number of features are extracted. Extracted features can be applied to different type of models. [40]

1.5 Statistical Test

To decide whether exist differences between two or more groups, statistical testing is a tool to reach this target. A statistical test assumes a null hypothesis H_0 and an alternative hypothesis H_a. The idea is to find whether the data sufficiently support the null hypothesis H_0. A measure that tells us if the null hypothesis is rejected or not is the *p-value*, it is the probability of no difference. The p-value measures how likely the difference between the groups is due to change. A small p-value means that this observation would be unlikely under H_0, therefore it is rejected. Usually, a threshold of 5% or 1% for the p-value is used to reject H_0.

1.5.1 Parametric and Nonparametric statistical test

Statistical tests are divided into two categories: *parametric* and *nonparametric* tests.
Parametric tests work only if some assumptions are held by the data that they are testing, these assumptions:

- Normality: it assumes that each group is normally distributed. For a dataset with more than 30 samples for the group, usually, the normality can be assumed and can be checked by using a `Q-Q plot`. For a small dataset with less than 30 samples for each group, the `Shapiro-Wilk test` and/or `Anderson-Darling test` can be used to determine the normality assumption.
- Equal variance: assumes that the variance of each group is almost equal. It can be checked using a boxplot or through the `F-test` or `Levene's test`.
- Independence: it assumes that the observation in each group is independent of observations in the other group.
- No outliers: it assumes that there are no outliers in any group. It can be checked by a boxplot or through the `Grubbs's Test`.

If the data do not hold these hypotheses for both groups, parametric tests do not give a statistically important result and nonparametric tests are needed. Nonparametric tests do not have assumptions to hold and for these reasons, they can be used even for small sample sizes. The drawback is that nonparametric tests have lower statistical power than their parametric equivalents.

1.5.2 Comparison tests

Comparison tests look for differences among group means. `T-test` is used to compare the means of two independent groups, while `ANOVA` compares the mean of two or more groups. The respective non-parametric tests are the `Mann-Whitheny rank test` as an alternative t-test and the `Kruskal-Wallis test` as an alternative ANOVA test.

1.5.3 Independence test

When both the input variables and the output variables are categorical, it is possible to use a statistical test to know if there is a relationship between them. A test is `Chi-squared` based on the *Contingency table* between the input variable and the output variable. The contingency table summarises the samples putting the value of the variables on the rows and columns, respectively. Each cell in the table corresponds to the frequency of the observation.

The Chi-Square test assumes as a null hypothesis H_0 that the two categorical variables are not related.
`Fisher exact test` and `Barnard exact test` are alternatives that can be used to determine the dependence.

Chapter 2

Epilepsy

2.1 Overview of Epilepsy

Epilepsy is a brain disorder characterized by a lasting predisposition to generate spontaneous epileptic seizures and has many neurobiological, cognitive, and psychosocial consequences [42]. Epilepsy affects over 50 million people worldwide, making it one of the most common neurological diseases globally [1]. More than 75% of those with active epilepsy are untreated [43].

Epilepsy incidence is bimodally distributed with two peaks: the first in the paediatric population less than 5 years old, and the second in people over the age of 50 years. The incidence is higher in low-income countries than in high-income countries, thanks to a contribution of poor hygiene, poor basic sanitation, and a higher risk of infection [44]. Regardless of the geographical location, the prevalence of active epilepsy is usually between 4 and 12 per 1000, with a risk factor that varies with age [45].

The risk of death for a person with epilepsy is higher compared to the non-epileptic population. Mortality in epilepsy can be divided into direct (e.g., status epilepticus, injuries, sudden unexpected death [46]) or indirect (e.g., suicide, drowning) disease-related death [47].
Sudden Unexpected Death in Epilepsy (SUDEP) is one of the causes of epilepsy-related death, "it refers to the death of an epileptic patient that is not due to trauma, drowning, status epilepticus, or other known causes but for which there is often evidence of an associated seizure" [48, 49]. The exact cause of SUDEP is not well understood, but it is thought to be related to abnormalities in the electrical activity of the brain during seizures, which can affect the heart and breathing [50]. SUDEP is most seen in people with uncontrolled seizures, particularly those with generalized tonic-clonic seizures [50].

Epilepsy rarely stands alone, and the presence of comorbidities is the norm:

from Thijs et al., "more than 50% of people with epilepsy have one or several added medical problems" [44]. These comorbidities include not only psychiatric conditions (e.g., depression, anxiety disorder, psychosis, autism spectrum disorder, dementia) but even somatic conditions (e.g., type 1 diabetes, arthritis, digestive tract ulcers) [51].

Definitions

Epilepsy

The given definition of Epilepsy is usually practically applied as having two unprovoked seizures occurring more than 24h apart. But the International League Against Epilepsy (ILAE) proposed that epilepsy be a disease of the brain due to any of the following conditions:

- "At least two unprovoked seizures that occurred more than 24 hours apart" [42].
- "A single unprovoked seizure if recurrence risk is high (>60% over the next 10 years)" [42].
- "Diagnosis of epilepsy syndrome" [42].

Seizure

From Wikipedia and the World Health Organization, "an epileptic seizure is the clinical manifestation of an abnormal, excessive, purposeless, and synchronized electrical discharge in the neurons, that may lead to involuntary movement that may involve a part of the body (partial) or the entire body (generalized)" [1, 52]. Another type of generalized seizure is the absence seizure which is accompanied by loss of consciousness with periods of blanking out or staring into space for a few seconds [53].

Pathophysiology

A seizure can be conceptualised as occurring when there is a distortion of the normal balance between excitation and inhibition within a neural network [54].

In focal epilepsies, focal functional disruption results in seizures that begin in a localised fashion in one hemisphere, commonly limbic or neocortical, which then spread by recruitment of other brain areas. The site of the focus, the speed and extent of spread define the clinical manifestation of the seizure [55, 56]. For generalized epilepsies the electrical discharges affect both hemispheres of the brain, typically losing consciousness [57].

Seizures are not only caused by an increase in excitation or a loss of inhibition. But, an increase in inhibition can also be a cause of seizures in some circumstances, such as the absence of seizures [58].

Types of epilepsy

Classification is made of three levels: seizure type, epilepsy type, and epilepsy syndromes. [56]

Seizure type

From Thijs et al. [44] "seizures are first classified by onset as either focal, generalized, or unknown", as shown in Figure 2.1.

- Focal Onset: Usually limited to a specific brain region, called the focus. Focused seizures are divided into degrees of awareness: retained awareness and impaired awareness [44]. From the article of Fisher et al. about the classification of seizure types "retained awareness means that the person is aware of self and environment during the seizure, even if immobile" [56]. In addition, focal seizures are sub-grouped as those with motor and non-motor manifestations.

- Generalized Onset: Affects most or all of the brain. Typically, congenital and occurs simultaneously in both hemispheres of the brain. They are often accompanied by impaired awareness. Motor and non-motor (absence) seizures are distinct types of generalized seizures [44].

- Unknown: It is the case in which the onset is missed or obscured.

Epilepsy type

Epilepsies are divided into focal, generalized, combined generalized and focal, and unknown, as shown in Figure 2.2. The category combined epilepsy is used for those presenting both types of seizures.

Causes of epilepsy

Each type of classification can have different causes, as shown in Figure 2.2: structural, genetic, infectious, metabolic, immune, and unknown. Established acquired causes include serious brain trauma, stroke, tumours, and brain problems resulting from an earlier infection. [44, 56]

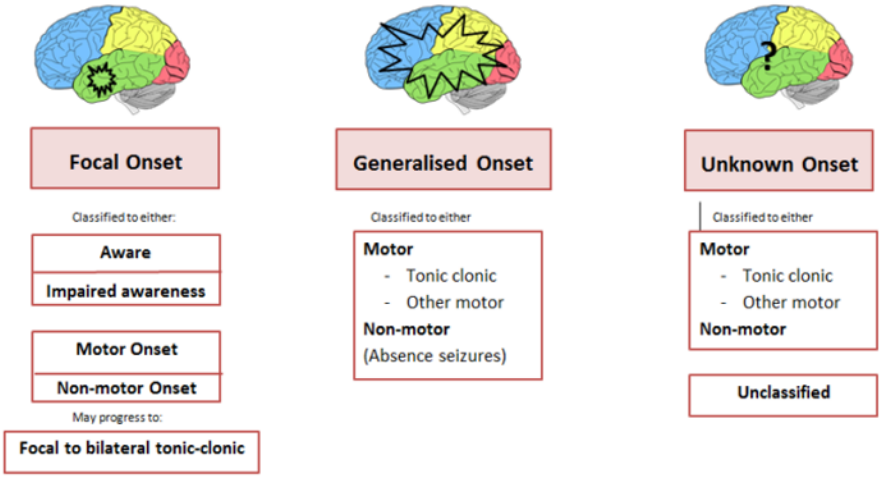

Figure 2.1: The International League Against Epilepsy. [59]

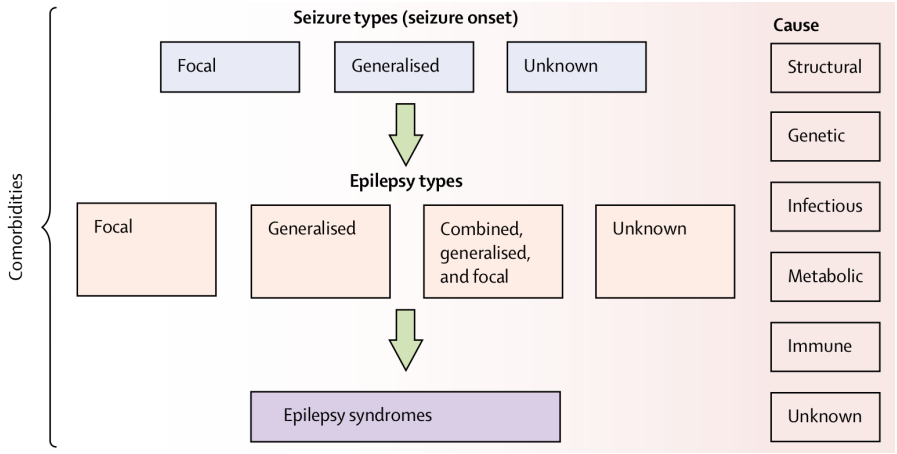

Figure 2.2: The International League Against Epilepsy. [44, 56]

Treatments

For most people with epilepsy, Anti-epileptic drugs (AEDs) are the first line of treatment. However, it has been reported that AEDs are effective in only 60-70% of individuals, a percentage that is further reduced in low-income countries [55].

Up to a third of individuals with epilepsy are refractory to AEDs [2]. From the article written by Kwan et al., "drug-resistant epilepsy (DRE) may be defined as failure of adequate trials of two tolerated, appropriately chosen and used at correct dosage antiseizure drug schedules to achieve sustained seizure freedom" [60]. In those cases, alternative non-pharmacological treatments including surgery and/or neurostimulator interventions should be considered. When surgery is not

possible because of the presence of multifocal or generalized epilepsy or whenever the epileptogenic focus lies in areas that cannot be removed, neurostimulation techniques are palliative options [61].

Three neurostimulation devices are approved by the Food and Drug Administration (FDA) for the treatment of DRE [62].

- VNS (Vagus Nerve Stimulation) is a device placed under the skin and sends intermittent signals to the vagus nerve. It is not brain surgery and is approved for the treatment of epilepsy when surgery is not possible. [63]
- RNS (Responsive Neurostimulation) is a device that can record seizure activity directly from the brain and delivers stimulation to stop seizures. RNS is implanted near the seizure focus on the skull. It delivers pulses only when detects abnormal activity in the seizure focus. [63]
- DBS (Deep Brain Stimulation) sends signals to brain electrodes to stop signals that trigger a seizure. The connected DBS electrodes are typically placed inside the thalamus, and the electrical pulses are delivered constantly or not. [63]

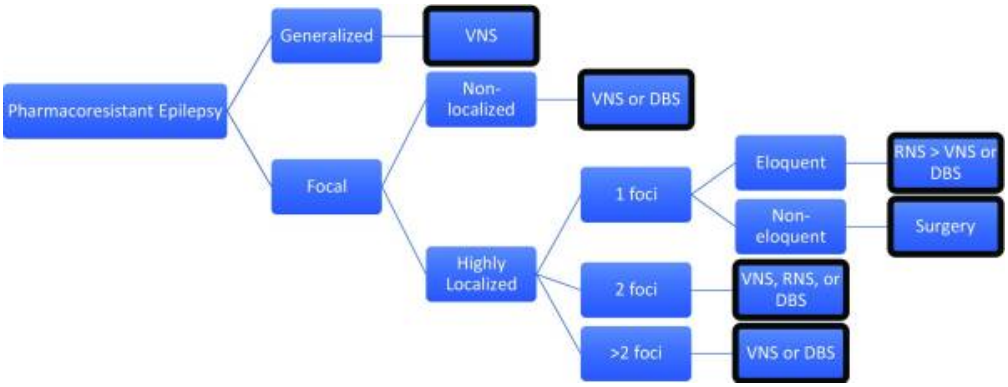

Figure 2.3: Graph showing a possible way to select the best neurostimulation device depending on the epilepsy type. [62]

2.2 Vagus Nerve Stimulation

Vagus Nerve Stimulation (VNS) showed positive effects in multiple other medical conditions, including essential tremors gastroparesis [64], chronic tinnitus, stroke, post-traumatic stress disorder [65], chronic pain, Parkinson's disease, eating disorders, multiple sclerosis, migraine, and Alzheimer's disease [66, 67].

VNS was implanted first time in four epilepsy patients by Penry and Dean in 1988 [68]. After several large clinical studies, it was approved for seizures by the European Community in 1994 and FDA in 1997. Clinical trials prove that 24 to 48 months after implantation of the device, 60% of the patients were considered responders and 8% of the implanted patients were seizure-free [3]. Responders (R) to VNS will be defined as those who experience a $> 50\%$ reduction in seizure frequency after VNS [5], partial responders (PR) who experience a reduction between 30% and 50% in seizure frequency and non-responders (NR) who experience a $< 30\%$ reduction in seizure frequency. Although VNS is used in clinical practice, the exact mechanism of its effect in modulating seizures is still poorly understood.

VNS consists of a device implanted in the upper left thoracic region with a helical electrode placed around the left cervical nerve, which delivers intermittent electrical impulses to activate the vagus nerve, as shown in Figure 2.4. Studies in dogs show that right-sided VNS result in a greater degree of bradycardia as compared to left-sided VNS because the right vagus nerve innervates more densely in the heart [69]. Because of those studies, VNS is suggested only for stimulating the left vagus nerve.

Side effects of VNS are commonly limited to coughing and/or hoarseness of the voice. In a study, voice alternation was reported in 66% of patients on high stimulation and 30% on low stimulation and cough was reported in 45% of patients. [70] To avoid cardiac side effects, a cuff electrode can be implanted on the left vagal nerve.

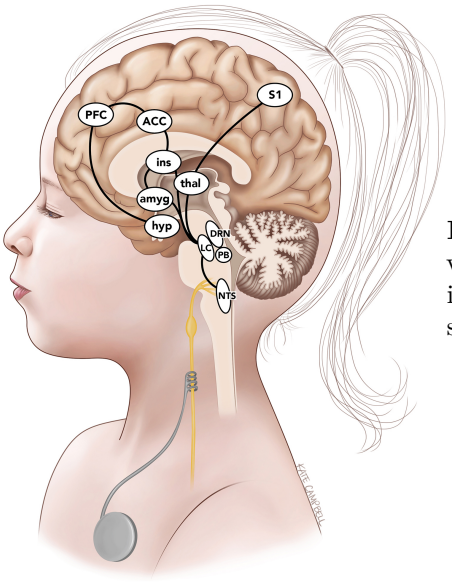

Figure 2.4: A Kate Campbell illustration [71] of the vagus afferent network. Schematic diagram showing the important brainstem centres and subcortical and cortical structures. [72]

Vagus Nerve Anatomy and Connections

The vagal nerve is the longest cranial nerve and exerts a wide range of effects on the body. It includes two nerves, the left and right vagus nerves and both sensory and motor fibres. The vagal nerve is a mixed nerve made up of 75% sensory(afferent) fibres responsible for the seen side effects (e.g., coughing, difficulties or swallowing, voice modification effects), and 25% efferent fibres which send feedback from the heart, lungs, stomach, and upper bowel [73].

The vagal nerve is composed of afferents neurons projecting to the nucleus tractus solitarius (NTS), which sends fibres to other brainstem nuclei that modulate the activity of subcortical and cortical circuitry [72], as shown in Figure 2.4. The vagus afferent network is considered by Hanchem et al. as "the reason for VNS efficacy" [72]. The NTS receives direct inputs from the vagal nerve and projects to other brainstem nuclei: the locus coeruleus (LC), dorsal raphe nucleus (DRN), and parabrachial nucleus (PBN) [74].

The LC is characterized by widely diffused projections to both subcortical and cortical structures. The projections of the LC are small unmyelinated fibres, forming a wide anteroposterior branching network to reach the raphe nuclei, the cerebellum, and many areas of the midbrain and forebrain regions. The main source of norepinephrine is the LC [75, 76]. NE is a neurotransmitter that has been associated with the clinical effects of VNS by preventing seizure development and by inducing long-term plastic changes that could restore the normal function of the brain circuitry. Indeed, short bursts of VNS increase neuronal firing in the LC, leading to elevations in NE concentrations. [77]

Studies have shown an indirect projection of the LC to the DRN, which sends widespread projections to upper cortical regions. DRN appears to have a more delayed response to VNS [72].

From a study done by Hanchem, Wong and Ibrahim [72] "Vagal afferents link the PBN to NTS and LC. Stimuli are sent from the PBN to the thalamus, insular cortex, amygdala and hypothalamus. Furthermore, PBN regulates thalamocortical circuity and can be involved in seizure generation".

The Vagus Afferent Network

Structural and Functional connectivity

Structural connectivity and functional connectivity are two different ways to describe the relations between brain structures. Structural connectivity refers to the anatomical organization of the brain by fibre tracts that connect different brain regions [78]. Functional connectivity refers to the statistical dependence or correlation of neural activity patterns between different brain regions [79]. Structural connectivity is often measured by dMRI. Functional connectivity is

often measured by electroencephalography (EEG) or functional magnetic resonance imaging (fMRI)[1] [78].

The main difference between structural connectivity and functional connectivity is that structural connectivity reflects the physical architecture of the brain, while functional connectivity reflects the dynamic interactions of neural activity, as shown in Figure 2.5. Functional connectivity can appear from direct or indirect structural connections, as well as from external inputs or intrinsic dynamics.

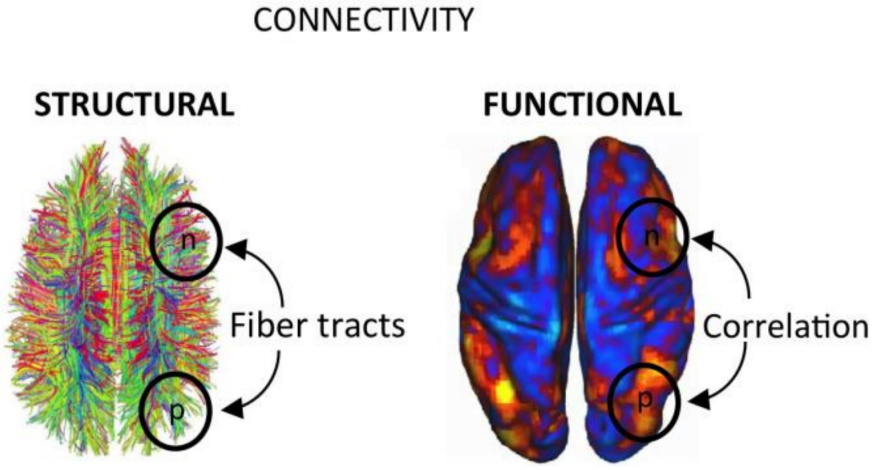

Figure 2.5: Differences between structural and functional connectivity [80].

Functional connectivity results in VNS

In a study done by Liu et al., the VNS treatment response was associated with thalamic activation measured by BOLF fMRI [81]. The importance of thalamocortical connections increased after a study by Ibrahim et al., which used resting-state functional MRI (rs-fMRI) data pre-VNS implantation and it found "an association of greater VNS efficacy with larger connectivity between the thalami to the anterior cingulate cortex and left insular cortex" [5]. Functional connectivity in MEG[2] also supports the role of intrinsic thalamocortical connectivity in R, was found that a functional network is significantly more active in R [4, 83].

[1] fMRI is a non-invasive neuroimaging technique that detects the changes in blood oxygenation and flow that occur in response to neural activity

[2] Magnetoencephalography: from Wikipedia "is a functional neuroimaging technique that maps brain activity by recording magnetic fields produced by electrical currents occurring naturally in the brain, using sensitive magnetometers" [82].

Structural connectivity results in VNS

Significantly greater FA was seen in R (lateralized to the left), particularly within anterior and retro-lenticular limbs of the internal capsule, anterior, superior, and posterior corona radiata, and posterior thalamic radiation [4].

In a study of 56 children done by Mithani et al. [4], "significantly greater FA (within the left side) was observed in R in the left internal capsule, external capsule, corona radiata, posterior thalamic radiation, fornix and stria terminalis, superior longitudinal fasciculus, inferior longitudinal fasciculus, and inferior front-occipital fasciculus". The mean FA value in these tracts was 0.352 (standard deviation (SD) = 0.048) in R and 0.309 (SD = 0.064) in NR. No significant voxels were seen in the right hemisphere. Furthermore, no statistically significant differences were registered in any other DTI parameters, including MD, RD, and AD. Healthy controls showed that the profile of R was more closely related to healthy children than NR. The mean FA value in significant tracts for matched controls was 0.377 (SD = 0.0274) in healthy controls [4].
A study conducted on a 4-year-old boy with intractable epilepsy 10 months after implantation of VNS showed increased FA in the right fimbria-fornix at the level of both cerebral peduncles. [84]

Tracts of interest

Thalamocortical connections are believed to be an important substrate of VNS responsiveness because they modulate cortical excitability, making the brain less susceptible to seizures. The thalamus receives direct inputs from the NTS and PBN [85].

The limbic system is a collection of neuronal structures involved in controlling emotion, memory, behaviour, and motivation. The fornix is the main efferent tract of the hippocampus that projects to the mammillary bodies, nucleus accumbens, septal nuclei, anterior thalamic nuclei, and cingulate cortex. While the stria terminalis forms the major input tract from the amygdala to the hypothalamus.

Association fibres are defined in Gray's anatomy book [86] as "fibres linking different cortical areas in the same hemisphere". They may enable transmission of the modulatory stimulus to epileptogenic and/or symptomatogenic regions, which would be augmented by increased WM microstructure in those tracts.

Thalamocortical radiations

Thalamocortical radiations are fascicles of nerves that connect the thalamus with the cerebral cortex. These fibres start from different nuclei of the thalamus and connect different cerebral cortex areas. They are parallel to each other, and they can be divided into four main pathways: anterior thalamic radiations, posterior

thalamic radiations, superior thalamic radiations, and inferior thalamic radiations [87]. Different pathways are shown in Figure 2.6.

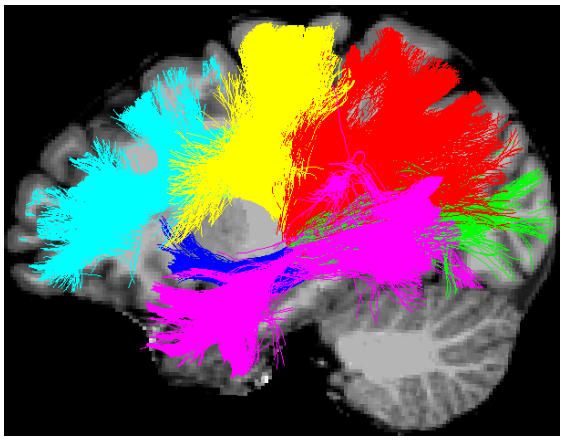

Figure 2.6: Visualization from a sagittal view of the thalamocortical radiations of a subject of the study. In cyan the anterior thalamic radiation, in red and green the posterior thalamic radiation respectively for the parietal and occipital lobe, in yellow the superior thalamic radiation, and in blue and purple the inferior thalamic radiation respectively for the tracts to the insula and to the temporal lobe.

Fornix and Stria Terminalis

The *fornix* is a part of the limbic system and is a C-shaped bundle of nerve fibres that act as the major output tract of the hippocampus. [88] The *stria terminalis* (ST) is a fasciculus of fibres running along the lateral margin of the thalamus. It is the major output pathway of the amygdala. [89] Both fornix and ST are represented in Figure 2.7

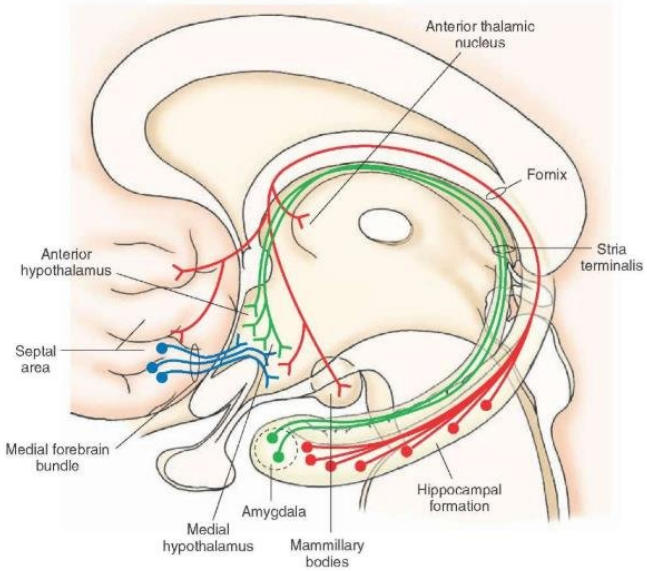

Figure 2.7: Illustration of anatomical structure and boundaries of ST and fornix. [90]

Association fibres

The *Superior Longitudinal Fasciculus* (SLF) is a bundle of tracts that connects the lobes of a hemisphere, as shown in Figure 2.8a, it can be divided into three separate components. The first (SLF I) is in the WM of the superior parietal and superior frontal lobes. The second, (SLF II) occupies the central core of the WM above the insula. While the last one, (SLF III) is situated in the WM of the parietal and frontal opercula. [91]

The *inferior longitudinal fasciculus* (ILF) is an associative WM pathway that connects the occipital and temporal-occipital areas to the anterior temporal areas, as shown in Figure 2.8b.

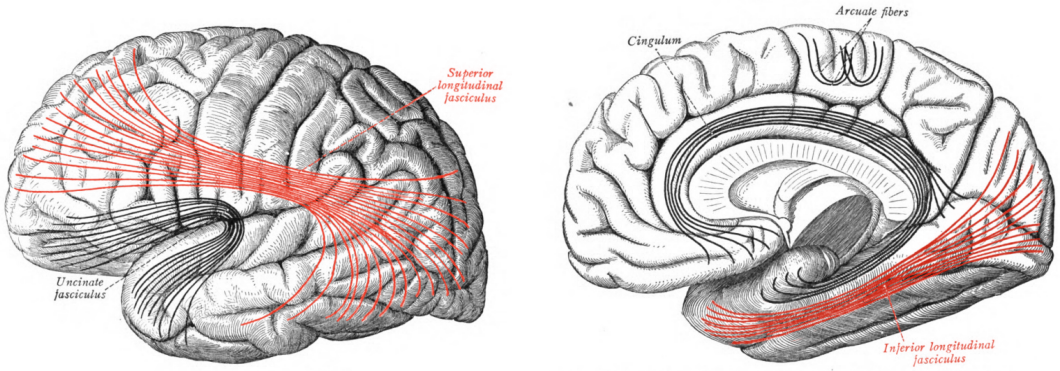

(a) **(b)**

Figure 2.8: Representation of longitudinal fascicles: (a) SLF; (b) ILF. [92]

Chapter 3

Methods

3.1 Data

3.1.1 Subjects

Our study is made up of 19 subjects with medically intractable epilepsy and implanted with a cervical VNS device. Participants ranged in age from 21 to 65 years. Of these 8 are R, 4 are PR, and 7 are NR.

Subject 3 has a congenital malformation, subject 12 has insular atrophy, and subject 19 had an amygdalohippocampectomy associated with a resection of a right temporo-occipital dysplasia.

Subject 16 was excluded from the analysis of tracts generated by TRACULA by FreeSurfer, further explained in Section 3.4.1, since the software did not extract all the tracts for unknown reasons. In Appendix C the Regions Of Interest (ROI) where the subject is excluded are highlighted in yellow, and in the analysis done in Section 4.3, the subject is excluded since it considers all the regions.

3.1.2 Data acquisition

The MRI acquisitions were realized following the *LivaNova guidelines*, requiring the neurostimulators to be turned off during the acquisitions. A trained neurologist used the programming system to set the device's output current to 0 mA and turn off the sensing before the patients entered the MRI acquisition room.

The imaging data were acquired using the *SIGNA™ Premier 3T MRI* system (GE Healthcare, Milwaukee, WI, USA), with a 48-channel head coil.
T1-anatomical images were acquired using a *Magnetization Prepared - RApid Gradient Echo* (MPRAGE) sequence with the following parameters: $TR = 2186ms$, $TE = 2.95ms$, $FA = 8°$, $TI = 900ms$, bandwidth = $244.14Hz$, matrix size = 256 x 256, 156 axial slices, imaging frequency = $127.77Hz$, voxel size = 1 x 1 x 1 mm^3,

acquisition time = 5:26 min.
T2-weighted images were acquired to improve the patient-specific segmentation of specific structures, further discussed in Section 3.3.1. The T2-weighted images were acquired using a Spin-Echo (SE) sequence: $TR = 2.5ms$, $TE = 91ms$, $FA = 90$ř, matrix size = 255 x 255, 141 sagittal slices, voxel size = 1 x 1 x 1 mm^3, acquisition time = 2:01 min.
Diffusion MRI data were acquired with a PGSE sequence with the following parameters: $TR = 4837ms$, $TE = 80.5ms$ and flip angle = 90°. A multi-shell diffusion scheme was used and was composed of 64 gradients at b = 1000, and 32 gradients at b = 2000, 3000 and 5000 $[s \cdot mm^{-2}]$, interleaved with 7 b0 images. The in-plane FOV was 220 x 220 mm^2 and the data contained 68 axial slices with a $2mm$ thickness (no inter-slice gap, $2mm$ isotropic voxels). A multi-slice excitation scheme was used during the acquisition with a hyperband slice factor of 3 to reduce the acquisition time. The total acquisition time was 13:33 min.
The images files were initially in DICOM format (`.dcm`), and they have been converted into NIfTI (`.nii.gz`) with the MRIcroGL software using the command `dcm2niix`.
Anatomical images are composed of files in NIfTI format containing the measured signals. T1 and T2 images are shown in Figure 3.1 and Figure 3.2.

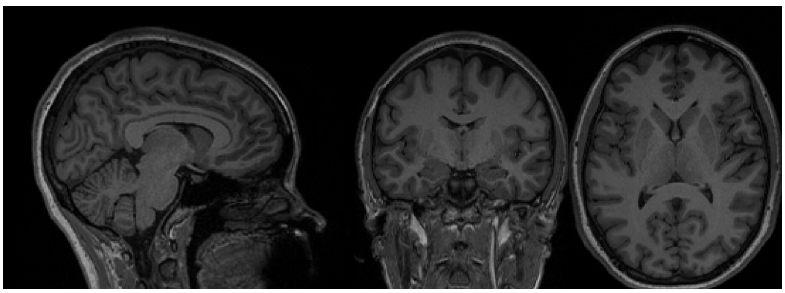

Figure 3.1: Anatomical volume slices of a T1 in the sagittal, frontal, and axial views

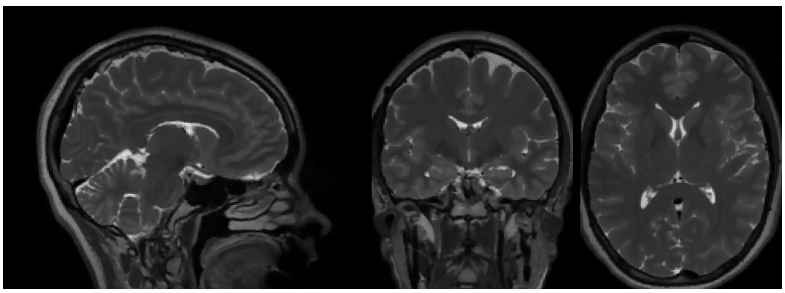

Figure 3.2: Anatomical volume slices of a T2 in the sagittal, frontal, and axial views

Diffusion files are composed of a NIfTI file and a JSON file plus two text files

(`.bval`) and (`.bvec`) having the b-values and the b-vectors. Axial slices at different b-values are shown in Figure 3.3.

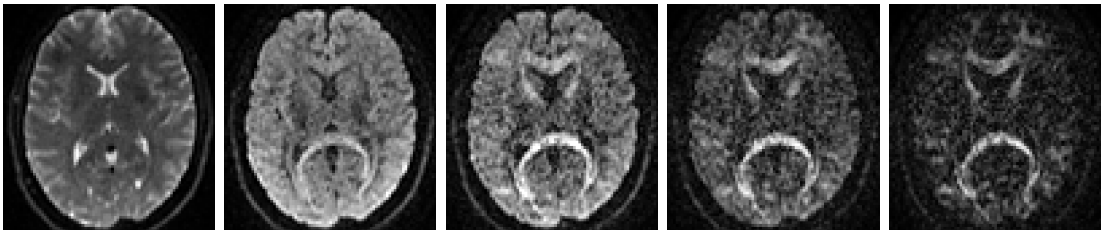

(a) (b) (c) (d) (e)

Figure 3.3: Raw diffusion volume slices of a patient for a b-value of: (a) $0s/mm^2$; (b) $1000s/mm^2$; (c) $2000s/mm^2$; (d) $3000s/mm^2$; (e) $5000s/mm^2$.

3.2 Preprocessing of DW-MRI images

Analysing the b0 volumes of the DW-MRI set of volumes is possible to see a darker zone in the slices with respect to the rest of the image, as shown in Figure 3.4, this artifact can be solved using a bias field correction. Therefore, it is possible to reduce the Rician noise usually present in the MRI volumes and correct the eddy current-induced distortions. Susceptibility-induced distortion is estimated and then corrected at the same time as the eddy current correction. After a visual inspection, no Gibbs ringing artifact was found in the images.

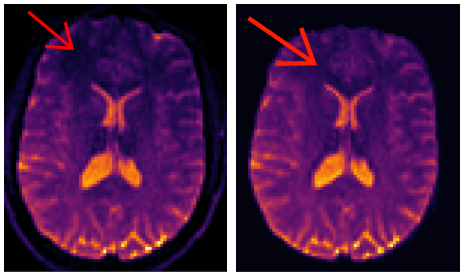

(a) (b)

Figure 3.4: Axial slice of b0 diffusion image, where is possible to see an intensity inhomogeneity in the frontal lobe: (a) Before the correction, in the frontal lobe is possible to see a darker area. (b) After the correction, the correction adjusts the intensity inhomogeneity but does not solve it completely.

To correct all the artifacts recognised, we use the library ElikoPy [93, 94]. ElikoPy is a Python library for preprocessing dMRI images and skull stripping. In Figure 3.5 is represented the Pipeline used in the library to preprocess the volumes.

For preprocessing, all corrections except the Gibbs-ringing artifact removal were performed. ElikoPy also has a mandatory step which is skull stripping to avoid noise coming from the skull. Therefore, the brain-extracted images were used for the computation of the microstructural metrics. The susceptibility field correction

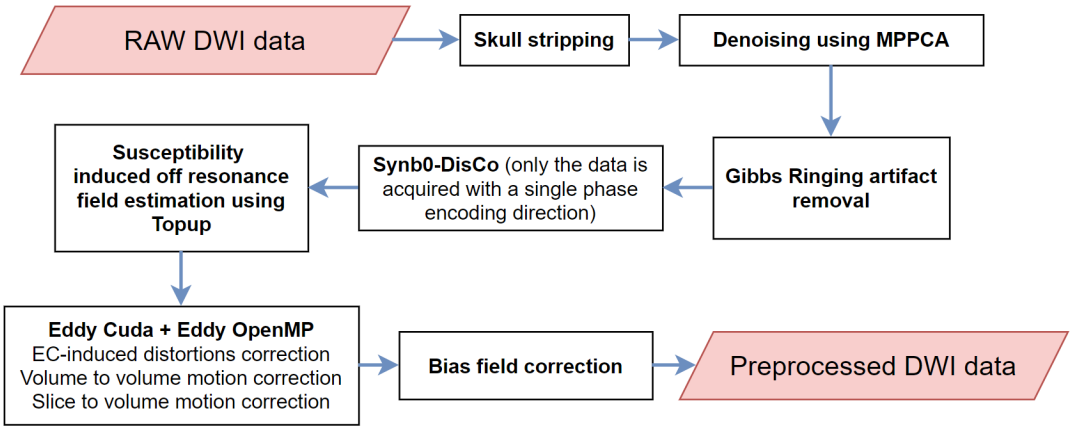

Figure 3.5: Representation of all the preprocessing steps done by the ElikoPy pipeline. [95]

is done by using the T1 image, even if the T1 and dMRI are not aligned here we do not need to register them because the registration is done automatically by ElikoPy. The results and comparisons between before and after the preprocessing are shown in Figure 3.4.

Workflow

All the methods and steps used to retrieve the diffusion metrics along the tracts are summarised in the following Figure 3.6.

3.3 Region-Of-Interest extraction

To extract the tracts of interest and the (ROI) selected after studying the literature about brain regions involved in the antiepileptic effects of VNS, we must define a method that could automatically extract ROI in a batch of patients. Different methods are used for ROI and tracts extraction, as explained in the following section.

3.3.1 ROI extraction with FreeSurfer

For ROI extraction, we use FreeSurfer [96–109], which is an open-source neuroimaging toolkit with many functions including labelling regions of the brain and registration. To extract the regions, we do a parcellation of the whole brain through FreeSurfer that allows us to save specific ROIs.

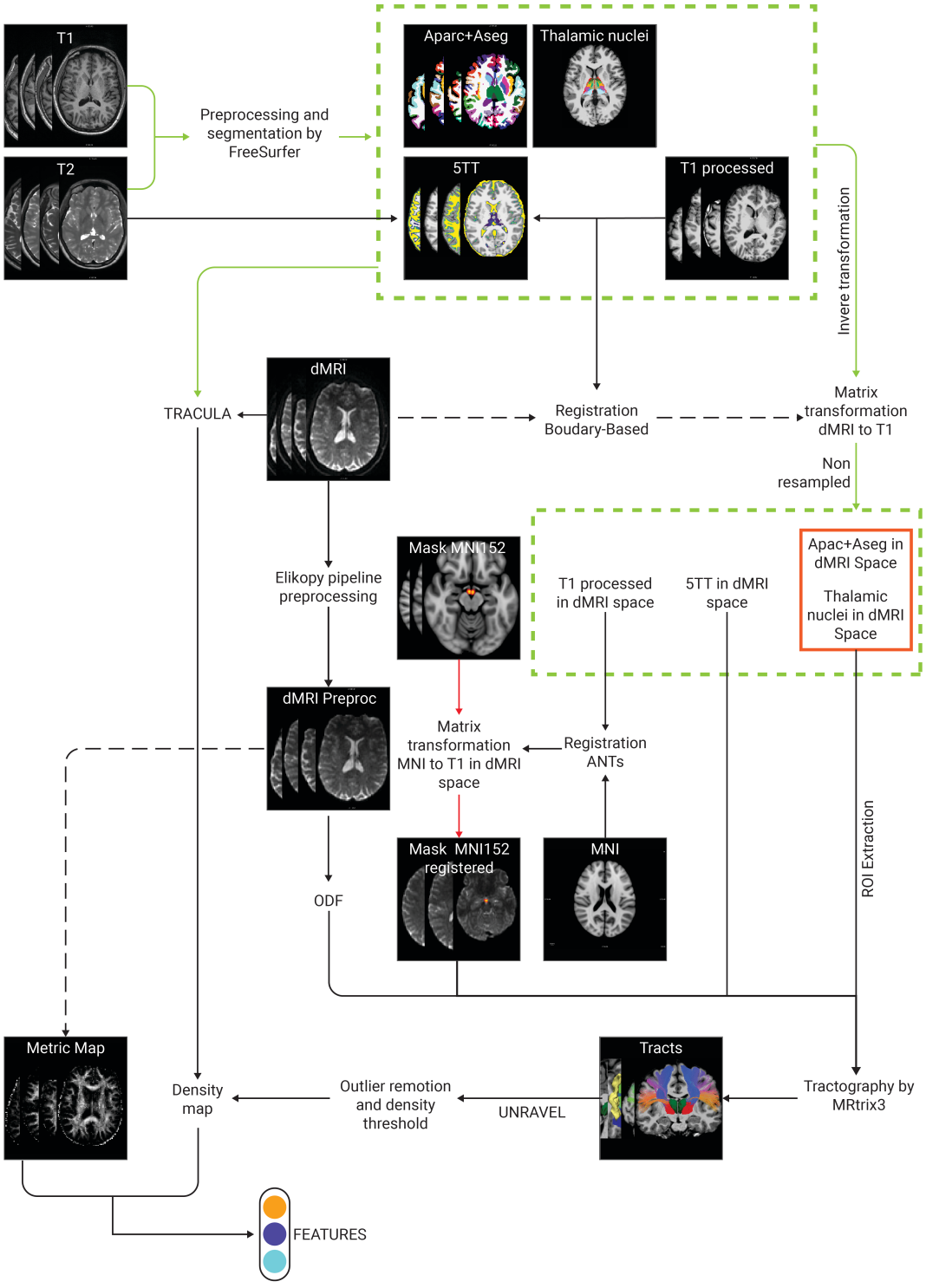

Figure 3.6: Graph explaining all the methods and steps used to extract the model metrics for each tract.

To label the brain we use the Freesurfer command `recon-all` taking as input the T1 image and the name of the subject, then the algorithm can improve the quality of segmentation if a T2 image is given as input. In our study, all epileptic patients had a T2 image, therefore, it was used.

Internally `recon-all` does a preprocessing of the T1 images including motion correction, non-uniform intensity normalization, Talairach transformation, normal intensity normalization and skull-stripping. Then, the T2 image is normalized and registered in the T1 space. As output, we will have many volumes including the segmented brain `aseg.mgz` and the segmented brain with cortical parcellation `aparc+aseg.mgz`, the algorithm segments the cortex also with different atlases: the Densika-Killiany Atlas (that was used in the present study) or the Destrieux Atlas. As output, the software also gives us the preprocessed brain from the T1 volume in `brain.mgz`, later used for the registration.

FreeSurfer gives the possibility to segment the thalamus into different thalamic nuclei. The parcellation is based on the result of `recon-all` and can be computed using the script `segmentThalamicNuclei.sh` [110]. As output, we will have the labelled thalamic nuclei `ThalamicNuclei.mgz` in the T1 space. The volume of the thalamus, as can be seen in Figure 3.7b, differs from the volume extracted by `recon-all` pipeline, this is because different analyses are used by the two algorithms. The estimates made by the script have been proven more accurate than the pipeline [110], for this reason in the study we consider the thalamic region as the union of all the thalamic nuclei, as shown in Figure 3.7c.

The segmented volume gives different labels for each ROI, to visualise and recognise their names, we use `freeview` that through a *Look Up Table* it distinguishes the different zones, as shown in Figure 3.7. Then to extract them we use `mri_extract_label` giving as input the value of the regions to be extracted. The extracted brain regions are 3D binary masks in the T1 space, as shown in Figure 3.7c. The full list of ROI extracted from FreeSurfer can be found in Appendix A.

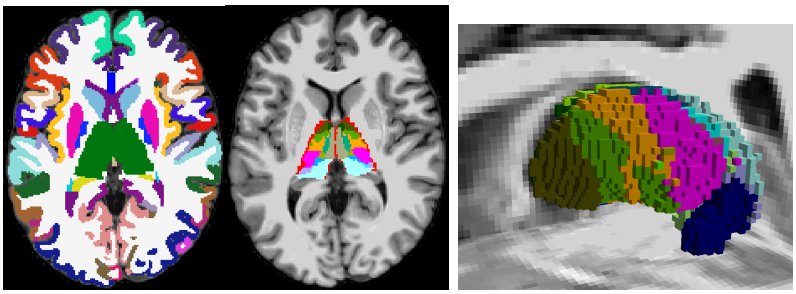

(a) **(b)** **(c)**

Figure 3.7: Images of a subject brain: (a) Whole brain segmentation with FreeSurfer, with the thalamus shown in dark green, (b) Segmentation of the different sub-regions of the thalamus (different thalamic nuclei), (c) 3D-visualization of the thalamic nuclei after segmentation.

Registration FreeSurfer ROI

To avoid interpolation of the collected diffusion data, we keep fixed the diffusion image and transform the T1 from its space to the space of the dMRI image. Since different b0 images are present, we use the mean of them as fixed dMRI image, this is done thanks to two MRtrix3 tools: `dwiextract` with `-bzero` parameters and `mrmath mean` with `-axis 3` parameter. Then, we use the command `bbregister` from FreeSurfer to compute the transformation matrix from the mean of the preprocessed b0 image to the preprocessed skull stripped T1 image given by FreeSurfer and use it to transform the T1 image and the segmented brain into the diffusion space using an inverse transformation through the command `mri_vol2vol`.

The program `bbregister` uses a *boundary-based* cost function to register images of different modal within-subject, it performs a rigid transformation (6 degrees of freedom).

After the computation of the transformation matrix, `mri_vol2vol` moves an input image into the space of the fixed image. One of the features is that the input image can keep its resolution after the transformation with `-no-resample` parameter. This characteristic is used to generate better tracts when the ROIs are used to define regions of inclusion and/or region of exclusion during the tractography.
Registration results are shown in Figure 3.8.

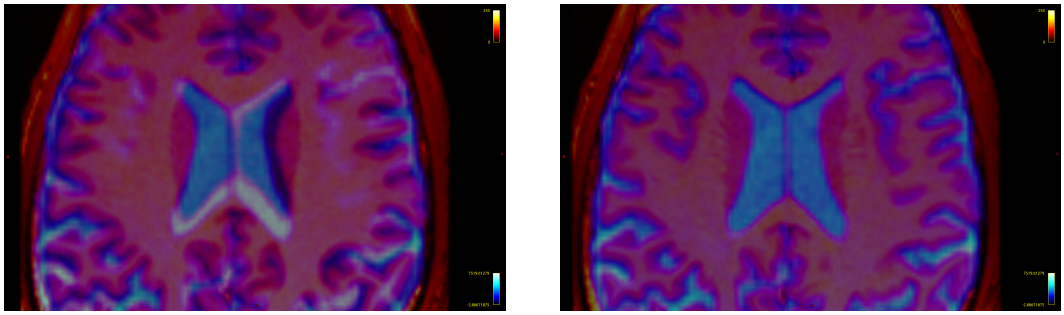

(a) **(b)**

Figure 3.8: Registration of T1 into the dMRI space: (a) Before the registration. (b) After the registration

3.3.2 ROI extraction and definition from Atlases in MNI space

For the tractography, we need to define the regions of inclusion and exclusion from where the streamlines must pass through or not. FreeSurfer does not give the parcellation of all the regions we need, for example, the mammillary body or the

internal capsule, for this reason, we use the pre-segmented regions on MNI spaces available on FSL. The full list of ROI extracted from the atlases can be found in Appendix A. FSL is a library with different tools for the analysis of MRI, fMRI and dMRI brain images, and it offers a tool called `fsleyes` where we can visualize the MNI152 T1 images[1] and extract different regions from the different atlases present on it. The atlases that we used are JHU ICBM-DTI-81 White-Matter Labels, Juelich Histological Atlas and XTRACT HCP Probabilistic Tract Atlas.

The ROIs defined in the atlases are not binary masks, but heatmap masks, where the intensity of each voxel is the probability that it belongs to a specific ROI (in the MNI space). To use all of them we do an average of them and threshold the voxels removing the ones with probability ≤ 0.1, as n in Figure 3.9. It is not possible to directly use them as regions of the patient's brain because, in our dataset, many patients have damaged brain structures, therefore we reconstruct them through tractography.

Hand-drawn slice of ROI

The extracted ROIs from the atlases are both subcortical structures and fibre bundles. The ROIs of a fascicle are not used directly, but, since we want to find them through the tractography, we use hand-drawn slices of them as inclusion regions to redirect the pathfinding during the tractography. The slice regions were hand-drawn using the MRtrix3 toolbox with the visualization tool `MRview` and the tool `ROI editor`. The planes are drawn so that they cut the extracted region, as shown in Figure 3.9c, to guide the tract to follow a path and cover all our selected regions till the end region. The strength of this method is that the planes are drawn only one time in the MNI space and used for all the subjects.

Registration into the space of the subject

As for the anatomical images of the patient we need to register the ROI and the drawn slices into the space of dMRI images. This is a different case than before because the MNI space an averaged, therefore, a non-rigid registration was needed for the registration. We divide the registration into two parts: from the MNI space to the T1 space of the subject (using the reprocessed T1 image given by FreeSurfer), and then from the T1 space of the subject to the dMRI space. The process is better explained in Section 3.2.

To reach our result, we use ANTs software, which is considered a state-of-the-art medical image registration toolkit. The transformation matrix from the T1

[1]MNI152 is a T1 image derived from averaging 152 structural images after high-dimensional nonlinear registration into the common MNI152 coordinate system

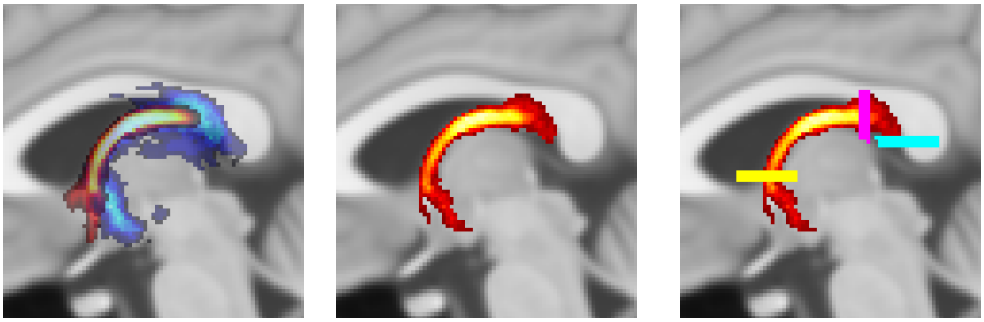

(a) (b) (c)

Figure 3.9: Method used for the extraction of the Fornix based on the parcellation of the MNI152 T1 image defined in FSLeyes atlases (a) superimposition of the fornix probabilistic map in the Juelich Histological Atlas (blue) and the XTRACT HCP Probabilistic Tract Atlas (red); (b) computation of the mean probability between the two atlases; (c) hand-drawn planes to refine the tractography of the fornix.

space of the subject to the dMRI space was already computed in Section 3.3.1 through `bbregister`, which gives us the T1 image in the dMRI space. While the transformation matrix from MNI space to the T1 in dMRI space is computed with ANTs by a symmetric normalization transformation and elastic regularization with the option `ElasticSyN`. We register the regions with nearest neighbour interpolation and resample to the dMRI space, therefore we lose the high resolution of the masks. Results are shown in Figure 3.10.

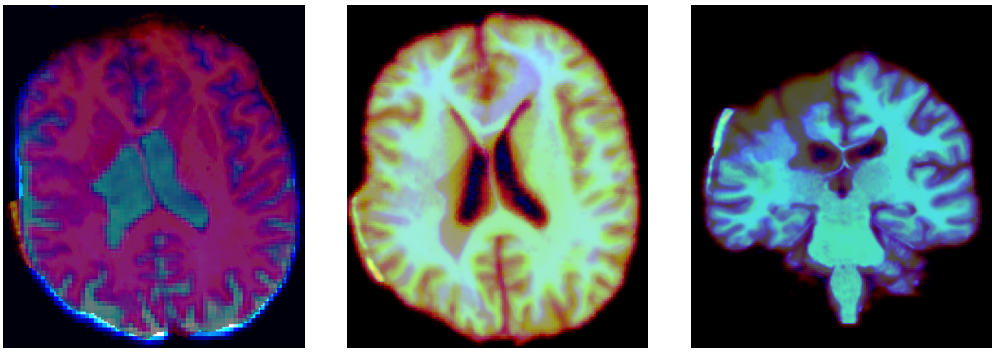

(a) (b) (c)

Figure 3.10: Worst case scenario of registration in a patient with congenital malformation: (a) Axial view of the registration of the T1 image (red) into the dMRI patient space (blue). (b) Axial view of the registration of MNI152 T1 image (red) into T1 registered (blue) in the dMRI space. (c) Coronal view of the registration of MNI152 T1 image (red) into T1 registered (blue) in the dMRI space.

3.4 Tractography

To generate the streamlines that connect different regions of the brain we used TRACULA implemented in FreeSurfer and the library MRtrix3 which gives many tools for the processing of diffusion-weighted images.

3.4.1 Tractography using FreeSurfer

TRACULA (TRActs Constrained by UnderLying Anatomy)[111–113] is a tool from FreeSurfer, for automatic reconstruction of the major tract based on DW-MRI data. TRACULA needs the cortical and sub-cortical parcellation from T1 data given from the commands `recon-all` and `segmentThalamicNuclei.sh`, and it uses the relative positions of anatomical structures with respect to each other to reconstruct the tractography of the main pathways. The pathways are computed using the command `tract-all`, which needs a configuration file where is specified the dMRI image and its b-value information.
TRACULA follows different steps for the reconstruction of the pathways:

1. Preprocessing of the raw images, with the parameter `-prep`. Since we have already done the preprocessing with ElikoPy we skipped some of these steps.

   The preprocessing steps are: image corrections, image quality assessment, intra-subject registration, tensor fit, inter-subject registration and estimation of anatomical neighbourhood priors for the pathways of interest.

2. Ball-and-stick model fitting, by the parameter `-bedp`.

3. Pathway-of-interest reconstruction, using the parameter `-path`.

4. Statistical measures on the tracts, through the parameter `-stat`. We use this step for the data used for plotting Figure 3.24.

All computed streamlines are grouped in the `merged_avg[...].mgz`, as shown in Figure 3.11a. For every single tract exists a file having a probability map of the tract called `path.pd.nii.gz` and a file having only voxels with the highest probability called `path.map.nii.gz`. We will use the latter map to compute our metrics as in the second step of Section 3.4.3. An example of the two files for a tract is shown in Figures 3.11b and 3.11c.

TRACULA gives the tractography of 42 pathways connections[2] including the fornix, the cingulum, the longitudinal fasciculus, and the anterior thalamic radiation.

[2]White-matter tract atlas. URL: `https://dmri.mgh.harvard.edu/tract-atlas/` (visited on 08/05/2023)

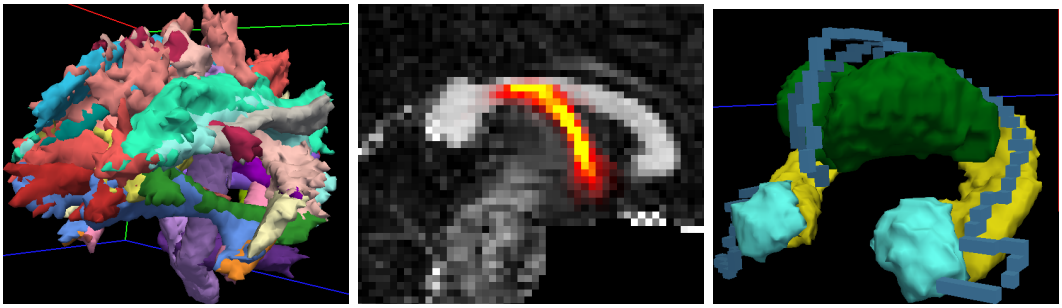

(a) (b) (c)

Figure 3.11: Output of `tract-all` steps: (a) 3D view of all the tracts given from the `-path` parameter after TRACULA execution. (b) Probability map of the Fornix tract. (c) In blue the voxels with the highest probability in the Fornix tract.

But it does not give the rest of the thalamic radiations: posterior thalamic radiation, superior thalamic radiation, and thalamo-insular tracts. For this reason, we need to generate the streamlines using `tckgen` of MRtrix3. Tracts in common with TRACULA are also generated, as the SLF, the ILF and the fornix, and the results are compared in Appendix C.

As already mentioned in Section 3.1.1, TRACULA did not compute all the tracts for subject 16, in Appendix C the non-computed tracts for him are highlighted in yellow. Therefore, in the analysis of these tracts, this subject will be excluded.

3.4.2 Tractography using MRtrix3

The tract regions that are extracted using MRtrix3 are listed in Section 3.4.4. The program `tckgen` of MRtrix3 supplies both deterministic and probabilistic tracking algorithms, see Section 1.2.3. The iFOD2 algorithm is used in our study, it is a probabilistic algorithm that takes as input a FOD. The FOD is computed using the MSMT-CSD model, implemented in MRtrix3 and it can be visualized as the distribution of water diffusion in each voxel, as shown in Figure 3.12.

There are two different methods for reconstructing fibre bundles: Targeted tracking and Tract selection. [114]

- **Targeted Tracking**: the streamline generation is constrained by different parameters, like seed, inclusion, exclusion, and target regions, that the tract must follow. Usually, the generation is done unidirectionally from the seed to the target, and vice versa from the target to the seed, and then the tracts are joined together. The benefit of this method is that it can produce a dense reconstruction for small paths. However, in some situations, unexpected results can be obtained, such that no tract or noisy unrealistic paths are

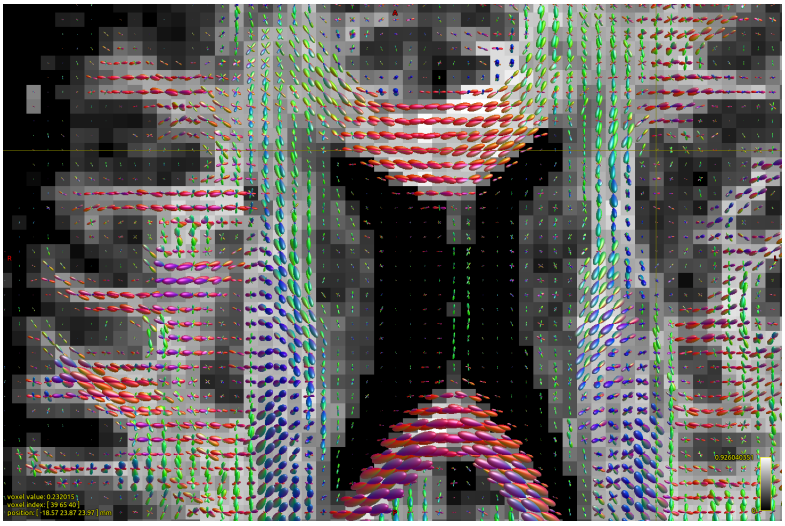

Figure 3.12: Visualization of FOD for each voxel.

reconstructed. Another drawback is that the tract must be re-generated every time a change is made.

- **Tract selection**: Divide the reconstruction into two parts, it performs the whole brain tracking and then applies the constraints to isolate the tract of interest. The advantages are that it does not need to regenerate the tract at every change, so it is faster in the debug phase, and it allows the user to visualise the tracts with different ROIs without further computations. The disadvantage is that for small tracts with a complex structure, this method may not reconstruct many streamlines (or even no streamline) or streamline of no interest.

The ideal way is to use both methods in separate phases of the study, in the design phase use the tract selection method to fine-tune all the parameters for the algorithm and the regions of inclusion and exclusion. Then once the best parameters are found, use the Target tracking to find all the tracts.

The MRtrix3 tool `tckgen` gives as output a tract file in the format `.tck`, it is a format designed by MRtrix3 and not all the tools for track visualization support it. Another popular format is `.trk` from Trackvis [115]. Since we need both types for the analysis and visualisation, we use DiPy [116] for the conversion.

3.4.3 False positive connections

One of the major problems of probabilistic tractography is the presence of false positive connections [117].

- The false continuity issue consists of streamlines that continue even after the target. A way to solve this problem is adding the argument `-stop` to the algorithm, and it stops as soon as the target is reached.

- Another difficulty is the tracts that correctly connect the source to the target but follow a path that is not anatomically correct to our expectations. In this case, the Anatomically-constrained tractography (ACT) [118] framework can be used to prune only anatomically correct tracts. To use it we need to add the arguments `-act [5tt_vol] -backtrack -crop_at_gmwmi`, where the `5tt` volume is a five-tissue-type (5TT) file. It contains a 4D image composed of five 3D volumes each of which corresponds to a different tissue type: cortical GM, sub-cortical GM, WM, CSF and pathological tissue.

  The 5TT file can be generated by using the MRtrix3 command `5ttgen fsl` passing as argument T1 and T2 images. As before, it is registered in dMRI space with the transformation matrix computed in Section 3.3.1, as shown in Figure 3.13.

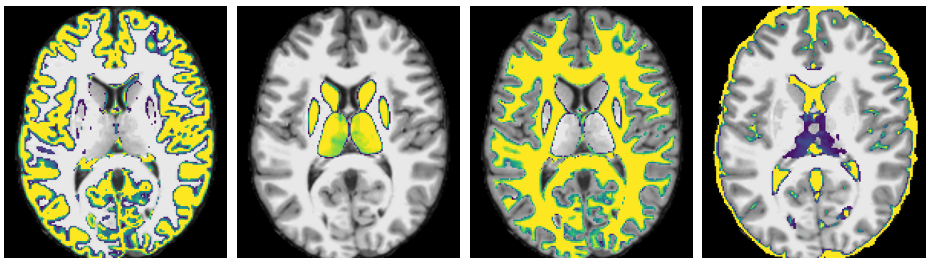

(a) (b) (c) (d)

Figure 3.13: Slice of an axial view of a subject of 5tt image, in yellow the corresponding tissue. (a) Cortical GM. (b) Sub-cortical GM. (c) WM. (d) CSF.

We use ACT or `-stop` depending on the tract.
From the literature exist some other correction algorithms, for example, TIP (Topology-Informed Pruning) Algorithm discussed in [117]. They compute the density map of the tracts and then remove the voxels with low-track density.

The approach used in our study is based on densities and is composed of two steps.

1. The first step removes the streamlines that are too short or too long with respect to the mean length. We use the Interquartile Range (IQR) method where any streamlines that are shorter than 1.5 IQR below Q1 (first quartile) or longer than 1.5 IQR above Q3 (quartile) are considered outliers, as shown in Figure 3.14.

2. The second step is thresholding voxels with low-track density. The density function is computed using the tool from UNRAVEL [119, 120] `get_streamline_density()` that computes for each voxel the number of streamlines passing through it, then we scale the values with a *MinMaxScaler* in the range [0, 1] and remove all the voxels with a value below a default threshold of 0.1. When a limited number of tracts is obtained, the path is noisy and has high uncertainty, as shown in Figure 3.14. We want to filter voxels where streamlines pass through and are coherent with other streamlines' directions, for this, we introduce the concept of near streamlines and compute a score for each voxel depending on how many streamlines pass close to it. The score is computed by convolving a 3D Gaussian kernel of $3x3x3$ voxels. It generates a blurred weighted map that then is thresholded as explained before.

3.4.4 Tracts of interest

This section explains the parameters and the inclusion and exclusion regions used to extract the tracts that were discussed in Chapter 2.2. All the settings used to generate the tracts can be consulted in Appendix B.

Stria Terminalis

Anatomical landmarks described in Chapter 2.2 were used to tract the ST. We set as seed region the mask of the amygdala extracted with FreeSurfer and as target the Bed Nucleus of Stria Terminalis extracted through the Atlases in MNI space. Then to constrain the tract to follow a path some drawn planes were inserted as inclusion regions, and the thalamus as exclusion region. ST was excluded during the study because it coincided with the tract of the Fornix since the resolution of the DW-MRI images is not high enough.

Fornix

Tracts of the Fornix arising from the hippocampus go over the thalamus and descend to the Mammillary body, as explained in Section 2.2. The hippocampus from the FreeSurfer parcellation was set as seed masks, and a plane intersecting the Mammillary body is set as the target region since it is not present in the FreeSurfer

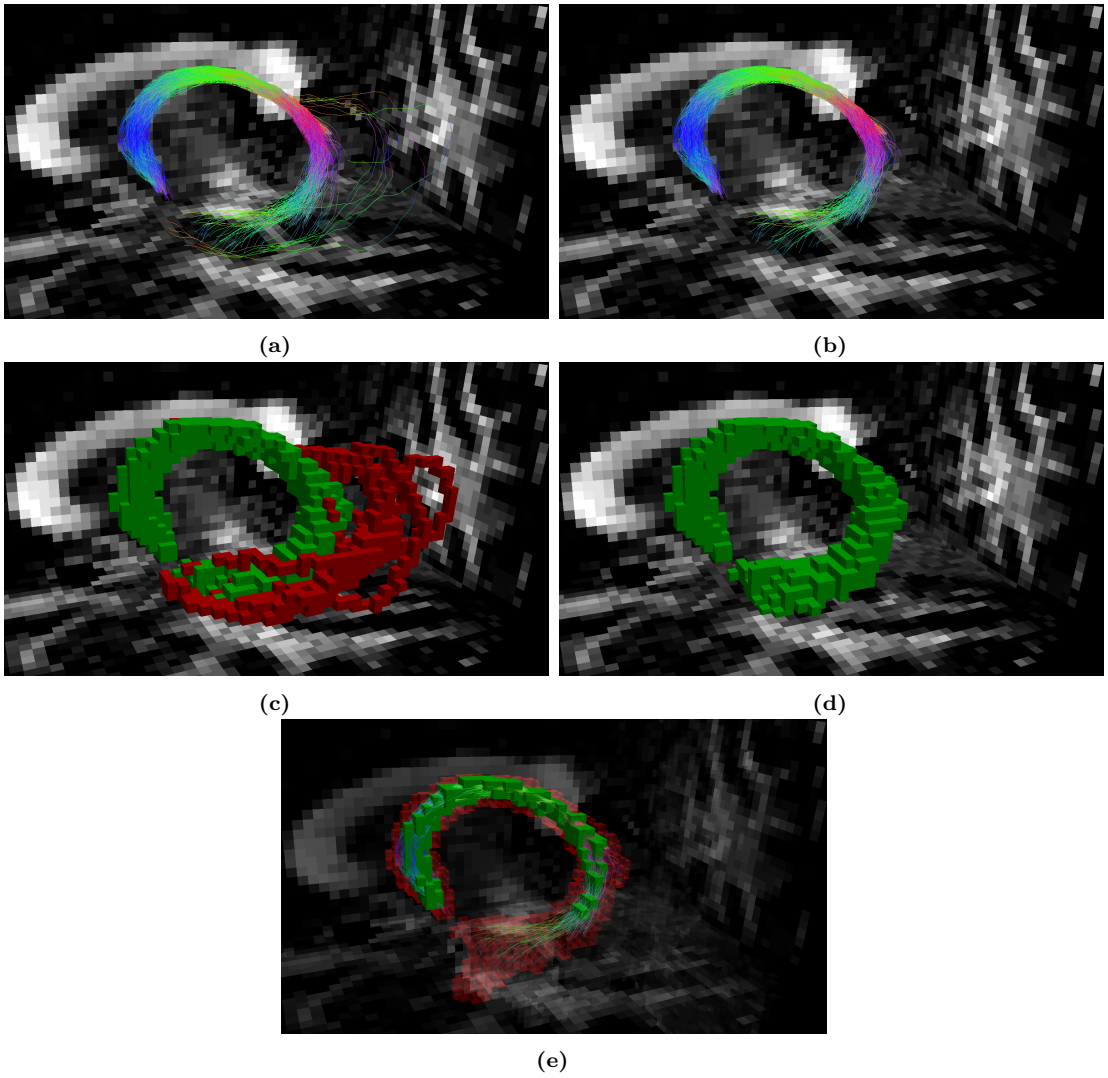

Figure 3.14: Example for the fornix of the steps used to correct the extracted voxels from the tracts. (a) Streamlines without correction. (b) Streamlines with length removal correction, longer and shorter paths are removed with the IQR rule. (c) Visualization of extracted voxels from tractography without any correction, red voxels are the ones that do not respect the IQR. (d) Visualization of extracted voxels after the length removal correction. (e) Region of the tract after the threshold of voxels with high streamline density. In green the voxels were kept, in red they were removed.

labelling table. The method used to draw the plane is explained in Section 3.3.2. To correctly direct the path some planes cutting the Fornix are inserted as inclusion regions. As exclusion regions are used the Thalamus and the Lateral Ventricle are eroded by one voxel. The used Regions are shown in Figure 3.15.

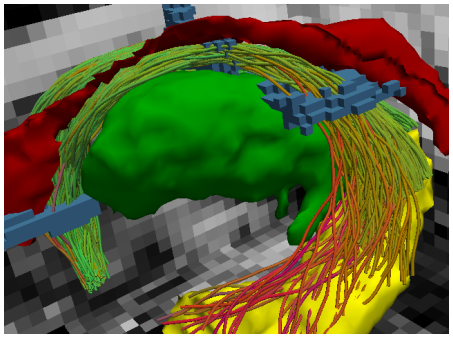

Figure 3.15: Visualization of Fornix tract and all the regions used to generate it. In green is the Thalamus, in yellow is the Hippocampus, in red is the Lateral Ventricle, and in blue are the registered inclusion planes initially drawn in the MNI152 space.

Superior Longitudinal Fasciculus

The SLF is composed of three segments, but for extraction, we consider all of them as a unique fascicle. We set the seed region in the frontal lobe and as target region in the parietal lobe, using the WM mask (generated in FreeSurfer) as the target region to improve the prediction of the tracts. The frontal and parietal lobes are built by combining different regions of the FreeSurfer cortex parcellation. Occipital and temporal lobe regions were used as exclusion regions since some tracts ended in them. Regions and tract are shown in Figure 3.16. The lobe mapping is done by following an approximate mapping of ROIs to the lobes, described in the Appendix of [121].

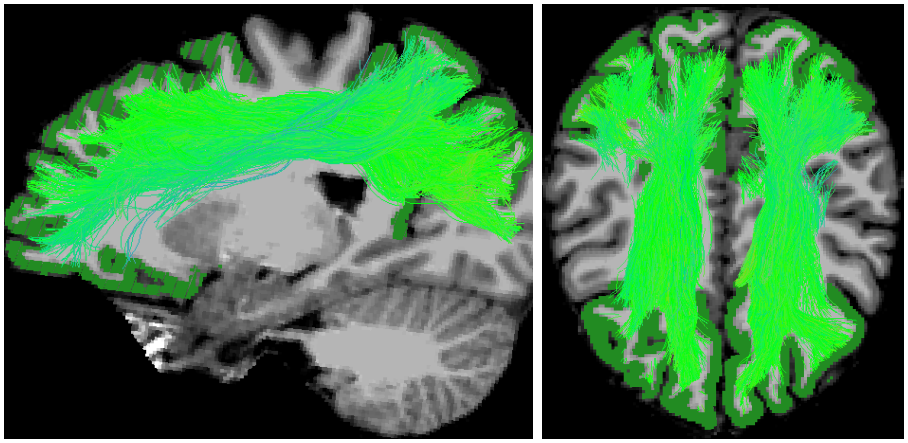

(a) **(b)**

Figure 3.16: (a) Sagittal and (b) axial views of the SLF, with the frontal and parietal lobes (the seed regions) highlighted in green.

Inferior Longitudinal Fasciculus

The ILF is computed the same way as the SLF. The occipital lobe was used as the seed region, and the temporal lobe as the target region for the tracking. The avoidance regions used are the frontal and the parietal lobes. The regions used for the tractography and the final tracts are shown in Figure 3.17.

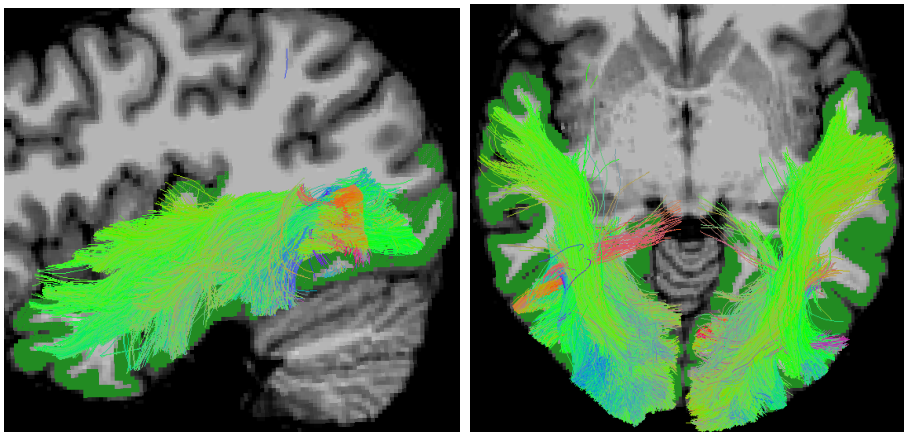

(a) (b)

Figure 3.17: (a) Sagittal and (b) axial views of the ILF, with the occipital and temporal lobes (the seed regions) highlighted in green.

Thalamocortical radiations

As discussed in Section 2.2 other tracts of interest are the connections between the thalamus and the cortex. Thalamocortical radiations are divided into anterior, posterior, superior, and inferior thalamic radiation. The posterior thalamic radiations can be further divided into posterior thalamic radiations projecting ending up in the parietal and the occipital lobes. The inclusion and exclusion regions are explained hereunder and were previously described in [87].

- Anterior thalamic radiations: they start from the thalamus, pass through the anterior limb of the internal capsule, and arrive in the frontal lobe, as shown in Figure 3.18a.
- Posterior thalamic radiations: this tract connects the thalamus with the parietal and occipital lobe through the posterior limb of the internal capsule, as shown in Figures 3.18b and 3.18c.
- Superior thalamic radiations: they start from the thalamus, pass through the posterior limb of the internal capsule, and arrive in the central gyrus, as shown in Figure 3.18d.

- Inferior thalamic radiations: this tract connects the thalamus with the insular cortex through the sublenticular part of the internal capsule, as shown in Figure 3.18e.

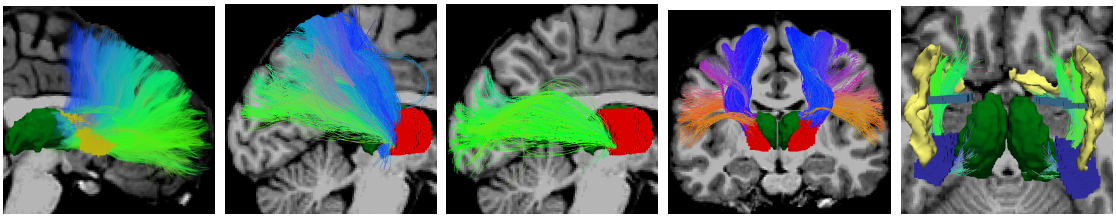

(a) (b) (c) (d) (e)

Figure 3.18: Different views of thalamic radiations. In green is the thalamus, in yellow the anterior limb of the internal capsule, in red the posterior limb of the internal capsule and in blue the retrolenticular portion of the internal capsule. (a) Sagittal view of the anterior thalamic radiations. (b, c) Sagittal view of the posterior thalamic radiations to parietal lobe (b) and to occipital lobe (c). (d) Coronal view of the superior thalamic radiations. (e) Axial view of the inferior thalamic radiations to the insular cortex, in light yellow the insular cortex and in light blue a plane that was drawn to refine the tractography.

3.5 Microstructure estimation

In this section, we discuss the different metrics that can be estimated by different microstructure models. All of them are estimated using the ElikoPy library, which wraps the execution of them. DTI maps were obtained with DiPy Library, they are illustrated in Figure 3.19. The NODDI model was applied to the data using the DMIPY library [122, 123], and the output maps are shown in Figure 3.20. DIAMOND maps were computed using Benoit Scherrer's model [7], and they are shown in Figure 3.21. The MF model was performed using the Python code provided by Rensonnet G [8, 124] in the ElikoPy library, which gives as input a pre-computed dictionary made available by Nicolas Delinte. The output maps are shown in Figure 3.22.

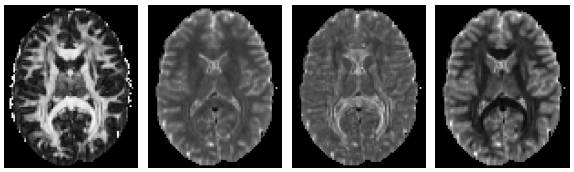

(a) (b) (c) (d)

Figure 3.19: Slices of an axial view of a subject with different DTI metrics. (A) FA; (b) MD; (c) AD; (d) RD.

(a) (b) (c) (d) (e) (f)

Figure 3.20: Axial view of a subject with different NODDI metrics. (A) icvf; (b) ODI; (c) fbundle; (d) fextra; (e) fintra; (f) fiso

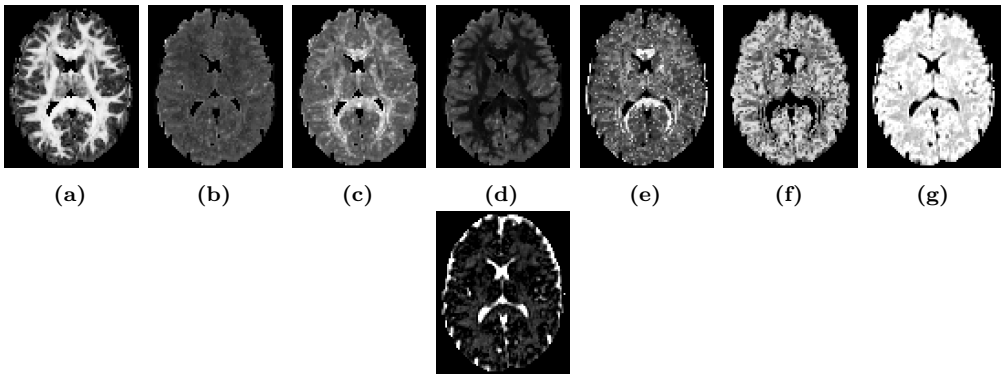

(a) (b) (c) (d) (e) (f) (g)

(h)

Figure 3.21: Slices of an axial view of a subject with different DIAMOND metrics. (A) wFA; (b) wMD; (c) wAD; (d) wRD; (e) frac_f0; (f) frac_f1; (g) frac_ftot; (h) frac_csf

3.6 Feature extraction from the metric maps

In this section, we will discuss the method used to extract a significant value from each metric map per ROI and tract of interest. For each region, we extract FA, AD, RD, and MD from DTI, icvf, ODI, fbundle, fextra and fintra from NODDI, wFA, wAD, wRD, wMD and frac_ctot from DIAMOND and fvf_tot, wfvf and frac_ftot from MF.

In total 17 different metrics were extracted. Three types of study have been done:

- **Study with biological interpretation**: we study the distribution of the metrics in the extracted regions. To characterize a distribution, we compute the **weighted mean**, **weighted SD**, **weighted skewness**, and **weighted kurtosis**, which are defined as the first four moments.

  The SD measures the amount of variation of a set of values from the mean. Skewness measures the asymmetry of a distribution concerning a normal

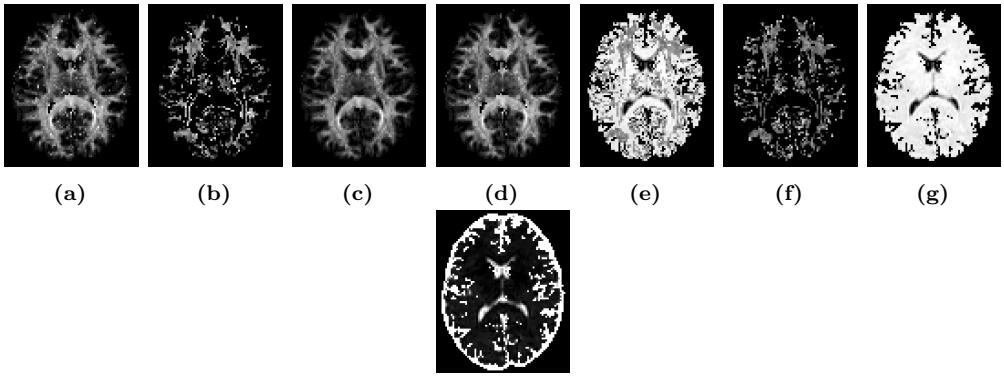

Figure 3.22: Axial view of a subject with the estimated MF metrics. (A) fvf_f0; (b) fvf_f1; (c) fvf_tot; (d) wfvf; (e) frac_f0; (f) frac_f1; (g) frac_ftot; (h) frac_csf

distribution. A distribution with positive skew has a long tail on the right side, while with a negative skew, it has a long tail on the left side [125]. The term kurtosis measures the propensity to produce outliers [126].

- **Study without biological interpretation**: we extract the features defined in the radiomics approach. As explained in Section 1.4, radiomics features include statistical features such as mean, SD, skewness, and kurtosis that differ from the attributes obtained in the extraction with biological interpretation because radiomics ones are not weighted on density maps.

- **Deep learning classification**: we use the computed 3D metrics map to train a deep learning model capable of classifying R and NR, without using ROI and feature extraction.

3.6.1 Metric extraction from ROI

The ROIs selected for the study are the thalamus, hippocampus, amygdala, accumbens, putamen and pallidum. They are taken from the FreeSurfer parcellation and registered on the diffusion map space using trilinear interpolation, to give a lower weight to voxels that are on the margin of the region because they will be a wrong approximation due to the up-scaling. Therefore, the masks are used as a density map for the computation of the weighted metrics. Higher density (weight) will give more importance to a determinate voxel than others. An example is shown in Figure 3.23.

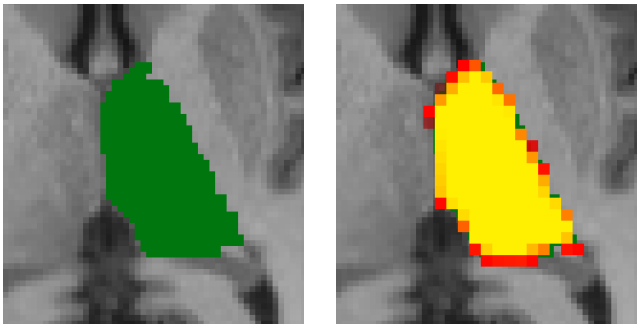

(a) (b)

Figure 3.23: Visualization of the Thalamus region before and after the trilinear interpolation. (a) In green the Thalamus registered in dMRI space and same resolution of T1. (b) Heatmap of the Thalamus registered and upscaled in dMRI space with the trilinear interpolation, is possible to see the green region not upscaled in the background.

3.6.2 Metric extraction from tractograms

The tracts of interest are the tracts discussed in Section 3.4.4. To extract the weights from them we use the same method as explained in Section 3.4.3 to keep only the most important voxels of a tractogram.

Unlike ROI, the extracted tract passes through different zones in the brain, therefore it has different values depending on the point on the pathway, as shown in Figure 3.24a and Figure 3.24c. The analysis in this study takes an approximation of it without considering the spatial information (see Limitation Section 5.5), as shown in Figure 3.24c and Figure 3.24d. Using the four moments explained above, we try to get all the information on the distribution along the pathway.

3.7 Statistical Analysis

Since the study aims to assess differences in microstructural features between R and NR to VNS, we need a tool capable of telling us if the differences have statistical significance. To reach our aim, we use a comparison test for the means of two independent samples as explained in Section 1.5.2.
A comparison test quantifies the difference between the distribution of two samples to decide if the two populations are statistically different.

- Null hypothesis: $H_0 : \mu_2 = \mu_1$
- Alternative hypothesis $H_a : \mu_2 \neq \mu_1$

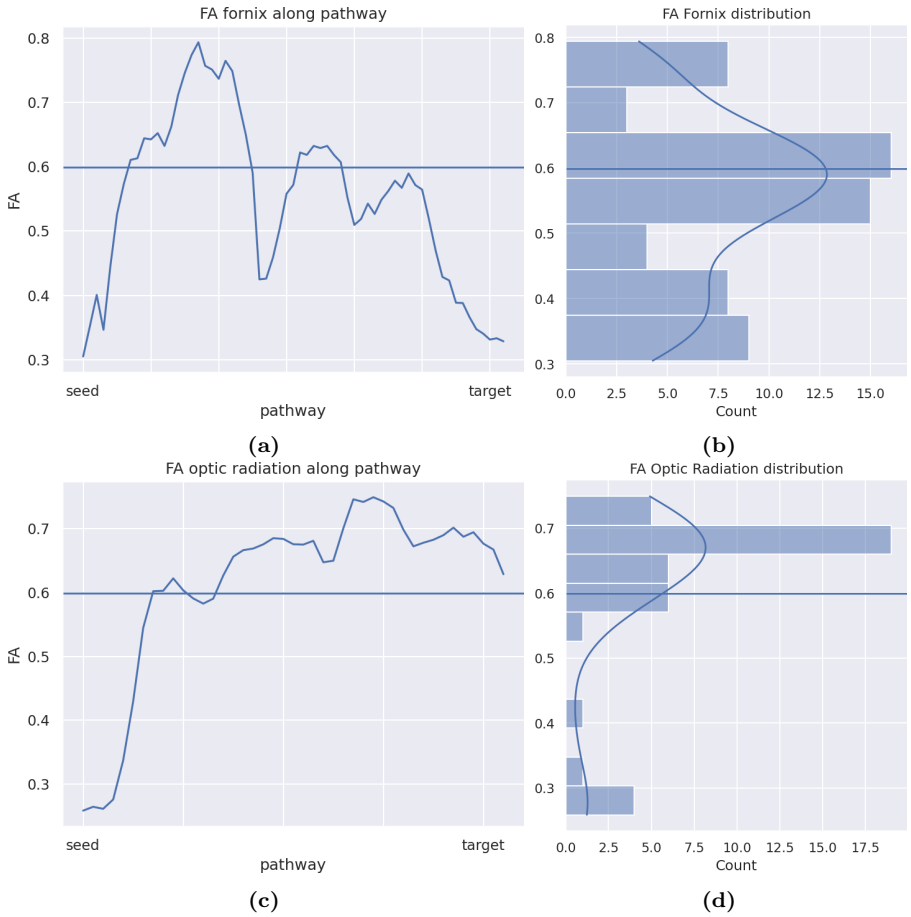

Figure 3.24: Two examples of distribution of FA values along the pathway of interest: (a) the fornix tract; (c) the optic radiation tract. On the right are the distributions of values on the tract. The horizontal lines are the mean of the tracts. Data taken from TRACULA by FreeSurfer, and idea inspired to tract plots of FreeSurfer. URL: `https://dmri.mgh.harvard.edu/tract-atlas/` (visited on 08/05/2023).

Due to the relative number of patients included in the present study, the hypotheses to use a parametric test were not held, as discussed in Section 1.5.1, therefore **Mann-Whitney U** rank test was used to assess the statistical difference in diffusion metrics between R and NR.

In the case we compare the means between R, PR, and NR we cannot anymore use the Mann-Whitney U rank test since we have more than two groups. The **Kruskal-Wallis** test is used to compare two or more groups. It is a nonparametric test, chosen for the same reason as the one described above.

To check if the patient's categorical information is related to being a R or not, Chi2, Fisher and Barnard tests are used. Due to its suitability for small datasets

(in comparison to Chi2 or the Fisher tests), the Barnard test was used to compare categorical information of R and NR. The drawback of Barnard's exact test is that it works only for 2x2 contingency matrices.

The statistical analyses were conducted using the `scipy.stat` library: `mannwhitneyu()` was used to compare statistical features between R and NR; `kruskal()` for Kruskal-Wallis testy; `barnard_exact()` to check differences in categorical variables between R and NR.

3.8 Selection of interpretable features

The purpose of the study is to find the best microstructural features able to classify the two classes of subjects, R, and NR. To select the best microstructural features, we use different machine learning (ML) algorithms and the sequential feature selection algorithm.

3.8.1 Scaling

Different extracted metrics have different scales, and most ML algorithms work only with scaled features. Therefore, we need to scale our data before going further. Different scaling approaches have been used: standard scaler, min max scaler and robust scaler. The best accuracy was found using the standard scaler. A robust scaler works like a min max scaler and can be useful when outliers are present in the dataset.

3.8.2 Algorithms and hyperparameters

ML algorithms need different hyperparameters, they control how the parameters are chosen during the learning process and they depend on the model. Therefore, hyperparameters can improve the quality of an algorithm if they are chosen correctly. The optimization of hyperparameters is done using the grid search approach, defining first all the different values that we want to try and then all the combinations are tried, choosing at the end the best combination that gives the highest score. Since our dataset is small, we do not have a real view of the samples in the feature space, therefore we need to regularize the algorithms as much as possible, and linear models are preferred over nonlinear ones. The tuned algorithms used in this study are from scikit-learn [127] and are the following:

- Logistic Regression
- Linear SVM

- SVM with polynomial kernel
- SVM with rbf kernel

3.8.3 Feature Selection Algorithm

The purpose of the study is to find the subset of microstructural features capable to differentiate between R and NR subjects, therefore we cannot apply dimensionality reduction algorithms like PCA or ICA, because the obtained features would not be interpreted as microstructural features anymore, but as a transformation of one or more of them. In this study, we select only the features that most influence the decision of the classification without transforming them. Sequential Feature Selection algorithm (SFS) by mlxted [128] with the floating method [129] is used in this study. After the selection, new scores are computed on the algorithm trained on the selected features, and decision boundaries are displayed.

3.8.4 Scoring approximation

An approximation of balanced accuracy, log loss and AUC scores are used to select the best model. Thanks to the small number of samples present in the dataset, score approximations are computed through the Leave One Out (LOO) CV technique. After the probability estimation of the 18 models trained in the LOO CV loop, the results are stacked and considered as a single batch. The metrics scores are computed on the computed batch.

3.9 Radiomics pipeline for classification

In this part of the study, we do not pose any limitations on the biological interpretation of the extracted features. Therefore, as explained in Section 1.4, to derive as much as possible information from the ROI we use different image transformations for our metric maps. PyRadiomics [130] is the tool used to extract Radiomics features. The image transformation done by PyRadiomics and used on our metric maps are:

- Original, no filter is applied;
- Wavelet, decomposition and approximation of wavelet transform done by PyWavelet [131];
- Laplacian of Gaussian image, it is obtained by convolving the image with the second derivative;
- Square of image intensities;

- The square root of image intensities;
- The logarithm of absolute intensities plus one;
- Exponential of absolute intensities;
- The Image gradient;
- Local Binary Pattern in 3D using spherical harmonics.

The exact computation and explanation of the transformations are in the PyRadiomics documentation API [3]. For each of them, PyRadiomios extract the features already discussed in Section 1.4, which amount to about a thousand features.

Considering all the models and all the tracts and regions extracted by FreeSurfer, the number of extracted features reached a million and a half in this study. Therefore, a massive dimensionality reduction is necessary to extract representative and informative features since Radiomic features are frequently redundant. The strategy and different models implemented to extract informative features are explained in the following sections.

3.9.1 Constant, duplicate and outlier features

A fixed filtering of constant, duplicate and unreliable features is performed. From PyRadiomics documentation some of the features computed are symmetrical to other features or unreliable, so we filter them. The removed features are joint average, sum average, sum squares, minimum, maximum, 10 percentile, 90 percentile, interquartile range, range, maximum 2D diameter column, maximum 2D diameter row, maximum 2D diameter slice, and maximum 3D diameter.
Many features on the dataset are almost constant and redundant, we resolved this problem by dropping all the features with these characteristics using a Python library for feature engineering and selection: Feature-engine [4]. The used methods are `DropConstantFeautes()` and `DropDuplicateFeatures()`. A feature is considered constant if at least 62% of its values are equal.

The features where outliers are present are dropped using the Median Absolute Deviation (MAD) rule [5]. Since our study has a limited set of samples, the MAD rule is known as more robust than the z-score rule since it is based on the median instead of the mean. The maximum deviation from the median imposed for this study is 3.

---

[3]PyRadiomics: `pyradiomics.readthedocs.io`

[4]Feature-engine python libary: `feature-engine.trainindata.com`

[5]Explanation of MAD algorithm: `https://eurekastatistics.com/using-the-median-absolute-deviation-to-find-outliers/`

After the fixed reduction techniques, the features are scaled in the same range by a robust scaler offered by Sci-kit Learn [127], chosen for the limited number of samples of our dataset.

3.9.2 Univariate filtering

Univariate filters select the features that better perform for a given metric. Different typologies of univariate filtering were tried:

- F-ratio
- Kendal correlation
- Relief F
- Spearman correlation
- Mannwhiten
- Mannwhite + Kruscal

The first four are computed using the Python library ITMO_FS[6], which provides a large set of feature selection algorithms. The last two univariate filters are based on non-parametric tests and they select the features with p-values less than 0.05, as explained in Section 3.7, and they are followed by a correlation selection that keeps only features that correlate less than 0.95. The correlation selection is done using the `SmartCorrelatedFeatures()` function of the Feature-engine library. Up to one thousand features were extracted by this selection.

3.9.3 Multivariate filtering

Multivariate filters select the set of features that together maximize a given metric. Different multivariate filtering algorithms were tried:

- CFR: maximize the correlation and minimize the redundancy
- Conditional infomax feature extraction (CIFE)
- Dynamic change of selected feature (DCSF)
- Interaction capping (ICAP)
- Max relevance and max independence (MRI)
- Minimum redundancy maximum relevance (MRMR)

[6]ITMP_FS documentation: `iitmo-fs.readthedocs.io`

These algorithms are offered by the Python library ITMO_FS, and they are used to select only 20 features.

SFS is applied to reduce the number of features, the same algorithm as in Section 3.8.3 was used, with 3-fold CV, and AUC-score as the scoring function.

3.9.4 Classification algorithms

Differently from the study with biological interpretation, here we used a higher set of algorithms with hyperparameter optimization. The algorithms selected for this analysis are the following:

- Logistic regression with 3-fold CV hyperparameters tuning and negative log loss scoring function.
- RBF-SVM classifier with 3-fold CV hyperparameters tuning and AUC-score scoring function.
- k-nearest neighbours classifier with 3-fold CV hyperparameters tuning and negative log loss scoring function.
- Multi-layer perceptron classifier with 3-fold CV hyperparameters tuning and negative log loss scoring function;
- Gaussian Naive Bayes.

3.9.5 Scoring approximation

Same scoring approximation method as in Section 3.8.4 was applied.

3.10 Deep Learning classification

One of the main problems of classifying NR from R patients was defining the ROI or the tract to look for any change in a metric. Deep learning is a solution to this problem since it does not need a region of interest, but through training, it can learn where to see to distinguish between the two classes. The library used for this analysis is PyTorch[7]. PyTorch requires a `Dataset` class where inputs and targets can easily accessed, and a `DataLoader` where, through the `Dataset`, it gives a batch of the inputs and targets. Then, a good model is required to extract information from 3D images or potentially a vector of volumes (considering more metric maps per subject). These problems are being asked in the following sections.

[7]PyTorch libary: `https://pytorch.org/`

3.10.1 Volumes menagement

The management of volumes was done through the library TorchIO [8] [132]. It is an open-source library for efficient loading, preprocessing, augmentation and patch-based sampling of 3D medical images in deep learning. TorchIO implements different classes to represent a subject in a `Dataset` class.

The first are the `Image` classes where the volume information is stored, they are the `ScalarImage` and the `LabelMap` classes. They use a lazy loading approach, therefore the data is not loaded from disk when the classes are instantiated, but when they are needed for computation. A subject can have more than one image, in our case a subject has many model metric maps, and together with the target value, they are stored in the `Subject` class.

Different instances of Subjects are grouped into the `SubjectDataset` class that directly inherits properties from the PyTorch `Dataset`.

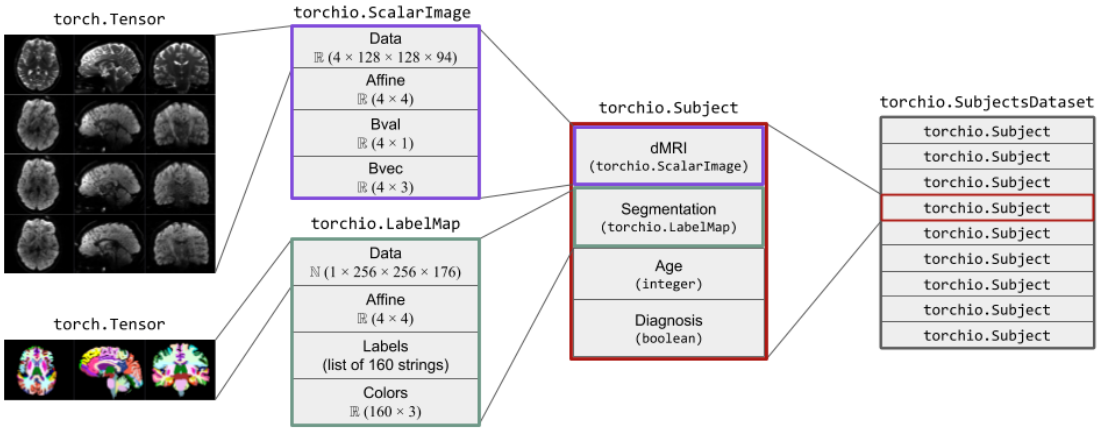

Figure 3.25: Representation of `Image`, `Subject` and `SubjectsDataset` classes in TorchIO [132]

Since `SubjectDataset` class is a subclass of PyTorch `Dataset` class it can be passed to the `DataLoader`. As soon as the `DataLoader` request a batch of data the images are loaded in memory and the transformations are applied.

3.10.2 Image transformations

Before feeding the model with the volumes, they can be preprocessed and augmented with volume transformation. TorchIO gives a large set of functions for preprocessing and augmentation in the CPU. However, it does not give a function for registering all the images in a common space.

[8] TorchIO library: `https://torchio.readthedocs.io/`

Before the preprocessing steps, images are registered with ANTs in the common space HCP1065 with a Rigid transformation of the FA map. During the registration an interpolation of the volume resampled itself to a $1mm$ per voxel, this will be then adjusted by resampling the volume into $2mm$ per voxel.

After registration, the following preprocessing steps are applied:

- Reorder the volume data to a canonical orientation (RAS+);
- Resampling the volume to a $2mm$ per voxel space;
- Cropping or Padding the volume to a fixed size;
- Standardization of the voxel intensities;

The generalization ability of the model was increased by using augmentation methods. Furthermore, the augmentation transformation was used to increase the size of the dataset. The transformations were applied only after the splitting of the dataset in training, validation and training set. The following transformations were applied to the training set through TorchIO:

- Random affine transformation: the volume is randomly scaled, rotated and translated with a probability of 0.8;
- Random anisotropy: it simulates an image acquired with random anisotropic spacing with a probability of 0.2;
- Random biasfield: it adds a random bias field artifact with a probability of 0.2;
- Random blur: it blurs the volume with a random Gaussian filter with a probability of 0.2;
- Random gamma: it randomly changes the contrast of the image with a probability of 0.2;
- Random noise: it adds a random Gaussian noise with a probability of 0.2;
- One Random motion or Random Ghosting or Random Spike: simulates one of these artifacts with a probability of 0.1;
- Random swap: it swaps random cubes of the volume of prefixed dimension with a probability of 0.1.

3.10.3 Model

To model our classification model was used MONAI[9] framework. MONAI is a PyTorch-based, open-source framework for deep learning in healthcare imaging,

[9]MONAI main page: `https://monai.io`

part of the PyTorch Ecosystem. MONAI framework presents different domain-specific models for healthcare imaging, including state-of-the-art transformer-based 3D Segmentation algorithms like UNEST.

Training a deep model without having pre-trained weights and a big dataset as in our case did not give good results. For this reason, transfer learning is applied from a similar domain. The weights of a pre-trained UNEST model for volumetric brain segmentation with T1 images from MONAI Model Zoo were chosen for our study. UNEST model has a design similar to U-net for 3D images. The pre-trained model takes as input a 96x96x96 volume and returns a segmented brain with the same dimensions, as shown in Figure 3.26.

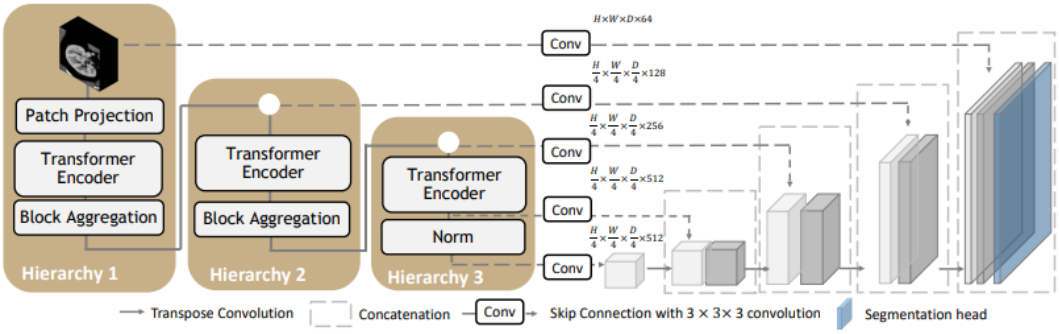

Figure 3.26: The network architecture of UNEST Base model [133].

To change the model behaviour from segmentation to classification, we cut the U-shape in the point between the encoder and decoder sections, where the spatial information is reduced and the feature information is increased. The lowest part of the model reduces the volume from `1x96x96x96` to `1024x3x3x3`. We continue the reduction by adding a non-pre-trained 3D convolution block with dropout and ReLU activation, reducing the dimensions to `2048x1x1x1`. After, a flatter transformation is applied followed by a fully-connected linear layer, that takes as input `2048` features and returns a single output value for binary classification.

The loading phase from CPU to GPU is the bottleneck of this model since the loading and the transformations of a batch take up to 2 minutes with all the metrics, while 10 seconds with a single metric. The bottleneck can be reduced using a higher number of workers in the DataLoader, in this study 8 CPUs were used.

Overall, there is a trade-off between speed, memory and multiple metrics consideration, this model is oriented to high speed and reduced memory usage for each patient, but it is needed to choose the metric to use.

Chapter 4

Results

The analysis conducted is divided into two parts: the first in which the PR are considered as R and the second where the NR, PR and R are treated as distinct groups.

4.1 Statistical Analysis of Categorical features

We start by analysing categorical features, such as the sex of the subject, if it takes benzodiazepines and the typology of epilepsy as discussed in Section 2.1.

The contingency table summarises the frequencies of the categorical features, as explained in 1.5.3. It is possible to see it through a bar plot, as shown in Figure 4.1.

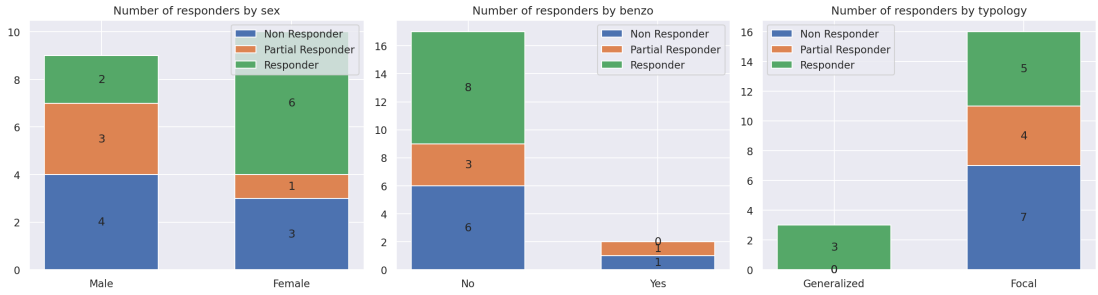

(a) **(b)** **(c)**

Figure 4.1: Box plots of contingency matrix

Considering both PR as R or NR, through a Bernard exact test, all the possible hypotheses are rejected. Therefore, considering our samples, the R are not dependent on sex, typology, or benzodiazepines.

We cannot say anything about statistical dependency considering three distinct groups, NR, PR, and R since Bernard's exact test works only for a 2x2 contingency

matrix and Chi2 does not have enough samples to give us a statistical answer, as explained in Section 3.7.

4.2 Statistical Analysis of Microstructural features

In this section, we show the results by ROIs and fascicles, and for each of them, the microstructural features are compared between R and NR. Multiple test corrections can be applied to have more statistical power, *Bonferroni* and *Benjamini Hochberg* were tried, but none of the p-values survived the correction. Therefore, to have higher statistical power on our results, only p-values lower than 0.01 are considered significant, without any corrections.

Due to the numerous tracts explored and the different diffusion metrics extracted, only the significant tracts already discussed in the literature were shown in the present section. A full table with the details of all statistical tests for the different tracts and all diffusion metrics can be consulted in Appendix C.

4.2.1 Anterior Thalamic Radiation

The anterior thalamic radiation goes from the thalamus to the frontal lobe through the anterior limb of the internal capsule, as shown in Figure 3.18.

Microstructure Fingerprinting

A higher `frac_ftot` was found in R compared to NR (right: $p = 0.003$), as shown in Figure 4.2a, as well as a corresponding lower `frac_csf` (right: $p = 0.003$).
To avoid redundancy for the rest of the analyses, only the `frac_tot` will be reported, without reporting the `frac_csf` since a linear relationship exists between them and equal p-values are obtained for these metrics.

DIAMOND

A higher `wAD` was found in NR compared to R (right: $p = 0.009$), as shown in Figure 4.2b.

NODDI

Statistical mean differences have been found in the mean of NODDI metrics:

- A lower `ODI` was found in NR compared to R (left: $p = 0.003$, right: $p = 0.003$), as shown in Figure 4.2c.

- A lower `fintra` was found in NR compared to R (right: $p = 0.004$), as shown in Figure 4.2d.

DTI

Statistical mean differences have been found in the mean of DTI metrics.

- A greater `MD` was found in NR compared to R (right: $p = 0.009$), as shown in Figure 4.2e.
- A greater `AD` was found in NR compared to R (left: $p = 0.006$, right: $p = 0.003$), as shown in Figure 4.2f.

4.2.2 Posterior Thalamic Radiation - Parietal

The posterior thalamic radiation goes from the thalamus to the parietal lobe through the posterior limb of the internal capsule, as shown in Figure 3.18.

DTI

Statistical mean differences have been found in the mean of DTI metrics:

- A greater `MD` was found in NR compared to R (right: $p = 0.006$), as shown in Figure 4.3a.
- A greater `AD` was found in NR compared to R (right: $p = 0.003$), as shown in Figure 4.3a.

4.2.3 Posterior Thalamic Radiation - Occipital

The posterior thalamic radiation goes from the thalamus to the occipital lobe through the posterior limb of the internal capsule, as shown in Figure 3.18.

NODDI

Statistical mean differences have been found in the mean of NODDI metrics:

- A lower `fintra` was found in NR compared to R (right: $p = 0.005$), as shown in Figure 4.4a.
- A lower `icvf` was found in NR compared to R (left: $p = 0.005$, right: $p = 0.004$), as shown in Figure 4.4b.
- A greater `fextra` was found in NR compared to R (left: $p = 0.004$, right: $p = 0.005$), as shown in Figure 4.4c.

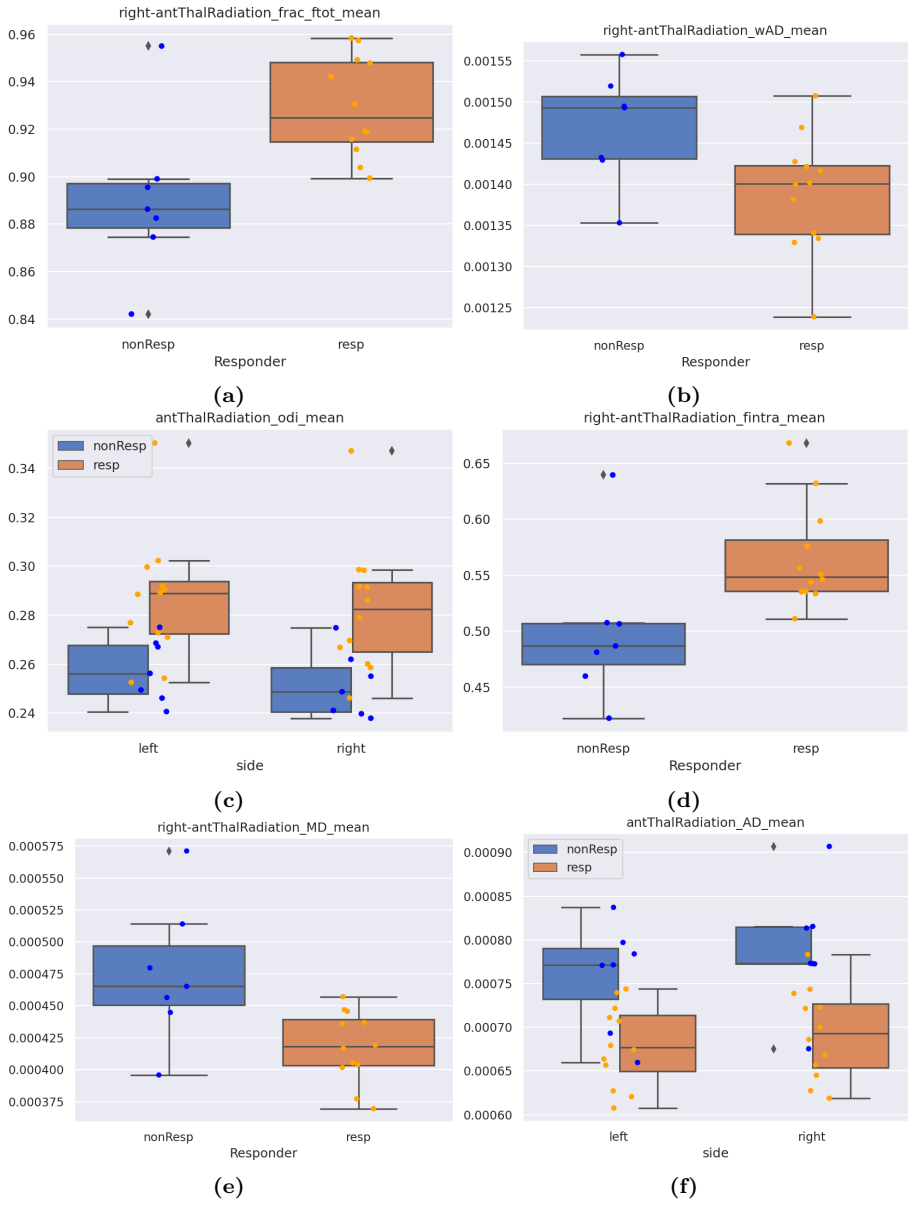

Figure 4.2: Box plot of diffusion metrics in the left and right anterior thalamocortical radiations in R and NR: (a) `frac_ftot` mean; (b) `wAD` mean; (c) `ODI` mean; (d) `fintra` mean; (e) `MD` mean; (f) `AD` mean.

DTI

Statistical mean differences have been found in the mean of DTI metrics:

- A greater `MD` was found in NR compared to R (right: $p = 0.005$), as shown in Figure 4.4d.

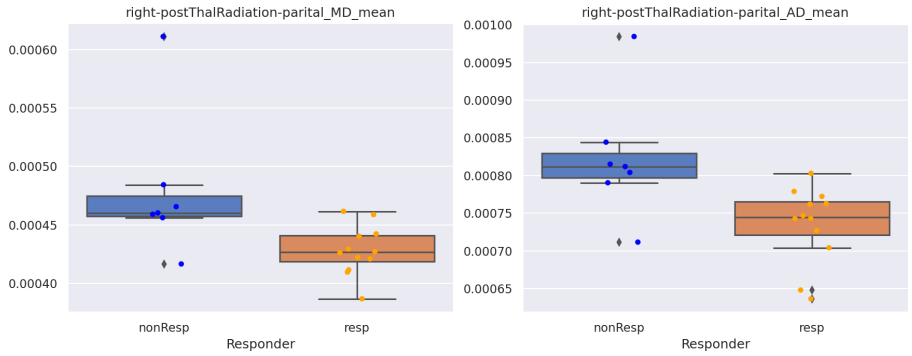

(a) **(b)**

Figure 4.3: Box plot of diffusion metrics in the right posterior thalamocortical radiations in R and NR: (a) `MD` mean; (b) `AD` mean.

- A greater `RD` was found in NR compared to R (right: $p = 0.006$), as shown in Figure 4.4e.
- A greater `AD` was found in NR compared to R (right: $p = 0.009$), as shown in Figure 4.4f.

4.2.4 Inferior Thalamic Radiation - Insula

The inferior thalamic radiation goes from the thalamus to the insular cortex passing through the sublenticular part of the internal capsule, as shown in Figure 3.18.

NODDI

Statistical mean differences have been found in the mean of NODDI metrics:

- A lower `icvf` was found in NR compared to R (left: $p = 0.005$, right: $p = 0.0002$), as shown in Figure 4.5a.
- A greater `fextra` was found in NR compared to R (left: $p = 0.002$, right: $p = 0.0003$), as shown in Figure 4.5b.

DTI

Statistical mean differences have been found in the mean of DTI metrics:

- A greater `MD` was found in NR compared to R (right: $p = 0.004$), as shown in Figure 4.5c.
- A greater `AD` was found in NR compared to R (right: $p = 0.003$), as shown in Figure 4.5d.

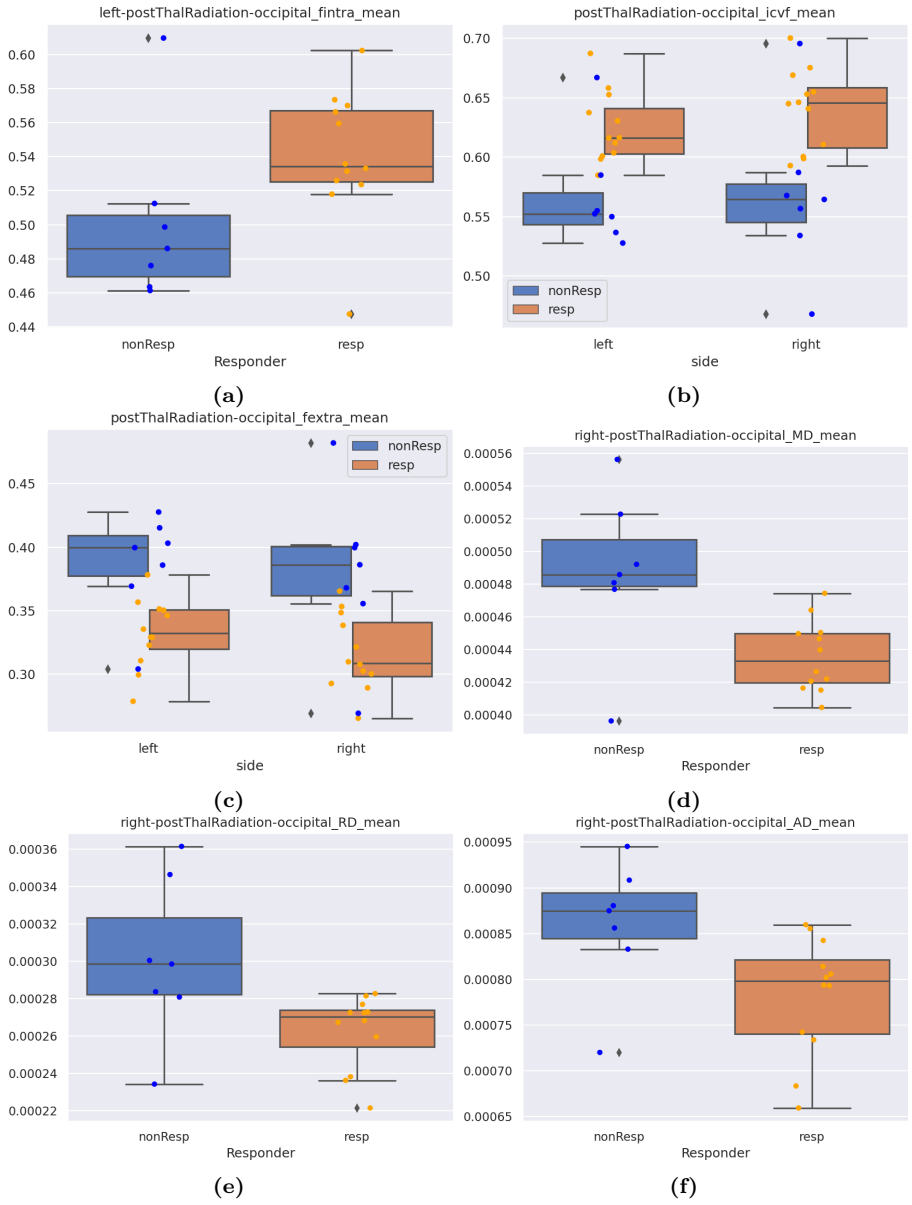

Figure 4.4: Box plot of diffusion metrics in the left and right posterior thalamocortical radiations in R and NR: (a) `fintra` mean; (b) `icvf` mean; (c) `fextra` mean (d) `MD` mean; (e) `RD` mean; (f) `AD` mean.

4.2.5 Fornix

The fornix goes from the hippocampus to the mammillary body passing over the thalamus, as explained in Section 2.2.

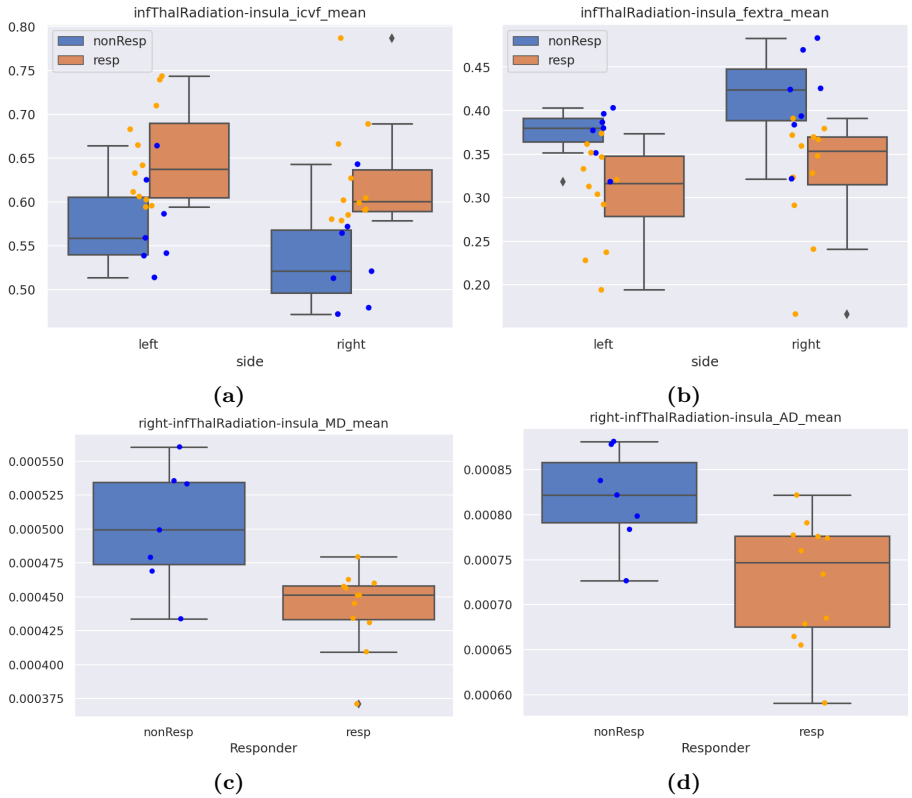

Figure 4.5: Box plot of diffusion metrics in the left and right inferior thalamocortical radiations in R and NR: (a) `icvf` mean; (b) `fextra` mean; (c) `MD` mean; (d) `AD` mean.

NODDI

Statistical mean differences have been found in the mean of NODDI metrics:

- A lower `icvf` was found in NR compared to R (left: $p = 0.009$, right: $p = 0.006$), as shown in Figure 4.6a.

DTI

Statistical mean differences have been found in the mean of DTI metrics.

- A greater `MD` was found in NR compared to R (left: $p = 0.0004$, right: $p = 0.0004$), as shown in Figure 4.6b.
- A greater `RD` was found in NR compared to R (left: $p = 0.0004$, right: $p = 0.0001$), as shown in Figure 4.6c.
- A greater `AD` was found in NR compared to R (left: $p = 0.008$, right: $p = 0.006$), as shown in Figure 4.6d.

Statistical mean differences have been found considering the three classes:

- On `MD` (left: $p = 0.006$, right: $p = 0.005$), as shown in Figure 4.6e.
- On `RD` (left: $p = 0.007$, right: $p = 0.004$), as shown in Figure 4.6f.

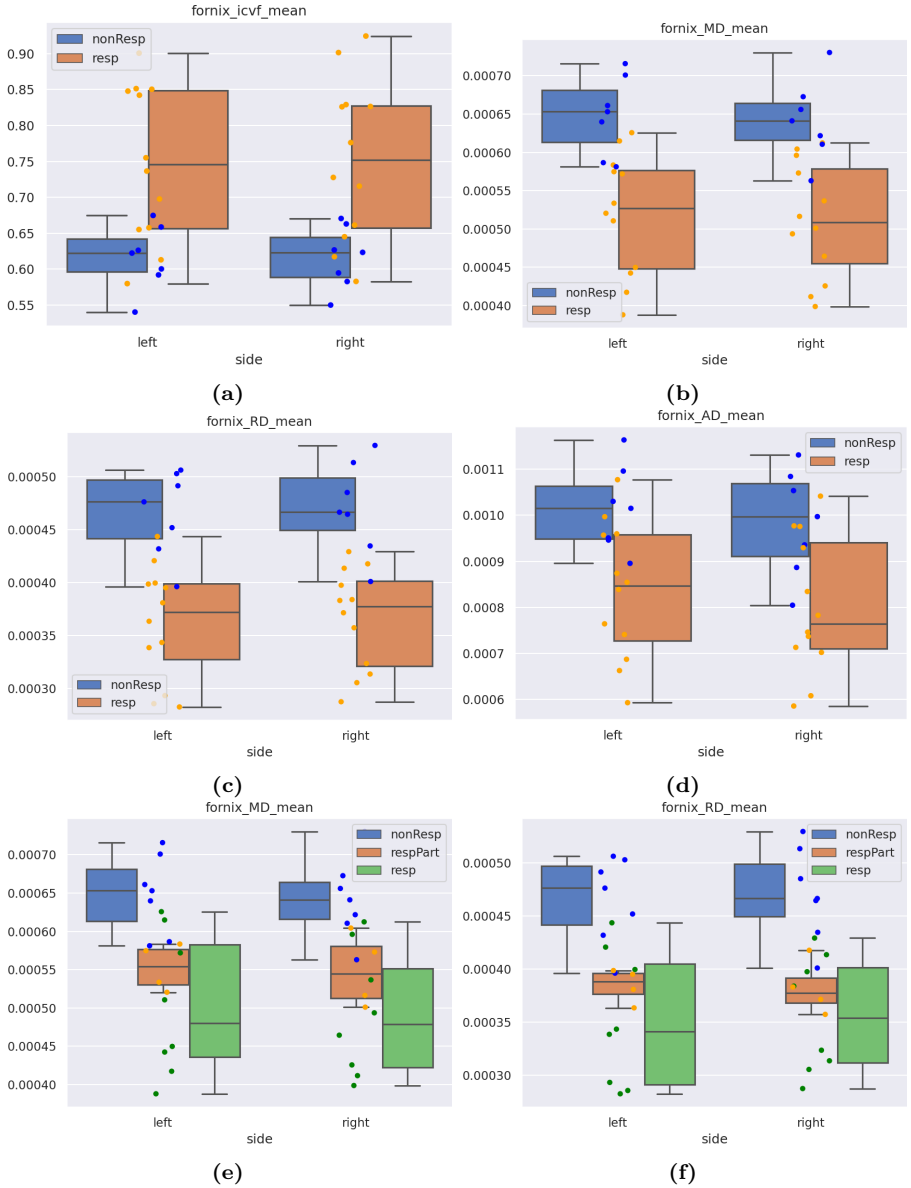

Figure 4.6: Box plot of diffusion metrics in the left and right fornix: (a) `icvf` mean; (a) `MD` mean in R and NR; (b) `RD` mean in R and NR; (c) `AD` mean in R and NR; (a) `MD` mean in R, PR and NR; (b) `RD` mean in R, PR and NR.

4.2.6 Superior Longitudinal Fasciculus

The SLF goes from the frontal lobe to the parietal lobe, and it is divided into three sub-fascicles: SLF I, SLF II, and SLF III, as explained in Section 2.2 For this tract is used the heat map is computed by TRACULA since it can compute the three tracts separately, as explained in Section 3.4.1. Subject 16 was excluded from the analysis for this tract, as explained in Section 3.4.1.

NODDI

Statistical mean differences have been found in the mean of NODDI metrics:

- A lower `fbundle` was found in NR compared to R in SLF I (right: $p = 0.008$), as well as a corresponding lower `fiso` (right: $p = 0.008$), as shown in Figure 4.7a.

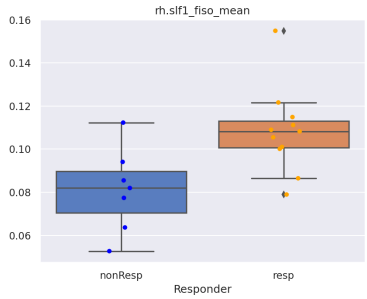

(a)

Figure 4.7: Box plot of diffusion metrics in the left and right SLF in R and NR: (a) `fiso` mean of SLF I.

4.3 Selection of interpretable features

In this section, we show the result of the SFS to find the best subset of features capable of correctly classifying R and NR.
The selection was made using only the mean of microstructural features in the region.
In the case of the Logistic Regression, the most frequent features selected during the SFS were:

- the RD mean of the right accumbens area
- the weighted FA mean in the temporal body of the corpus callosum
- the MD and AD mean of the left fornix

- the mean of the total fibre volume fraction in the anterior commissure.
- the RD mean of the right fornix

The model reached an accuracy of 0.643 and an AUC score of 0.610. The three most frequent features selected by SFS with Logistic Regression are shown in Figure 4.8.

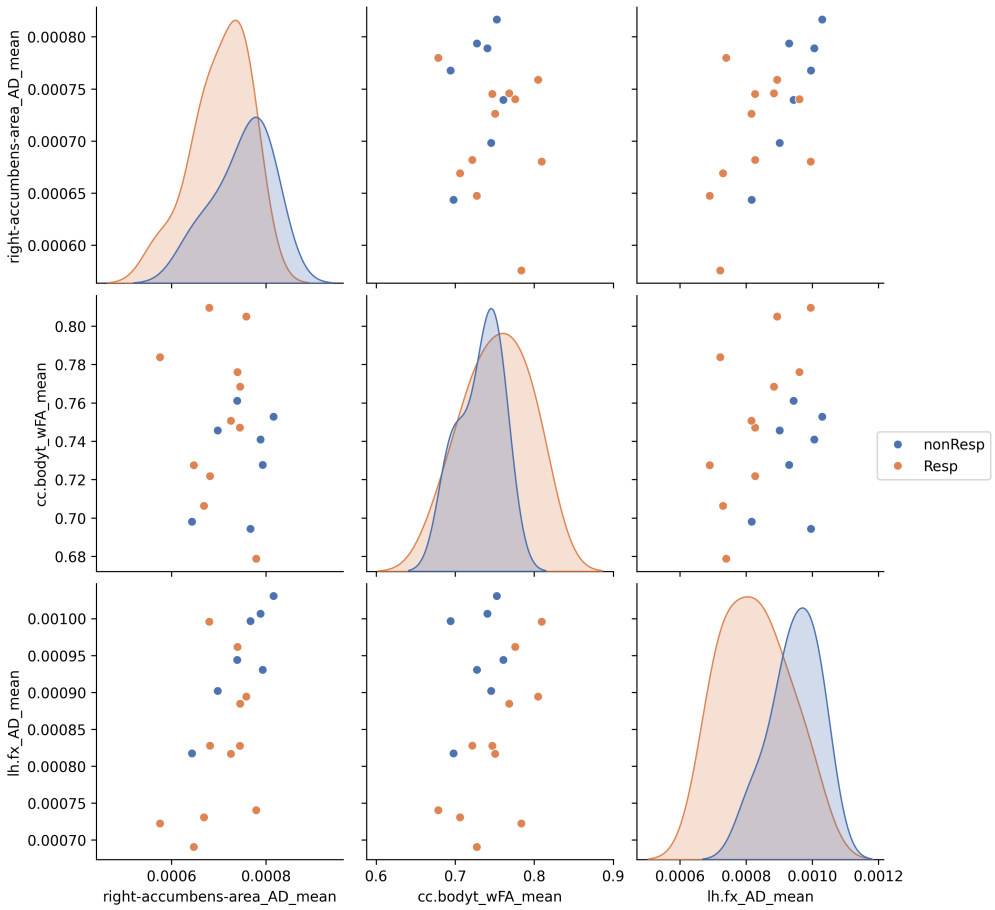

Figure 4.8: Most frequent selected features by SFS with Logistic Regression: RD mean of the right accumbens area; weighted FA mean in the temporal body of the corpus callosum; AD mean of the left fornix.

An equal frequency of selected features was found in the SFS with the Linear SVM algorithm. The model reached an accuracy of 0.643 and an AUC score of 0.571.

SFS with RBF SVM reached an accuracy of 0.812 and an AUC of 0.779. The most frequent features selected were:

- the mean of the total fibre volume fraction of the premotor body of the corpus callosum

- the mean of the extra-cellular volume fraction of the left posterior thalamocortical radiation to the occipital lobe
- the MD mean of the left fornix

The most frequent features selected by SFS with RBF SVM are shown in Figure 4.9.

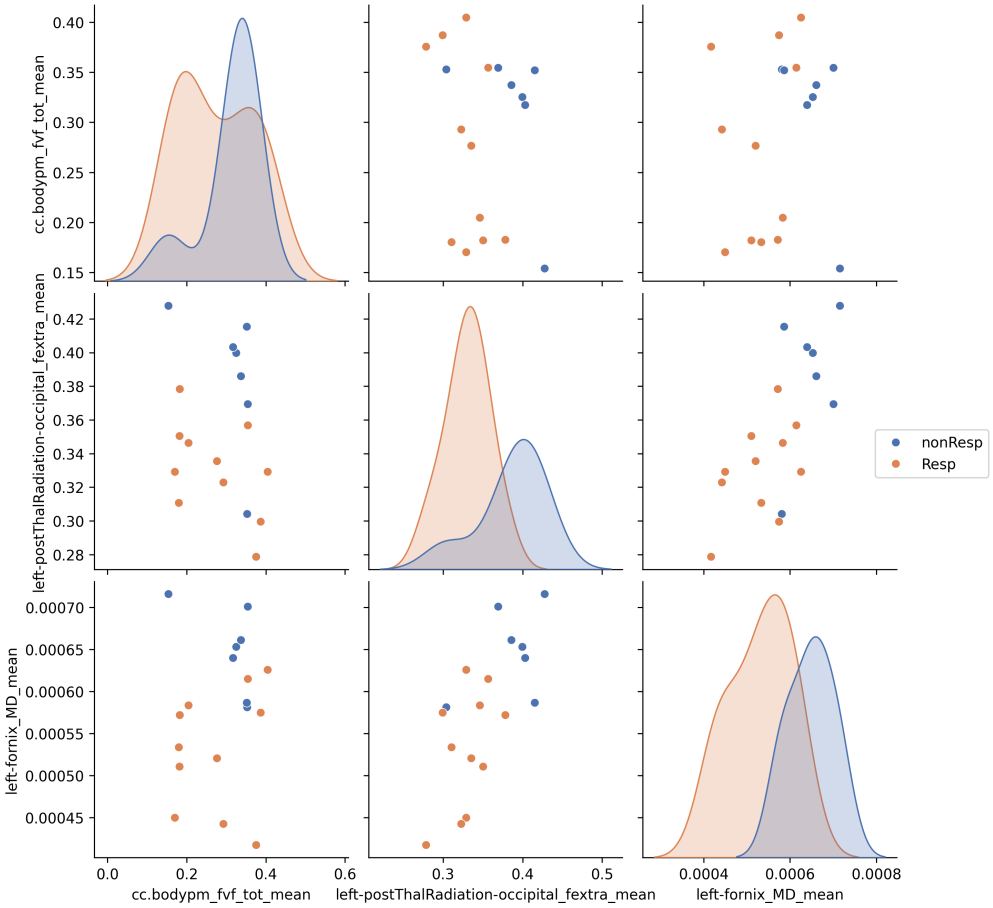

Figure 4.9: Most frequent selected features by SFS with RBF SVM: mean of the total fibre volume fraction of the premotor body of the corpus callosum; mean of the extra-cellular volume fraction of the left posterior thalamocortical radiation to the occipital lobe; MD mean of the left fornix

Selecting the features with an SVM with a polynomial kernel the most frequent features selected were:

- the mean of the total fraction of fibres in the right inferior longitudinal fasciculus

- the AD mean of the right accumbens area
- the AD mean of the right extreme capsule

The model reached an accuracy score and an AUC score of 1. The three most frequent features selected by SFS with SVM with polynomial kernel are shown in Figure 4.10.

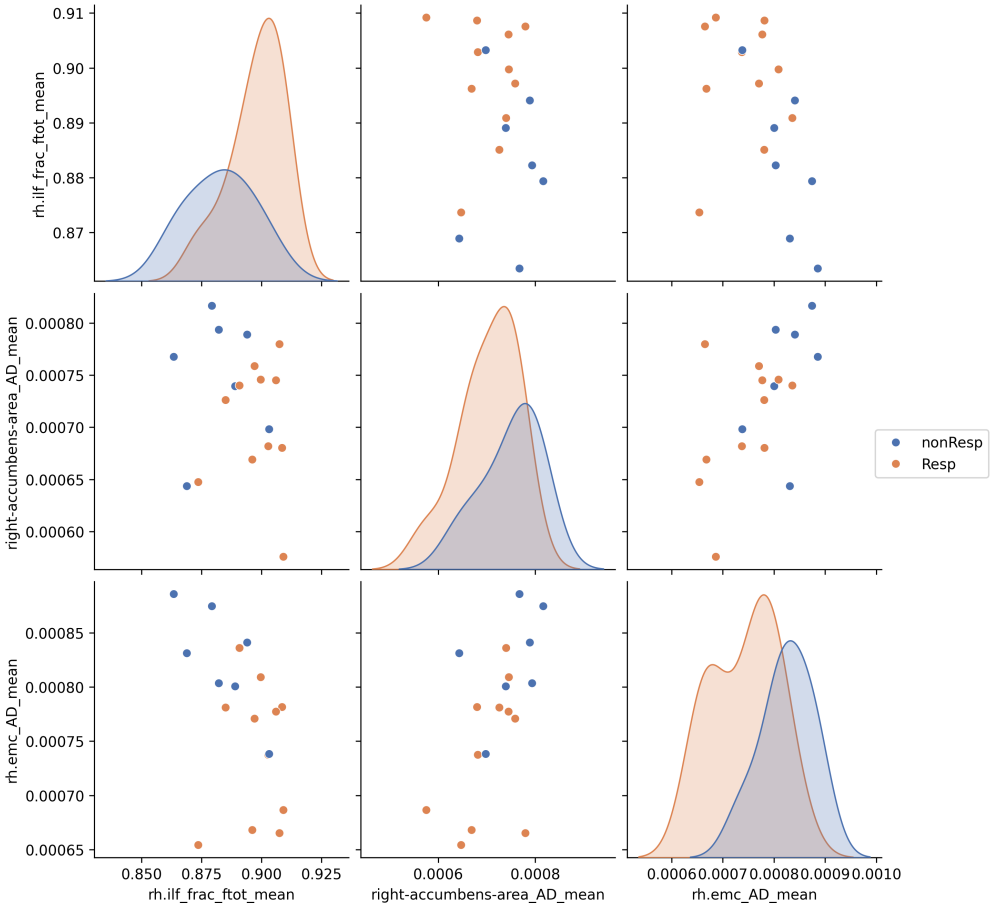

Figure 4.10: Most frequent selected features by SFS with polynomial kernel SVM: mean of the total fraction of fibres in the right inferior longitudinal fasciculus; AD mean of the right accumbens area, AD mean of the right extreme capsule

4.4 Responsiveness Prediction with Radiomics

In this section, we show the results of the Radiomics pipeline introduced in the Method Section 3.9 to classify unseen patient between R and NR.

The optimal model pipeline was determined by training the combination of all univariate and multivariate filters.
The best algorithms are shown in the Figure 4.11, the scores of the rest of the algorithms are shown in Appendix D.

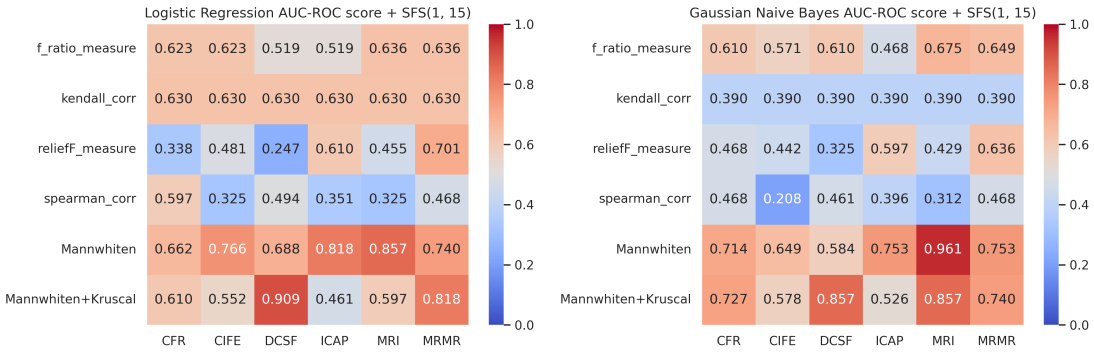

(a) **(b)**

Figure 4.11: AUC scores computed from the combination of all univariate and multivariate filters. (a) Scores computed using Logistic Regression algorithm; (b) Scores computed using Gaussian Naive Bayes algorithm. Both models are followed by an SFS which reduces the number of features into a set that contains the optimizing features with a length variable between one and fifteen.

The best results were obtained using the non-parametric test filtering with AUC scores above 0.9.
By training singularly the best models, confusion matrix and scores were obtained, as shown in Figure 4.12:

An ensemble model has been built on both Gaussian models since a good AUC score was found in the first and good accuracy in the latter. The confusion matrix and scores are shown in Figure 4.12d.

Hierarchical clustering

A similar pipeline used for radiomics classification was used before applying hierarchical clustering. The most relevant result was found by selecting only the features from `frac_csf_mf`. The result is shown in Figure 4.13.

Confirming the results of the classification models, most of the selected features come from the wavelet transformation.

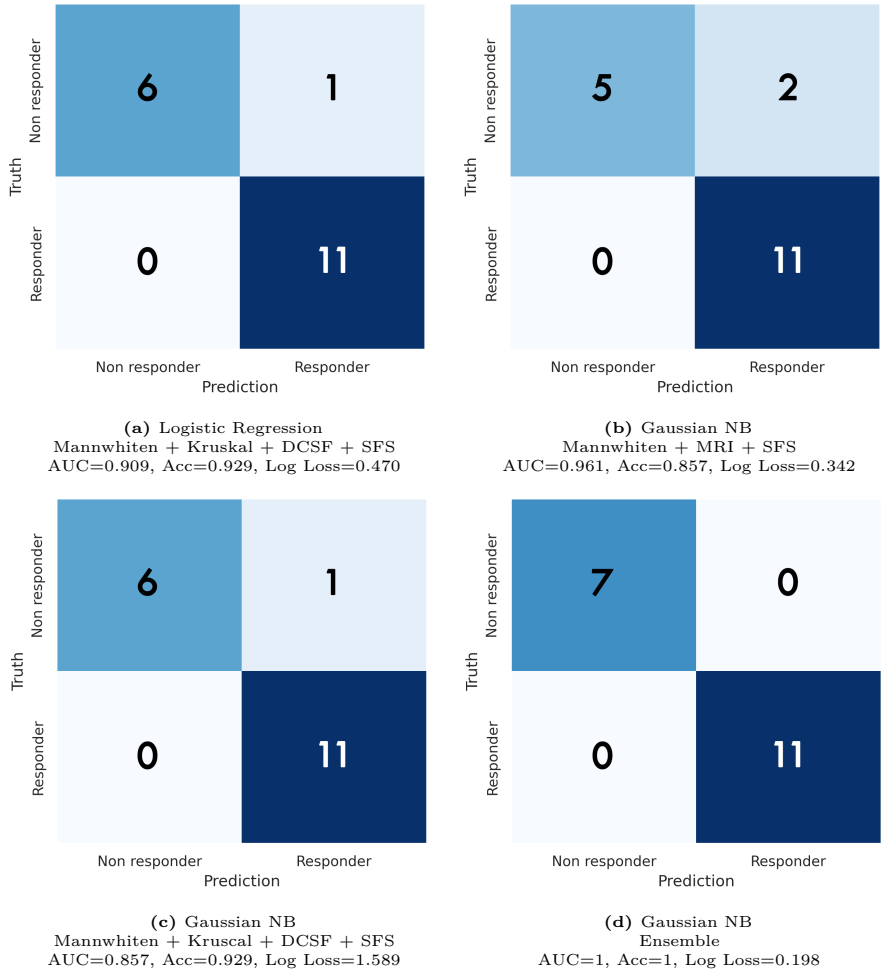

(a) Logistic Regression
Mannwhiten + Kruskal + DCSF + SFS
AUC=0.909, Acc=0.929, Log Loss=0.470

(b) Gaussian NB
Mannwhiten + MRI + SFS
AUC=0.961, Acc=0.857, Log Loss=0.342

(c) Gaussian NB
Mannwhiten + Kruscal + DCSF + SFS
AUC=0.857, Acc=0.929, Log Loss=1.589

(d) Gaussian NB
Ensemble
AUC=1, Acc=1, Log Loss=0.198

Figure 4.12: Confusion matrix of the four best classification models: (a) Logistic Regression with Mannwhiten, Kruscal and DCSF filters; (b) Gaussian NB with Mannwhiten and MRI filters; (c) Gaussian NB with Mannwhiten, Kruscal and DCSF filters; (d) Ensemble model of the fusion of the two Gaussian NB models.

4.5 Responsiveness Prediction with Deep Learning

In this section, we show the results of the Deep Learning model introduced in the Method Section 3.10 to classify unseen patients between R and NR. The model was trained using a single channel: **wfvf**.

Different models were trained using a Grid Search, batch size was fixed to 16 volumes per batch and the training and validation datasets were augmented with an increase of sample size of 20 times. Learning rates raged between $5 \cdot 10^{-3}$ and $1 \cdot 10^{-6}$ in an SGD optimizer with a momentum of 0.9 and a learning rate scheduler.

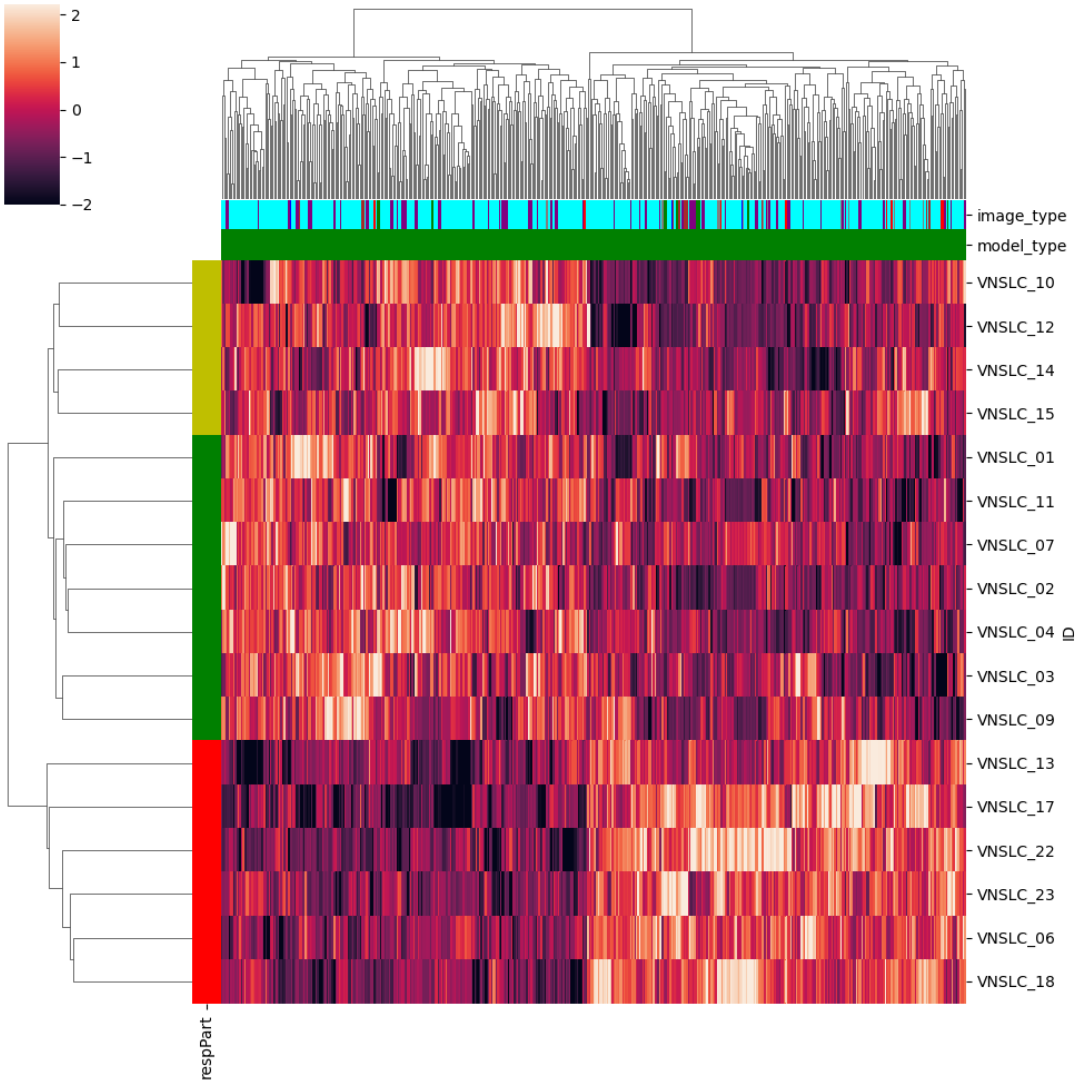

Figure 4.13: Heatmap and hierarchical clustering of the features filtered by `frac_csf_mf`. On the left, the targets are divided into R (dark green), PR (light green) and NR (red). On top, the model type represents the microstructural model from where the features come from: Microstructure Fingerprinting (Green). After, the image type explains the transformation applied to the image to get the feature: original (blue), exponential (orange), gradient (green), lpb-3D (purple), logarithm (pink), square (grey), square root (olive), wavelet (cyan).

The learning rate scheduler every n batch decremented the learning rate by a gamma factor. Different scheduler step sizes and gamma factors were tried:

- Gamma: 0.1, 0.3, 0.01
- Batch step size: 7, 15, 25

Training and validation scores are shown in Figure 4.14.

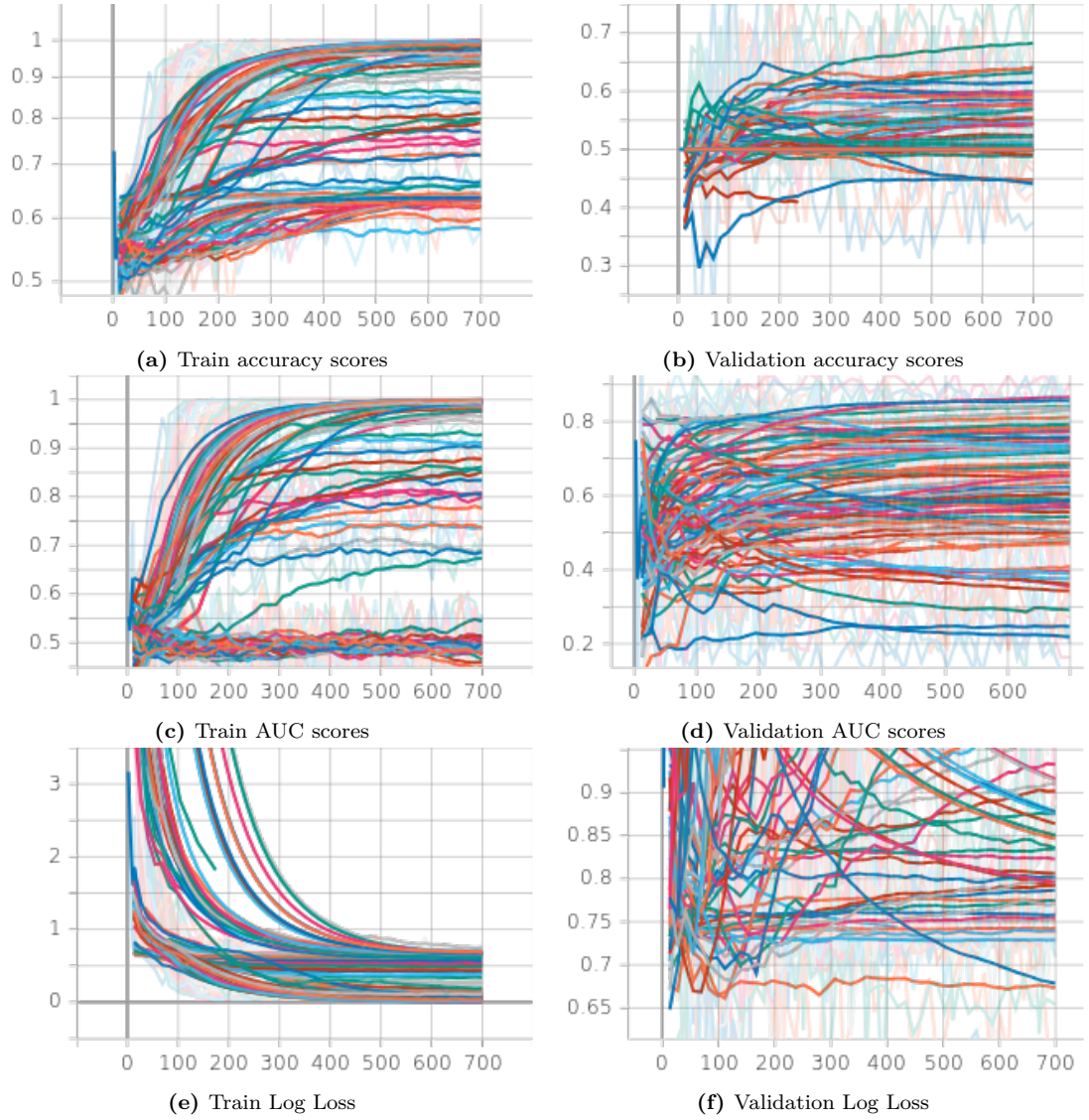

(a) Train accuracy scores

(b) Validation accuracy scores

(c) Train AUC scores

(d) Validation AUC scores

(e) Train Log Loss

(f) Validation Log Loss

Figure 4.14: Train and validation scores. Smoothed curve in the foreground.

The training set reached an accuracy and AUC of 1 while the validation set had an accuracy of 0.7 and an AUC score of 0.85, these result where obtained using a batch size of 16, learning rate equal to $1 \cdot 10^{-4}$ with decay of $1 \cdot 10^{-2}$ every 7 epochs in a AdamW optimizer. The size of the training and validation set were augmented with a multiplier factor of 20 times the original size.

Chapter 5

Discussion

In this chapter, we discuss the result extracted from the earlier Chapter 4.

5.1 Univariate analysis

Differences in values between R and NR can be observed by analysing each tract metric individually.
Globally greater MD and AD were observed in NR in the right anterior, posterior (projecting to the parietal lobe), and inferior (projecting to the insular cortex) thalamocortical radiations, right optic radiation, and anterior commissure.
Greater MD, RD and AD were found in NR in the right posterior thalamocortical radiations (projecting to the occipital lobe) and left and right fornix.
Greater RD was recorded in NR in the prefrontal body and the splenium of the corpus callosum and in the right extreme capsule.
Greater AD and decreased ODI were seen in NR in the anterior thalamocortical radiation.
Lower fraction of intra-cellular volume and greater fraction of extra-cellular volume were observed in NR in the posterior (projecting to the occipital), and inferior (projecting to the insular cortex) thalamocortical radiations, left optic radiation and middle longitudinal fasciculus.
A case of lower CSF volume fraction was found in NR in the right SLF I.
Greater fraction of CSF (MF) was recorded in NR in the parietal and premotor body of the corpus callosum and the right side of anterior thalamocortical radiation.
Fornix, anterior commissure and right anterior thalamocortical radiation were the only tracts capable of better distinguishing between the three classes R, PR and NR through DTI metrics.

In the present study, no differences in FA and `fvf` values were seen between R and NR. A previous study by Mithani et al. [4] reported greater FA values in an array of tracts (including left internal and external capsule, anterior, superior and posterior corona radiata, posterior thalamic radiation, fornix and ST, SLF, ILF, and inferior, fronto-occipital fasciculus) in R compared to NR. Our findings are not coherent with Mithani et al. results since the method by which the data are taken is different, they used a combination of tract-based spatial statistics (TBSS) analysis and regions taken from atlases in MNI152 space to compute their values.

Greater SD was found in NR in the MD of the central, parietal, and premotor parts of the corpus callosum body, in ODI of ILF, and in the fibre fraction of the posterior thalamocortical radiations (projecting to the parietal lobe). While a lower SD of the weighted fibre volume fraction was registered in NR in the right SLF II and right arcuate fasciculus.

Model metrics observations

In the NODDI model, the thresholded intra-cellular volume fraction was capable to find more statistical differences between R and NR than the non-thresholded one. The only exception was the right anterior thalamocortical radiation, where the non-thresholded intra-cellular volume fraction has a lower p-value than the thresholded one.

Statistical test analysis did not find many differences in DIAMOND metrics, but in some tracts, it confirmed the results found by the DTI model. This was the case of the right anterior thalamocortical radiation where the increase of AD was confirmed by the increase of wAD. DIAMOND was considered to be more reliable since it considers more compartments in a single voxel.

No differences were found in the MF metric fibre volume fraction, which was an accurate metric of the integrity of the fibre bundle.

5.2 Multivariate analysis

5.2.1 Interpretable features

Based on DTI metrics, a previous study done by Mithani et al. [4] included a training cohort of 38 children and a validation cohort of 18 children with DRE. They used tracts regions taken from the intersection of the FA skeleton recovered from a TBSS analysis and the JHU ICBM DTI-81 White Matter Atlas, from where they retrieved an estimation of the classification accuracy of 89.5% ($AUC = 0.93$).

Our analysis of microstructure means showed the great potential of dMRI models to predict the treatment response in patients with DRE. The fitted classification models on the weighted mean selected more frequently the fornix tract and the accumbens area.

The SFS with polynomial kernel selected the fornix tract 7 times over 18 models. While Accumbens area 5 times over 18 models. We consider the fornix tract an important region to identify R or NR patients with DRE. Despite the Accubens area being one of the most selected ROI from the SFS algorithm it cannot discriminate a patient alone. As we can see in the univariate analysis it has only the left side RD mean p-value lower than 0.01. This is one of the powers of SFS which can find patterns in a multidimensional context.

The classification models built in the study are robust since an accurate classification was achieved with a lower number of patients and considering only three features. However, more robust and reliable models could be built using larger datasets, which could give the possibility to add a validation cohort and a more precise approximation of the accuracy of the model in predicting R.

5.2.2 Radiomics

No literature was found on the use of radiomics feature extraction from DTI model maps.

Different feature selection models were tried with different classification algorithms to extract informative features. From the obtained results, statistical univariate filtering was well suited for the task of reducing the feature size.

It is possible to see from the previous analysis that the patients can be classified with a high accuracy considering only the mean, but through the feature selection done by the radiomic models hardly it was selected.

The model based on Logistic Regression and Gaussian (DCSF) most frequently selected the `Size-Zone Non-Uniformity Normalized` feature from the `wavelet` transform of the RD in the Right Hippocampus and the wavelet transform of the wfvf in the Right Thalamus. The first was selected 50% of the time and the latter 20% of the time. Size-Zone Non-Uniformity Normalize measures the variability of size zone volumes throughout the image, with a lower value indicating more homogeneity among zone size volumes in the image [130].

Overall, in all of the models, the best-selected features were found in the `wavelet` and `local binary pattern 3D` transforms.

Hierarchical clustering

A hierarchical clustering was applied to the radiomic features after the statistical test filtering. From the resulting heatmaps and clusters is possible to see a possible pattern in the responsiveness to the treatment. One of the best results is the heatmap taken by filtering only the features of the fraction of CSF volume from the Microstructure Fingerprinting model, and it correctly groups similar patients. It is possible to note that most of the features selected in the filtering steps come from the wavelet transform.

5.2.3 Deep Learning

Deep Learning models showed great potential in classifying patients despite the few samples available in our dataset. The weights of the pre-trained encoder model were a good initialization for the model, even if the input images were different from our task. The training set in many models reached an accuracy and AUC of 1 in less than 300 steps. But, the validation never got over a mean accuracy of 0.7.

From these results, we can see that the model easily overfit, even with regularization techniques, due to the lack of a robust dataset.

5.3 Biological interpretations

In all of the tracts discussed above in Section 4.2, there was a higher MD in NR, suggesting fibre damage in the WM tracts [14, 20, 134].

Some of the tracts had also demonstrated a greater AD in NR patients, this can be explained by saying that the analysed tract was crossed by other fibres fascicle and one of the two was damaged or reduced favouring the highlighting of the other tract in the voxel. Therefore, a greater AD and a lower ODI can be observed.

A greater MD was observed in conjunction with a greater RD in NR, together with a greater fraction of extra-cellular volume and a lower fraction of intra-cellular volume, this effect can be associated with variations in the fraction of microglial cells [135], which influence the myelination of the fibres [136].

Differences in the SD along the tract, from the seed to the target, mean that the variation of the metric around the mean value differs between R and NR. It can be interpreted as damage, reduction, or demyelination (depending on the metric) at a specific point in the tract that makes the value more stable or variable around the mean.

5.4 Explanation of the desynchronising effect

Epilepsy is characterized by abnormal synchronous neuronal firing in the brain, which can lead to seizures. It has also been shown that R demonstrate global neural desynchronisation after chronic stimulation and that this desynchronisation is responsible for the antiepileptic effects of the therapy. Cortical desynchronisation may serve as a mechanism to mitigate the spread of seizures [137].

The Corpus callosum and anterior commissure are a bundle of nerve fibres that connect the two hemispheres of the brain, the latter is smaller than the corpus callosum and connects the two temporal lobes. The corpus callosum is the main propagation pathway between the two hemispheres, for this reason, callosotomy is used to prevent bilateral spread and synchronisation [138]. A study by Lieb et al. [139] suggests that the anterior commissure had no contribution to the spread between the hemispheres. Based on the DTI and NODDI metrics, fibre damages and demyelination were found in the anterior commissure and the temporal body of corpus callosum of NR compared to R. While, based on MF metrics, a greater CSF was found in the parietal and premotor body of corpus callosum of NR compared to R. Further research is needed to understand the role of these two tracts in mediating the antiepileptic effect of VNS.

It has been shown that VNS alters the structure function of the limbic system [4] which can be associated with the therapeutic mechanism of VNS [140, 141]. In our study, in NR the fornix had a lower myelin and a greater damage compared to the R. On both sides of the fornix, greater variance was found in MD of NR respect to R, meaning that the damage of the fibres could interest only a sub-segment of the entire tract. Increased connectivity in the fornix predicts positive treatment outcomes [4], showing the importance of this tract in the antiseizure effects of VNS.

From the studies done by Ibrahim et al., the vagus afferents project to the thalamus, which has long been involved in seizure activity [5, 137]. Furthermore, alterations in thalamocortical connections are involved in epileptogenesis. Thalamocortical radiations, therefore, play a significant role in VNS antiseizure effects [5, 142].

In our study, thalamocortical radiations were divided into anterior, posterior, superior, and inferior. No differences have been found between R and NR in the superior thalamocortical radiations.

Based on DTI, NODDI and MF metrics, a lower fraction of crossing fibres was found on the left side of the anterior thalamocortical radiation of NR, and a reduction and damage of fibre were found on the fibres of the right side. Therefore, the damage and the reduction of fibre fraction were lower in the left hemisphere but still greater compared to R.

Similar results were found in the posterior thalamic radiation which in our study is divided into radiation to the parietal and occipital lobes. Left posterior thalamic radiations had a demyelination in NR compared to R in the tracts projecting to the occipital lobe, and no statistical differences in the tracts projecting to the left parietal lobe. Based on the DTI and NODDI metrics in NR compared to R, fibre demyelination was registered on both sides of the projection to the occipital lobe, but fibre damage was only found in the right hemisphere. Compared to anterior thalamic radiation, in NR the left side has less damage compared to the right, but still greater than in R. The same results were found in the study by [4] where a more robust WM microstructure was observed in R in the posterior thalamic radiation.

Inferior thalamocortical radiation projecting to the insular cortex in NR concerning R presents demyelinated fibres on both sides with damage on the right side.

From the study by Mithani et al., [4] "It is possible that effective modulation of cortical excitability through indirect thalamic stimulation via the vagus nerve is facilitated by robust thalamocortical white matter tracts". Therefore, from our study, the modulation was stronger in the left hemisphere, but still lower in NR compared to R.

In general, thalamocortical radiations have minor damage to the side corresponding to the implantation side of the device. The higher integrity on the left side compared to the right side may reflect the neuroplasticity effects of the therapy. However, this hypothesis remains to be proved by longitudinal studies assessing changes in microstructure over time in the left and right white matter tracts, independently.

From the study conducted by [4] the hemisphere association fibres were reported with greater FA in R, including the superior and inferior longitudinal fasciculus. In our study, we found a lower CSF fraction on the right side of SLF I of NR concerning R, without any variation of FA. Having a decrease of CSF means having an increase of fibre fraction, which is in contrasts with the results of Mithani et al. [4] where NR had a lower FA which means a reduction of axonal integrity.

From [4] "It is possible that association fibres enable the transmission of the modulatory stimulus to the epileptogenic and/or symptomatogenic regions of the brain, which would be increased by the increased microstructure of white matter in those tracts". In NR the SLF I can better transmit the modulatory stimulus between regions on the right side of the brain compared to R. SLF I was the only tract where the fibre conditions of NR were better than R. Further research is required to explain better the role of these tracts in mediating antiepileptic effect of VNS.

As we showed DTI and NODDI metrics were useful to characterise the WM tracts microstructure in DRE patients with implanted VNS. These techniques could help to develop new biomarkers of VNS response to better understand the mechanisms of action of the therapy and the requisites to become R to VNS.

5.5 Limitations

In this section, we explain the limitations of our study.

Sample size

First, the main limitation of the study was the number of subjects at our disposal. As mentioned in Section 3.1.1, we have only 19 samples. The statistical student t-test is a parametric test and assumes that the data is normally distributed, this assumption does not hold with small datasets. For those reasons, we need nonparametric tests. However, the inferences they make are not as strong as with parametric tests. Furthermore, training a ML model capable of classifying the population with a few samples is an arduous task, for this reason, high regularisation terms and only linear models are used in this study. Therefore, an increasing number of patients available for this study would allow a higher accuracy both in statistical tests and in classification tasks. With a larger sample size, it would be possible to divide the dataset into training and validation cohorts and, therefore, assess a more precise approximation of the model scores. Furthermore, having a larger number of patients would allow us to study R and NR alone (since in our results they would be completely separable) and consider the case of PR separately, to understand in which regions it behaves like R or NR.

Healthy control inclusion

A further study could include the healthy control (HC) patients where their microstructural features are compared with R, PR, and NR. Possible expected results could be that R and PR have characteristics more similar to those of HC than those of NR. In this study, the comparison between HC and epileptic patients was not performed due to time reasons.

Registration

Another important limitation was the use of MNI152 atlases for regions that were not covered by FreeSurfer. Many of the regions used as inclusion regions in tractogram generation were taken from probabilistic atlases in the MNI152 space. Therefore, the MNI ROIs must be registered in the diffusion patient space, bringing some

imperfections into regions where the patients' brains present important lesions. To reduce the impact of the error a diffeomorphic transformation with elastic regularization (`ElasticSyN`) is used. An example of registration in a subject with a congenital malformation is shown in Figure 3.10. The development of a tool capable of labelling subcortical structures more precisely is an improvement over what FreeSurfer already does, increasing the number of regions would improve the definition of seed and target regions.

Tractography

There were many limitations in computed tractography using MRtrix3. A higher resolution of the dMRI images would increase the quality of the tractography and would allow us to tract the ST that in this study was excluded for resolution reasons. Then, the correction method proposed in Section 3.4.3 excludes many voxels near the seed and the target region if these two were defined as spread regions. For example, in the entire SLF most of the removed 'outliers' were near the seed and target regions, since the frontal and parietal lobes have a large surface area, the probability of a tract passing near them is lower than in the middle of the tract. The same problem was found in the anterior thalamic radiation, where the frontal lobe was set as the target. An extreme solution could be the one used by FreeSurfer, where the path with the highest probability is used, but it would not work properly since it keeps only one tract excluding all the other feasible paths of a fascicle. A trade-off solution would be between our solution and FreeSurfer, in which instead of keeping the voxels with a probability higher than a threshold, are kept only the tracts with a probability higher than a threshold.

Metric distribution and evolution

In this study, we have analysed only the distribution of a metric value in the region, excluding the spatial information. Along the pathway of a tractogram the value of metric changes depending on the position in the tract, as shown in Figure 3.24 of Section 3.6.2. Further studies can consider spatial information in tract regions by analysing changes along the path or considering only a subsegment of it. It is expected that different regions follow a main shape that could differ between patients. For example, in Figure 5.1 the evolutions of FA and MD of the right SLF III are shown. In Figure 5.1a the mean of MD along the path is different for R and NR, a result that is consistent with our analysis where a p-value of 0.02206 was found for the mean. While in Figure 5.1c is shown the FA along the path, in our analysis we did not find any difference between the means, but here a depression in a subsegment of the tract is visible in NR. In Figure 5.1b and Figure 5.1d same results but considering the three classes. Therefore, this type of analysis could give more precise results about the exact point where axonal damage is present. These

plots are done by using DTI metrics from TRACULA that compute them with the parameter `-stat`. For time reasons we did not implement it with the result of MRtrix3 and for all the other models (NODDI, DIAMOND, MF).

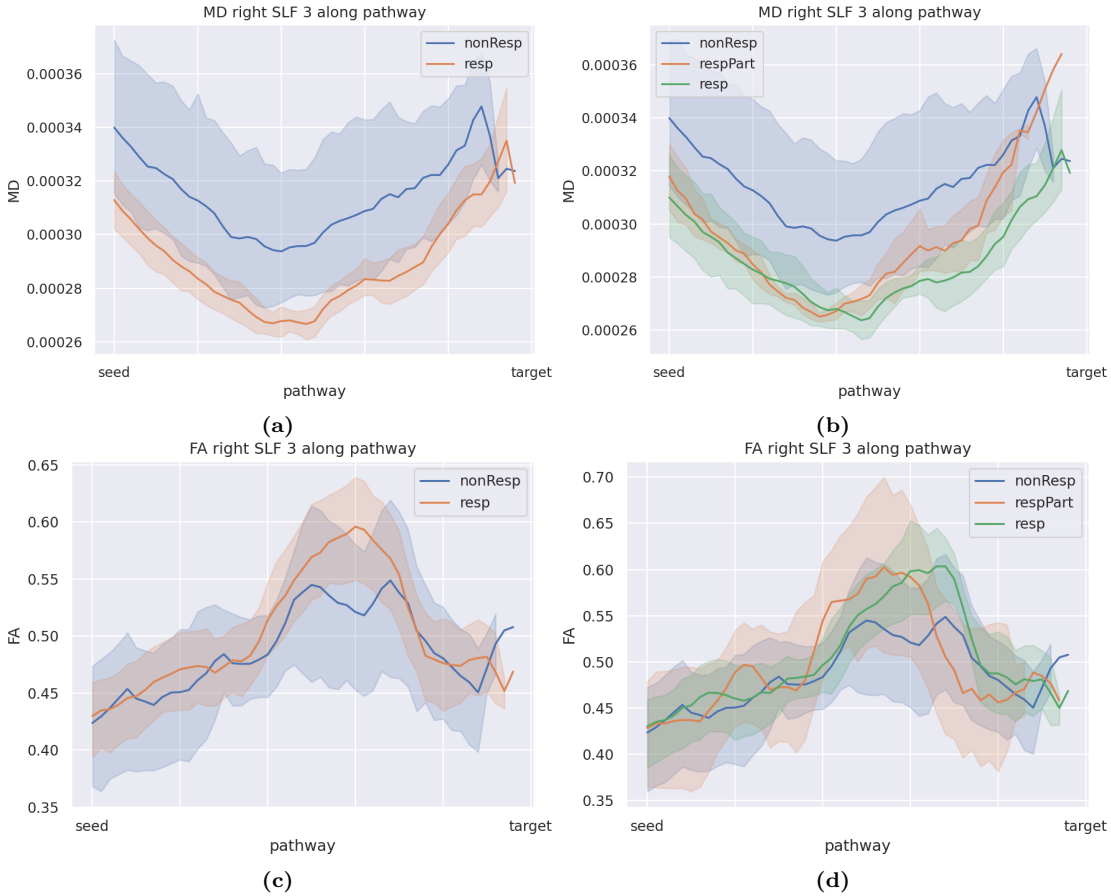

Figure 5.1: Evolution of MD (a, b) and FA (c, d) metrics along the right SLF III pathway, considering PR as R (a, c) or separately (b, c).

Deep Learning Limitation

A limitation of the modified UNEST model for classification is that it cannot accept more than a volume per subject. The model accepts a volume with a single channel, while in our study multiple channels are present considering all the model metrics extracted in DTI, NODDI, DIAMOND and Microstructure Fingerprinting. Therefore, the computed model metrics cannot be analysed together in this model.

A possible solution to the multi-channel problem is to use different encoders as the number of types of maps. The feature extracted for each of them is then concatenated in a single input that feeds a fully connected NN.

The management of volumes is extremely important since many maps are computed per subject and each of them has big sizes. With time, brain images are always better defined with increasing size. Good libraries that give the possibility to preprocess the volumes in GPU are needed to reduce the size of the bottleneck due to the CPU preprocessing.

Conclusion

Quantifying biomarkers that can find potential R to VNS gives a deeper understanding of the neurological mechanism of VNS.
Multi-compartment dMRI models (NODDI, DIAMOND and MF) were used to generate possible biomarkers. These models have never been used in the literature to quantify brain differences in DRE patients with implanted VNS.

By combining dMRI models with statistical analysis and ML models, we built different classifiers that can discriminate between R and NR with high accuracy. Using different ML models we have analysed the strengths and weaknesses of each. However further studies must be done with more samples to confirm the obtained results and improve Deep Learning scores.
Taking PR as R, the fornix was the metric with the highest difference between R and NR. Greater integrity was found in WM of R in thalamocortical radiations, the fornix and anterior commissure with respect to NR. Taking into account the DTI metrics, the right lateralised thalamocortical radiations were found to be more different between R and NR. Considering NODDI metrics, no differences were found between the two sides, but only demyelination was found in thalamocortical radiations and middle longitudinal fasciculus.

It was seen that DTI and NODDI had a greater discriminatory capability than DIAMOND and MF for drug-resistant epileptic patients. DIAMOND and MF are multi-compartment models that consider different compartments in each voxel, and the latter is the most biologically interpretable. An greater CSF (MF) was observed in NR in the corpus callosum and anterior thalamocortical radiation.

We showed that microstructural connections together with ML may play a key role to classify R and NR and to find biomarkers. Therefore, we advance personalised treatment approaches by adjusting the parameters of VNS or reducing unnecessary VNS implantations.

Bibliography

[1] WHO. *Epilepsy Fact sheet*. 2023. URL: https://www.who.int/en/news-room/fact-sheets/detail/epilepsy (cit. on pp. 1, 28, 29).

[2] Susan Spencer and Linda Huh. «Outcomes of epilepsy surgery in adults and children». In: *The Lancet Neurology* 7.6 (2008), pp. 525–537 (cit. on pp. 1, 31).

[3] Dario J Englot, John D Rolston, Clinton W Wright, Kevin H Hassnain, and Edward F Chang. «Rates and predictors of seizure freedom with vagus nerve stimulation for intractable epilepsy». In: *Neurosurgery* 79.3 (2016), p. 345 (cit. on pp. 1, 33).

[4] Karim Mithani et al. «Connectomic profiling identifies responders to vagus nerve stimulation». In: *Annals of neurology* 86.5 (2019), pp. 743–753 (cit. on pp. 1, 35, 36, 86, 89, 90).

[5] George M Ibrahim et al. «Presurgical thalamocortical connectivity is associated with response to vagus nerve stimulation in children with intractable epilepsy». In: *NeuroImage: Clinical* 16 (2017), pp. 634–642 (cit. on pp. 1, 33, 35, 89).

[6] Hui Zhang, Torben Schneider, Claudia A Wheeler-Kingshott, and Daniel C Alexander. «NODDI: practical in vivo neurite orientation dispersion and density imaging of the human brain». In: *Neuroimage* 61.4 (2012), pp. 1000–1016 (cit. on pp. 1, 16–18, 20).

[7] Benoit Scherrer, Armin Schwartzman, Maxime Taquet, Mustafa Sahin, Sanjay P Prabhu, and Simon K Warfield. «Characterizing brain tissue by assessment of the distribution of anisotropic microstructural environments in diffusion-compartment imaging (DIAMOND)». In: *Magnetic resonance in medicine* 76.3 (2016), pp. 963–977 (cit. on pp. 1, 19–21, 56).

[8] Gaëtan Rensonnet, Benoit Scherrer, Gabriel Girard, Aleksandar Jankovski, Simon K Warfield, Benoit Macq, Jean-Philippe Thiran, and Maxime Taquet. «Towards microstructure fingerprinting: estimation of tissue properties from a dictionary of Monte Carlo diffusion MRI simulations». In: *NeuroImage* 184 (2019), pp. 964–980 (cit. on pp. 1, 21, 22, 56).

[9] F. Peeters. «Medical Imaging, Chapter 4 : Magnetic Resonance Imaging». LGBIO2050 (cit. on pp. 2–8).

[10] D. Vetter B. Kastler. *Comprendre l'IRM: Manuel d'auto-apprenissage*. Imagerie médicale DIAGNOSTIC, 1988 (cit. on pp. 3, 6, 7, 12).

[11] Spinney R. Kennepohl D. Farmer S. «Theory of Nuclear Magnetic Resonance (NMR)». In: MindTouch, 2019. Chap. 13. URL: https://chem.libretexts.org/Courses/Nassau_Community_College/Organic_Chemistry_I_and_II/13%3A_Nuclear_Magnetic_Resonance_Spectroscopy/13.01%3A_Theory_of_Nuclear_Magnetic_Resonance_%28NMR%29 (cit. on p. 3).

[12] M. Coriasco O. Rampado. *Elementi di risonanza magnetica*. Springer, 2017 (cit. on pp. 4–11, 14).

[13] Qureshi Sameer. *Magnetic Resonance Imaging (MRI) in Orthopaedics*. 2017. URL: http://youngorthopod.blogspot.com/2017/03/magnetic-resonance-imaging-mri-in.html (visited on 04/28/2023) (cit. on p. 9).

[14] Stefan Sunaert Wim Van Hecke Louise Emsell. *Diffusion Tensor Imaging, A Pratical Handbook*. Springer, 2015 (cit. on pp. 11, 13, 88).

[15] Eduardo HMSG de Figueiredo, Arthur FNG Borgonovi, and Thomas M Doring. «Basic concepts of MR imaging, diffusion MR imaging, and diffusion tensor imaging». In: *Magnetic Resonance Imaging Clinics* 19.1 (2011), pp. 1–22 (cit. on p. 12).

[16] Peter J Basser, James Mattiello, and Denis LeBihan. «MR diffusion tensor spectroscopy and imaging». In: *Biophysical journal* 66.1 (1994), pp. 259–267 (cit. on pp. 12, 14).

[17] Do Tromp. *The diffusion tensor, and its relation to FA, MD, AD and RD*. Available at https://www.diffusion-imaging.com/2015/10/what-is-diffusion-tensor.html. 2015. URL: https://www.diffusion-imaging.com/2015/10/what-is-diffusion-tensor.html (cit. on p. 13).

[18] Jose Soares, Paulo Marques, Victor Alves, and Nuno Sousa. «A hitchhiker's guide to diffusion tensor imaging». In: *Frontiers in Neuroscience* 7 (2013). ISSN: 1662-453X. DOI: 10.3389/fnins.2013.00031. URL: https://www.frontiersin.org/articles/10.3389/fnins.2013.00031 (cit. on p. 14).

[19] *Reconstruction of the diffusion signal with the Tensor model*. URL: https://dipy.org/documentation/1.1.1./examples_built/reconst_dti/ (visited on 08/05/2023) (cit. on p. 14).

[20] Do Tromp. *DTI Scalars (FA, MD, AD, RD) - How do they relate to brain structure?* 2013. URL: https://www.diffusion-imaging.com/2013/01/relation-between-neural-microstructure.html (visited on 08/05/2023) (cit. on pp. 14, 88).

[21] Rodrigo D Perea, Jennifer S Rabin, Megan G Fujiyoshi, Taylor E Neal, Emily E Smith, Koene RA Van Dijk, and Trey Hedden. «Connectome-derived diffusion characteristics of the fornix in Alzheimer's disease». In: *NeuroImage: Clinical* 19 (2018), pp. 331–342 (cit. on p. 14).

[22] Peter J Basser. «Fiber-tractography via diffusion tensor MRI (DT-MRI)». In: *Proceedings of the 6th Annual Meeting ISMRM, Sydney, Australia*. Vol. 1226. 1998 (cit. on p. 14).

[23] Peter J Basser and Carlo Pierpaoli. «Microstructural and physiological features of tissues elucidated by quantitative-diffusion-tensor MRI». In: *Journal of magnetic resonance* 213.2 (2011), pp. 560–570 (cit. on p. 14).

[24] Peter J Basser, Sinisa Pajevic, Carlo Pierpaoli, Jeffrey Duda, and Akram Aldroubi. «In vivo fiber tractography using DT-MRI data». In: *Magnetic resonance in medicine* 44.4 (2000), pp. 625–632 (cit. on p. 15).

[25] J-Donald Tournier, Fernando Calamante, and Alan Connelly. «Robust determination of the fibre orientation distribution in diffusion MRI: non-negativity constrained super-resolved spherical deconvolution». In: *Neuroimage* 35.4 (2007), pp. 1459–1472 (cit. on p. 15).

[26] J-Donald Tournier, Fernando Calamante, David G Gadian, and Alan Connelly. «Direct estimation of the fiber orientation density function from diffusion-weighted MRI data using spherical deconvolution». In: *Neuroimage* 23.3 (2004), pp. 1176–1185 (cit. on p. 15).

[27] Ning Xiang and Christopher Landschoot. «Bayesian inference for acoustic direction of arrival analysis using spherical harmonics». In: *Entropy* 21.6 (2019), p. 579 (cit. on p. 15).

[28] Dennis M Healy Jr, Harrie Hendriks, and Peter T Kim. «Spherical deconvolution». In: *Journal of Multivariate Analysis* 67.1 (1998), pp. 1–22 (cit. on p. 15).

[29] Ben Jeurissen, Jacques-Donald Tournier, Thijs Dhollander, Alan Connelly, and Jan Sijbers. «Multi-tissue constrained spherical deconvolution for improved analysis of multi-shell diffusion MRI data». In: *NeuroImage* 103 (2014), pp. 411–426 (cit. on p. 15).

[30] Timothy EJ Behrens, H Johansen Berg, Saad Jbabdi, Matthew FS Rushworth, and Mark W Woolrich. «Probabilistic diffusion tractography with multiple fibre orientations: What can we gain?» In: *neuroimage* 34.1 (2007), pp. 144–155 (cit. on p. 16).

[31] Eleftherios Garyfallidis. «Towards an accurate brain tractography». PhD thesis. University of Cambridge, 2013 (cit. on p. 16).

[32] Maira Tariq, Torben Schneider, Daniel C Alexander, Claudia A Gandini Wheeler-Kingshott, and Hui Zhang. «Bingham–NODDI: Mapping anisotropic orientation dispersion of neurites using diffusion MRI». In: *Neuroimage* 133 (2016), pp. 207–223 (cit. on p. 17).

[33] Thomas D Parker et al. «Cortical microstructure in young onset Alzheimer's disease using neurite orientation dispersion and density imaging». In: *Human brain mapping* 39.7 (2018), pp. 3005–3017 (cit. on p. 18).

[34] Dmitriy A Yablonskiy, G Larry Bretthorst, and Joseph JH Ackerman. «Statistical model for diffusion attenuated MR signal». In: *Magnetic Resonance in Medicine: An Official Journal of the International Society for Magnetic Resonance in Medicine* 50.4 (2003), pp. 664–669 (cit. on p. 19).

[35] J.P. Hornak. *The basic of MRI - Spin Physics*. URL: `https://www.cis.rit.edu/htbooks/mri/chap-3/chap-3.htm#:~:text=A%20spin%20packet%20is%20a,represented%20by%20a%20magnetization%20vector.` (visited on 08/11/2023) (cit. on p. 19).

[36] Gaëtan Rensonnet. «Generation of a dictionary of DW-MRI signals from arbitrary brain microstructure configurations». MA thesis. Ecole polytechnique de Louvain,f Université catholique de Louvain, 2015 (cit. on p. 22).

[37] Alexander Berger. «Quantifying microstructural brain anomalies in patients with Alzheimer's disease via diffusion Magnetic Resonance Imaging». MA thesis. Ecole polytechnique de Louvain, Université catholique de Louvain, 2020 (cit. on p. 23).

[38] Quentin Dessain, Nicolas Delinte, Benoit Macq, and Gaëtan Rensonnet. «Fast multi-compartment microstructure fingerprinting using deep neural networks». In: *Proc. Intl. Soc. Mag. Reson. Med.* Vol. 30. 2022, p. 0560 (cit. on p. 23).

[39] Gaëtan Rensonnet. *In vivo diffusion magnetic resonance imaging of the white matter microstructure from dictionaries generated by Monte Carlo simulations: development and validation*. Tech. rep. EPFL, 2019 (cit. on pp. 23, 24).

[40] Marius E Mayerhoefer, Andrzej Materka, Georg Langs, Ida Häggström, Piotr Szczypiński, Peter Gibbs, and Gary Cook. «Introduction to radiomics». In: *Journal of Nuclear Medicine* 61.4 (2020), pp. 488–495 (cit. on pp. 24, 25).

[41] Robert J Gillies, Paul E Kinahan, and Hedvig Hricak. «Radiomics: images are more than pictures, they are data». In: *Radiology* 278.2 (2016), pp. 563–577 (cit. on p. 24).

[42] Robert S Fisher et al. «ILAE official report: a practical clinical definition of epilepsy». In: *Epilepsia* 55.4 (2014), pp. 475–482 (cit. on pp. 28, 29).

[43] Shekhar Saxena and Shichuo Li. «Defeating epilepsy: a global public health commitment». In: *Epilepsia open* 2.2 (2017), pp. 153–155 (cit. on p. 28).

[44] Roland D Thijs, Rainer Surges, Terence J O'Brien, and Josemir W Sander. «Epilepsy in adults». In: *The Lancet* 393.10172 (2019), pp. 689–701 (cit. on pp. 28–31).

[45] Kirsten M Fiest, Khara M Sauro, Samuel Wiebe, Scott B Patten, Churl-Su Kwon, Jonathan Dykeman, Tamara Pringsheim, Diane L Lorenzetti, and Nathalie Jetté. «Prevalence and incidence of epilepsy: a systematic review and meta-analysis of international studies». In: *Neurology* 88.3 (2017), pp. 296–303 (cit. on p. 28).

[46] Y Langan, L Nashef, and JWAS Sander. «Sudden unexpected death in epilepsy: a series of witnessed deaths». In: *Journal of Neurology, Neurosurgery & Psychiatry* 68.2 (2000), pp. 211–213 (cit. on p. 28).

[47] Orrin Devinsky, Tanya Spruill, David Thurman, and Daniel Friedman. «Recognizing and preventing epilepsy-related mortality: a call for action». In: *Neurology* 86.8 (2016), pp. 779–786 (cit. on p. 28).

[48] L Nashef. «Sudden unexpected death in epilepsy: terminology and definitions». In: *Epilepsia* 38 (1997), S6–S8 (cit. on p. 28).

[49] Shah VB Pathak SJ Yousaf MIK. «Sudden Unexpected Death in Epilepsy». In: *StatPearls [Internet]. Treasure Island (FL): StatPearls Publishing* (2023). URL: https://www.ncbi.nlm.nih.gov/books/NBK559104/ (visited on 08/16/2023) (cit. on p. 28).

[50] Orrin Devinsky. «Sudden, unexpected death in epilepsy». In: *New England Journal of Medicine* 365.19 (2011), pp. 1801–1811 (cit. on p. 28).

[51] Alan WC Yuen, Mark R Keezer, and Josemir W Sander. «Epilepsy is a neurological and a systemic disorder». In: *Epilepsy & Behavior* 78 (2018), pp. 57–61 (cit. on p. 29).

[52] Wikipedia contributors. *Epilepsy — Wikipedia, The Free Encyclopedia*. https://en.wikipedia.org/w/index.php?title=Epilepsy&oldid=1168148356. [Online; accessed 16-August-2023]. 2023 (cit. on p. 29).

[53] Patty Obsorne Shafer Elaine Kiriakopoulos. *Absence Seizures | Symptoms & Risks | Epilepsy Foundation*. https://www.epilepsy.com/what-is-epilepsy/seizure-types/absence-seizures. (Accessed on 05/03/2023). 2019 (cit. on p. 29).

[54] Robert S Fisher, Walter Van Emde Boas, Warren Blume, Christian Elger, Pierre Genton, Phillip Lee, and Jerome Engel Jr. «Epileptic seizures and epilepsy: definitions proposed by the International League Against Epilepsy (ILAE) and the International Bureau for Epilepsy (IBE)». In: *Epilepsia* 46.4 (2005), pp. 470–472 (cit. on p. 29).

[55] John S Duncan, Josemir W Sander, Sanjay M Sisodiya, and Matthew C Walker. «Adult epilepsy». In: *The Lancet* 367.9516 (2006), pp. 1087–1100 (cit. on pp. 29, 31).

[56] Robert S Fisher et al. «Operational classification of seizure types by the International League Against Epilepsy: Position Paper of the ILAE Commission for Classification and Terminology». In: *Epilepsia* 58.4 (2017), pp. 522–530 (cit. on pp. 29–31).

[57] Jahangir Moini and Pirouz Piran. «Chapter 6 - Cerebral cortex». In: *Functional and Clinical Neuroanatomy*. Ed. by Jahangir Moini and Pirouz Piran. Academic Press, 2020, pp. 177–240. ISBN: 978-0-12-817424-1. DOI: https://doi.org/10.1016/B978-0-12-817424-1.00006-9. URL: https://www.sciencedirect.com/science/article/pii/B9780128174241000069 (cit. on p. 29).

[58] Didier Pinault and Terence John O'brien. «Cellular and network mechanisms of genetically-determined absence seizures». In: *Thalamus & related systems* 3.3 (2005), pp. 181–203 (cit. on p. 30).

[59] Ingrid E Scheffer et al. «ILAE classification of the epilepsies: Position paper of the ILAE Commission for Classification and Terminology». In: *Epilepsia* 58.4 (2017), pp. 512–521 (cit. on p. 31).

[60] Patrick Kwan et al. *Definition of drug resistant epilepsy: consensus proposal by the ad hoc Task Force of the ILAE Commission on Therapeutic Strategies*. 2010 (cit. on p. 31).

[61] Dario J Englot, Anthony T Lee, Catherine Tsai, Cathra Halabi, Nicholas M Barbaro, Kurtis I Auguste, Paul A Garcia, and Edward F Chang. «Seizure types and frequency in patients who "fail" temporal lobectomy for intractable epilepsy». In: *Neurosurgery* 73.5 (2013), pp. 838–844 (cit. on p. 32).

[62] Stephen Wong, Ram Mani, and Shabbar Danish. «Comparison and selection of current implantable anti-epileptic devices». In: *Neurotherapeutics* 16 (2019), pp. 369–380 (cit. on p. 32).

[63] *Neuromodulation, University of Florida*. `https://neurology.ufl.edu/divisions/epilepsy/neuromodulation-vns-rns-dbs/`. (Accessed on 05/02/2023) (cit. on p. 32).

[64] Scott E Krahl, Fredricka C Martin, and Adrian Handforth. «Vagus nerve stimulation inhibits harmaline-induced tremor». In: *Brain research* 1011.1 (2004), pp. 135–138 (cit. on p. 32).

[65] Seth A Hays, Robert L Rennaker, and Michael P Kilgard. «Targeting plasticity with vagus nerve stimulation to treat neurological disease». In: *Progress in brain research* 207 (2013), pp. 275–299 (cit. on p. 32).

[66] A Broncel, R Bocian, P Kłos-Wojtczak, K Kulbat-Warycha, and J Konopacki. «Vagal nerve stimulation as a promising tool in the improvement of cognitive disorders». In: *Brain research bulletin* 155 (2020), pp. 37–47 (cit. on p. 32).

[67] JP Beekwilder and T Beems. «Overview of the clinical applications of vagus nerve stimulation». In: *Journal of clinical neurophysiology* 27.2 (2010), pp. 130–138 (cit. on p. 32).

[68] J Kiffin Penry and J Christine Dean. «Prevention of intractable partial seizures by intermittent vagal stimulation in humans: preliminary results». In: *Epilepsia* 31 (1990), S40–S43 (cit. on p. 33).

[69] JEFFREY L Ardell and WALTER C Randall. «Selective vagal innervation of sinoatrial and atrioventricular nodes in canine heart». In: *American Journal of Physiology-Heart and Circulatory Physiology* 251.4 (1986), H764–H773 (cit. on p. 33).

[70] Elinor Ben-Menachem. «Vagus nerve stimulation, side effects, and long-term safety». In: *Journal of clinical neurophysiology* 18.5 (2001), pp. 415–418 (cit. on p. 33).

[71] Kate Campbell. *Medical and science illustration, animations and Communications*. URL: `http://www.katecampbell.ca/` (cit. on p. 33).

[72] Laureen D Hachem, Simeon M Wong, and George M Ibrahim. «The vagus afferent network: emerging role in translational connectomics». In: *Neurosurgical focus* 45.3 (2018), E2 (cit. on pp. 33, 34).

[73] Bruno Bonaz, Valérie Sinniger, and Sonia Pellissier. «The vagus nerve in the neuro-immune axis: implications in the pathology of the gastrointestinal tract». In: *Frontiers in immunology* 8 (2017), p. 1452 (cit. on p. 34).

[74] Juarez A Ricardo and Edward Tongju Koh. «Anatomical evidence of direct projections from the nucleus of the solitary tract to the hypothalamus, amygdala, and other forebrain structures in the rat». In: *Brain research* 153.1 (1978), pp. 1–26 (cit. on p. 34).

[75] Jeremy Hofmeister and Virginie Sterpenich. «A role for the locus ceruleus in reward processing: encoding behavioral energy required for goal-directed actions». In: *Journal of Neuroscience* 35.29 (2015), pp. 10387–10389 (cit. on p. 34).

[76] Susan J Sara and Sebastien Bouret. «Orienting and reorienting: the locus coeruleus mediates cognition through arousal». In: *Neuron* 76.1 (2012), pp. 130–141 (cit. on p. 34).

[77] Alexandre Berger, Simone Vespa, Laurence Dricot, Manon Dumoulin, Evelina Iachim, Pascal Doguet, Gilles Vandewalle, and Riëm El Tahry. «How is the norepinephrine system involved in the antiepileptic effects of vagus nerve stimulation?» In: *Frontiers in neuroscience* 15 (2021), p. 1655 (cit. on p. 34).

[78] Olaf Sporns. «Structure and function of complex brain networks». In: *Dialogues in clinical neuroscience* (2022) (cit. on pp. 34, 35).

[79] Scott T Grafton and Lukas J Volz. «From ideas to action: The prefrontal–premotor connections that shape motor behavior». In: *Handbook of clinical neurology* 163 (2019), pp. 237–255 (cit. on p. 34).

[80] Joana Cabral, Morten L Kringelbach, and Gustavo Deco. «Functional connectivity dynamically evolves on multiple time-scales over a static structural connectome: Models and mechanisms». In: *NeuroImage* 160 (2017), pp. 84–96 (cit. on p. 35).

[81] WC Liu, K Mosier, AJ Kalnin, and DBOLD Marks. «BOLD fMRI activation induced by vagus nerve stimulation in seizure patients». In: *Journal of Neurology, Neurosurgery & Psychiatry* 74.6 (2003), pp. 811–813 (cit. on p. 35).

[82] Wikipedia contributors. *Magnetoencephalography — Wikipedia, The Free Encyclopedia*. `https://en.wikipedia.org/w/index.php?title=Magnetoencephalography&oldid=1170415779`. [Online; accessed 16-August-2023]. 2023 (cit. on p. 35).

[83] Karim Mithani et al. «Somatosensory evoked fields predict response to vagus nerve stimulation». In: *NeuroImage: Clinical* 26 (2020), p. 102205 (cit. on p. 35).

[84] Pi-Chuan Fan, Steven Shinn-Forng Peng, Ruoh-Fang Yen, Jeng-Yi Shieh, and Meng-Fai Kuo. «Neuroimaging and electroencephalographic changes after vagus nerve stimulation in a boy with medically intractable myoclonic astatic epilepsy». In: *Journal of the Formosan Medical Association* 113.4 (2014), pp. 258–263 (cit. on p. 36).

[85] Robert M Beckstead, Joel R Morse, and Ralph Norgren. «The nucleus of the solitary tract in the monkey: projections to the thalamus and brain stem nuclei». In: *Journal of Comparative Neurology* 190.2 (1980), pp. 259–282 (cit. on p. 36).

[86] Susan Standring, H Ellis, J Healy, D Johnson, A Williams, P Collins, and C Wigley. «Gray's anatomy: the anatomical basis of clinical practice». In: *American journal of neuroradiology* 26.10 (2005), p. 2703 (cit. on p. 36).

[87] Kevin George et al. «Neuroanatomy, thalamocortical radiations». In: (2019) (cit. on pp. 37, 55).

[88] Alexandru Andrușca Gordana Sendić. *Fornix of the brain: Anatomy and functions | Kenhub*. `https://www.kenhub.com/en/library/anatomy/fornix-of-the-brain`. (Accessed on 05/02/2023). 2022 (cit. on p. 37).

[89] Bertalan Dudas. «Part I - Morphology of the human hypothalamus: Anatomy, blood supply, nuclei and pathways». In: *Atlas of the Human Hypothalamus*. Ed. by Bertalan Dudás. Academic Press, 2021, pp. 1–24. ISBN: 978-0-12-822051-1. DOI: https://doi.org/10.1016/B978-0-12-822051-1.00001-8. URL: https://www.sciencedirect.com/science/article/pii/B9780128220511000018 (cit. on p. 37).

[90] Abdulwahab Alahmari. «Neuroimaging Role in Mental Illnesses J». In: *International Journal of Neural Plasticity* 4.1 (2021) (cit. on p. 37).

[91] Nikos Makris, David N Kennedy, Sean McInerney, A Gregory Sorensen, Ruopeng Wang, Verne S Caviness Jr, and Deepak N Pandya. «Segmentation of subcomponents within the superior longitudinal fascicle in humans: a quantitative, in vivo, DT-MRI study». In: *Cerebral cortex* 15.6 (2005), pp. 854–869 (cit. on p. 38).

[92] Dr. Johannes Sobotta. *Sobotta's Atlast and Textbook of Human Anatomy*. National Library of Medicine, 1908. DOI: https://doi.org/10.1002/ar.1090020705 (cit. on p. 38).

[93] Quentin Dessain, Mathieu Simon, and Benoit Macq. «Development of an image processing pipeline for large-scale in vivo population studies of the brain microstructure». PhD thesis. Master's thesis, UCLouvain, 2021 (cit. on p. 41).

[94] Quentin Dessain, Nicolas Delinte, and Simon Mathieu. *ElikoPy*. URL: https://github.com/Hyedryn/elikopy (visited on 08/05/2023) (cit. on p. 41).

[95] Quentin Dessain, Nicolas Delinte, and Simon Mathieu. *ElikoPy documentation*. URL: https://elikopy.readthedocs.io/en/latest/preprocessing_dmri.html (visited on 08/05/2023) (cit. on p. 42).

[96] *FreeSrufer documentation*. URL: https://surfer.nmr.mgh.harvard.edu/fswiki/FreeSurferWiki (visited on 08/05/2023) (cit. on p. 42).

[97] Jorge Jovicich et al. «Reliability in multi-site structural MRI studies: Effects of gradient non-linearity correction on phantom and human data». In: *NeuroImage* 30.2 (2006), pp. 436–443. ISSN: 1053-8119. DOI: DOI:10.1016/j.neuroimage.2005.09.046. URL: http://www.sciencedirect.com/science/article/B6WNP-4HM7S0B-2/2/4fa5ff26cad90ba3c9ed12b7e12ce3b6 (cit. on p. 42).

[98] Xiao Han et al. «Reliability of MRI-derived measurements of human cerebral cortical thickness: The effects of field strength, scanner upgrade and manufacturer». In: *NeuroImage* 32.1 (2006), pp. 180–194 (cit. on p. 42).

[99] F. Segonne, A. M. Dale, E. Busa, M. Glessner, D. Salat, H. K. Hahn, and B. Fischl. «A hybrid approach to the skull stripping problem in MRI». In: *NeuroImage* 22.3 (2004), pp. 1060–1075. ISSN: 1053-8119. DOI: DOI:10.1016/j.neuroimage.2004.03.032. URL: http://www.sciencedirect.com/science/article/B6WNP-4CF5CNY-1/2/33cc73136f06f019b2c11023e7a95341 (cit. on p. 42).

[100] Martin Reuter, Herminia Diana Rosas, and Bruce Fischl. «Highly Accurate Inverse Consistent Registration: A Robust Approach». In: *NeuroImage* 53.4 (2010), pp. 1181–1196. DOI: 10.1016/j.neuroimage.2010.07.020. URL: http://dx.doi.org/10.1016/j.neuroimage.2010.07.020 (cit. on p. 42).

[101] Martin Reuter, Nicholas J. Schmansky, Herminia Diana Rosas, and Bruce Fischl. «Within-Subject Template Estimation for Unbiased Longitudinal Image Analysis». In: *NeuroImage* 61.4 (2012), pp. 1402–1418. DOI: 10.1016/j.neuroimage.2012.02.084. URL: http://dx.doi.org/10.1016/j.neuroimage.2012.02.084 (cit. on p. 42).

[102] Anders Dale, Bruce Fischl, and Martin I. Sereno. «Cortical Surface-Based Analysis: I. Segmentation and Surface Reconstruction». In: *NeuroImage* 9.2 (1999), pp. 179–194 (cit. on p. 42).

[103] Bruce Fischl and Anders M. Dale. «Measuring the thickness of the human cerebral cortex from magnetic resonance images». In: *Proceedings of the National Academy of Sciences of the United States of America* 97.20 (2000), pp. 11050–11055. eprint: http://www.pnas.org/content/97/20/11050.full.pdf+html (cit. on p. 42).

[104] B. Fischl, A. Liu, and A. M. Dale. «Automated manifold surgery: constructing geometrically accurate and topologically correct models of the human cerebral cortex». In: *IEEE Medical Imaging* 20.1 (Jan. 2001), pp. 70–80 (cit. on p. 42).

[105] B. Fischl et al. «Whole brain segmentation: automated labeling of neuroanatomical structures in the human brain». In: *Neuron* 33 (2002), pp. 341–355 (cit. on p. 42).

[106] Bruce Fischl, David H. Salat, André J.W. van der Kouwe, Nikos Makris, Florent Ségonne, Brian T. Quinn, and Anders M. Dale. «Sequence-independent segmentation of magnetic resonance images». In: *NeuroImage* 23.Supplement 1 (2004). Mathematics in Brain Imaging, S69–S84. ISSN: 1053-8119. DOI: DOI:10.1016/j.neuroimage.2004.07.016. URL: http://www.sciencedirect.com/science/article/B6WNP-4DCMGVT-2/2/7eee26326dc63f931b826eac33becc8b (cit. on p. 42).

[107] Bruce Fischl, Martin I. Sereno, and Anders Dale. «Cortical Surface-Based Analysis: II: Inflation, Flattening, and a Surface-Based Coordinate System». In: *NeuroImage* 9.2 (1999), pp. 195–207 (cit. on p. 42).

[108] Bruce Fischl, Martin I. Sereno, Roger B.H. Tootell, and Anders M. Dale. «High-resolution intersubject averaging and a coordinate system for the cortical surface». In: *Human Brain Mapping* 8.4 (1999), pp. 272–284. ISSN: 1097-0193. DOI: 10.1002/(SICI)1097-0193(1999)8:4<272::AID-HBM10>3.0.CO;2-4. URL: http://dx.doi.org/10.1002/(SICI)1097-0193(1999)8:4%3C272::AID-HBM10%3E3.0.CO;2-4 (cit. on p. 42).

[109] Bruce Fischl et al. «Automatically Parcellating the Human Cerebral Cortex». In: *Cerebral Cortex* 14.1 (2004), pp. 11–22. DOI: 10.1093/cercor/bhg087. eprint: http://cercor.oxfordjournals.org/content/14/1/11.full.pdf+html. URL: http://cercor.oxfordjournals.org/content/14/1/11.abstract (cit. on p. 42).

[110] Juan Eugenio Iglesias et al. *A probabilistic atlas of the human thalamic nuclei combining ex vivo MRI and histology*. 2018. arXiv: 1806.08634 [q-bio.NC] (cit. on p. 44).

[111] *TRACULA documentation*. URL: https://surfer.nmr.mgh.harvard.edu/fswiki/Tracula (visited on 08/05/2023) (cit. on p. 48).

[112] Anastasia Yendiki et al. «Automated probabilistic reconstruction of white-matter pathways in health and disease using an atlas of the underlying anatomy». In: *Frontiers in neuroinformatics* 5 (2011), p. 23 (cit. on p. 48).

[113] C Maffei et al. «Using diffusion MRI data acquired with ultra-high gradients to improve tractography in routine-quality data». In: *bioRxiv* (2021), pp. 2021–06 (cit. on p. 48).

[114] Robert Smith. *Reconstruction of bundles of interest*. https://community.mrtrix.org/t/reconstruction-of-bundles-of-interest/5729. Apr. 2012 (cit. on p. 49).

[115] Ruopeng Wang, Thomas Benner, Alma Gregory Sorensen, and Van Jay Wedeen. «Diffusion toolkit: a software package for diffusion imaging data processing and tractography». In: *Proc Intl Soc Mag Reson Med*. Vol. 15. 3720. Berlin. 2007. URL: https://trackvis.org/ (visited on 08/05/2023) (cit. on p. 50).

[116] Eleftherios Garyfallidis, Matthew Brett, Bagrat Amirbekian, Ariel Rokem, Stefan Van Der Walt, Maxime Descoteaux, Ian Nimmo-Smith, and Dipy Contributors. «Dipy, a library for the analysis of diffusion MRI data». In: *Frontiers in neuroinformatics* 8 (2014), p. 8. URL: https://dipy.org/ (visited on 08/05/2023) (cit. on p. 50).

[117] Fang-Cheng Yeh, Sandip Panesar, Jessica Barrios, David Fernandes, Kumar Abhinav, Antonio Meola, and Juan C Fernandez-Miranda. «Automatic removal of false connections in diffusion MRI tractography using topology-informed pruning (TIP)». In: *Neurotherapeutics* 16 (2019), pp. 52–58 (cit. on p. 51).

[118] Robert E Smith, Jacques-Donald Tournier, Fernando Calamante, and Alan Connelly. «Anatomically-constrained tractography: improved diffusion MRI streamlines tractography through effective use of anatomical information». In: *Neuroimage* 62.3 (2012), pp. 1924–1938 (cit. on p. 51).

[119] Nicolas Delinte, Laurence Dricot, Benoit Macq, Claire Gosse, Marie Van Reybroeck, and Gaetan Rensonnet. «Unraveling multi-fixel microstructure with tractography and angular weighting». In: *Frontiers in Neuroscience* 17 (2023). ISSN: 1662-453X. DOI: 10.3389/fnins.2023.1199568. URL: https://www.frontiersin.org/articles/10.3389/fnins.2023.1199568 (cit. on p. 52).

[120] Nicolas Delinte, Laurence Dricot, Benoit Macq, Claire Gosse, Marie Van Reybroeck, and Gaetan Rensonnet. *UNRAVEL documentation*. URL: https://unravel.readthedocs.io/en/latest/ (visited on 08/05/2023) (cit. on p. 52).

[121] Arno Klein and Jason Tourville. «101 labeled brain images and a consistent human cortical labeling protocol». In: *Frontiers in neuroscience* 6 (2012), p. 171 (cit. on p. 54).

[122] Rutger HJ Fick, Demian Wassermann, and Rachid Deriche. «The dmipy toolbox: Diffusion mri multi-compartment modeling and microstructure recovery made easy». In: *Frontiers in neuroinformatics* 13 (2019), p. 64 (cit. on p. 56).

[123] Rutger HJ Fick, Demian Wassermann, and Rachid Deriche. *The dmipy toolbox repository*. URL: https://github.com/AthenaEPI/dmipy/tree/master (visited on 08/05/2023) (cit. on p. 56).

[124] Gaëtan Rensonnet, Benoit Scherrer, Gabriel Girard, Aleksandar Jankovski, Simon K Warfield, Benoit Macq, Jean-Philippe Thiran, and Maxime Taquet. *Microstructure fingerprinting*. URL: https://github.com/rensonnetg/microstructure_fingerprinting (visited on 08/05/2023) (cit. on p. 56).

[125] J. Toby Mordkoff. *Descriptive Statistics*. URL: http://www2.psychology.uiowa.edu/faculty/mordkoff/GradStats/part%201/I.05%20dscrptvs.pdf (visited on 08/03/2023) (cit. on p. 58).

[126] Peter H Westfall. «Kurtosis as peakedness, 1905–2014. RIP». In: *The American Statistician* 68.3 (2014), pp. 191–195 (cit. on p. 58).

[127] F. Pedregosa et al. «Scikit-learn: Machine Learning in Python». In: *Journal of Machine Learning Research* 12 (2011), pp. 2825–2830 (cit. on pp. 61, 64).

[128] Sebastian Raschka. «MLxtend: Providing machine learning and data science utilities and extensions to Python's scientific computing stack». In: *The Journal of Open Source Software* 3.24 (Apr. 2018). DOI: 10.21105/joss.00638. URL: https://joss.theoj.org/papers/10.21105/joss.00638 (cit. on p. 62).

[129] Pavel Pudil, Jana Novovičová, and Josef Kittler. «Floating search methods in feature selection». In: *Pattern recognition letters* 15.11 (1994), pp. 1119–1125 (cit. on p. 62).

[130] Joost JM Van Griethuysen et al. «Computational radiomics system to decode the radiographic phenotype». In: *Cancer research* 77.21 (2017), e104–e107 (cit. on pp. 62, 87).

[131] Gregory Lee, Ralf Gommers, Filip Waselewski, Kai Wohlfahrt, and Aaron O'Leary. «PyWavelets: A Python package for wavelet analysis». In: *Journal of Open Source Software* 4.36 (2019), p. 1237 (cit. on p. 62).

[132] Fernando Pérez-García, Rachel Sparks, and Sébastien Ourselin. «TorchIO: a Python library for efficient loading, preprocessing, augmentation and patch-based sampling of medical images in deep learning». In: *Computer Methods and Programs in Biomedicine* (2021), p. 106236. ISSN: 0169-2607. DOI: https://doi.org/10.1016/j.cmpb.2021.106236. URL: https://www.sciencedirect.com/science/article/pii/S0169260721003102 (cit. on p. 66).

[133] Xin Yu et al. «Characterizing renal structures with 3D block aggregate Transformers». In: *arXiv preprint arXiv:2203.02430* (2022) (cit. on p. 68).

[134] Emilia Sbardella, Francesca Tona, Nikolaos Petsas, Patrizia Pantano, et al. «DTI measurements in multiple sclerosis: evaluation of brain damage and clinical implications». In: *Multiple sclerosis international* 2013 (2013) (cit. on p. 88).

[135] Sue Y Yi, Brian R Barnett, Maribel Torres-Velázquez, Yuxin Zhang, Samuel A Hurley, Paul A Rowley, Diego Hernando, and John-Paul J Yu. «Detecting microglial density with quantitative multi-compartment diffusion MRI». In: *Frontiers in neuroscience* 13 (2019), p. 81 (cit. on p. 88).

[136] Patrick Friedrich, Christoph Fraenz, Caroline Schlüter, Sebastian Ocklenburg, Burkhard Mädler, Onur Güntürkün, and Erhan Genç. «The Relationship Between Axon Density, Myelination, and Fractional Anisotropy in the Human Corpus Callosum». In: *Cerebral Cortex* 30.4 (Feb. 2020), pp. 2042–2056. ISSN: 1047-3211. DOI: 10.1093/cercor/bhz221. eprint: https://academic.oup.com/cercor/article-pdf/30/4/2042/33111945/bhz221.pdf. URL: https://doi.org/10.1093/cercor/bhz221 (cit. on p. 88).

[137] Adriana M Workewych, Olivia N Arski, Karim Mithani, and George M Ibrahim. «Biomarkers of seizure response to vagus nerve stimulation: a scoping review». In: *Epilepsia* 61.10 (2020), pp. 2069–2085 (cit. on p. 89).

[138] Iris Unterberger, Richard Bauer, Gerald Walser, and Gerhard Bauer. «Corpus callosum and epilepsies». In: *Seizure* 37 (2016), pp. 55–60 (cit. on p. 89).

[139] Jeffrey P Lieb, Khabirul Hoque, Charles E Skomer, and Xue-Wen Song. «Inter-hemispheric propagation of human mesial temporal lobe seizures: a coherence/phase analysis». In: *Electroencephalography and clinical neurophysiology* 67.2 (1987), pp. 101–119 (cit. on p. 89).

[140] Robert M Beckstead, Joel R Morse, and Ralph Norgren. «The nucleus of the solitary tract in the monkey: projections to the thalamus and brain stem nuclei». In: *Journal of Comparative Neurology* 190.2 (1980), pp. 259–282 (cit. on p. 89).

[141] Kristl Vonck, Veerle De Herdt, Tommy Bosman, Stefanie Dedeurwaerdere, Koen Van Laere, and Paul Boon. «Thalamic and limbic involvement in the mechanism of action of vagus nerve stimulation, a SPECT study». In: *Seizure* 17.8 (2008), pp. 699–706 (cit. on p. 89).

[142] Nebras M Warsi et al. «Vagus Nerve Stimulation Modulates Phase-Amplitude Coupling in Thalamic Local Field Potentials». In: *Neuromodulation: Technology at the Neural Interface* 26.3 (2023), pp. 601–606 (cit. on p. 89).

Appendix A

Extracted regions

ROI from FreeSurfer

Here below are reported all the regions extracted from FreeSurfer and their number associated with the FreeSurfer Look Up Table (LUT): [1].

- Hippocampus: left {17}, right {53}
- Amygdala: left {18}, right {54}
- Accumbens: left {26}, right {58}
- Putamen: left {12}, right {51}
- Pallidum: left {12}, right {52}
- Thalamus: left {8103-8134}, right {8203-8234}
  (All the nuclei from the thalamus segmentation)
- Lateral Ventricle: left {4}, right {43}
- White matter: left {2}, right {41}
- Brain stem: {16}
- Ventral lateral anterior thalamic nuclei[2]: left {8128}, right {8228}
- Ventral lateral posterior thalamic nuclei: left {8129}, right {8229}
- Medial geniculate thalamic nuclei: left {8115}, right {8215}

---

[1]FreeSurfer color LUT `https://surfer.nmr.mgh.harvard.edu/fswiki/FsTutorial/AnatomicalROI/FreeSurferColorLUT` (Accessed on 17/08/2023)

[2]Name association by the original article: `https://arxiv.org/pdf/1806.08634.pdf` (Accessed on 05/08/2023)

- Insular cortex: left {1035}, right {2035}
- Frontal lobe: superior frontal cortex, rostral and caudal middle frontal cortex, pars opercularis, pars triangularis, and pars orbitalis, lateral and medial orbitofrontal cortex and frontal pole. Precentral and paracentral cortex are not considered.

  left {1028, 1027, 1003, 1018, 1019, 1020, 1012, 1014, 1032}, right {2028, 2027, 2003, 2018, 2019, 2020, 2012, 2014, 2032}.
- Temporal lobe: superior, middle, and inferior temporal cortex, banks of the superior temporal sulcus, fusiform gyrus, transverse temporal cortex, entorhinal and temporal pole. Without considering the parahippocampal cortex.

  left {1030, 1015, 1009, 1001, 1007, 1034, 1006, 1033}, right {2030, 2015, 2009, 2001, 2007, 2034, 2006, 2033}.
- Parietal lobe: superior parietal cortex, inferior parietal cortex and precuneus. Without considering postcentral and supramarginal cortex.

  left {1008, 1029, 1025}, right {2008, 2029, 2025}.
- Occipital lobe: lateral occipital cortex, lingual gyrus, cuneus and pericalcarine.

  left {1011, 1013, 1005, 1021}, right {2011, 2013, 2005, 2021}.
- Supramarginal gyrus: left {1031}, right {2031}
- Gyrus central: left {1022, 1024}, right {2022, 2024}

ROI from MNI space

Here below are reported all the regions taken from the Atlases in MNI space.

- Fornix:
  - Juelich Histological Atlas
  - XTRACT HCP Probabilistic Tract Atlases
- Mammillary body:
  - Juelich Histological Atlas
- Anterior limb of the internal capsule:
  - JHU ICBM-DTI-81 White-Matter Labels
- Posterior limb of the internal capsule:

  - JHU ICBM-DTI-81 White-Matter Labels
- Retrolenticular portion of internal capsule:
  - JHU ICBM-DTI-81 White-Matter Labels
- SLF I:
  - XTRACT HCP Probabilistic Tract Atlases

Appendix B

Settings for tractography with MRtrix3

```
{
"antThalRadiation":
    {
        "seed_images": ["thalamus"],
        "include_ordered" : ["AntLimbIntCapsule", "frontal-lobe"],
        "stop" : false,
        "act" : true,
        "angle" : 15
    },
"postThalRadiation-parietal":
    {
        "seed_images": ["thalamus"],
        "include_ordered" : ["PostLimbIntCapsule", "parietal-lobe"],
        "exclude" : ["VLa", "VLp"],
        "stop" : false,
        "act" : true,
        "angle" : 10
    },
"postThalRadiation-occipital":
    {
        "seed_images": ["thalamus"],
        "include_ordered" : ["PostLimbIntCapsule", "occipital-lobe"],
        "exclude" : ["VLa", "VLp", "plane1-SLF1"],
        "stop" : false,
        "act" : true,
        "angle" : 10
    },
"supThalRadiation":
    {
        "seed_images": ["thalamus"],
        "include_ordered" : ["PostLimbIntCapsule", "gyrus-central"],
        "stop" : false,
        "act" : true,
        "angle" : 15
    },
"infThalRadiation-insula":
    {
        "seed_images": ["thalamus"],
```

```
39          "include_ordered" : ["RetroLenticularIntCapsule", "plane-insula", "insula"],
40          "exclude" : ["MGN", "temporal-lobe-dilated-1", "parietal-lobe-dilated-1",
    ↪  "gyrus-central-dilated-1", "frontal-lobe-dilated-1", "supramarginal-dilated-1", "brainStem"],
41          "stop" : false,
42          "act" : true,
43          "angle" : 15
44      },
45
46  "sup-longi-fasci":
47      {
48          "seed_images" : ["frontal-lobe"],
49          "include_ordered" : ["parietal-lobe"],
50          "masks" : ["cerebral-white-matter", "frontal-lobe", "parietal-lobe"],
51          "exclude" : ["occipital-lobe-dilated-1", "temporal-lobe-dilated-1",
    ↪  "gyrus-central-dilated-1", "plane-insula"],
52          "angle" : 10,
53          "stop" : false,
54          "act" : true
55      },
56  "inf-longi-fasci":
57      {
58          "seed_images" : ["occipital-lobe"],
59          "include" : ["temporal-lobe"],
60          "masks" : ["cerebral-white-matter", "occipital-lobe", "temporal-lobe"],
61          "exclude" : ["frontal-lobe-dilated-1", "parietal-lobe-dilated-1",
    ↪  "gyrus-central-dilated-1"],
62          "angle" : 10,
63          "stop" : false,
64          "act" : true
65      },
66
67  "fornix":
68      {
69          "seed_images" : ["plane-mammillary-body"],
70          "include_ordered" : ["plane-ort-fornix", "plane-fornix", "hippocampus"],
71          "exclude" : ["Thalamus-eroded-1", "Lateral-Ventricle-eroded-1"],
72          "angle" : 15,
73          "stop" : true,
74          "act" : false
75      }
76  }
```

Appendix C

P-values tables

In the following tables, the next notation is used:

- Nothing: Not significant, $0.05 < p \leq 1$
- * : $0.01 < p \leq 0.05$
- ** : $0.001 < p \leq 0.01$
- *** : $p \leq 0.001$

		MF			DIAMOND				NODDI					DTI			
	Region	frac_ftot	fvf_tot	wfvf	frac_ctot	wFA	wMD	wRD	wAD	icvf	fintra	fextra	fiso	odi	FA	MD	RD	AD
tckgen() by MRtrix3	left-thalamus	0.14956	0.45090	0.41847	0.21598	0.26792	0.35542	0.48357	0.21598	0.00649**	0.09778	0.01792*	0.41847	0.02247*	0.21598	0.00649**	0.00649**	0.00359**
	right-thalamus	0.26792	0.41847	0.51643	0.24121	0.09778	0.24121	0.38662	0.02782*	0.01105*	0.05992	0.01792*	0.32518	0.00649**	0.07111	0.00853**	0.01105*	0.00649**
	left-hippocampus	0.51643	0.41847	0.38662	0.29590	0.21598	0.35542	0.38662	0.32518	0.02782*	0.01417*	0.05992	0.48357	0.26792	0.19223	0.00359**	0.00060***	0.01792*
	right-hippocampus	0.32518	0.41847	0.32518	0.09778	0.24121	0.48357	0.48357	0.35542	0.08367	0.01792*	0.21598	0.19223	0.45090	0.11342	0.02782*	0.04156*	0.04156*
	left-amygdala	0.38662	0.24121	0.38662	0.45090	0.01105*	0.24121	0.45090	0.21598	0.09778	0.04156*	0.13071	0.45090	0.48357	0.01417*	0.00853**	0.00853**	0.01105*
	right-amygdala	0.41847	0.48357	0.45090	0.29590	0.21598	0.32518	0.32518	0.29590	0.08367	0.05992	0.09778	0.38662	0.51643	0.17012	0.05992	0.07111	0.05992
	left-accumbens	0.21598	0.45090	0.41847	0.41847	0.26792	0.05013	0.32518	0.03417*	0.01792*	0.07111	0.01792*	0.17012	0.24121	0.14956	0.01417*	0.00649**	0.01417*
	right-accumbens	0.29590	0.41847	0.41847	0.32518	0.29590	0.35542	0.41847	0.21598	0.09778	0.17012	0.05992	0.38662	0.26792	0.19223	0.08367	0.07111	0.07111
	left-putamen	0.02782*	0.48357	0.51643	0.04156*	0.51643	0.14956	0.24121	0.29590	0.05013	0.07111	0.08367	0.21598	0.08367	0.41847	0.00853**	0.01792*	0.00089***
	right-putamen	0.03417*	0.17012	0.26792	0.05013	0.48357	0.05992	0.11342	0.09778	0.00649**	0.00853**	0.00853**	0.32518	0.05992	0.08367	0.00359**	0.00262**	0.00853**
	left-pallidum	0.08367	0.45090	0.29590	0.38662	0.24121	0.24121	0.35542	0.48357	0.04156*	0.02782*	0.05992	0.29590	0.26792	0.24121	0.01792*	0.01792*	0.05013
	right-pallidum	0.01417*	0.48357	0.38662	0.19223	0.05013	0.32518	0.11342	0.38662	0.02247*	0.02782*	0.02247*	0.32518	0.45090	0.05013	0.01792*	0.00649**	0.14956
	left-antThalRadiation	0.02782*	0.51643	0.48357	0.13071	0.45090	0.21598	0.38662	0.13071	0.04156*	0.03417*	0.09778	0.41847	0.00262**	0.35542	0.02782*	0.09778	0.00649**
	right-antThalRadiation	0.00262**	0.51643	0.38662	0.05013	0.35542	0.08367	0.45090	0.00853**	0.03417*	0.00359**	0.14956	0.17012	0.00262**	0.32518	0.00853**	0.05013	0.00262**
	left-postThalRadiation-parital	0.08367	0.41847	0.38662	0.41847	0.08367	0.21598	0.17012	0.48357	0.01105*	0.05992	0.01105*	0.32518	0.29590	0.14956	0.01105*	0.11342	0.02247*
	right-postThalRadiation-parital	0.05013	0.41847	0.48357	0.21598	0.26792	0.08367	0.24121	0.04156*	0.01105*	0.05013	0.02247*	0.29590	0.01417*	0.48357	0.00649**	0.08367	0.00262**
	left-postThalRadiation-occipital	0.03417*	0.48357	0.45090	0.09778	0.26792	0.11342	0.08367	0.38662	0.00488**	0.02247*	0.00359**	0.11342	0.29590	0.24121	0.01105*	0.03417*	0.07111
	right-postThalRadiation-occipital	0.01105*	0.48357	0.51643	0.08367	0.32518	0.02782*	0.26792	0.09778	0.00359**	0.00488**	0.00488**	0.35542	0.13071	0.35542	0.00488**	0.00649**	0.00853**
	left-supThalRadiation	0.07111	0.41847	0.35542	0.05992	0.29590	0.45090	0.45090	0.41847	0.05013	0.11342	0.07111	0.48357	0.13071	0.45090	0.08367	0.21598	0.09778
	right-supThalRadiation	0.01792*	0.41847	0.38662	0.14956	0.51643	0.21598	0.48357	0.21598	0.02782*	0.03417*	0.05013	0.48357	0.11342	0.32518	0.01105*	0.07111	0.02782*
	left-infThalRadiation-insula	0.26792	0.45090	0.29590	0.51643	0.26792	0.13071	0.11342	0.41847	0.00488**	0.08367	0.00187**	0.45090	0.09778	0.45090	0.01417*	0.01417*	0.02247*
	right-infThalRadiation-insula	0.14956	0.41847	0.45090	0.45090	0.48357	0.07111	0.38662	0.04156*	0.00187**	0.03417*	0.00262**	0.13071	0.08367	0.48357	0.00359**	0.04156*	0.00262**
	left-sup-longi-fasci	0.08367	0.41847	0.45090	0.48357	0.14956	0.45090	0.19223	0.51643	0.04156*	0.19223	0.04156*	0.08367	0.51643	0.26792	0.09778	0.21598	0.19223
	right-sup-longi-fasci	0.08367	0.51643	0.51643	0.11342	0.11342	0.24121	0.24121	0.48357	0.04156*	0.24121	0.04156*	0.02247*	0.35542	0.19223	0.04156*	0.07111	0.13071
	left-inf-longi-fasci	0.04156*	0.41847	0.41847	0.35542	0.24121	0.08367	0.21598	0.14956	0.05013	0.04156*	0.03417*	0.11342	0.51643	0.45090	0.02782*	0.09778	0.02247*
	right-inf-longi-fasci	0.01792*	0.51643	0.45090	0.29590	0.03417*	0.13071	0.07111	0.14956	0.01417*	0.01792*	0.01417*	0.07111	0.04156*	0.04156*	0.01417*	0.01417*	0.13071
	left-fornix	0.17012	0.32518	0.32518	0.48357	0.26792	0.32518	0.38662	0.35542	0.00853**	0.08367	0.02782*	0.38662	0.09778	0.24121	0.00038***	0.00038***	0.00853**
	right-fornix	0.26792	0.26792	0.19223	0.35542	0.38662	0.51643	0.41847	0.45090	0.00649**	0.01792*	0.09778	0.48357	0.11342	0.41847	0.00038***	0.00014***	0.00649**
TRACULA by Freesurfer	acomm (Anterior commissure)	0.32518	0.51643	0.48357	0.38662	0.29590	0.19223	0.29590	0.13071	0.00089***	0.04156*	0.00187**	0.13071	0.02247*	0.41847	0.00060***	0.01792*	0.00131**
	cc.bodyc (Corpus call. body central)	0.03417*	0.45090	0.35542	0.17012	0.14956	0.38662	0.29590	0.32518	0.01417*	0.14956	0.04156*	0.07111	0.21598	0.45090	0.01792*	0.09778	0.05013
	cc.bodyp (Corpus call. body parietal)	0.00853**	0.48357	0.38662	0.32518	0.11342	0.14956	0.19223	0.48357	0.01792*	0.01417*	0.02782*	0.29590	0.41847	0.32518	0.01105*	0.03417*	0.03417*
	cc.bodypf (Corpus call. body prefrontal)	0.05992	0.21598	0.21598	0.11342	0.48357	0.48357	0.24121	0.09778	0.05013	0.03417*	0.29590	0.26792	0.13071	0.48357	0.02247*	0.19223	0.00853**
	cc.bodypm (Corpus call. body premotor)	0.00853**	0.48357	0.38662	0.32518	0.11342	0.14956	0.19223	0.48357	0.01792*	0.01417*	0.02782*	0.29590	0.41847	0.32518	0.01105*	0.03417*	0.03417*
	cc.bodyt (Corpus call. body temporal)	0.01417*	0.45090	0.48357	0.13071	0.11342	0.04156*	0.11342	0.13071	0.00131**	0.00853**	0.00187**	0.26792	0.17012	0.32518	0.00359**	0.01105*	0.01417*
	cc.genu (Corpus call. genu)	0.24121	0.21598	0.24121	0.24121	0.26792	0.51643	0.45090	0.24121	0.07111	0.14956	0.14956	0.38662	0.09778	0.26792	0.05992	0.29590	0.02782*
	cc.rostrum (Corpus call. rostrum)	0.32518	0.26792	0.26792	0.38662	0.51643	0.38662	0.45090	0.48357	0.04156*	0.13071	0.08367	0.32518	0.29590	0.41847	0.05992	0.24121	0.08367
	cc.splenium (Corpus call. splenium)	0.05013	0.51643	0.48357	0.48357	0.32518	0.09778	0.26792	0.24121	0.01792*	0.05992	0.01417*	0.24121	0.29590	0.45090	0.02782*	0.13071	0.00853**
	mcp (Middle cerebellar peduncle)	0.01417*	0.11342	0.11342	0.04156*	0.35542	0.51643	0.19223	0.29590	0.24121	0.05013	0.21598	0.29590	0.14956	0.26792	0.13071	0.26792	0.11342
	lh.af (Arcuate fasciculus)	0.11342	0.45090	0.38662	0.26792	0.24121	0.21598	0.17012	0.35542	0.02782*	0.05013	0.01792*	0.19223	0.19223	0.26792	0.04156*	0.19223	0.05992
	rh.af (Arcuate fasciculus)	0.01105*	0.51643	0.51643	0.19223	0.38662	0.38662	0.38662	0.41847	0.02782*	0.01105*	0.04156*	0.19223	0.32518	0.21598	0.02782*	0.03417*	0.13071
	lh.ar (Acoustic radiation)	0.17012	0.32518	0.35542	0.21598	0.51643	0.11342	0.24121	0.05013	0.00649**	0.17012	0.01417*	0.51643	0.08367	0.48357	0.02247*	0.11342	0.01417*
	rh.ar (Acoustic radiation)	0.17012	0.32518	0.38662	0.32518	0.38662	0.04156*	0.24121	0.05992	0.01417*	0.09778	0.02247*	0.48357	0.38662	0.32518	0.01792*	0.05992	0.05013
	lh.atr (Ant. thalamic radiations)	0.04156*	0.41847	0.35542	0.11342	0.26792	0.35542	0.45090	0.05992	0.03417*	0.05013	0.05992	0.45090	0.02247*	0.35542	0.02782*	0.11342	0.00359**
	rh.atr (Ant. thalamic radiations)	0.02247*	0.32518	0.29590	0.05992	0.35542	0.35542	0.38662	0.05992	0.05013	0.04156*	0.08367	0.24121	0.03417*	0.35542	0.01105*	0.17012	0.00187**
	lh.cbd (Cingulum bundle dorsal)	0.09778	0.35542	0.29590	0.45090	0.29590	0.45090	0.21598	0.29590	0.00649**	0.13071	0.01417*	0.11342	0.35542	0.48357	0.02247*	0.08367	0.11342
	rh.cbd (Cingulum bundle dorsal)	0.11342	0.32518	0.29590	0.32518	0.19223	0.38662	0.38662	0.21598	0.02782*	0.08367	0.05013	0.07111	0.51643	0.41847	0.02782*	0.14956	0.07111
	lh.cbv (Cingulum bundle ventral)	0.09778	0.45090	0.38662	0.24121	0.24121	0.45090	0.29590	0.21598	0.01417*	0.13071	0.00853**	0.45090	0.48357	0.35542	0.01417*	0.04156*	0.17012
	rh.cbv (Cingulum bundle ventral)	nan	nan	nan	nan	nan	nan	nan	nan	nan	nan	nan	nan	nan	nan	nan	nan	nan
	lh.cst (Corticospinal tract)	0.12315	0.32950	0.26801	0.26801	0.36212	0.50000	0.36212	0.43005	0.21258	0.23947	0.21258	0.36212	0.23947	0.36212	0.08956	0.14272	0.14272
	rh.cst (Corticospinal tract)	0.10546	0.23947	0.21258	0.26801	0.10546	0.50000	0.26801	0.14272	0.18747	0.23947	0.18747	0.50000	0.05210	0.07545	0.14272	0.23947	0.06297
	lh.emc (Extreme capsule)	0.06297	0.39571	0.43005	0.26801	0.46490	0.23947	0.32950	0.06297	0.03463*	0.14272	0.05210	0.46490	0.12315	0.43005	0.03463*	0.08956	0.02206*
	rh.emc (Extreme capsule)	0.05210	0.39571	0.29808	0.08956	0.29808	0.18747	0.50000	0.02206*	0.07545	0.10546	0.06297	0.39571	0.06297	0.29808	0.01339*	0.18747	0.00569**
	lh.fat (Frontal aslant tract)	0.04267*	0.18747	0.21258	0.36212	0.43005	0.32950	0.46490	0.32950	0.08956	0.18747	0.08956	0.10546	0.23947	0.39571	0.14272	0.18747	0.08956
	rh.fat (Frontal aslant tract)	0.03463*	0.36212	0.29808	0.23947	0.23947	0.50000	0.32950	0.29808	0.10546	0.07545	0.08956	0.03463*	0.23947	0.50000	0.04267*	0.08956	0.12315
	lh.fx (Fornix)	0.36212	0.26801	0.43005	0.36212	0.26801	0.10546	0.07545	0.08956	0.04267*	0.26801	0.00415**	0.21258	0.02778*	0.36212	0.01339*	0.01339*	0.00770**
	rh.fx (Fornix)	0.14272	0.39571	0.46490	0.21258	0.32950	0.43005	0.26801	0.46490	0.01021*	0.06297	0.10546	0.36212	0.36212	0.23947	0.00295**	0.00569**	0.01021*
	lh.ilf (Inf. longi. fasci.)	0.06297	0.46490	0.50000	0.23947	0.32950	0.02778*	0.21258	0.02206*	0.01728*	0.02206*	0.01339*	0.23947	0.01339*	0.39571	0.01339*	0.08956	0.00569**
	rh.ilf (Inf. longi. fasci.)	0.01339*	0.39571	0.39571	0.10546	0.18747	0.21258	0.18747	0.43005	0.04267*	0.03463*	0.07545	0.50000	0.46490	0.29808	0.02778*	0.18747	0.14272
	lh.mlf (Middle longi. fasci.)	0.21258	0.43005	0.46490	0.16415	0.39571	0.16415	0.26801	0.10546	0.00569**	0.05210	0.00569**	0.18747	0.07545	0.32950	0.01339*	0.12315	0.01728*
	rh.mlf (Middle longi. fasci.)	0.02206*	0.39571	0.36212	0.26801	0.32950	0.02778*	0.14272	0.12315	0.00415**	0.01021*	0.00569**	0.10546	0.32950	0.50000	0.00770**	0.03463*	0.01339*
	lh.or (Optic radiation)	0.08956	0.43005	0.50000	0.32950	0.43005	0.08956	0.21258	0.10546	0.00569**	0.05210	0.00569**	0.05210	0.07545	0.36212	0.01021*	0.08956	0.02778*
	rh.or (Optic radiation)	0.04267*	0.43005	0.43005	0.07545	0.39571	0.39571	0.43005	0.29808	0.00415**	0.03463*	0.05210	0.46490	0.12315	0.50000	0.00415**	0.03463*	0.00770**
	lh.slf1 (Sup. longi. fasci. I)	0.12315	0.16415	0.21258	0.32950	0.43005	0.32950	0.29808	0.46490	0.10546	0.26801	0.07545	0.14272	0.29808	0.46490	0.07545	0.50000	0.06297
	rh.slf1 (Sup. longi. fasci. I)	0.43005	0.21258	0.21258	0.02206*	0.26801	0.29808	0.39571	0.39571	0.29808	0.46490	0.23947	0.00770**	0.46490	0.46490	0.32950	0.39571	0.32950
	lh.slf2 (Sup. longi. fasci. II)	0.04267*	0.46490	0.46490	0.29808	0.29808	0.32950	0.21258	0.39571	0.03463*	0.08956	0.03463*	0.18747	0.29808	0.29808	0.10546	0.23947	0.08956
	rh.slf2 (Sup. longi. fasci. II)	0.04267*	0.39571	0.43005	0.43005	0.36212	0.36212	0.39571	0.29808	0.02206*	0.07545	0.02206*	0.06297	0.36212	0.29808	0.05210	0.12315	0.18747
	lh.slf3 (Sup. longi. fasci. III)	0.10546	0.36212	0.36212	0.32950	0.50000	0.50000	0.26801	0.50000	0.07545	0.18747	0.05210	0.23947	0.43005	0.29808	0.23947	0.14272	0.23947
	rh.slf3 (Sup. longi. fasci. III)	0.02206*	0.43005	0.29808	0.39571	0.39571	0.39571	0.43005	0.21258	0.03463*	0.01339*	0.03463*	0.08956	0.50000	0.36212	0.02206*	0.07545	0.10546
	lh.uf (Uncinate fasciculus)	0.18747	0.46490	0.46490	0.43005	0.32950	0.18747	0.23947	0.29808	0.02206*	0.12315	0.01339*	0.26801	0.16415	0.50000	0.01728*	0.06297	0.05210
	rh.uf (Uncinate fasciculus)	0.32950	0.36212	0.32950	0.32950	0.46490	0.39571	0.43005	0.23947	0.06297	0.16415	0.04267*	0.18747	0.08956	0.46490	0.02206*	0.16415	0.01339*

Table C.1: Table of Mann-Whitney U rank test p-values of **MEANS** of the distribution of metrics. As rows all the extracted ROI, as columns the models metrics. Highlighted in yellow are the TRACULA regions where the p-values are computed without considering the patient `VNSLC_16`. In red the values computed with `alternative = "less"` (the distribution of non-responder subjects is stochastic *less* than the distribution of responder subjects), in green the values computed with `alternative = "greater"` (the distribution of non-responder subjects is stochastic *greater* than the distribution of responder subjects), the rest is computed with `alternative = "two-sided"` and non-statistical significant.

		MF			DIAMOND					NODDI					DTI			
	Region	frac_ftot	fvf_tot	wfvf	frac_ctot	wFA	wMD	wRD	wAD	icvf	fintra	fextra	fiso	odi	FA	MD	RD	AD
tckgen() by MRtrix3	left-thalamus	0.19223	0.32518	0.32518	0.51643	0.32518	0.35542	0.17012	0.17012	0.13071	0.35542	0.17012	0.45090	0.09778	0.38662	0.00359**	0.00488**	0.05013
	right-thalamus	0.48357	0.38662	0.48357	0.35542	0.29590	0.45090	0.08367	0.11342	0.21598	0.21598	0.17012	0.26792	0.03417*	0.38662	0.02247*	0.01792*	0.02247*
	left-hippocampus	0.35542	0.48357	0.38662	0.32518	0.45090	0.32518	0.48357	0.17012	0.38662	0.29590	0.45090	0.45090	0.11342	0.45090	0.09778	0.11342	0.14956
	right-hippocampus	0.38662	0.48357	0.41847	0.17012	0.35542	0.11342	0.14956	0.13071	0.41847	0.08367	0.17012	0.24121	0.35542	0.45090	0.07111	0.13071	0.04156*
	left-amygdala	0.48357	0.45090	0.17012	0.26792	0.35542	0.14956	0.45090	0.09778	0.45090	0.21598	0.51643	0.51643	0.13071	0.19223	0.14956	0.45090	0.11342
	right-amygdala	0.48357	0.38662	0.51643	0.19223	0.41847	0.45090	0.35542	0.45090	0.48357	0.29590	0.48357	0.48357	0.24121	0.19223	0.08367	0.19223	0.01417*
	left-accumbens	0.13071	0.02247*	0.03417*	0.24121	0.00262**	0.35542	0.01792*	0.51643	0.07111	0.17012	0.05992	0.17012	0.05013	0.04156*	0.09778	0.07111	0.11342
	right-accumbens	0.35542	0.45090	0.41847	0.51643	0.48357	0.29590	0.48357	0.07111	0.35542	0.51643	0.32518	0.38662	0.38662	0.21598	0.48357	0.48357	0.29590
	left-putamen	0.00024***	0.48357	0.21598	0.00649**	0.48357	0.32518	0.32518	0.45090	0.45090	0.21598	0.45090	0.09778	0.07111	0.32518	0.48357	0.11342	0.32518
	right-putamen	0.02247*	0.01105*	0.08367	0.04156*	0.00038***	0.17012	0.26792	0.45090	0.26792	0.48357	0.45090	0.11342	0.00131**	0.00488**	0.21598	0.38662	0.45090
	left-pallidum	0.01105*	0.04156*	0.07111	0.02782*	0.38662	0.26792	0.24121	0.24121	0.01105*	0.32518	0.00853**	0.00853**	0.26792	0.26792	0.35542	0.01417*	0.35542
	right-pallidum	0.03417*	0.17012	0.29590	0.05013	0.35542	0.45090	0.35542	0.24121	0.21598	0.51643	0.05992	0.00038***	0.13071	0.48357	0.29590	0.00359**	0.35542
	left-antThalRadiation	0.05013	0.29590	0.17012	0.17012	0.41847	0.41847	0.45090	0.14956	0.13071	0.19223	0.03417*	0.09778	0.13071	0.11342	0.05992	0.00488**	0.21598
	right-antThalRadiation	0.02247*	0.45090	0.26792	0.13071	0.04156*	0.26792	0.19223	0.35542	0.02782*	0.05992	0.00488**	0.05013	0.00187**	0.51643	0.01105*	0.00187**	0.04156*
	left-postThalRadiation-parital	0.00488**	0.29590	0.21598	0.26792	0.14956	0.24121	0.41847	0.32518	0.51643	0.11342	0.24121	0.26792	0.05992	0.05992	0.07111	0.01417*	0.14956
	right-postThalRadiation-parital	0.00089***	0.13071	0.14956	0.13071	0.29590	0.35542	0.51643	0.24121	0.29590	0.13071	0.04156*	0.14956	0.38662	0.05992	0.05992	0.00089***	0.07111
	left-postThalRadiation-occipital	0.07111	0.13071	0.07111	0.26792	0.11342	0.48357	0.32518	0.45090	0.38662	0.11342	0.45090	0.29590	0.32518	0.02782*	0.32518	0.01417*	0.51643
	right-postThalRadiation-occipital	0.01792*	0.48357	0.45090	0.13071	0.17012	0.38662	0.26792	0.41847	0.41847	0.21598	0.26792	0.26792	0.26792	0.29590	0.38662	0.01417*	0.32518
	left-supThalRadiation	0.13071	0.35542	0.24121	0.45090	0.24121	0.09778	0.21598	0.24121	0.38662	0.11342	0.45090	0.32518	0.19223	0.51643	0.24121	0.13071	0.11342
	right-supThalRadiation	0.02782*	0.24121	0.24121	0.17012	0.41847	0.51643	0.26792	0.13071	0.32518	0.05013	0.14956	0.09778	0.29590	0.24121	0.08367	0.02247*	0.08367
	left-infThalRadiation-insula	0.19223	0.41847	0.45090	0.45090	0.35542	0.48357	0.41847	0.41847	0.41847	0.45090	0.26792	0.41847	0.41847	0.09778	0.04156*	0.00853**	0.09778
	right-infThalRadiation-insula	0.19223	0.26792	0.17012	0.32518	0.48357	0.07111	0.21598	0.38662	0.26792	0.07111	0.32518	0.38662	0.29590	0.14956	0.11342	0.01417*	0.29590
	left-sup-longi-fasci	0.08367	0.29590	0.24121	0.35542	0.35542	0.35542	0.41847	0.35542	0.41847	0.02247*	0.51643	0.29590	0.26792	0.38662	0.14956	0.19223	0.38662
	right-sup-longi-fasci	0.00262**	0.05013	0.05013	0.29590	0.13071	0.45090	0.35542	0.41847	0.38662	0.09778	0.38662	0.41847	0.21598	0.13071	0.13071	0.05992	0.45090
	left-inf-longi-fasci	0.08367	0.24121	0.19223	0.26792	0.01105*	0.51643	0.41847	0.07111	0.13071	0.32518	0.21598	0.48357	0.00008***	0.00262**	0.13071	0.01417*	0.03417*
	right-inf-longi-fasci	0.13071	0.51643	0.51643	0.21598	0.02782*	0.38662	0.17012	0.21598	0.45090	0.26792	0.41847	0.26792	0.00024***	0.03417*	0.19223	0.02247*	0.19223
	left-fornix	0.04156*	0.32518	0.11342	0.17012	0.35542	0.05013	0.35542	0.09778	0.00359**	0.38662	0.01105*	0.02782*	0.32518	0.32518	0.01417*	0.05013	0.04156*
	right-fornix	0.24121	0.26792	0.11342	0.21598	0.48357	0.14956	0.48357	0.17012	0.05013	0.08367	0.13071	0.51643	0.48357	0.11342	0.00488**	0.03417*	0.01417*
TRACULA by Freesurfer	acomm (Anterior commissure)	0.45090	0.21598	0.14956	0.38662	0.48357	0.51643	0.24121	0.35542	0.11342	0.09778	0.24121	0.41847	0.17012	0.48357	0.21598	0.05992	0.21598
	cc.bodyc (Corpus call. body central)	0.00853**	0.48357	0.41847	0.24121	0.26792	0.45090	0.32518	0.41847	0.32518	0.01105*	0.35542	0.24121	0.24121	0.45090	0.00089***	0.01105*	0.05013
	cc.bodyp (Corpus call. body parietal)	0.01792*	0.41847	0.24121	0.14956	0.05013	0.38662	0.35542	0.13071	0.35542	0.09778	0.41847	0.11342	0.05013	0.32518	0.00089***	0.01105*	0.04156*
	cc.bodypf (Corpus call. body prefrontal)	0.35542	0.45090	0.17012	0.41847	0.38662	0.38662	0.32518	0.32518	0.48357	0.32518	0.45090	0.29590	0.11342	0.48357	0.05013	0.26792	0.09778
	cc.bodypm (Corpus call. body premotor)	0.01792*	0.41847	0.24121	0.14956	0.05013	0.38662	0.35542	0.13071	0.35542	0.09778	0.41847	0.11342	0.05013	0.32518	0.00089***	0.01105*	0.04156*
	cc.bodyt (Corpus call. body temporal)	0.05992	0.48357	0.35542	0.14956	0.14956	0.13071	0.41847	0.05992	0.48357	0.21598	0.24121	0.14956	0.09778	0.29590	0.01792*	0.03417*	0.01792*
	cc.genu (Corpus call. genu)	0.51643	0.45090	0.48357	0.19223	0.21598	0.29590	0.17012	0.24121	0.35542	0.21598	0.38662	0.45090	0.41847	0.14956	0.29590	0.41847	0.17012
	cc.rostrum (Corpus call. rostrum)	0.24121	0.32518	0.29590	0.48357	0.24121	0.41847	0.13071	0.11342	0.17012	0.09778	0.21598	0.51643	0.32518	0.02247*	0.45090	0.41847	0.17012
	cc.splenium (Corpus call. splenium)	0.02247*	0.51643	0.29590	0.09778	0.02782*	0.29590	0.48357	0.01417*	0.38662	0.24121	0.26792	0.04156*	0.00853**	0.41847	0.24121	0.07111	0.00853**
	mcp (Middle cerebellar peduncle)	0.24121	0.32518	0.32518	0.38662	0.21598	0.13071	0.29590	0.45090	0.38662	0.48357	0.38662	0.19223	0.38662	0.17012	0.17012	0.29590	0.41847
	lh.af (Arcuate fasciculus)	0.14956	0.02782*	0.04156*	0.11342	0.05992	0.45090	0.14956	0.41847	0.24121	0.41847	0.32518	0.29590	0.48357	0.51643	0.14956	0.48357	0.11342
	rh.af (Arcuate fasciculus)	0.24121	0.00262**	0.00359**	0.48357	0.02782*	0.32518	0.24121	0.21598	0.14956	0.29590	0.21598	0.35542	0.19223	0.14956	0.38662	0.41847	0.45090
	lh.ar (Acoustic radiation)	0.38662	0.05992	0.05992	0.51643	0.45090	0.29590	0.35542	0.45090	0.13071	0.32518	0.19223	0.45090	0.24121	0.48357	0.38662	0.14956	0.29590
	rh.ar (Acoustic radiation)	0.26792	0.35542	0.32518	0.29590	0.19223	0.38662	0.48357	0.41847	0.41847	0.29590	0.35542	0.38662	0.08367	0.38662	0.11342	0.02782*	0.07111
	lh.atr (Ant. thalamic radiations)	0.05013	0.48357	0.38662	0.51643	0.17012	0.29590	0.51643	0.24121	0.26792	0.19223	0.09778	0.38662	0.11342	0.14956	0.17012	0.01417*	0.26792
	rh.atr (Ant. thalamic radiations)	0.29590	0.17012	0.05992	0.19223	0.38662	0.48357	0.26792	0.51643	0.26792	0.21598	0.11342	0.11342	0.26792	0.17012	0.11342	0.01105*	0.08367
	lh.cbd (Cingulum bundle dorsal)	0.09778	0.26792	0.26792	0.32518	0.45090	0.19223	0.45090	0.35542	0.38662	0.09778	0.48357	0.29590	0.41847	0.29590	0.17012	0.08367	0.35542
	rh.cbd (Cingulum bundle dorsal)	0.05992	0.48357	0.45090	0.48357	0.24121	0.19223	0.48357	0.29590	0.38662	0.17012	0.32518	0.45090	0.17012	0.29590	0.19223	0.08367	0.17012
	lh.cbv (Cingulum bundle ventral)	0.21598	0.32518	0.41847	0.13071	0.26792	0.32518	0.45090	0.45090	0.29590	0.32518	0.45090	0.17012	0.32518	0.38662	0.09778	0.14956	0.19223
	rh.cbv (Cingulum bundle ventral)	nan	nan	nan	nan	nan	nan	nan	nan	nan	nan	nan	nan	nan	nan	nan	nan	nan
	lh.cst (Corticospinal tract)	0.36212	0.08956	0.08956	0.26801	0.23947	0.18747	0.07545	0.18747	0.43005	0.46490	0.43005	0.10546	0.12315	0.39571	0.26801	0.50000	0.36212
	rh.cst (Corticospinal tract)	0.16415	0.10546	0.07545	0.36212	0.04267*	0.18747	0.05210	0.50000	0.43005	0.46490	0.50000	0.39571	0.12315	0.43005	0.46490	0.43005	0.21258
	lh.emc (Extreme capsule)	0.12315	0.26801	0.26801	0.46490	0.50000	0.21258	0.36212	0.14272	0.32950	0.29808	0.32950	0.32950	0.46490	0.26801	0.02778*	0.01021*	0.06297
	rh.emc (Extreme capsule)	0.16415	0.36212	0.43005	0.16415	0.43005	0.29808	0.18747	0.39571	0.43005	0.12315	0.39571	0.18747	0.50000	0.36212	0.05210	0.03463*	0.10546
	lh.fat (Frontal aslant tract)	0.02206*	0.39571	0.36212	0.06297	0.12315	0.07545	0.18747	0.23947	0.12315	0.32950	0.07545	0.07545	0.29808	0.36212	0.23947	0.36212	0.14272
	rh.fat (Frontal aslant tract)	0.46490	0.50000	0.50000	0.21258	0.36212	0.26801	0.46490	0.18747	0.21258	0.26801	0.23947	0.36212	0.16415	0.16415	0.46490	0.14272	0.43005
	lh.fx (Fornix)	0.43005	0.26801	0.08956	0.14272	0.43005	0.43005	0.46490	0.46490	0.05210	0.21258	0.03463*	0.26801	0.26801	0.18747	0.02778*	0.08956	0.01339*
	rh.fx (Fornix)	0.26801	0.39571	0.36212	0.39571	0.36212	0.07545	0.29808	0.05210	0.43005	0.06297	0.07545	0.21258	0.29808	0.29808	0.01728*	0.07545	0.00569**
	lh.ilf (Inf. longi. fasci.)	0.46490	0.10546	0.12315	0.32950	0.18747	0.39571	0.10546	0.18747	0.08956	0.39571	0.21258	0.39571	0.26801	0.46490	0.23947	0.04267*	0.08956
	rh.ilf (Inf. longi. fasci.)	0.50000	0.39571	0.36212	0.18747	0.26801	0.29808	0.32950	0.46490	0.18747	0.43005	0.29808	0.32950	0.10546	0.12315	0.43005	0.14272	0.23947
	lh.mlf (Middle longi. fasci.)	0.50000	0.16415	0.12315	0.26801	0.16415	0.39571	0.14272	0.50000	0.12315	0.43005	0.18747	0.32950	0.32950	0.32950	0.14272	0.21258	0.18747
	rh.mlf (Middle longi. fasci.)	0.12315	0.32950	0.23947	0.08956	0.16415	0.43005	0.29808	0.23947	0.21258	0.21258	0.21258	0.18747	0.05210	0.29808	0.10546	0.04267*	0.10546
	lh.or (Optic radiation)	0.43005	0.06297	0.03463*	0.32950	0.29808	0.36212	0.21258	0.29808	0.26801	0.32950	0.39571	0.46490	0.39571	0.26801	0.26801	0.18747	0.21258
	rh.or (Optic radiation)	0.12315	0.39571	0.26801	0.06297	0.32950	0.43005	0.29808	0.39571	0.46490	0.36212	0.23947	0.08956	0.16415	0.23947	0.39571	0.21258	0.50000
	lh.slf1 (Sup. longi. fasci. I)	0.26801	0.14272	0.23947	0.32950	0.21258	0.23947	0.50000	0.46490	0.26801	0.04267*	0.46490	0.21258	0.06297	0.06297	0.18747	0.08956	0.06297
	rh.slf1 (Sup. longi. fasci. I)	0.04267*	0.23947	0.36212	0.32950	0.07545	0.29808	0.43005	0.26801	0.32950	0.01021*	0.12315	0.39571	0.02206*	0.14272	0.06297	0.02778*	0.36212
	lh.slf2 (Sup. longi. fasci. II)	0.50000	0.05210	0.04267*	0.26801	0.07545	0.46490	0.26801	0.43005	0.50000	0.14272	0.50000	0.18747	0.36212	0.21258	0.23947	0.36212	0.21258
	rh.slf2 (Sup. longi. fasci. II)	0.08956	0.00569**	0.00770**	0.39571	0.26801	0.32950	0.36212	0.16415	0.46490	0.05210	0.46490	0.32950	0.36212	0.14272	0.16415	0.23947	0.50000
	lh.slf3 (Sup. longi. fasci. III)	0.32950	0.23947	0.23947	0.26801	0.43005	0.21258	0.26801	0.43005	0.29808	0.50000	0.43005	0.46490	0.12315	0.21258	0.43005	0.39571	0.16415
	rh.slf3 (Sup. longi. fasci. III)	0.07545	0.01021*	0.02778*	0.46490	0.50000	0.36212	0.39571	0.36212	0.32950	0.36212	0.50000	0.46490	0.50000	0.50000	0.46490	0.12315	0.36212
	lh.uf (Uncinate fasciculus)	0.43005	0.21258	0.26801	0.46490	0.39571	0.32950	0.26801	0.39571	0.39571	0.46490	0.46490	0.46490	0.46490	0.32950	0.46490	0.08956	0.05210
	rh.uf (Uncinate fasciculus)	0.43005	0.46490	0.50000	0.43005	0.26801	0.46490	0.43005	0.21258	0.39571	0.39571	0.46490	0.23947	0.23947	0.43005	0.16415	0.12315	0.04267*

Table C.2: Table of Mann-Whitney U rank test p-values of **STANDARD DEVIATIONS** of the distribution of metrics. As rows all the extracted ROI, as columns the models metrics. Highlighted in yellow are the TRACULA regions where the p-values are computed without considering the patient `VNSLC_16`. In red the values computed with `alternative = "less"` (the distribution of non-responder subjects is stochastic *less* than the distribution of responder subjects), in green the values computed with `alternative = "greater"` (the distribution of non-responder subjects is stochastic *greater* than the distribution of responder subjects), the rest is computed with `alternative = "two-sided"` and non-statistical significant.

		MF			DIAMOND				NODDI					DTI			
	Region	frac_ftot	fvf_tot	wfvf	frac_ctot	wFA	wMD	wRD	wAD	icvf	fintra	fextra	fiso	odi	FA	MD	RD	AD
tckgen() by MRtrix3	left-thalamus	0.45090	0.41847	0.51643	0.21598	0.21598	0.05992	0.24121	0.35542	0.01105*	0.01417*	0.08367	0.41847	0.01417*	0.41847	0.09778	0.17012	0.41847
	right-thalamus	0.41847	0.41847	0.51643	0.38662	0.01105*	0.01105*	0.29590	0.11342	0.00853**	0.13071	0.19223	0.32518	0.29590	0.21598	0.07111	0.51643	0.45090
	left-hippocampus	0.48357	0.45090	0.19223	0.41847	0.21598	0.13071	0.24121	0.21598	0.29590	0.24121	0.45090	0.29590	0.29590	0.29590	0.01105*	0.14956	0.09778
	right-hippocampus	0.29590	0.14956	0.24121	0.11342	0.38662	0.05992	0.19223	0.02782*	0.45090	0.21598	0.45090	0.48357	0.24121	0.09778	0.00649**	0.02247*	0.08367
	left-amygdala	0.48357	0.08367	0.01105*	0.21598	0.32518	0.04156*	0.05992	0.09778	0.45090	0.45090	0.26792	0.32518	0.14956	0.48357	0.26792	0.26792	0.41847
	right-amygdala	0.41847	0.38662	0.41847	0.38662	0.14956	0.07111	0.03417*	0.14956	0.51643	0.48357	0.41847	0.21598	0.45090	0.35542	0.02782*	0.01417*	0.48357
	left-accumbens	0.45090	0.26792	0.24121	0.21598	0.35542	0.02782*	0.03417*	0.05992	0.19223	0.41847	0.17012	0.24121	0.24121	0.51643	0.32518	0.45090	0.51643
	right-accumbens	0.04156*	0.09778	0.17012	0.21598	0.48357	0.41847	0.41847	0.41847	0.19223	0.51643	0.45090	0.38662	0.19223	0.32518	0.14956	0.24121	0.21598
	left-putamen	0.24121	0.38662	0.38662	0.19223	0.26792	0.14956	0.21598	0.32518	0.11342	0.38662	0.02782*	0.11342	0.35542	0.14956	0.08367	0.32518	0.11342
	right-putamen	0.09778	0.08367	0.32518	0.48357	0.51643	0.29590	0.03417*	0.19223	0.24121	0.32518	0.26792	0.45090	0.45090	0.08367	0.01792*	0.29590	0.48357
	left-pallidum	0.35542	0.24121	0.19223	0.38662	0.19223	0.05992	0.14956	0.45090	0.05013	0.14956	0.08367	0.45090	0.51643	0.13071	0.35542	0.29590	0.45090
	right-pallidum	0.45090	0.11342	0.11342	0.35542	0.19223	0.48357	0.07111	0.41847	0.17012	0.19223	0.11342	0.29590	0.21598	0.02782*	0.13071	0.35542	0.24121
	left-antThalRadiation	0.35542	0.05992	0.13071	0.05013	0.21598	0.17012	0.41847	0.26792	0.38662	0.41847	0.11342	0.21598	0.51643	0.51643	0.29590	0.08367	0.19223
	right-antThalRadiation	0.38662	0.07111	0.07111	0.26792	0.01105*	0.01792*	0.35542	0.03417*	0.38662	0.13071	0.51643	0.45090	0.29590	0.26792	0.32518	0.05992	0.35542
	left-postThalRadiation-parital	0.45090	0.32518	0.14956	0.45090	0.45090	0.24121	0.32518	0.17012	0.48357	0.32518	0.11342	0.14956	0.05992	0.26792	0.14956	0.08367	0.51643
	right-postThalRadiation-parital	0.45090	0.24121	0.21598	0.13071	0.24121	0.41847	0.13071	0.29590	0.05992	0.38662	0.26792	0.24121	0.38662	0.38662	0.01105*	0.04156*	0.17012
	left-postThalRadiation-occipital	0.51643	0.13071	0.13071	0.19223	0.41847	0.45090	0.45090	0.19223	0.26792	0.26792	0.09778	0.24121	0.13071	0.41847	0.17012	0.41847	0.17012
	right-postThalRadiation-occipital	0.21598	0.45090	0.38662	0.29590	0.41847	0.35542	0.32518	0.05992	0.41847	0.26792	0.26792	0.26792	0.05992	0.32518	0.08367	0.41847	0.48357
	left-supThalRadiation	0.41847	0.13071	0.21598	0.21598	0.24121	0.17012	0.26792	0.09778	0.41847	0.48357	0.35542	0.14956	0.21598	0.24121	0.29590	0.11342	0.09778
	right-supThalRadiation	0.24121	0.29590	0.13071	0.14956	0.21598	0.05013	0.35542	0.02782*	0.35542	0.24121	0.17012	0.19223	0.38662	0.24121	0.17012	0.32518	0.32518
	left-infThalRadiation-insula	0.19223	0.26792	0.19223	0.38662	0.11342	0.29590	0.07111	0.38662	0.13071	0.08367	0.04156*	0.51643	0.13071	0.17012	0.29590	0.38662	0.08367
	right-infThalRadiation-insula	0.07111	0.32518	0.11342	0.26792	0.41847	0.32518	0.45090	0.26792	0.26792	0.13071	0.01792*	0.29590	0.13071	0.01792*	0.14956	0.41847	0.26792
	left-sup-longi-fasci	0.26792	0.14956	0.08367	0.19223	0.35542	0.17012	0.38662	0.41847	0.45090	0.14956	0.21598	0.08367	0.26792	0.38662	0.13071	0.13071	0.17012
	right-sup-longi-fasci	0.26792	0.09778	0.08367	0.03417*	0.48357	0.48357	0.26792	0.11342	0.45090	0.48357	0.05992	0.00649**	0.19223	0.45090	0.03417*	0.14956	0.51643
	left-inf-longi-fasci	0.14956	0.11342	0.17012	0.35542	0.35542	0.48357	0.38662	0.45090	0.21598	0.45090	0.26792	0.14956	0.19223	0.35542	0.29590	0.51643	0.38662
	right-inf-longi-fasci	0.13071	0.13071	0.14956	0.32518	0.09778	0.35542	0.07111	0.51643	0.38662	0.17012	0.48357	0.11342	0.09778	0.14956	0.41847	0.32518	0.38662
	left-fornix	0.24121	0.41847	0.29590	0.32518	0.35542	0.48357	0.17012	0.38662	0.00488**	0.11342	0.08367	0.19223	0.04156*	0.45090	0.38662	0.19223	0.11342
	right-fornix	0.41847	0.17012	0.38662	0.51643	0.51643	0.35542	0.08367	0.51643	0.00853**	0.38662	0.13071	0.32518	0.19223	0.32518	0.13071	0.29590	0.05013
TRACULA by Freesurfer	acomm (Anterior commissure)	0.26792	0.41847	0.51643	0.51643	0.29590	0.05013	0.26792	0.24121	0.00187**	0.35542	0.00089***	0.14956	0.38662	0.41847	0.07111	0.21598	0.01792*
	cc.bodyc (Corpus call. body central)	0.09778	0.11342	0.17012	0.51643	0.38662	0.32518	0.11342	0.48357	0.14956	0.05013	0.24121	0.26792	0.38662	0.45090	0.51643	0.04156*	0.32518
	cc.bodyp (Corpus call. body parietal)	0.05013	0.11342	0.11342	0.09778	0.41847	0.19223	0.05013	0.38662	0.24121	0.51643	0.05992	0.21598	0.05992	0.48357	0.24121	0.05013	0.05013
	cc.bodypf (Corpus call. body prefrontal)	0.26792	0.07111	0.13071	0.41847	0.21598	0.48357	0.19223	0.41847	0.38662	0.48357	0.45090	0.29590	0.07111	0.45090	0.29590	0.11342	0.51643
	cc.bodypm (Corpus call. body premotor)	0.05013	0.11342	0.11342	0.09778	0.41847	0.19223	0.05013	0.38662	0.24121	0.51643	0.05992	0.21598	0.05992	0.48357	0.24121	0.05013	0.05013
	cc.bodyt (Corpus call. body temporal)	0.04156*	0.51643	0.32518	0.21598	0.19223	0.03417*	0.05992	0.13071	0.01105*	0.48357	0.00131**	0.09778	0.11342	0.24121	0.32518	0.45090	0.41847
	cc.genu (Corpus call. genu)	0.26792	0.14956	0.11342	0.45090	0.21598	0.19223	0.29590	0.35542	0.29590	0.45090	0.38662	0.51643	0.11342	0.17012	0.45090	0.51643	0.08367
	cc.rostrum (Corpus call. rostrum)	0.41847	0.14956	0.13071	0.17012	0.35542	0.26792	0.38662	0.48357	0.13071	0.45090	0.08367	0.13071	0.41847	0.45090	0.26792	0.19223	0.26792
	cc.splenium (Corpus call. splenium)	0.08367	0.38662	0.48357	0.11342	0.41847	0.00649**	0.14956	0.01105*	0.00359**	0.32518	0.00038***	0.17012	0.26792	0.41847	0.19223	0.09778	0.32518
	mcp (Middle cerebellar peduncle)	0.45090	0.26792	0.17012	0.17012	0.17012	0.26792	0.24121	0.35542	0.11342	0.26792	0.19223	0.45090	0.05013	0.02782*	0.17012	0.03417*	0.32518
	lh.af (Arcuate fasciculus)	0.11342	0.26792	0.38662	0.35542	0.51643	0.03417*	0.48357	0.32518	0.48357	0.32518	0.21598	0.19223	0.45090	0.38662	0.26792	0.29590	0.05013
	rh.af (Arcuate fasciculus)	0.13071	0.19223	0.21598	0.19223	0.48357	0.32518	0.29590	0.19223	0.29590	0.45090	0.05992	0.08367	0.14956	0.45090	0.45090	0.11342	0.35542
	lh.ar (Acoustic radiation)	0.19223	0.09778	0.17012	0.01792*	0.26792	0.29590	0.35542	0.24121	0.48357	0.19223	0.19223	0.19223	0.02247*	0.19223	0.14956	0.45090	0.51643
	rh.ar (Acoustic radiation)	0.19223	0.29590	0.26792	0.45090	0.51643	0.41847	0.48357	0.38662	0.48357	0.32518	0.26792	0.45090	0.41847	0.29590	0.19223	0.38662	0.00262**
	lh.atr (Ant. thalamic radiations)	0.41847	0.07111	0.05992	0.21598	0.29590	0.29590	0.21598	0.24121	0.41847	0.48357	0.45090	0.29590	0.05992	0.38662	0.11342	0.21598	0.32518
	rh.atr (Ant. thalamic radiations)	0.07111	0.07111	0.13071	0.19223	0.11342	0.35542	0.41847	0.13071	0.48357	0.41847	0.26792	0.24121	0.14956	0.48357	0.24121	0.05992	0.35542
	lh.cbd (Cingulum bundle dorsal)	0.35542	0.26792	0.35542	0.35542	0.35542	0.35542	0.21598	0.09778	0.11342	0.05013	0.08367	0.24121	0.02247*	0.35542	0.48357	0.45090	0.48357
	rh.cbd (Cingulum bundle dorsal)	0.32518	0.14956	0.21598	0.45090	0.32518	0.26792	0.45090	0.51643	0.48357	0.29590	0.14956	0.24121	0.19223	0.45090	0.29590	0.24121	0.07111
	lh.cbv (Cingulum bundle ventral)	0.05013	0.38662	0.41847	0.13071	0.38662	0.35542	0.35542	0.41847	0.38662	0.41847	0.24121	0.09778	0.41847	0.38662	0.29590	0.41847	0.26792
	rh.cbv (Cingulum bundle ventral)	nan	nan	nan	nan	nan	nan	nan	nan	nan	nan	nan	nan	nan	nan	nan	nan	nan
	lh.cst (Corticospinal tract)	0.05210	0.50000	0.50000	0.14272	0.43005	0.50000	0.36212	0.18747	0.08956	0.14272	0.05210	0.10546	0.03463*	0.29808	0.16415	0.43005	0.10546
	rh.cst (Corticospinal tract)	0.02778*	0.14272	0.26801	0.08956	0.36212	0.12315	0.08956	0.46490	0.05210	0.07545	0.02206*	0.03463*	0.14272	0.21258	0.50000	0.39571	0.21258
	lh.emc (Extreme capsule)	0.12315	0.08956	0.08956	0.46490	0.39571	0.32950	0.43005	0.07545	0.29808	0.50000	0.21258	0.29808	0.08956	0.43005	0.36212	0.29808	0.29808
	rh.emc (Extreme capsule)	0.16415	0.16415	0.14272	0.21258	0.23947	0.06297	0.29808	0.21258	0.36212	0.16415	0.36212	0.43005	0.23947	0.32950	0.21258	0.36212	0.12315
	lh.fat (Frontal aslant tract)	0.01728*	0.23947	0.26801	0.23947	0.36212	0.12315	0.36212	0.29808	0.16415	0.46490	0.16415	0.43005	0.29808	0.46490	0.32950	0.26801	0.29808
	rh.fat (Frontal aslant tract)	0.14272	0.14272	0.07545	0.18747	0.46490	0.36212	0.43005	0.18747	0.21258	0.46490	0.36212	0.10546	0.18747	0.46490	0.00569**	0.50000	0.18747
	lh.fx (Fornix)	0.39571	0.50000	0.32950	0.21258	0.26801	0.02206*	0.06297	0.07545	0.00060***	0.50000	0.00770**	0.21258	0.14272	0.36212	0.04267*	0.16415	0.14272
	rh.fx (Fornix)	0.21258	0.26801	0.29808	0.26801	0.39571	0.50000	0.02206*	0.46490	0.10546	0.43005	0.32950	0.32950	0.05210	0.46490	0.29808	0.21258	0.39571
	lh.ilf (Inf. longi. fasci.)	0.10546	0.29808	0.16415	0.46490	0.32950	0.26801	0.29808	0.43005	0.43005	0.29808	0.16415	0.50000	0.36212	0.23947	0.46490	0.43005	0.32950
	rh.ilf (Inf. longi. fasci.)	0.39571	0.29808	0.23947	0.46490	0.18747	0.16415	0.36212	0.06297	0.32950	0.26801	0.21258	0.50000	0.50000	0.12315	0.18747	0.14272	0.08956
	lh.mlf (Middle longi. fasci.)	0.32950	0.18747	0.21258	0.39571	0.39571	0.05210	0.26801	0.46490	0.43005	0.23947	0.10546	0.21258	0.06297	0.12315	0.29808	0.39571	0.43005
	rh.mlf (Middle longi. fasci.)	0.02206*	0.29808	0.32950	0.01339*	0.26801	0.01339*	0.06297	0.00569**	0.10546	0.46490	0.00770**	0.00569**	0.46490	0.46490	0.12315	0.36212	0.06297
	lh.or (Optic radiation)	0.36212	0.04267*	0.05210	0.32950	0.50000	0.43005	0.50000	0.29808	0.26801	0.29808	0.01021*	0.18747	0.46490	0.36212	0.23947	0.43005	0.46490
	rh.or (Optic radiation)	0.10546	0.50000	0.50000	0.16415	0.23947	0.12315	0.32950	0.06297	0.29808	0.50000	0.05210	0.26801	0.06297	0.39571	0.43005	0.23947	0.01021*
	lh.slf1 (Sup. longi. fasci. I)	0.18747	0.21258	0.18747	0.46490	0.32950	0.29808	0.39571	0.04267*	0.12315	0.32950	0.32950	0.26801	0.29808	0.50000	0.32950	0.50000	0.26801
	rh.slf1 (Sup. longi. fasci. I)	0.05210	0.39571	0.29808	0.00207**	0.21258	0.50000	0.39571	0.01339*	0.26801	0.36212	0.50000	0.00770**	0.21258	0.36212	0.00207**	0.07545	0.32950
	lh.slf2 (Sup. longi. fasci. II)	0.29808	0.26801	0.29808	0.32950	0.39571	0.18747	0.46490	0.50000	0.26801	0.43005	0.14272	0.14272	0.29808	0.39571	0.08956	0.26801	0.18747
	rh.slf2 (Sup. longi. fasci. II)	0.06297	0.06297	0.05210	0.05210	0.36212	0.43005	0.26801	0.10546	0.39571	0.36212	0.12315	0.04267*	0.46490	0.43005	0.36212	0.50000	0.14272
	lh.slf3 (Sup. longi. fasci. III)	0.50000	0.50000	0.50000	0.14272	0.32950	0.43005	0.50000	0.14272	0.29808	0.46490	0.14272	0.01728*	0.16415	0.23947	0.21258	0.50000	0.39571
	rh.slf3 (Sup. longi. fasci. III)	0.36212	0.07545	0.07545	0.26801	0.50000	0.46490	0.39571	0.08956	0.50000	0.21258	0.36212	0.03463*	0.29808	0.50000	0.43005	0.50000	0.14272
	lh.uf (Uncinate fasciculus)	0.01339*	0.50000	0.46490	0.46490	0.43005	0.43005	0.46490	0.10546	0.02778*	0.32950	0.00569**	0.18747	0.04267*	0.39571	0.18747	0.18747	0.46490
	rh.uf (Uncinate fasciculus)	0.16415	0.39571	0.32950	0.50000	0.43005	0.26801	0.26801	0.39571	0.43005	0.18747	0.16415	0.26801	0.16415	0.32950	0.23947	0.18747	0.16415

Table C.3: Table of Mann-Whitney U rank test p-values of **SKEWNESS** of the distribution of metrics. As rows all the extracted ROI, as columns the models metrics. Highlighted in yellow are the TRACULA regions where the p-values are computed without considering the patient `VNSLC_16`. In red the values computed with `alternative = "less"` (the distribution of non-responder subjects is stochastic *less* than the distribution of responder subjects), in green the values computed with `alternative = "greater"` (the distribution of non-responder subjects is stochastic *greater* than the distribution of responder subjects), the rest is computed with `alternative = "two-sided"` and non-statistical significant.

		MF			DIAMOND				NODDI					DTI			
	Region	frac_ftot	fvf_tot	wfvf	frac_ctot	wFA	wMD	wRD	wAD	icvf	fintra	fextra	fiso	odi	FA	MD	RD	AD
tckgen() by MRtrix3	left-thalamus	0.35542	0.41847	0.29590	0.35542	0.09778	0.05992	0.29590	0.13071	0.01417*	0.21598	0.17012	0.38662	0.00649**	0.38662	0.04156*	0.07111	0.17012
	right-thalamus	0.51643	0.24121	0.38662	0.45090	0.02247*	0.01792*	0.01792*	0.04156*	0.01417*	0.45090	0.13071	0.24121	0.38662	0.26792	0.19223	0.14956	0.21598
	left-hippocampus	0.38662	0.41847	0.17012	0.38662	0.35542	0.14956	0.35542	0.19223	0.24121	0.03417*	0.35542	0.35542	0.35542	0.32518	0.51643	0.48357	0.24121
	right-hippocampus	0.41847	0.14956	0.35542	0.14956	0.29590	0.29590	0.29590	0.38662	0.26792	0.01417*	0.48357	0.38662	0.07111	0.14956	0.13071	0.51643	0.38662
	left-amygdala	0.48357	0.05992	0.02782*	0.24121	0.26792	0.05992	0.02247*	0.29590	0.51643	0.14956	0.21598	0.32518	0.48357	0.45090	0.35542	0.51643	0.41847
	right-amygdala	0.48357	0.48357	0.48357	0.38662	0.24121	0.21598	0.41847	0.41847	0.48357	0.24121	0.35542	0.21598	0.01105*	0.38662	0.48357	0.07111	0.01417*
	left-accumbens	0.35542	0.38662	0.41847	0.29590	0.26792	0.26792	0.51643	0.09778	0.19223	0.14956	0.17012	0.24121	0.09778	0.41847	0.17012	0.04156*	0.41847
	right-accumbens	0.05013	0.07111	0.14956	0.19223	0.35542	0.48357	0.51643	0.19223	0.11342	0.07111	0.21598	0.38662	0.03417*	0.26792	0.45090	0.38662	0.26792
	left-putamen	0.21598	0.26792	0.29590	0.14956	0.19223	0.38662	0.29590	0.48357	0.07111	0.48357	0.17012	0.09778	0.19223	0.24121	0.21598	0.02782*	0.05013
	right-putamen	0.11342	0.45090	0.26792	0.41847	0.02782*	0.17012	0.07111	0.09778	0.21598	0.05992	0.32518	0.38662	0.00262**	0.05013	0.45090	0.05992	0.48357
	left-pallidum	0.35542	0.24121	0.14956	0.41847	0.38662	0.13071	0.38662	0.21598	0.26792	0.29590	0.24121	0.35542	0.21598	0.26792	0.14956	0.13071	0.45090
	right-pallidum	0.45090	0.01792*	0.05992	0.38662	0.26792	0.08367	0.48357	0.07111	0.32518	0.38662	0.13071	0.41847	0.21598	0.14956	0.05013	0.24121	0.09778
	left-antThalRadiation	0.17012	0.26792	0.26792	0.21598	0.13071	0.29590	0.26792	0.24121	0.26792	0.38662	0.17012	0.24121	0.45090	0.09778	0.45090	0.45090	0.32518
	right-antThalRadiation	0.45090	0.32518	0.51643	0.21598	0.00262**	0.26792	0.24121	0.48357	0.45090	0.41847	0.29590	0.45090	0.21598	0.38662	0.21598	0.05013	0.48357
	left-postThalRadiation-parital	0.35542	0.09778	0.07111	0.41847	0.45090	0.26792	0.38662	0.45090	0.19223	0.08367	0.48357	0.29590	0.05992	0.48357	0.24121	0.24121	0.32518
	right-postThalRadiation-parital	0.17012	0.00359**	0.00187**	0.17012	0.24121	0.14956	0.09778	0.51643	0.45090	0.38662	0.51643	0.51643	0.45090	0.13071	0.03417*	0.29590	0.38662
	left-postThalRadiation-occipital	0.45090	0.26792	0.11342	0.48357	0.45090	0.21598	0.32518	0.48357	0.51643	0.21598	0.29590	0.26792	0.05013	0.45090	0.07111	0.32518	0.24121
	right-postThalRadiation-occipital	0.24121	0.02247*	0.03417*	0.21598	0.41847	0.09778	0.41847	0.51643	0.41847	0.32518	0.17012	0.45090	0.01417*	0.26792	0.08367	0.48357	0.29590
	left-supThalRadiation	0.19223	0.45090	0.32518	0.24121	0.26792	0.09778	0.41847	0.09778	0.29590	0.09778	0.38662	0.32518	0.08367	0.08367	0.41847	0.24121	0.21598
	right-supThalRadiation	0.19223	0.00649**	0.00853**	0.41847	0.11342	0.32518	0.24121	0.11342	0.17012	0.35542	0.29590	0.41847	0.24121	0.32518	0.11342	0.45090	0.38662
	left-infThalRadiation-insula	0.19223	0.51643	0.32518	0.19223	0.07111	0.35542	0.04156*	0.38662	0.26792	0.51643	0.41847	0.29590	0.05013	0.07111	0.35542	0.19223	0.14956
	right-infThalRadiation-insula	0.11342	0.45090	0.35542	0.45090	0.29590	0.11342	0.35542	0.21598	0.13071	0.48357	0.26792	0.32518	0.13071	0.32518	0.35542	0.51643	0.26792
	left-sup-longi-fasci	0.11342	0.04156*	0.03417*	0.14956	0.41847	0.01417*	0.41847	0.38662	0.26792	0.26792	0.24121	0.07111	0.26792	0.45090	0.13071	0.17012	0.19223
	right-sup-longi-fasci	0.08367	0.00187**	0.00187**	0.14956	0.48357	0.02782*	0.14956	0.35542	0.00853**	0.04156*	0.01417*	0.04156*	0.19223	0.45090	0.02782*	0.24121	0.48357
	left-inf-longi-fasci	0.08367	0.14956	0.32518	0.38662	0.24121	0.21598	0.38662	0.24121	0.45090	0.24121	0.09778	0.26792	0.05013	0.13071	0.17012	0.38662	0.48357
	right-inf-longi-fasci	0.08367	0.14956	0.19223	0.51643	0.08367	0.13071	0.08367	0.14956	0.35542	0.07111	0.45090	0.14956	0.01105*	0.03417*	0.48357	0.35542	0.48357
	left-fornix	0.05013	0.51643	0.38662	0.05992	0.05992	0.01417*	0.21598	0.00853**	0.05992	0.09778	0.05992	0.02247*	0.03417*	0.51643	0.02247*	0.19223	0.26792
	right-fornix	0.24121	0.24121	0.26792	0.24121	0.48357	0.14956	0.13071	0.21598	0.14956	0.41847	0.17012	0.45090	0.14956	0.35542	0.26792	0.45090	0.41847
TRACULA by Freesurfer	acomm (Anterior commissure)	0.38662	0.13071	0.45090	0.45090	0.35542	0.01792*	0.45090	0.17012	0.00131**	0.11342	0.00488**	0.35542	0.19223	0.26792	0.01105*	0.09778	0.14956
	cc.bodyc (Corpus call. body central)	0.09778	0.05992	0.17012	0.41847	0.35542	0.26792	0.11342	0.17012	0.35542	0.02782*	0.26792	0.41847	0.45090	0.51643	0.35542	0.13071	0.45090
	cc.bodyp (Corpus call. body parietal)	0.05013	0.02782*	0.32518	0.51643	0.26792	0.00649**	0.04156*	0.02782*	0.02782*	0.19223	0.07111	0.38662	0.05992	0.41847	0.41847	0.11342	0.21598
	cc.bodypf (Corpus call. body prefrontal)	0.35542	0.17012	0.41847	0.45090	0.19223	0.35542	0.21598	0.45090	0.32518	0.32518	0.41847	0.17012	0.01417*	0.29590	0.29590	0.08367	0.38662
	cc.bodypm (Corpus call. body premotor)	0.05013	0.02782*	0.32518	0.51643	0.26792	0.00649**	0.04156*	0.02782*	0.02782*	0.19223	0.07111	0.38662	0.05992	0.41847	0.41847	0.11342	0.21598
	cc.bodyt (Corpus call. body temporal)	0.04156*	0.01792*	0.14956	0.51643	0.21598	0.01417*	0.13071	0.24121	0.00131**	0.48357	0.19223	0.48357	0.17012	0.19223	0.19223	0.41847	0.32518
	cc.genu (Corpus call. genu)	0.48357	0.29590	0.32518	0.19223	0.14956	0.14956	0.38662	0.21598	0.03417*	0.17012	0.45090	0.48357	0.04156*	0.17012	0.29590	0.45090	0.24121
	cc.rostrum (Corpus call. rostrum)	0.45090	0.41847	0.41847	0.05013	0.32518	0.45090	0.32518	0.24121	0.03417*	0.41847	0.14956	0.11342	0.41847	0.32518	0.32518	0.24121	0.35542
	cc.splenium (Corpus call. splenium)	0.05992	0.32518	0.45090	0.38662	0.35542	0.24121	0.29590	0.32518	0.00359**	0.35542	0.04156*	0.45090	0.21598	0.32518	0.17012	0.19223	0.21598
	mcp (Middle cerebellar peduncle)	0.45090	0.19223	0.21598	0.07111	0.14956	0.08367	0.26792	0.24121	0.35542	0.29590	0.21598	0.29590	0.21598	0.09778	0.21598	0.05992	0.14956
	lh.af (Arcuate fasciculus)	0.38662	0.35542	0.26792	0.48357	0.38662	0.08367	0.38662	0.41847	0.07111	0.19223	0.17012	0.11342	0.32518	0.21598	0.29590	0.24121	0.11342
	rh.af (Arcuate fasciculus)	0.26792	0.01417*	0.00187**	0.24121	0.32518	0.02782*	0.14956	0.19223	0.51643	0.48357	0.48357	0.32518	0.14956	0.29590	0.41847	0.19223	0.48357
	lh.ar (Acoustic radiation)	0.24121	0.13071	0.21598	0.00488**	0.38662	0.00262**	0.51643	0.00359**	0.05013	0.26792	0.35542	0.09778	0.03417*	0.35542	0.26792	0.45090	0.29590
	rh.ar (Acoustic radiation)	0.19223	0.38662	0.48357	0.08367	0.48357	0.04156*	0.41847	0.41847	0.45090	0.45090	0.24121	0.41847	0.48357	0.41847	0.14956	0.32518	0.13071
	lh.atr (Ant. thalamic radiations)	0.41847	0.45090	0.21598	0.05013	0.17012	0.17012	0.14956	0.35542	0.21598	0.38662	0.17012	0.14956	0.04156*	0.45090	0.26792	0.48357	0.38662
	rh.atr (Ant. thalamic radiations)	0.05013	0.19223	0.32518	0.11342	0.13071	0.24121	0.29590	0.05992	0.45090	0.35542	0.48357	0.45090	0.14956	0.45090	0.41847	0.41847	0.21598
	lh.cbd (Cingulum bundle dorsal)	0.38662	0.32518	0.38662	0.35542	0.45090	0.21598	0.35542	0.13071	0.32518	0.24121	0.26792	0.35542	0.11342	0.24121	0.51643	0.41847	0.51643
	rh.cbd (Cingulum bundle dorsal)	0.17012	0.01417*	0.00853**	0.48357	0.29590	0.26792	0.41847	0.41847	0.32518	0.21598	0.45090	0.41847	0.24121	0.32518	0.29590	0.32518	0.11342
	lh.cbv (Cingulum bundle ventral)	0.08367	0.35542	0.26792	0.08367	0.29590	0.02782*	0.45090	0.08367	0.24121	0.48357	0.41847	0.17012	0.35542	0.26792	0.26792	0.45090	0.41847
	rh.cbv (Cingulum bundle ventral)	nan	nan	nan	nan	nan	nan	nan	nan	nan	nan	nan	nan	nan	nan	nan	nan	nan
	lh.cst (Corticospinal tract)	0.16415	0.05210	0.03463*	0.18747	0.29808	0.16415	0.18747	0.29808	0.14272	0.46490	0.43005	0.08956	0.02778*	0.46490	0.18747	0.08956	0.50000
	rh.cst (Corticospinal tract)	0.10546	0.14272	0.23947	0.16415	0.39571	0.46490	0.10546	0.02778*	0.29808	0.23947	0.29808	0.07545	0.07545	0.32950	0.43005	0.29808	0.02778*
	lh.emc (Extreme capsule)	0.26801	0.26801	0.21258	0.29808	0.43005	0.14272	0.36212	0.26801	0.10546	0.32950	0.21258	0.36212	0.14272	0.43005	0.14272	0.18747	0.26801
	rh.emc (Extreme capsule)	0.18747	0.14272	0.32950	0.18747	0.14272	0.23947	0.10546	0.39571	0.26801	0.39571	0.21258	0.36212	0.14272	0.26801	0.50000	0.46490	0.23947
	lh.fat (Frontal aslant tract)	0.02778*	0.50000	0.43005	0.36212	0.21258	0.02206*	0.14272	0.21258	0.06297	0.39571	0.21258	0.29808	0.36212	0.29808	0.21258	0.50000	0.46490
	rh.fat (Frontal aslant tract)	0.36212	0.05210	0.07545	0.26801	0.46490	0.07545	0.36212	0.36212	0.04267*	0.29808	0.16415	0.36212	0.07545	0.07545	0.03463*	0.46490	0.10546
	lh.fx (Fornix)	0.39571	0.36212	0.08956	0.18747	0.36212	0.16415	0.26801	0.32950	0.01021*	0.43005	0.23947	0.12315	0.05210	0.32950	0.18747	0.36212	0.10546
	rh.fx (Fornix)	0.12315	0.50000	0.29808	0.18747	0.12315	0.23947	0.12315	0.10546	0.02778*	0.14272	0.21258	0.18747	0.16415	0.23947	0.18747	0.36212	0.10546
	lh.ilf (Inf. longi. fasci.)	0.18747	0.18747	0.32950	0.43005	0.32950	0.46490	0.26801	0.10546	0.29808	0.18747	0.43005	0.50000	0.07545	0.16415	0.43005	0.29808	0.18747
	rh.ilf (Inf. longi. fasci.)	0.46490	0.21258	0.43005	0.46490	0.16415	0.12315	0.32950	0.16415	0.32950	0.12315	0.43005	0.39571	0.46490	0.29808	0.26801	0.16415	0.06297
	lh.mlf (Middle longi. fasci.)	0.43005	0.05210	0.06297	0.21258	0.39571	0.43005	0.39571	0.46490	0.36212	0.16415	0.26801	0.50000	0.21258	0.16415	0.10546	0.46490	0.50000
	rh.mlf (Middle longi. fasci.)	0.06297	0.21258	0.23947	0.01728*	0.32950	0.00569**	0.06297	0.50000	0.10546	0.50000	0.18747	0.01728*	0.39571	0.46490	0.08956	0.39571	0.01021*
	lh.or (Optic radiation)	0.43005	0.06297	0.08956	0.43005	0.50000	0.50000	0.32950	0.21258	0.05210	0.23947	0.08956	0.29808	0.16415	0.32950	0.43005	0.23947	0.26801
	rh.or (Optic radiation)	0.06297	0.10546	0.05210	0.43005	0.14272	0.03463*	0.36212	0.06297	0.14272	0.36212	0.36212	0.50000	0.02206*	0.10546	0.26801	0.21258	0.01728*
	lh.slf1 (Sup. longi. fasci. I)	0.23947	0.39571	0.50000	0.29808	0.39571	0.01021*	0.46490	0.12315	0.01728*	0.29808	0.00770**	0.36212	0.32950	0.46490	0.39571	0.46490	0.46490
	rh.slf1 (Sup. longi. fasci. I)	0.07545	0.14272	0.18747	0.00207**	0.23947	0.01021*	0.46490	0.32950	0.02778*	0.05210	0.02778*	0.01021*	0.36212	0.46490	0.00060***	0.04267*	0.46490
	lh.slf2 (Sup. longi. fasci. II)	0.23947	0.23947	0.21258	0.29808	0.46490	0.26801	0.50000	0.50000	0.36212	0.10546	0.46490	0.16415	0.16415	0.32950	0.16415	0.29808	0.21258
	rh.slf2 (Sup. longi. fasci. II)	0.05210	0.00415**	0.00207**	0.07545	0.23947	0.00569**	0.14272	0.26801	0.39571	0.50000	0.46490	0.18747	0.39571	0.10546	0.50000	0.26801	0.12315
	lh.slf3 (Sup. longi. fasci. III)	0.50000	0.36212	0.32950	0.46490	0.43005	0.32950	0.39571	0.02778*	0.18747	0.07545	0.32950	0.23947	0.08956	0.14272	0.21258	0.39571	0.18747
	rh.slf3 (Sup. longi. fasci. III)	0.23947	0.00415**	0.00415**	0.39571	0.46490	0.21258	0.29808	0.32950	0.43005	0.39571	0.50000	0.46490	0.43005	0.43005	0.12315	0.50000	0.08956
	lh.uf (Uncinate fasciculus)	0.05210	0.05210	0.03463*	0.46490	0.46490	0.04267*	0.43005	0.32950	0.03463*	0.36212	0.05210	0.32950	0.06297	0.46490	0.21258	0.18747	0.29808
	rh.uf (Uncinate fasciculus)	0.43005	0.43005	0.32950	0.50000	0.32950	0.32950	0.29808	0.50000	0.26801	0.23947	0.23947	0.46490	0.07545	0.12315	0.29808	0.23947	0.39571

Table C.4: Table of Mann-Whitney U rank test p-values of **KURTOSIS** of the distribution of metrics. As rows all the extracted ROI, as columns the models metrics. Highlighted in yellow are the TRACULA regions where the p-values are computed without considering the patient `VNSLC_16`. In red the values computed with `alternative = "less"` (the distribution of non-responder subjects is stochastic *less* than the distribution of responder subjects), in green the values computed with `alternative = "greater"` (the distribution of non-responder subjects is stochastic *greater* than the distribution of responder subjects), the rest is computed with `alternative = "two-sided"` and non-statistical significant.

		MF			DIAMOND				NODDI					DTI			
	Region	frac_ftot	fvf_tot	wfvf	frac_ctot	wFA	wMD	wRD	wAD	icvf	fintra	fextra	fiso	odi	FA	MD	RD	AD
tckgen() by MRtrix3	left-thalamus	0.52951	0.94517	0.88084	0.65512	0.76286	0.89966	0.98018	0.69235	0.03503*	0.33868	0.09067	0.96837	0.10328	0.69235	0.02853*	0.03180*	0.01929*
	right-thalamus	0.51002	0.83513	0.90961	0.46353	0.37528	0.70994	0.93457	0.14871	0.02721*	0.12876	0.07112	0.79987	0.02529*	0.31253	0.01802*	0.03155*	0.01160*
	left-hippocampus	0.42629	0.96265	0.90552	0.83725	0.67748	0.80394	0.84508	0.65790	0.10021	0.08849	0.15841	0.82390	0.71194	0.64741	0.02672*	0.00889**	0.08247
	right-hippocampus	0.12912	0.91812	0.87935	0.25691	0.36578	0.38536	0.32973	0.37160	0.35043	0.06878	0.69783	0.62852	0.81512	0.40726	0.11922	0.19627	0.18830
	left-amygdala	0.79807	0.51261	0.68690	0.34407	0.07017	0.27529	0.12525	0.35671	0.13989	0.05463	0.19205	0.63190	0.72470	0.08920	0.05441	0.05694	0.05980
	right-amygdala	0.66293	0.93299	0.96973	0.69411	0.59122	0.23205	0.27552	0.32465	0.22835	0.18260	0.35863	0.91450	0.74817	0.58393	0.26673	0.28597	0.27258
	left-accumbens	0.69235	0.69607	0.83513	0.96265	0.51002	0.10705	0.54434	0.04413*	0.01811*	0.15357	0.03179*	0.58393	0.46353	0.45217	0.05732	0.03503*	0.02959*
	right-accumbens	0.75112	0.59945	0.59945	0.85877	0.82576	0.40852	0.59945	0.20730	0.06766	0.21982	0.11192	0.94384	0.27770	0.64232	0.06878	0.08296	0.03708*
	left-putamen	0.15108	0.72470	0.74817	0.14171	0.86241	0.54650	0.70994	0.83890	0.12218	0.25403	0.18162	0.44849	0.35531	0.94570	0.03631*	0.07112	0.00724**
	right-putamen	0.17707	0.15778	0.22263	0.22439	0.99382	0.24648	0.40726	0.29150	0.02853*	0.05441	0.04031*	0.87935	0.23277	0.29456	0.01717*	0.01822*	0.02471*
	left-pallidum	0.25909	0.58856	0.53809	0.26426	0.70994	0.73127	0.75622	0.87589	0.18830	0.14960	0.20035	0.69411	0.67234	0.68112	0.10617	0.10047	0.22439
	right-pallidum	0.07053	0.78579	0.83020	0.64741	0.21066	0.75836	0.42449	0.79807	0.11627	0.15078	0.12483	0.83372	0.92305	0.21066	0.09067	0.04361*	0.52951
	left-antThalRadiation	0.14960	0.42629	0.29522	0.36116	0.52386	0.55176	0.68690	0.46497	0.05463	0.12912	0.08259	0.59945	0.02539*	0.72124	0.04230*	0.13989	0.03180*
	right-antThalRadiation	0.02268*	0.36764	0.31253	0.23949	0.60625	0.29456	0.50260	0.05888	0.05260	0.02731*	0.09232	0.51566	0.02474*	0.54434	0.02471*	0.03045*	0.01984*
	left-postThalRadiation-parital	0.23614	0.66293	0.56387	0.21269	0.18162	0.69783	0.51566	0.70356	0.05980	0.25439	0.04581*	0.48642	0.82576	0.54650	0.07228	0.40726	0.12706
	right-postThalRadiation-parital	0.21443	0.21269	0.24767	0.64613	0.51002	0.35601	0.46353	0.20216	0.05537	0.23902	0.10328	0.83725	0.08797	0.92019	0.04880*	0.22835	0.02474*
	left-postThalRadiation-occipital	0.13646	0.87589	0.92305	0.33140	0.78269	0.44773	0.35043	0.87219	0.03006*	0.11023	0.02484*	0.21871	0.78601	0.68112	0.05537	0.17742	0.27113
	right-postThalRadiation-occipital	0.05537	0.89158	0.90961	0.35601	0.87416	0.11922	0.62746	0.37013	0.02841*	0.03466*	0.03247*	0.88557	0.41961	0.89966	0.03655*	0.04880*	0.05616
	left-supThalRadiation	0.30702	0.72450	0.72124	0.24214	0.82576	0.81512	0.77741	0.83513	0.15361	0.44508	0.09850	0.99578	0.25317	0.50260	0.29456	0.62605	0.23929
	right-supThalRadiation	0.10702	0.53566	0.54312	0.52431	0.80803	0.59122	0.76588	0.46379	0.11620	0.16623	0.13781	0.92019	0.38612	0.83372	0.05067	0.21522	0.10675
	left-infThalRadiation-insula	0.76286	0.38126	0.34107	0.94811	0.45755	0.44433	0.27716	0.59945	0.03006*	0.25154	0.01940*	0.83301	0.25691	0.50260	0.06315	0.02959*	0.12706
	right-infThalRadiation-insula	0.36249	0.83513	0.77741	0.34407	0.96483	0.30702	0.91450	0.20579	0.01998*	0.08298	0.02579*	0.20176	0.28093	0.66050	0.02549*	0.07610	0.02499*
	left-sup-longi-fasci	0.21269	0.78247	0.71698	0.05198	0.48070	0.50260	0.64741	0.74817	0.11451	0.63853	0.06486	0.02841*	0.80803	0.71194	0.26568	0.46379	0.45833
	right-sup-longi-fasci	0.18931	0.74817	0.74817	0.14028	0.44508	0.74438	0.74880	0.99578	0.18830	0.73127	0.12814	0.03373*	0.64577	0.51189	0.18830	0.28597	0.35063
	left-inf-longi-fasci	0.17853	0.78247	0.78247	0.87687	0.70994	0.31876	0.69783	0.35053	0.17430	0.17853	0.13646	0.21871	0.42629	0.98517	0.11922	0.39975	0.07070
	right-inf-longi-fasci	0.10287	0.86241	0.92305	0.78601	0.17464	0.39161	0.29807	0.25561	0.06504	0.10287	0.04180*	0.19461	0.14171	0.20216	0.05928	0.08374	0.23211
	left-fornix	0.54388	0.65790	0.75836	0.96483	0.79515	0.85877	0.90552	0.91218	0.05138	0.31314	0.14495	0.90552	0.35863	0.74438	0.00636**	0.00705**	0.04423*
	right-fornix	0.71194	0.73479	0.41608	0.85635	0.42187	0.86241	0.96265	0.77741	0.03503*	0.10723	0.33868	0.93299	0.19086	0.47303	0.00547**	0.00415**	0.02529*
TRACULA by Freesurfer	acomm (Anterior commissure)	0.83372	0.80803	0.78579	0.93457	0.83725	0.45833	0.66199	0.41060	0.01207*	0.14171	0.01998*	0.41961	0.12706	0.91812	0.00971**	0.09067	0.01361*
	cc.bodyc (Corpus call. body central)	0.17022	0.77741	0.77282	0.44735	0.38612	0.92905	0.77522	0.71054	0.08574	0.43125	0.18830	0.31253	0.24420	0.65346	0.09601	0.40054	0.12218
	cc.bodyp (Corpus call. body parietal)	0.05830	0.82390	0.90552	0.75836	0.33497	0.50501	0.54850	0.89158	0.09601	0.08259	0.11620	0.75112	0.21269	0.65790	0.04581*	0.17568	0.08298
	cc.bodypf (Corpus call. body prefrontal)	0.26411	0.53778	0.49402	0.24767	0.99578	0.93299	0.64577	0.39426	0.07930	0.17742	0.17298	0.37191	0.43651	0.84199	0.02807*	0.57059	0.02842*
	cc.bodypm (Corpus call. body premotor)	0.05830	0.82390	0.90552	0.75836	0.33497	0.50501	0.54850	0.89158	0.09601	0.08259	0.11620	0.75112	0.21269	0.65790	0.04581*	0.17568	0.08298
	cc.bodyt (Corpus call. body temporal)	0.07557	0.81512	0.78579	0.49139	0.44773	0.19627	0.42449	0.44433	0.01487*	0.05028	0.01861*	0.71194	0.59440	0.79987	0.03230*	0.07017	0.08259
	cc.genu (Corpus call. genu)	0.70994	0.27059	0.23461	0.73127	0.52742	0.68458	0.71698	0.68112	0.06905	0.43125	0.11268	0.66686	0.35863	0.52742	0.03012*	0.17298	0.05003
	cc.rostrum (Corpus call. rostrum)	0.87935	0.42282	0.32328	0.66686	0.86241	0.92905	0.88208	0.93299	0.11451	0.48848	0.11788	0.19314	0.66199	0.78247	0.05676	0.31921	0.09968
	cc.splenium (Corpus call. splenium)	0.05957	0.97659	0.96483	0.72470	0.48642	0.28300	0.47504	0.60505	0.06878	0.17657	0.05339	0.68112	0.50118	0.52386	0.14638	0.23211	0.05138
	mcp (Middle cerebellar peduncle)	0.08659	0.27716	0.30651	0.20216	0.91398	0.94811	0.58081	0.75112	0.68112	0.21443	0.57852	0.50118	0.54542	0.71194	0.49528	0.79358	0.40726
	lh.af (Arcuate fasciculus)	0.24767	0.75772	0.62605	0.27770	0.74438	0.67748	0.58393	0.88557	0.13961	0.23205	0.08462	0.33094	0.62235	0.71194	0.19627	0.62235	0.27529
	rh.af (Arcuate fasciculus)	0.05980	0.61903	0.61903	0.34494	0.90552	0.90552	0.92905	0.88084	0.15108	0.07017	0.19627	0.45833	0.87416	0.69921	0.14871	0.17568	0.49528
	lh.ar (Acoustic radiation)	0.59793	0.65790	0.72124	0.69235	0.80803	0.33497	0.60505	0.22439	0.04581*	0.59440	0.08797	0.55316	0.34155	0.98018	0.11627	0.40726	0.08920
	rh.ar (Acoustic radiation)	0.51566	0.42955	0.60539	0.75836	0.79807	0.11451	0.41421	0.25793	0.01727*	0.23929	0.09563	0.70356	0.88432	0.79987	0.05015	0.11192	0.15361
	lh.atr (Ant. thalamic radiations)	0.20579	0.41281	0.31921	0.21871	0.62746	0.64577	0.71698	0.21173	0.05260	0.21066	0.04650*	0.38126	0.12119	0.81835	0.06753	0.11815	0.01929*
	rh.atr (Ant. thalamic radiations)	0.11023	0.27552	0.19627	0.27474	0.37160	0.58624	0.48151	0.27529	0.04627*	0.10112	0.06878	0.51261	0.17707	0.77282	0.01087*	0.04392*	0.00999**
	lh.cbd (Cingulum bundle dorsal)	0.30807	0.72124	0.69411	0.95454	0.53809	0.46079	0.57852	0.53809	0.04102*	0.48848	0.08259	0.44508	0.52594	0.72470	0.07070	0.34494	0.21871
	rh.cbd (Cingulum bundle dorsal)	0.19086	0.83372	0.80485	0.65790	0.51189	0.72593	0.87219	0.68826	0.14155	0.28093	0.23949	0.19461	0.86241	0.83513	0.12500	0.53793	0.21522
	lh.cbv (Cingulum bundle ventral)	0.09371	0.86655	0.74480	0.10995	0.56022	0.97549	0.69411	0.44849	0.08374	0.32917	0.06065	0.75772	0.72470	0.66517	0.07557	0.15488	0.40933
	rh.cbv (Cingulum bundle ventral)	nan	nan	nan	nan	nan	nan	nan	nan	nan	nan	nan	nan	nan	nan	nan	nan	nan
	lh.cst (Corticospinal tract)	0.42199	0.63016	0.55143	0.58123	0.88554	0.93165	0.88554	0.94576	0.66255	0.74352	0.66255	0.55040	0.62977	0.85127	0.34081	0.48314	0.52579
	rh.cst (Corticospinal tract)	0.40110	0.66923	0.59898	0.72149	0.42067	0.99875	0.79358	0.48314	0.63333	0.73933	0.63016	0.72511	0.24298	0.30772	0.48314	0.73748	0.24977
	lh.emc (Extreme capsule)	0.28117	0.86417	0.86851	0.28117	0.91258	0.47355	0.74352	0.27404	0.06126	0.39216	0.03572*	0.33488	0.44675	0.97464	0.07224	0.22327	0.08789
	rh.emc (Extreme capsule)	0.24558	0.56260	0.56260	0.36650	0.80157	0.46183	0.72511	0.09637	0.18734	0.29322	0.17586	0.94754	0.27404	0.67555	0.02704*	0.37229	0.04028*
	lh.fat (Frontal aslant tract)	0.16528	0.63333	0.68966	0.09006	0.62076	0.50544	0.97647	0.50544	0.27559	0.63333	0.14682	0.14951	0.36857	0.45952	0.45694	0.63611	0.27559
	rh.fat (Frontal aslant tract)	0.04151*	0.80712	0.67555	0.18923	0.43026	0.79110	0.79110	0.68966	0.42199	0.23357	0.36650	0.03440*	0.31851	0.38149	0.20853	0.32741	0.20853
	lh.fx (Fornix)	0.88554	0.60539	0.68923	0.90859	0.76622	0.41752	0.23357	0.36857	0.13390	0.68065	0.03440*	0.66048	0.14876	0.75478	0.04335*	0.02248*	0.04144*
	rh.fx (Fornix)	0.50386	0.78517	0.80712	0.68065	0.83020	0.94576	0.63333	0.98879	0.05736	0.24977	0.42067	0.90348	0.85127	0.57579	0.01275*	0.02258*	0.05736
	lh.ilf (Inf. longi. fasci.)	0.22879	0.67555	0.65553	0.70143	0.88333	0.14876	0.68966	0.09103	0.10234	0.12483	0.08528	0.74352	0.06031	0.95051	0.08459	0.36650	0.03786*
	rh.ilf (Inf. longi. fasci.)	0.07985	0.86417	0.86417	0.39216	0.54218	0.63333	0.63333	0.16363	0.13661	0.15475	0.23357	0.76766	0.34017	0.45952	0.09469	0.57543	0.15130
	lh.mlf (Middle longi. fasci.)	0.42199	0.63333	0.59898	0.56827	0.88333	0.48314	0.58123	0.36193	0.04228*	0.23343	0.03786*	0.48893	0.32741	0.85931	0.07224	0.27404	0.10370
	rh.mlf (Middle longi. fasci.)	0.09637	0.81525	0.80712	0.35922	0.83020	0.09856	0.52612	0.30772	0.03510*	0.04825*	0.04376*	0.13825	0.50544	0.97647	0.03755*	0.17818	0.06138
	lh.or (Optic radiation)	0.15331	0.86851	0.72511	0.83020	0.86851	0.32741	0.68966	0.33677	0.04467*	0.20286	0.04467*	0.22822	0.29322	0.90859	0.05542	0.37229	0.10527
	rh.or (Optic radiation)	0.21024	0.87726	0.76622	0.29322	0.78517	0.75857	0.96916	0.33071	0.03530*	0.17064	0.24298	0.66923	0.30161	0.72511	0.03408*	0.17586	0.04604*
	lh.slf1 (Sup. longi. fasci. I)	0.20286	0.57869	0.67937	0.50544	0.81525	0.85931	0.80157	0.98940	0.40744	0.76622	0.30772	0.35586	0.20286	0.67555	0.31851	0.85127	0.24977
	rh.slf1 (Sup. longi. fasci. I)	0.07906	0.67937	0.67937	0.02561*	0.70011	0.77783	0.75857	0.93165	0.76766	0.52876	0.74352	0.02208*	0.67555	0.91258	0.83020	0.90348	0.74352
	lh.slf2 (Sup. longi. fasci. II)	0.13661	0.95051	0.95051	0.27976	0.62076	0.63016	0.67937	0.72511	0.16435	0.36857	0.12166	0.17064	0.57869	0.62076	0.29322	0.73748	0.27559
	rh.slf2 (Sup. longi. fasci. II)	0.12166	0.81525	0.75478	0.68923	0.90859	0.85127	0.95051	0.76766	0.11872	0.25547	0.11695	0.15563	0.90348	0.76766	0.24481	0.46971	0.60236
	lh.slf3 (Sup. longi. fasci. III)	0.21994	0.80712	0.80712	0.32741	0.94576	0.83020	0.79110	0.97647	0.29322	0.63611	0.19599	0.36857	0.76622	0.67555	0.72149	0.48314	0.73933
	rh.slf3 (Sup. longi. fasci. III)	0.08229	0.81525	0.62076	0.36857	0.94044	0.90348	0.96916	0.68065	0.17818	0.07134	0.16435	0.24977	0.94576	0.88554	0.12538	0.32741	0.41752
	lh.uf (Uncinate fasciculus)	0.63333	0.86417	0.86417	0.41752	0.87726	0.24298	0.52579	0.57869	0.03786*	0.30772	0.01189*	0.25999	0.48314	0.99875	0.02932*	0.13585	0.17987
	rh.uf (Uncinate fasciculus)	0.87726	0.63333	0.56827	0.87726	0.98879	0.83856	0.97464	0.42067	0.09931	0.48314	0.07676	0.46183	0.27559	0.98940	0.03135*	0.40744	0.04335*

Table C.5: Table of Kruskal-Wallis H-test p-values of **MEANS** of the distribution of metrics. As rows, all the extracted ROI, as columns, the models' metrics. The TRACULA regions highlighted in yellow where the p-values are calculated without considering the patient `VNSLC_16`. In blue the statistically significant values.

		MF			DIAMOND					NODDI				DTI			
	Region	frac_ftot	fvf_tot	wfvf	frac_ctot	wFA	wMD	wRD	wAD	icvf	fintra	fextra	fiso	odi	FA	MD	RD	AD
tckgen() by MRtrix3	left-thalamus	0.64741	0.42955	0.23205	0.97659	0.65790	0.81835	0.58393	0.56690	0.48848	0.91398	0.54388	0.91038	0.21299	0.74480	0.01128*	0.01713*	0.16921
	right-thalamus	0.99382	0.42187	0.63871	0.91218	0.69411	0.96973	0.25909	0.43725	0.67748	0.69783	0.44735	0.78734	0.17568	0.84508	0.09563	0.05015	0.08750
	left-hippocampus	0.40852	0.46575	0.72593	0.87416	0.75772	0.75836	0.95535	0.58393	0.78093	0.59272	0.83301	0.86655	0.33497	0.86655	0.37013	0.40726	0.54542
	right-hippocampus	0.10328	0.57300	0.47303	0.40933	0.46628	0.30651	0.35053	0.26389	0.53566	0.10555	0.33075	0.56022	0.77282	0.98517	0.08296	0.20176	0.15488
	left-amygdala	0.82390	0.38126	0.18734	0.42282	0.58624	0.48070	0.83301	0.35231	0.52386	0.27059	0.48848	0.68458	0.26389	0.59945	0.24427	0.71698	0.43725
	right-amygdala	0.63871	0.26426	0.48848	0.58081	0.88084	0.81512	0.77282	0.63190	0.87589	0.77522	0.98600	0.95535	0.74880	0.45833	0.35601	0.62852	0.07395
	left-accumbens	0.49139	0.07912	0.10600	0.56022	0.01877*	0.85635	0.07576	0.36764	0.11558	0.25489	0.24648	0.33075	0.14308	0.15488	0.38809	0.31253	0.44508
	right-accumbens	0.75622	0.65346	0.83513	0.90961	0.84199	0.77522	0.84199	0.27113	0.46628	0.48848	0.71054	0.84508	0.88432	0.68826	0.98018	0.89158	0.44609
	left-putamen	0.00558**	0.70356	0.31253	0.03912*	0.96483	0.42955	0.19314	0.97549	0.34407	0.53778	0.24503	0.23048	0.31438	0.87935	0.38536	0.40726	0.23205
	right-putamen	0.10328	0.03155*	0.29456	0.20216	0.00594**	0.59440	0.78734	0.83301	0.65790	0.63871	0.86655	0.40726	0.01559*	0.02751*	0.44849	0.48151	0.63190
	left-pallidum	0.03155*	0.03740*	0.08296	0.10995	0.79807	0.23574	0.46353	0.64577	0.02319*	0.65790	0.01253*	0.05982	0.79515	0.77043	0.58624	0.07861	0.91218
	right-pallidum	0.11380	0.40933	0.55645	0.18420	0.80394	0.71698	0.91398	0.74880	0.37181	0.94811	0.16446	0.00673**	0.41060	0.84199	0.83067	0.03129*	0.89966
	left-antThalRadiation	0.15361	0.83725	0.56690	0.54388	0.53566	0.96265	0.95454	0.48070	0.36116	0.57059	0.14680	0.39661	0.49528	0.44508	0.18260	0.00295**	0.55176
	right-antThalRadiation	0.03373*	0.52386	0.62746	0.38169	0.18830	0.76286	0.60779	0.81835	0.10021	0.24648	0.03995*	0.16921	0.01531*	0.80803	0.01087*	0.00999**	0.19627
	left-postThalRadiation-parital	0.03466*	0.53809	0.67082	0.77043	0.19086	0.74438	0.72450	0.87416	0.74817	0.30651	0.73127	0.74501	0.18260	0.11192	0.29807	0.07395	0.54113
	right-postThalRadiation-parital	0.01207*	0.49139	0.48070	0.48848	0.44609	0.90501	0.55316	0.74438	0.73790	0.44433	0.19627	0.52951	0.93457	0.21723	0.26411	0.01041*	0.29807
	left-postThalRadiation-occipital	0.31438	0.45859	0.27113	0.35541	0.38612	0.89158	0.87416	0.88208	0.88432	0.43725	0.96973	0.55645	0.79987	0.13527	0.71054	0.08659	0.68458
	right-postThalRadiation-occipital	0.10702	0.66050	0.63190	0.49528	0.56690	0.93457	0.74501	0.66293	0.94570	0.69783	0.69941	0.65790	0.51002	0.59272	0.92905	0.08937	0.27552
	left-supThalRadiation	0.48848	0.88557	0.74438	0.97549	0.46353	0.35231	0.61503	0.60505	0.91450	0.44508	0.97549	0.85877	0.58081	0.61903	0.56022	0.13894	0.43725
	right-supThalRadiation	0.07708	0.51261	0.60505	0.18734	0.78247	0.80803	0.57869	0.25317	0.87416	0.16921	0.51204	0.18734	0.73790	0.36578	0.22835	0.04699*	0.22835
	left-infThalRadiation-insula	0.37328	0.25554	0.34407	0.69607	0.77282	0.40485	0.59945	0.96837	0.83513	0.98517	0.78734	0.66293	0.72450	0.37013	0.19627	0.05830	0.30807
	right-infThalRadiation-insula	0.62852	0.62746	0.58393	0.85877	0.99382	0.31438	0.67748	0.62605	0.74501	0.17390	0.60199	0.92905	0.81283	0.45217	0.44773	0.08659	0.32465
	left-sup-longi-fasci	0.34155	0.80485	0.73127	0.88557	0.80394	0.64577	0.83513	0.17657	0.96265	0.11023	0.97659	0.75112	0.79515	0.68690	0.52951	0.18162	0.87219
	right-sup-longi-fasci	0.02554*	0.15886	0.18899	0.69411	0.31831	0.81512	0.72124	0.21269	0.88432	0.35231	0.94384	0.78247	0.55176	0.28556	0.49528	0.14638	0.97549
	left-inf-longi-fasci	0.25909	0.70994	0.60779	0.22263	0.07017	0.80803	0.91812	0.17390	0.29648	0.87935	0.44849	0.20532	0.00290**	0.02035*	0.39161	0.08849	0.10209
	right-inf-longi-fasci	0.32917	0.68458	0.48848	0.41772	0.12775	0.91450	0.58393	0.50887	0.34407	0.30772	0.53566	0.57869	0.00201**	0.10209	0.60779	0.11023	0.30341
	left-fornix	0.20216	0.79987	0.33497	0.56690	0.75622	0.21443	0.66517	0.39661	0.02350*	0.91450	0.07228	0.13961	0.60199	0.85877	0.08849	0.23574	0.12814
	right-fornix	0.74880	0.78734	0.33497	0.62605	0.92019	0.52431	0.70356	0.48314	0.18420	0.34155	0.47611	0.94811	0.84199	0.40726	0.03810*	0.15886	0.07395
TRACULA by Freesurfer	acomm (Anterior commissure)	0.81512	0.37181	0.46209	0.83020	0.40485	0.90961	0.64577	0.88557	0.30651	0.35231	0.41421	0.83513	0.33075	0.96483	0.55176	0.23277	0.67748
	cc.bodyc (Corpus call. body central)	0.04674*	0.87589	0.88084	0.46353	0.47504	0.94517	0.60199	0.78247	0.60199	0.07228	0.77282	0.51261	0.41421	0.96973	0.01107*	0.05537	0.18420
	cc.bodyp (Corpus call. body parietal)	0.09432	0.66293	0.56022	0.39773	0.21443	0.94198	0.54603	0.39161	0.58624	0.39661	0.88084	0.36178	0.08364	0.19314	0.01207*	0.04094*	0.17853
	cc.bodypf (Corpus call. body prefrontal)	0.87687	0.65346	0.40933	0.88084	0.94198	0.60539	0.87416	0.65790	0.44508	0.48642	0.71698	0.77522	0.38612	0.20532	0.10705	0.51002	0.09962
	cc.bodypm (Corpus call. body premotor)	0.09432	0.66293	0.56022	0.39773	0.21443	0.94198	0.54603	0.39161	0.58624	0.39661	0.88084	0.36178	0.08364	0.19314	0.01207*	0.04094*	0.17853
	cc.bodyt (Corpus call. body temporal)	0.26673	0.92019	0.87687	0.25561	0.43125	0.48848	0.96265	0.24214	0.87589	0.20730	0.70994	0.29060	0.37013	0.50118	0.10047	0.10600	0.10702
	cc.genu (Corpus call. genu)	0.31332	0.92305	0.84199	0.62852	0.16358	0.83890	0.48314	0.68112	0.58624	0.55176	0.84508	0.97549	0.47303	0.38612	0.20865	0.14219	0.08780
	cc.rostrum (Corpus call. rostrum)	0.19760	0.83372	0.82576	0.99382	0.36578	0.91812	0.48848	0.44508	0.33075	0.31607	0.32704	0.86241	0.23205	0.06244	0.46079	0.21269	0.15778
	cc.splenium (Corpus call. splenium)	0.09563	0.90961	0.77522	0.09962	0.10995	0.61053	0.66050	0.07395	0.87219	0.23461	0.62746	0.08825	0.03898*	0.91812	0.51261	0.27113	0.05694
	mcp (Middle cerebellar peduncle)	0.68112	0.87416	0.71054	0.91450	0.57852	0.46497	0.83725	0.69607	0.94198	0.98018	0.92905	0.64232	0.74480	0.29208	0.56690	0.77522	0.83513
	lh.af (Arcuate fasciculus)	0.54542	0.14155	0.20216	0.33497	0.24214	0.96973	0.52951	0.66293	0.70994	0.96265	0.87935	0.69411	0.95535	0.68458	0.38612	0.46575	0.30651
	rh.af (Arcuate fasciculus)	0.64577	0.02554*	0.03223*	0.87589	0.13527	0.87416	0.60505	0.41772	0.52951	0.78601	0.69921	0.88557	0.37328	0.54542	0.72593	0.59945	0.52386
	lh.ar (Acoustic radiation)	0.66686	0.21173	0.15841	0.21963	0.86655	0.59272	0.80394	0.81512	0.48848	0.83372	0.62235	0.69607	0.31921	0.98018	0.90552	0.54113	0.64522
	rh.ar (Acoustic radiation)	0.73479	0.22732	0.37486	0.61053	0.51189	0.66686	0.78579	0.53566	0.94570	0.81283	0.64577	0.68690	0.10555	0.68690	0.30651	0.11620	0.25403
	lh.atr (Ant. thalamic radiations)	0.00258**	0.99382	0.94198	0.99410	0.37013	0.83067	0.99410	0.70994	0.57869	0.49892	0.37013	0.78093	0.24767	0.51204	0.18734	0.01727*	0.73479
	rh.atr (Ant. thalamic radiations)	0.11473	0.58393	0.26411	0.45833	0.66686	0.89158	0.71194	0.90961	0.47504	0.69783	0.36178	0.36178	0.78269	0.58393	0.05281	0.00421**	0.35251
	lh.cbd (Cingulum bundle dorsal)	0.39975	0.69941	0.73479	0.60199	0.98517	0.62852	0.83301	0.66517	0.92905	0.26568	0.96483	0.69411	0.96265	0.77522	0.54388	0.32898	0.35371
	rh.cbd (Cingulum bundle dorsal)	0.26411	0.99382	0.98323	0.89158	0.74880	0.58081	0.70356	0.83890	0.92905	0.48314	0.83372	0.83301	0.59440	0.83725	0.58081	0.30102	0.54388
	lh.cbv (Cingulum bundle ventral)	0.23153	0.60199	0.53566	0.49626	0.32328	0.87416	0.65346	0.98323	0.82576	0.27552	0.88208	0.54388	0.75836	0.83020	0.25691	0.53793	0.59945
	rh.cbv (Cingulum bundle ventral)	nan	nan	nan	nan	nan	nan	nan	nan	nan	nan	nan	nan	nan	nan	nan	nan	nan
	lh.cst (Corticospinal tract)	0.84014	0.29991	0.32192	0.68065	0.69617	0.63333	0.30772	0.57543	0.96673	0.91258	0.86851	0.40744	0.07950	0.66048	0.76622	0.97647	0.67937
	rh.cst (Corticospinal tract)	0.55040	0.40744	0.32741	0.69617	0.20401	0.59337	0.22822	0.94576	0.91258	0.97647	0.85127	0.72511	0.36673	0.97464	0.91258	0.95051	0.68923
	lh.emc (Extreme capsule)	0.34081	0.78517	0.70011	0.91258	0.99875	0.68065	0.88554	0.48314	0.15130	0.50291	0.38365	0.38365	0.85931	0.79110	0.06345	0.02460*	0.22879
	rh.emc (Extreme capsule)	0.38149	0.11521	0.13018	0.48314	0.95051	0.56260	0.63611	0.81525	0.56401	0.17291	0.75857	0.63333	0.83020	0.79358	0.24481	0.13390	0.40110
	lh.fat (Frontal aslant tract)	0.02063*	0.56260	0.56827	0.06870	0.24070	0.31851	0.41752	0.74352	0.34081	0.83020	0.25547	0.14220	0.51924	0.91774	0.73748	0.80712	0.42624
	rh.fat (Frontal aslant tract)	0.94754	0.88554	0.79110	0.46648	0.48527	0.46971	0.73748	0.24298	0.56260	0.60539	0.69617	0.48527	0.36650	0.57869	0.98940	0.51924	0.91258
	lh.fx (Fornix)	0.96916	0.63333	0.19685	0.51924	0.97464	0.86851	0.80712	0.97647	0.15331	0.68065	0.06126	0.76622	0.77783	0.63016	0.11895	0.24977	0.07600
	rh.fx (Fornix)	0.79358	0.95051	0.80712	0.88333	0.88554	0.31851	0.84014	0.24298	0.91258	0.28400	0.14220	0.68065	0.84014	0.80157	0.09006	0.32516	0.04028*
	lh.ilf (Inf. longi. fasci.)	0.97647	0.37229	0.40110	0.85931	0.63016	0.33677	0.40110	0.05038	0.36857	0.72511	0.68966	0.88333	0.73748	0.85931	0.12993	0.17807	0.07338
	rh.ilf (Inf. longi. fasci.)	0.99875	0.49540	0.32091	0.14008	0.63333	0.83020	0.79110	0.39537	0.26877	0.13018	0.27976	0.27559	0.41361	0.23475	0.55143	0.45952	0.08152
	lh.mlf (Middle longi. fasci.)	0.76766	0.49540	0.42199	0.19501	0.52579	0.36857	0.32192	0.98940	0.20286	0.36673	0.26877	0.32741	0.87726	0.85931	0.17807	0.10686	0.59337
	rh.mlf (Middle longi. fasci.)	0.46971	0.85931	0.70143	0.19685	0.34017	0.91947	0.76766	0.73933	0.41752	0.19834	0.16068	0.17064	0.08701	0.77783	0.08459	0.11895	0.40110
	lh.or (Optic radiation)	0.91258	0.23357	0.12166	0.79110	0.80914	0.37793	0.68923	0.33071	0.75431	0.68923	0.83856	0.95051	0.78517	0.75431	0.23578	0.63016	0.41752
	rh.or (Optic radiation)	0.47089	0.72511	0.52612	0.28454	0.87726	0.68923	0.56260	0.31140	0.98879	0.56827	0.62192	0.37229	0.54218	0.73933	0.36857	0.68065	0.08701
	lh.slf1 (Sup. longi. fasci. I)	0.04673*	0.21329	0.37793	0.87726	0.06453	0.73748	0.58452	0.40110	0.06138	0.09258	0.19102	0.68065	0.09475	0.28454	0.10468	0.20401	0.21544
	rh.slf1 (Sup. longi. fasci. I)	0.10686	0.58452	0.75478	0.50544	0.30772	0.77783	0.76622	0.78517	0.27559	0.05542	0.27404	0.72511	0.11695	0.45694	0.19054	0.12483	0.87726
	lh.slf2 (Sup. longi. fasci. II)	0.93165	0.22822	0.20503	0.77783	0.30772	0.97464	0.77783	0.97464	0.99438	0.51827	0.99875	0.61572	0.88554	0.36857	0.72511	0.73933	0.60236
	rh.slf2 (Sup. longi. fasci. II)	0.09006	0.04028*	0.05124	0.69617	0.63333	0.83020	0.91947	0.32516	0.59898	0.06035	0.80157	0.56827	0.73933	0.52612	0.25950	0.73933	0.88554
	lh.slf3 (Sup. longi. fasci. III)	0.38365	0.69617	0.73748	0.78517	0.91947	0.55873	0.75431	0.86851	0.68966	0.96673	0.95051	0.98940	0.44340	0.59898	0.95051	0.91774	0.52579
	rh.slf3 (Sup. longi. fasci. III)	0.27559	0.06870	0.13585	0.94754	0.99438	0.69617	0.95051	0.91947	0.88333	0.90859	0.98940	0.97647	0.72511	0.79110	0.80157	0.42199	0.88554
	lh.uf (Uncinate fasciculus)	0.36673	0.68065	0.77783	0.85931	0.94044	0.83020	0.78517	0.83856	0.15331	0.74352	0.18734	0.73748	0.67555	0.68923	0.60539	0.14682	0.17064
	rh.uf (Uncinate fasciculus)	0.62076	0.40110	0.44591	0.94576	0.72149	0.97647	0.91947	0.59898	0.45952	0.63016	0.59898	0.72511	0.52579	0.95051	0.25950	0.46971	0.20905

Table C.6: Table of Kruskal-Wallis H-test p-values of **STANDARD DEVIATIONS** of the distribution of metrics. As rows, all the extracted ROI, as columns, the models' metrics. The TRACULA regions highlighted in yellow where the p-values are calculated without considering the patient `VNSLC_16`. In blue the statistically significant values.

		MF			DIAMOND				NODDI					DTI			
	Region	frac_ftot	fvf_tot	wfvf	frac_ctot	wFA	wMD	wRD	wAD	icvf	fintra	fextra	fiso	odi	FA	MD	RD	AD
tckgen() by MRtrix3	left-thalamus	0.83301	0.17494	0.48848	0.62605	0.55176	0.25793	0.70994	0.91398	0.02721*	0.08002	0.15913	0.96265	0.08849	0.78247	0.23929	0.56690	0.72450
	right-thalamus	0.66293	0.14219	0.55316	0.27983	0.07401	0.04581*	0.64522	0.21871	0.04031*	0.22181	0.45833	0.65790	0.44609	0.17390	0.17390	0.48848	0.77741
	left-hippocampus	0.50801	0.75772	0.41608	0.94570	0.46379	0.49626	0.70994	0.62605	0.78601	0.08832	0.92305	0.59272	0.55645	0.78601	0.01953*	0.31447	0.15501
	right-hippocampus	0.27778	0.43125	0.68112	0.33497	0.60539	0.26673	0.28995	0.14960	0.23048	0.31253	0.83301	0.99382	0.68112	0.39426	0.04804*	0.12119	0.30102
	left-amygdala	0.38536	0.25154	0.05980	0.59122	0.48642	0.18830	0.27097	0.33140	0.50260	0.88208	0.26329	0.75836	0.54542	0.96483	0.73479	0.27770	0.30341
	right-amygdala	0.59945	0.91450	0.94570	0.94198	0.50501	0.31253	0.17568	0.50501	0.21963	0.93299	0.35601	0.69235	0.77741	0.81835	0.15078	0.08374	0.66050
	left-accumbens	0.75772	0.79515	0.68112	0.69783	0.85635	0.14495	0.17568	0.22777	0.49892	0.72450	0.56690	0.74438	0.70994	0.80803	0.71054	0.58856	0.99410
	right-accumbens	0.19627	0.31607	0.40933	0.69235	0.84199	0.83513	0.88084	0.41281	0.21480	0.74817	0.50260	0.87219	0.49892	0.71054	0.32649	0.70994	0.32704
	left-putamen	0.74438	0.32963	0.38374	0.54850	0.65790	0.10558	0.64613	0.83372	0.43725	0.94384	0.12500	0.21871	0.48601	0.43125	0.29456	0.37486	0.19086
	right-putamen	0.40054	0.32898	0.87935	0.98600	0.99410	0.73790	0.17707	0.41608	0.41421	0.75836	0.10109	0.98323	0.38126	0.33356	0.09601	0.73790	0.92019
	left-pallidum	0.84460	0.64577	0.58081	0.38374	0.63853	0.23277	0.46209	0.81512	0.22131	0.43125	0.31314	0.98517	0.99410	0.49528	0.75622	0.83890	0.98517
	right-pallidum	0.98517	0.19086	0.21871	0.90501	0.62235	0.76588	0.21522	0.72450	0.59440	0.43028	0.36178	0.82576	0.69235	0.14495	0.45859	0.31921	0.56022
	left-antThalRadiation	0.77282	0.19450	0.44433	0.13781	0.40235	0.29208	0.07112	0.77043	0.60539	0.66293	0.09834	0.28428	1.00000	0.74817	0.03342*	0.04526*	0.34494
	right-antThalRadiation	0.32963	0.30702	0.31438	0.35541	0.05980	0.01690*	0.77282	0.17464	0.09563	0.03355*	0.90961	0.20313	0.83725	0.73479	0.08233	0.03012*	0.81835
	left-postThalRadiation-parital	0.77741	0.79987	0.54113	0.98517	0.29208	0.70994	0.60199	0.25489	0.44508	0.79987	0.44773	0.54650	0.12304	0.77043	0.19086	0.35601	0.61903
	right-postThalRadiation-parital	0.92305	0.70994	0.68826	0.49528	0.27529	0.30341	0.20176	0.53809	0.11192	0.56387	0.62746	0.74438	0.83020	0.83020	0.07357	0.18830	0.59793
	left-postThalRadiation-occipital	0.61903	0.26389	0.36116	0.18162	0.96265	0.44034	0.75772	0.45833	0.78269	0.22263	0.30807	0.23461	0.49139	0.94570	0.51566	0.91812	0.21982
	right-postThalRadiation-occipital	0.50887	0.77741	0.60539	0.39238	0.96265	0.58624	0.87935	0.25439	0.83513	0.56181	0.77043	0.45755	0.26673	0.85877	0.35531	0.72450	0.96483
	left-supThalRadiation	0.96265	0.12343	0.19577	0.14417	0.74438	0.58393	0.42282	0.39661	0.59945	0.40485	0.91398	0.16202	0.37181	0.64577	0.32465	0.40726	0.05092
	right-supThalRadiation	0.73127	0.53809	0.36116	0.03695*	0.68826	0.22131	0.31921	0.14495	0.52594	0.10995	0.59440	0.01313*	0.74480	0.70994	0.37013	0.83372	0.37486
	left-infThalRadiation-insula	0.37328	0.37191	0.47210	0.79807	0.16460	0.53809	0.31253	0.94384	0.25317	0.33356	0.17853	0.90961	0.13894	0.33075	0.80485	0.90552	0.10555
	right-infThalRadiation-insula	0.13402	0.27552	0.33497	0.40565	0.96265	0.71054	0.96973	0.77043	0.15361	0.25317	0.05015	0.42798	0.49528	0.08247	0.54650	0.96265	0.73479
	left-sup-longi-fasci	0.78734	0.50501	0.34494	0.18162	0.81835	0.18734	0.68690	0.35601	0.75772	0.52951	0.14417	0.09968	0.61157	0.78093	0.06787	0.49626	0.48314
	right-sup-longi-fasci	0.47504	0.35231	0.30102	0.17707	0.98018	0.82390	0.32328	0.44773	0.96973	0.78579	0.21723	0.04756*	0.28995	0.77741	0.15002	0.53793	0.68458
	left-inf-longi-fasci	0.46209	0.24767	0.40933	0.80394	0.85635	0.87589	0.79807	0.44034	0.31253	0.98323	0.65790	0.46209	0.43028	0.90501	0.48273	0.86241	0.62605
	right-inf-longi-fasci	0.22181	0.41961	0.42032	0.71054	0.38428	0.88557	0.29807	0.90961	0.68690	0.40933	0.84199	0.40726	0.39426	0.39773	0.30341	0.65790	0.93457
	left-fornix	0.73127	0.94570	0.75112	0.75836	0.91398	0.92019	0.48314	0.94198	0.03466*	0.40726	0.34155	0.58081	0.20216	0.88208	0.90552	0.34494	0.44773
	right-fornix	0.66293	0.54388	0.50189	0.97659	0.55316	0.80394	0.35251	0.86241	0.03631*	0.88432	0.45859	0.83372	0.63853	0.37486	0.48083	0.83890	0.13781
TRACULA by Freesurfer	acomm (Anterior commissure)	0.77043	0.83513	0.97659	0.80803	0.82576	0.17430	0.78734	0.68112	0.01998*	0.42750	0.01219*	0.54542	0.92905	0.66293	0.28597	0.68826	0.10287
	cc.bodyc (Corpus call. body central)	0.13989	0.27716	0.37013	0.90961	0.60539	0.48642	0.36178	0.46575	0.24427	0.12735	0.19760	0.79358	0.26426	0.86655	0.94811	0.20216	0.85877
	cc.bodyp (Corpus call. body parietal)	0.18420	0.44508	0.42449	0.09962	0.47303	0.18162	0.22977	0.44146	0.64577	0.18065	0.16446	0.69921	0.22777	0.57300	0.73127	0.22131	0.23902
	cc.bodypf (Corpus call. body prefrontal)	0.78734	0.31253	0.49626	0.35601	0.69783	0.63871	0.34494	0.83513	0.94198	0.40485	0.75772	0.42798	0.29807	0.86655	0.81283	0.30651	0.21963
	cc.bodypm (Corpus call. body premotor)	0.18420	0.44508	0.42449	0.09962	0.47303	0.18162	0.22977	0.44146	0.64577	0.18065	0.16446	0.69921	0.22777	0.57300	0.73127	0.22131	0.23902
	cc.bodyt (Corpus call. body temporal)	0.14171	0.61903	0.60199	0.69235	0.63853	0.11768	0.27258	0.41060	0.07017	0.78579	0.01584*	0.33140	0.33497	0.70994	0.83372	0.91038	0.88084
	cc.genu (Corpus call. genu)	0.78269	0.42032	0.24767	0.50260	0.67082	0.37328	0.37497	0.80394	0.75112	0.98323	0.15944	0.86241	0.30651	0.59793	0.58856	0.61903	0.25909
	cc.rostrum (Corpus call. rostrum)	0.72450	0.53793	0.44433	0.29208	0.91218	0.65790	0.74480	0.98600	0.45859	0.86655	0.13777	0.19205	0.72450	0.91038	0.03798*	0.21480	0.01610*
	cc.splenium (Corpus call. splenium)	0.13777	0.78093	0.84199	0.09834	0.66293	0.03503*	0.35053	0.01087*	0.02672*	0.79987	0.00579**	0.21982	0.52742	0.78247	0.62235	0.38809	0.02904*
	mcp (Middle cerebellar peduncle)	0.46079	0.42282	0.29208	0.54388	0.56690	0.71194	0.68112	0.88557	0.36178	0.47504	0.41608	0.46079	0.18899	0.10995	0.51566	0.09051	0.79987
	lh.af (Arcuate fasciculus)	0.38612	0.19776	0.36526	0.22732	0.86241	0.00847**	0.16821	0.54434	0.98600	0.37486	0.41772	0.10227	0.52386	0.79807	0.62746	0.78601	0.17430
	rh.af (Arcuate fasciculus)	0.26389	0.60779	0.67082	0.45833	0.98600	0.19314	0.59272	0.37328	0.83067	0.65346	0.21723	0.20486	0.51204	0.92305	0.63190	0.40726	0.66517
	lh.ar (Acoustic radiation)	0.59945	0.23048	0.33075	0.10389	0.67234	0.80485	0.54603	0.51261	0.70356	0.63853	0.47210	0.59945	0.11023	0.51189	0.50501	0.56690	0.61903
	rh.ar (Acoustic radiation)	0.64869	0.37497	0.42282	0.95454	0.80803	0.91812	0.70356	0.87219	0.40485	0.60199	0.30772	0.65346	0.88084	0.75112	0.54850	0.66686	0.02554*
	lh.atr (Ant. thalamic radiations)	0.14219	0.30702	0.26673	0.07651	0.75112	0.37497	0.19577	0.74880	0.04224*	0.93299	0.02687*	0.04379*	0.08162	0.68690	0.09834	0.09563	0.79987
	rh.atr (Ant. thalamic radiations)	0.23521	0.30702	0.47611	0.41608	0.33497	0.54603	0.91812	0.46497	0.98600	0.04224*	0.12536	0.07011	0.22219	0.92019	0.05500	0.02382*	0.66517
	lh.cbd (Cingulum bundle dorsal)	0.64577	0.42282	0.54603	0.10001	0.54603	0.06179	0.69783	0.17903	0.05281	0.22439	0.02211*	0.05500	0.10328	0.40852	0.95535	0.94517	0.98018
	rh.cbd (Cingulum bundle dorsal)	0.87935	0.38612	0.49402	0.02687*	0.87935	0.13432	0.97549	0.26389	0.40485	0.82576	0.11268	0.04264*	0.58081	0.95454	0.80485	0.56022	0.21522
	lh.cbv (Cingulum bundle ventral)	0.20250	0.83020	0.83513	0.38169	0.60539	0.72124	0.66517	0.72450	0.79807	0.41281	0.56022	0.29150	0.78247	0.50189	0.10665	0.59945	0.62746
	rh.cbv (Cingulum bundle ventral)	nan	nan	nan	nan	nan	nan	nan	nan	nan	nan	nan	nan	nan	nan	nan	nan	nan
	lh.cst (Corticospinal tract)	0.24070	0.44591	0.44591	0.42624	0.68923	0.96673	0.50291	0.63611	0.36650	0.45694	0.24558	0.32192	0.07120	0.83020	0.57869	0.94576	0.26343
	rh.cst (Corticospinal tract)	0.09856	0.24481	0.25999	0.36857	0.63333	0.45952	0.23052	0.97647	0.24481	0.31851	0.12258	0.14536	0.39537	0.63333	0.99875	0.95051	0.56260
	lh.emc (Extreme capsule)	0.02932*	0.36857	0.36857	0.98879	0.90348	0.79110	0.81525	0.29322	0.80914	0.58452	0.08459	0.57869	0.17118	0.97464	0.13661	0.84014	0.68966
	rh.emc (Extreme capsule)	0.55040	0.57869	0.51924	0.55873	0.70143	0.27404	0.72511	0.32516	0.80712	0.34017	0.42199	0.95051	0.70143	0.79110	0.42199	0.69617	0.20853
	lh.fat (Frontal aslant tract)	0.00970**	0.58452	0.60539	0.62977	0.91774	0.09856	0.63333	0.83020	0.09564	0.27976	0.07600	0.30907	0.80157	0.97464	0.07338	0.30772	0.29322
	rh.fat (Frontal aslant tract)	0.42919	0.52579	0.32741	0.46183	0.33488	0.75478	0.95051	0.63333	0.66255	0.74352	0.80712	0.37229	0.32741	0.27976	0.04228*	0.58452	0.40110
	lh.fx (Fornix)	0.94754	0.42199	0.68923	0.66048	0.73748	0.12538	0.17586	0.31851	0.00770**	0.03363*	0.05192	0.67937	0.35922	0.50291	0.20905	0.29916	0.14876
	rh.fx (Fornix)	0.68966	0.60539	0.63611	0.75431	0.91774	0.90348	0.11116	0.97464	0.32192	0.21063	0.85931	0.85931	0.22822	0.59898	0.67555	0.19501	0.78517
	lh.ilf (Inf. longi. fasci.)	0.30907	0.38558	0.29916	0.46648	0.56827	0.78517	0.82553	0.55143	0.97464	0.80914	0.57869	0.97647	0.67937	0.69617	0.98879	0.21063	0.44340
	rh.ilf (Inf. longi. fasci.)	0.39611	0.62076	0.37793	0.53509	0.63333	0.48314	0.90859	0.25999	0.56827	0.52612	0.68065	0.79110	0.99875	0.44675	0.24298	0.14876	0.32741
	lh.mlf (Middle longi. fasci.)	0.63016	0.48893	0.63333	0.17291	0.90348	0.07296	0.52612	0.53509	0.96916	0.43026	0.39216	0.32516	0.27148	0.23475	0.83020	0.13825	0.91258
	rh.mlf (Middle longi. fasci.)	0.12136	0.50291	0.63016	0.08046	0.79358	0.06138	0.28400	0.04376*	0.42199	0.86417	0.03863*	0.04467*	0.98879	0.86417	0.46971	0.42199	0.23357
	lh.or (Optic radiation)	0.88554	0.09258	0.10234	0.68923	0.44591	0.94576	0.90348	0.38558	0.79110	0.67555	0.06126	0.57543	0.04151*	0.37793	0.73748	0.10215	0.53509
	rh.or (Optic radiation)	0.40744	0.51406	0.55873	0.58123	0.37793	0.47355	0.50544	0.13059	0.62076	0.58452	0.21666	0.65553	0.22879	0.56260	0.87726	0.12483	0.06806
	lh.slf1 (Sup. longi. fasci. I)	0.15908	0.63333	0.56401	0.90859	0.68923	0.27976	0.59337	0.16528	0.14536	0.12052	0.22879	0.68065	0.44340	0.90348	0.07338	0.07911	0.79110
	rh.slf1 (Sup. longi. fasci. I)	0.07296	0.81525	0.76766	0.01706*	0.55873	0.96673	0.95051	0.08317	0.65553	0.43898	0.79110	0.04144*	0.66255	0.85127	0.02079*	0.14220	0.85931
	lh.slf2 (Sup. longi. fasci. II)	0.72511	0.28117	0.38558	0.18734	0.94754	0.48893	0.73748	0.99438	0.68065	0.94576	0.24481	0.02872*	0.80914	0.94754	0.37299	0.41361	0.63611
	rh.slf2 (Sup. longi. fasci. II)	0.21024	0.22879	0.20286	0.21063	0.91947	0.62076	0.76622	0.41752	0.28241	0.79358	0.17818	0.19685	0.98879	0.96673	0.80712	0.30161	0.24805
	lh.slf3 (Sup. longi. fasci. III)	0.62977	0.58452	0.58452	0.28117	0.88333	0.13585	0.44591	0.51924	0.29322	0.95051	0.07985	0.04144*	0.57869	0.69617	0.66255	0.21994	0.88333
	rh.slf3 (Sup. longi. fasci. III)	0.56827	0.27559	0.27559	0.30772	0.85127	0.23052	0.25950	0.37299	0.93165	0.32091	0.21024	0.10903	0.80157	0.97647	0.94576	0.99438	0.50386
	lh.uf (Uncinate fasciculus)	0.08459	0.70011	0.85931	0.85931	0.91258	0.95051	0.85931	0.29322	0.14951	0.85931	0.01954*	0.20503	0.10422	0.90348	0.14008	0.63611	0.73748
	rh.uf (Uncinate fasciculus)	0.42199	0.63016	0.56827	0.79110	0.94576	0.76622	0.65553	0.94754	0.96673	0.19210	0.36650	0.35922	0.56260	0.87726	0.66255	0.56401	0.29916

Table C.7: Table of Kruskal-Wallis H-test p-values of **SKEWNESS** of the distribution of metrics. As rows, all the extracted ROI, as columns, the models' metrics. The TRACULA regions highlighted in yellow where the p-values are calculated without considering the patient `VNSLC_16`. In blue the statistically significant values.

		MF			DIAMOND				NODDI					DTI			
	Region	frac_ftot	fvf_tot	wfvf	frac_ctot	wFA	wMD	wRD	wAD	icvf	fintra	fextra	fiso	odi	FA	MD	RD	AD
tckgen() by MRtrix3	left-thalamus	0.81835	0.59945	0.81283	0.80394	0.18734	0.27529	0.75112	0.49626	0.05732	0.68826	0.44735	0.94384	0.01731*	0.92905	0.16727	0.31438	0.33075
	right-thalamus	0.86241	0.73127	0.92905	0.75772	0.11627	0.08247	0.10702	0.20579	0.08259	0.71698	0.29648	0.64577	0.66686	0.18603	0.19232	0.08616	0.59122
	left-hippocampus	0.38374	0.72450	0.29208	0.94198	0.54603	0.53793	0.46628	0.59945	0.68112	0.06866	0.90501	0.72124	0.88557	0.79987	0.21963	0.66050	0.36578
	right-hippocampus	0.14219	0.43125	0.75622	0.38612	0.44609	0.77522	0.39238	0.91450	0.30772	0.07395	0.76588	0.87219	0.21522	0.54650	0.10232	0.97659	0.87219
	left-amygdala	0.52951	0.26673	0.09691	0.68112	0.65790	0.24214	0.12706	0.53809	0.42629	0.54650	0.11812	0.71054	0.92019	0.98323	0.35371	0.21963	0.41281
	right-amygdala	0.63871	0.96483	0.93299	0.83020	0.60505	0.53778	0.96265	0.94570	0.19238	0.04264*	0.70297	0.69921	0.04581*	0.90552	0.63871	0.23521	0.08849
	left-accumbens	0.64577	0.72593	0.72450	0.82576	0.40565	0.27770	0.80803	0.38809	0.41608	0.52951	0.13133	0.74438	0.39426	0.59945	0.59440	0.20216	0.91812
	right-accumbens	0.22131	0.31438	0.52431	0.64741	0.72124	0.89158	0.94811	0.30341	0.40726	0.29807	0.69921	0.78093	0.17742	0.71194	0.98323	0.72593	0.69941
	left-putamen	0.69783	0.15361	0.24872	0.48070	0.62852	0.88432	0.61053	0.50801	0.11558	0.46575	0.13133	0.20434	0.57059	0.73127	0.55176	0.08694	0.12218
	right-putamen	0.42449	0.27583	0.32328	0.96265	0.11620	0.54388	0.17390	0.07738	0.32704	0.27258	0.54434	0.91450	0.02554*	0.23949	0.65346	0.27258	0.46575
	left-pallidum	0.64577	0.02473*	0.02610*	0.83513	0.93457	0.38169	0.93457	0.27059	0.02168*	0.16207	0.01850*	0.75622	0.61503	0.71194	0.45217	0.41060	0.97549
	right-pallidum	0.96973	0.10555	0.27529	0.48151	0.78734	0.35531	0.50801	0.25403	0.83372	0.88432	0.32917	0.94570	0.20730	0.39773	0.16921	0.27529	0.31607
	left-antThalRadiation	0.59793	0.19776	0.10109	0.50887	0.49139	0.82576	0.16395	0.02473*	0.42282	0.56387	0.37013	0.60505	0.96973	0.35231	0.06118	0.20313	0.32328
	right-antThalRadiation	0.94517	0.79987	0.90961	0.28428	0.02499*	0.18603	0.36578	0.82390	0.44034	0.41281	0.78601	0.58856	0.65512	0.68690	0.20730	0.15361	0.70356
	left-postThalRadiation-parital	0.72124	0.39426	0.28597	0.96837	0.16642	0.78734	0.68690	0.69607	0.34494	0.35601	0.57300	0.83890	0.09115	0.32973	0.46353	0.68112	0.71054
	right-postThalRadiation-parital	0.59793	0.02841*	0.01653*	0.56690	0.16446	0.48070	0.13263	0.99410	0.58856	0.42187	0.74817	0.94811	0.63190	0.45859	0.17707	0.80485	0.91450
	left-postThalRadiation-occipital	0.63190	0.62746	0.27716	0.46575	0.97549	0.49402	0.60199	0.78579	0.97659	0.49402	0.37497	0.30772	0.23902	0.92305	0.30702	0.87416	0.16446
	right-postThalRadiation-occipital	0.70994	0.02807*	0.07930	0.65512	0.94570	0.39975	0.94570	0.80803	0.14219	0.65790	0.21982	0.32621	0.08937	0.79358	0.31876	0.89158	0.83890
	left-supThalRadiation	0.64741	0.65346	0.48642	0.41421	0.77043	0.15501	0.47303	0.20434	0.83725	0.33140	0.87219	0.27552	0.29456	0.34494	0.35601	0.46353	0.23153
	right-supThalRadiation	0.49892	0.03912*	0.03100*	0.25554	0.36178	0.60199	0.36578	0.33497	0.59793	0.81835	0.80485	0.21269	0.51261	0.32328	0.43725	0.46079	0.38374
	left-infThalRadiation-insula	0.33094	0.07345	0.19314	0.41608	0.19461	0.42750	0.20701	0.79807	0.51002	0.86241	0.91812	0.50118	0.09268	0.21522	0.88557	0.60779	0.38612
	right-infThalRadiation-insula	0.33497	0.75772	0.72124	0.81512	0.78601	0.42449	0.85635	0.65512	0.19205	0.93299	0.57869	0.42955	0.38169	0.75836	0.91398	0.90961	0.27770
	left-sup-longi-fasci	0.44773	0.20579	0.17022	0.12785	0.94570	0.06504	0.53566	0.94198	0.52742	0.76286	0.04264*	0.27113	0.61157	0.91038	0.12343	0.40933	0.64869
	right-sup-longi-fasci	0.14474	0.01267*	0.01267*	0.48070	0.98018	0.11922	0.24427	0.48601	0.02012*	0.08825	0.00978**	0.15488	0.53672	0.81512	0.15078	0.16446	0.59490
	left-inf-longi-fasci	0.35043	0.50501	0.75836	0.90552	0.73127	0.69783	0.88432	0.74438	0.52386	0.56022	0.17903	0.73479	0.23205	0.36116	0.33075	0.68690	0.27880
	right-inf-longi-fasci	0.29456	0.48931	0.25104	0.42629	0.34494	0.49139	0.30102	0.32649	0.35371	0.09850	0.50260	0.38612	0.05980	0.14680	0.32973	0.64577	0.95535
	left-fornix	0.23205	0.55316	0.78093	0.14044	0.18260	0.08659	0.41772	0.06017	0.20035	0.09962	0.25793	0.12706	0.17707	0.90961	0.10328	0.25104	0.76286
	right-fornix	0.41421	0.70994	0.77043	0.46353	0.76588	0.45217	0.29648	0.64613	0.36249	0.47303	0.58393	0.96973	0.50501	0.27097	0.78734	0.94517	0.72450
TRACULA by Freesurfer	acomm (Anterior commissure)	0.92905	0.36116	0.46079	0.98323	0.80394	0.10617	0.91038	0.56690	0.01584*	0.24767	0.03006*	0.91398	0.53672	0.78734	0.07228	0.39975	0.52431
	cc.bodyc (Corpus call. body central)	0.13989	0.24214	0.58393	0.88084	0.42750	0.51002	0.44508	0.58393	0.40852	0.14155	0.79515	0.83513	0.27583	1.00000	0.75622	0.41961	0.96973
	cc.bodyp (Corpus call. body parietal)	0.18420	0.12775	0.65790	0.90961	0.32328	0.00782**	0.20701	0.05847	0.05003	0.60779	0.28597	0.93457	0.27529	0.41281	0.91812	0.38612	0.67082
	cc.bodypf (Corpus call. body prefrontal)	0.91398	0.59440	0.83513	0.63190	0.60779	0.46628	0.31253	0.98323	0.12912	0.71054	0.11422	0.44735	0.08259	0.39238	0.83890	0.29456	0.79807
	cc.bodypm (Corpus call. body premotor)	0.18420	0.12775	0.65790	0.90961	0.32328	0.00782**	0.20701	0.05847	0.05003	0.60779	0.28597	0.93457	0.27529	0.41281	0.91812	0.38612	0.67082
	cc.bodyt (Corpus call. body temporal)	0.20216	0.08872	0.31447	0.31332	0.67748	0.03459*	0.49139	0.19760	0.01606*	0.63871	0.64869	0.32973	0.48314	0.64232	0.47210	0.72450	0.75836
	cc.genu (Corpus call. genu)	0.63871	0.13225	0.12912	0.49892	0.52431	0.19086	0.78093	0.68826	0.14001	0.48314	0.91038	0.96483	0.15488	0.56690	0.55645	0.56690	0.73127
	cc.rostrum (Corpus call. rostrum)	0.46079	0.41281	0.59945	0.09268	0.87416	0.63190	0.75836	0.41421	0.12912	0.72450	0.29060	0.19086	0.66293	0.71054	0.15886	0.36578	0.81835
	cc.splenium (Corpus call. splenium)	0.09614	0.60199	0.91038	0.56387	0.54603	0.51261	0.16207	0.83372	0.03198*	0.81835	0.17853	0.75772	0.49402	0.79987	0.44735	0.64869	0.09563
	mcp (Middle cerebellar peduncle)	0.58856	0.38754	0.67082	0.13402	0.54542	0.12434	0.71194	0.68112	0.81835	0.13225	0.69783	0.13225	0.49402	0.04383*	0.35671	0.15841	0.42032
	lh.af (Arcuate fasciculus)	0.92905	0.22732	0.23574	0.98600	0.87219	0.33356	0.31253	0.91812	0.29807	0.51189	0.59440	0.21871	0.65790	0.67748	0.64522	0.68112	0.38612
	rh.af (Arcuate fasciculus)	0.47504	0.07557	0.01861*	0.74880	0.83372	0.14960	0.45217	0.62852	1.00000	0.99382	0.99578	0.48642	0.54650	0.75112	0.53566	0.62852	0.93299
	lh.ar (Acoustic radiation)	0.70994	0.14713	0.05579	0.02488*	0.83020	0.01984*	0.48848	0.03129*	0.15886	0.78734	0.37160	0.29150	0.15606	0.89966	0.32328	0.34407	0.78601
	rh.ar (Acoustic radiation)	0.63853	0.74480	0.63871	0.30102	0.98600	0.20579	0.83513	0.66293	0.88208	0.88208	0.64577	0.47303	0.50801	0.83513	0.35053	0.54434	0.49626
	lh.atr (Ant. thalamic radiations)	0.88084	0.97549	0.69235	0.03045*	0.40933	0.51566	0.21149	0.10001	0.02539*	0.12909	0.04392*	0.04728*	0.07610	0.27583	0.15361	0.03967*	0.19461
	rh.atr (Ant. thalamic radiations)	0.12218	0.64869	0.87416	0.08088	0.32917	0.08832	0.44609	0.22777	0.00760**	0.15440	0.10089	0.06660	0.25561	0.58856	0.11422	0.01293*	0.11023
	lh.cbd (Cingulum bundle dorsal)	0.84508	0.83372	0.88432	0.37160	0.58856	0.46379	0.90501	0.44433	0.10372	0.19760	0.35541	0.21383	0.43725	0.46353	1.00000	0.96265	0.90961
	rh.cbd (Cingulum bundle dorsal)	0.56690	0.08374	0.05830	0.24767	0.80485	0.51002	0.94570	0.91812	0.23205	0.13508	0.75772	0.09067	0.68112	0.87935	0.73790	0.71054	0.27716
	lh.cbv (Cingulum bundle ventral)	0.18931	0.42750	0.42282	0.35043	0.59272	0.11922	0.75772	0.10555	0.68112	0.59490	0.59945	0.58393	0.81835	0.08701	0.42282	0.56690	0.66293
	rh.cbv (Cingulum bundle ventral)	nan	nan	nan	nan	nan	nan	nan	nan	nan	nan	nan	nan	nan	nan	nan	nan	nan
	lh.cst (Corticospinal tract)	0.54218	0.23711	0.15475	0.32741	0.44340	0.57869	0.35586	0.72511	0.51924	0.95051	0.81525	0.24977	0.06345	0.23052	0.52876	0.01189*	0.94576
	rh.cst (Corticospinal tract)	0.26343	0.48527	0.66923	0.54218	0.90348	0.67555	0.21994	0.14951	0.83856	0.74352	0.80914	0.18734	0.18734	0.74352	0.96916	0.40110	0.04028*
	lh.emc (Extreme capsule)	0.10157	0.78517	0.67937	0.83020	0.91258	0.45952	0.75478	0.68065	0.26343	0.87726	0.08459	0.61572	0.35586	0.91947	0.03786*	0.52876	0.70011
	rh.emc (Extreme capsule)	0.40110	0.45694	0.83020	0.52876	0.50544	0.62192	0.42067	0.10903	0.77783	0.90348	0.42199	0.79358	0.45952	0.79358	0.90348	0.74352	0.09931
	lh.fat (Frontal aslant tract)	0.01308*	0.14220	0.08291	0.69617	0.63611	0.12483	0.32192	0.66048	0.05281	0.90348	0.13059	0.51924	0.48527	0.45952	0.03765*	0.26793	0.46648
	rh.fat (Frontal aslant tract)	0.80712	0.24298	0.31851	0.63333	0.33488	0.10215	0.90859	0.73933	0.18923	0.67555	0.55040	0.63333	0.21063	0.25547	0.17552	0.98940	0.21994
	lh.fx (Fornix)	0.94044	0.48527	0.23052	0.63611	0.91947	0.56827	0.25999	0.87726	0.05086	0.10686	0.57579	0.47089	0.18734	0.87726	0.24298	0.87726	0.36193
	rh.fx (Fornix)	0.42624	0.51406	0.83020	0.57543	0.44675	0.69617	0.44675	0.40110	0.10527	0.06453	0.60236	0.57543	0.34017	0.22822	0.46183	0.55040	0.42067
	lh.ilf (Inf. longi. fasci.)	0.44591	0.59337	0.56827	0.68923	0.63016	0.39537	0.70011	0.34858	0.80157	0.60236	0.68923	0.98940	0.27559	0.56260	0.95051	0.20286	0.22879
	rh.ilf (Inf. longi. fasci.)	0.85931	0.60236	0.42919	0.02982*	0.56260	0.44675	0.85931	0.40744	0.32741	0.06600	0.29916	0.15331	0.90859	0.68966	0.21666	0.05956	0.21024
	lh.mlf (Middle longi. fasci.)	0.56401	0.24298	0.28400	0.27559	0.93165	0.96673	0.83856	0.80712	0.63333	0.36650	0.65553	0.42199	0.67937	0.42199	0.27976	0.15331	0.11200
	rh.mlf (Middle longi. fasci.)	0.27404	0.59898	0.66923	0.09057	0.87726	0.03510*	0.27404	0.65553	0.09469	0.62977	0.35586	0.08459	0.69617	0.97464	0.20401	0.15331	0.06806
	lh.or (Optic radiation)	0.96916	0.27404	0.36857	0.95051	0.58452	0.72511	0.74352	0.42199	0.21666	0.58452	0.25691	0.73748	0.01165*	0.56827	0.91258	0.27148	0.43898
	rh.or (Optic radiation)	0.26343	0.36193	0.20286	0.86851	0.24805	0.17552	0.14536	0.28400	0.39537	0.91774	0.32091	0.72511	0.09103	0.33677	0.46971	0.06605	0.09931
	lh.slf1 (Sup. longi. fasci. I)	0.06325	0.52579	0.48893	0.63611	0.63016	0.03619*	0.52876	0.20286	0.02002*	0.27976	0.01354*	0.91774	0.87726	0.91258	0.17291	0.19102	0.98940
	rh.slf1 (Sup. longi. fasci. I)	0.10215	0.32192	0.31140	0.01983*	0.66923	0.06600	0.97464	0.87726	0.10527	0.18734	0.11542	0.06126	0.87726	0.98879	0.00854**	0.10686	0.97464
	lh.slf2 (Sup. longi. fasci. II)	0.62977	0.23578	0.16068	0.62076	0.98879	0.79110	0.70011	0.58452	0.79358	0.38365	0.85931	0.28454	0.51535	0.87726	0.57869	0.40110	0.66255
	rh.slf2 (Sup. longi. fasci. II)	0.07296	0.01885*	0.01432*	0.27559	0.72149	0.03786*	0.45952	0.68065	0.56260	0.85127	0.60539	0.60236	0.91774	0.41361	0.99438	0.33071	0.46183
	lh.slf3 (Sup. longi. fasci. III)	0.38149	0.43898	0.44340	0.90859	0.81525	0.68923	0.56260	0.14876	0.62192	0.29322	0.68923	0.62977	0.36857	0.50544	0.60236	0.45952	0.63333
	rh.slf3 (Sup. longi. fasci. III)	0.32741	0.02392*	0.02392*	0.93165	0.95051	0.59898	0.27976	0.44340	0.41752	0.52579	0.26793	0.97647	0.97464	0.87726	0.47355	0.98940	0.29991
	lh.uf (Uncinate fasciculus)	0.16281	0.24481	0.17586	0.97464	0.94754	0.20905	0.96673	0.09469	0.10903	0.67937	0.05511	0.50544	0.11695	0.90859	0.13315	0.63611	0.62076
	rh.uf (Uncinate fasciculus)	0.48314	0.76622	0.68923	0.83020	0.87726	0.83020	0.80157	0.48893	0.75431	0.53509	0.27148	0.66923	0.29322	0.47355	0.84014	0.73933	0.01639*

Table C.8: Table of Kruskal-Wallis H-test p-values of **KURTOSIS** of the distribution of metrics. As rows, all the extracted ROI, as columns, the models' metrics. The TRACULA regions highlighted in yellow where the p-values are calculated without considering the patient `VNSLC_16`. In blue the statistically significant values.

Appendix D

Radiomics Results

The following are the heatmaps of the scores obtained with all the combinations of univariate and multivariate filtering. The models are followed by an SFS which reduces the number of features into a set that contains the optimizing features with a length variable between one and fifteen.

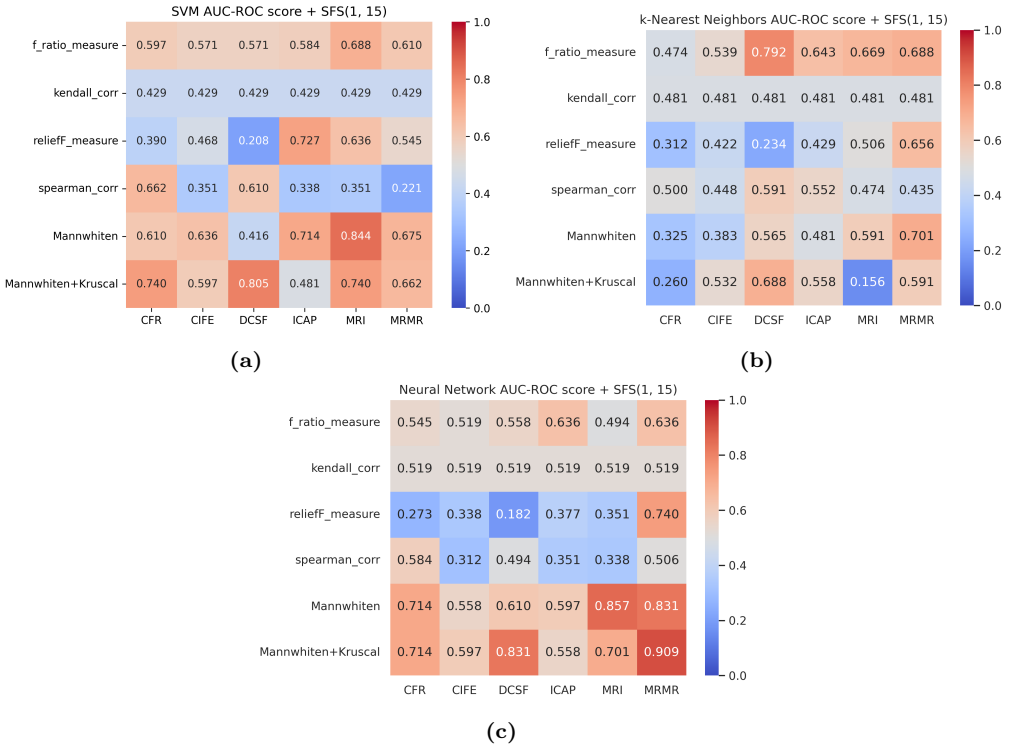

Figure D.1: AUC scores computed from the combination of all univariate and multivariate filters. (a) Scores computed using rbf SVM algorithm; (b) Scores computed using k-Nearest Neighbors algorithm; (c) Scores computed using MLP algorithm.